University of Southampton

Faculty of Engineering, Science and Mathematics

School of Chemistry & Institute of Sound and Vibration Research

An Electrochemical Study of Laser Induced Cavitation

by

Hanne-Maria Hirsimäki

A thesis submitted for degree of Doctor of Philosophy

June 2007

UNIVERSITY OF SOUTHAMPTON

ABSTRACT

Faculty of Engineering, Science and Mathematics
School of Chemistry
Institute of Sounds and Vibration Research

Doctor of Philosophy

AN ELECTROCHEMICAL STUDY OF LASER INDUCED CAVITATION

by Hanne-Maria Hirsimäki

In this project, electrochemical, acoustic and high-speed photographic techniques are used to study laser generated cavitation. The interaction between single bubbles and a nearby solid/liquid boundary is studied in an effort to understand the overall mechanism of cavitation erosion.

The experimental set up has been designed and constructed to create single cavitation bubbles (maximum radius ~ 1 mm) generated by focussing a 532 nm pulsed laser (Nd:YAG) discharge into an electrochemical cell. The conditions such as location, time, dimension and number of bubbles are well controlled and can be varied selectively.

A dual microelectrode is employed to study the electrochemical effects of optical cavitation on erosion of a solid surface (using a passivated 125 μm diameter Pb electrode or 250/500 μm diameter Aluminium electrode) and mass transfer (using a soluble redox species and a 25/50 μm diameter Pt or 25 μm diameter Au electrode) to the solid surface. These electrodes were set into a solid surface in closed proximity (e.g. <100 μm separation) to the laser generated cavitation bubble. The use of these dual microelectrodes has a number of important advantages over previous studies. First, they are small in size compared to the bubbles produced. Second, these electrodes allow the detection of cavitation effects at different locations with respect to the bubble centre. Third, the response time of the electrochemical systems employed allows high temporal definition of the processes occuring during the growth and collapse phases of the cavitation cycle. The experimental set up is optimised and improved throughout the project.

It is shown that electrochemical means are well suited for studying laser generated cavitation. On the erosion sensor, current-time transients are recorded when the laser fires and also when the bubble collapses. New mechanisms to explain how erosion occurs when a surface is exposed to laser-induced cavitation are proposed. On the mass transfer sensor, the bubble growth and collapse are recorded along with secondary collapses.

High-speed imaging has been employed to enable the bubble size and the distance between the bubble and electrode surface to be determined. Hence the results obtained enable further insight into the bubble dynamics of cavitation events. CFD (computational fluid dynamics) simulations that are based on the high speed images are presented. These simulations provide an insight into the events (data for pressure and velocities are given) during the bubble minimum which is too short-lived to be captures accurately by high-speed imaging.

Table of contents

Chapter 1
Introduction 1
1.1 Laser light and optical breakdown 2
1.1.1 Nature of light and laser radiation 2
1.1.2 Focussing geometry 3
1.1.3 Optical Breakdown 6
1.1.3.1 Breakdown Mechanisms 7
1.1.3.2 Plasma Expansion Mechanism - Moving Breakdown Model 8
1.2 Bubble Collapse and Damaging Mechanism 10
1.3 Effect of Bubbles on Electrochemistry 14
1.3.1 Mass Transfer 15
1.3.2 Erosion 17
1.4 Summary of the work presented 18

Chapter 2
Experimental 19
2.1 Optical equipment 20
2.1.1 Laser 20
2.1.2 Development of the optical arrangement 23
2.2 Electrochemical equipment 27
2.2.1 Electrodes 27
2.2.1.1 Mass transfer/Erosion Electrodes (Pb/Pt system) 27
2.2.1.2 Mass transfer electrodes 28
2.2.1.3 Mass transfer/Erosion Electrodes (Al/Pt system) 28
2.2.2 The electrochemical cell 29
2.2.3 Associated Equipment 29
2.3 High Speed Imaging 30
2.4 Measurement of acoustic pressure 35
2.5 Chemicals 35

Chapter 3
Initial experiments with Pb/Pt dual electrode to design the experimental-set-up 37
3.1 Voltammetric characterisation of Pb/Pt electrode 38
3.2 Pt microelectrode as sensor for laser cavitation 39
3.3 Employment of Pb/Pt dual microelectrode for simultaneous mass transfer and erosion studies 41
3.3.1 Varying of the vertical distance between the bubble and the electrode surface 42
3.3.2 Changing the potential 46
3.4 Experiments on a smaller time scale 48
3.5 Conclusions 52

Chapter 4
Mass transfer studies on Au microelectrode 53
4.1 Electrochemical characterisation of gold microelectrode 54
4.2 The effect of applied laser energy on mass transfer 55
4.3 Position of the electrode 61
4.3.1 Lateral position 61
4.3.2. Z approach 67

4.3.3 Damage caused to the electrode surface 69
4.4 Conclusions 71

Chapter 5
Employment of a Pt/Al dual electrode for simultaneous mass transfer and erosion studies73
5.1 Initial experiments on Pt/Al electrode in ferrocyanide 76
5.2 x,y,z-position in ferrocyanide with simultaneous hydrophone measurements 85
5.2.1 Moving the electrode horizontally 85
5.2.2 Moving the electrode in vertical (z) direction 92
5.3 Pt/Al dual electrode in KI system 96
5.3.1 Potential change for Pt electrode in KI 96
5.3.2 Potential change on Al electrode in Na_2SO_4 101
5.3.3 Simultaneous mass transfer and erosion in KI system 108
5.4 Conclusions 116

Chapter 6
High-speed imaging and CFD simulations 118
6.1 The collapse of a bubble at different values of γdetected by high-speed camera 119
6.2 CFD simulations for a bubble collapse 125
6.3 Electrochemical methods combined with high-speed imaging and CFD simulations1139
6.3.1 Mass transfer on Au microelectrode with high-speed images 140
6.3.2 Mass transfer on Pt and erosion on Al with simultaneous high-speed imaging 144
6.3.3 Erosion, high-speed imaging and CFD simulations 151
6.3.3.1 Erosion on Al and high-speed images 151
6.3.3.2 CFD simulations 153
6.4 Conclusions 161

Chapter 7
Experimental problems observed with high-speed imaging 163

Chapter 8
Conclusions and future work 169

Publications 173

Appendix A
Visual Basic Codes 174
1. Stepper motor 174
2. Acquisition software 175
3. Solenoid trigger for single pulses 181
4. Camera Trigger 183

References 185

Acknowledgements

I would like to thank the following people:

Dr Peter Birkin for all his help, enthusiasm and encouragement when I was conducting my research and for his patience while writing this thesis.

Professor Jeremy Frey for his contribution towards this study.

Professor Timothy Leighton for his invaluable help and interest in this work.

Dr Graham Ball and Kylie Osman for their involvement in this research and for the CFD simulations.

Members of the Frey Group for all their help with the lasers, especially the contribution of Lefteris, Tleyane and Jamie has been most valuable.

Doug and Chris for their help with all the cables and electrochemistry stuff.

Dr David Creasey from Photonics Solutions PLC for lending me their spare laser when mine broke down.

The Kingsgate Resource Centre for the use of their computers and printers.

All my friends in England and Finland for their support and friendship throughout the years. Special thanks to Steven for lending me his laptop for several months.

My parents, brother and extended family in Finland (and Norway) for all the support they have given me.

Ashley for everything.

I would also like to acknowledge EPSRC and AWE for funding.

Symbols and abbreviations

Symbols

c	speed of light in a vacuum
c_b	bulk concentration of electroactive species
c_{mat}	speed of light in a material
d	distance between bubble centre and solids surface
D	diffusion coefficient
E_{ph}	photon energy
F	Faraday's constant
h	Planck's constant
K_{sp}	solubility product
i	current
I	irradiance
l	distance
m	mass
n	refractive index
n_e	number of electrons
Q	electric charge
R	ideal gas constant
R_{max}	maximum radius of a cavitation bubble
p	pressure
p_v	vapour pressure
s'	distance between lens and focal point
z	distance
t	time
t_c	collapse time
T	temperature
z	length

ΔG^0	Gibbs free energy
Δz	distance between lenses
γ	d/R_{max}, dimensionless distance between the bubble centre and the solid liquid interface
λ	wavelength
ν	frequency
θ	focussing angle
ρ	density

Abbreviations

ADC	Analogue-to-digital conversion
CE	counter electrode
CV	cyclic voltammetry
fps	frames per second
KD*P	potassium dideuterium phosphate (KD_2PO_4)
Nd:YAG	neodymium (Nd^{3+}) in Yttrium-Aluminium Garnet ($Y_3Al_5O_{12}$)
RE	reference electrode
SCE	saturated calomel electrode
SEM	scanning electron microscope
TOC	total organic content
WE	working electrode

Chapter 1

Introduction

The process called "cavitation" can be defined as a rapid expansion and collapse of bubbles or voids within a liquid media [1-3]. The cavitation process has been investigated extensively since its discovery around the turn of the 20th century [4]. Cavitation has many beneficial applications and bubbles play an important role in several industrial, medical and environmental processes [5-7]. However, parasitic cavitation is a destructive and complex phenomenon that can be extremely costly for industry and is one of the longstanding problems of hydrodynamics and acoustics [8,9].

Cavitation can be generated by a number of different techniques. Hydraulic and acoustic cavitation are the two classical fields of cavitation [10]. Hydraulic cavitation mostly occurs around pumps, turbines and ship propellers [11]. It is a result of rapid pressure decreases caused by the high-speed movement of various bodies in liquid. Acoustic cavitation is caused by the propagation of sound waves through the liquid [12-14].

Cavitation erosion is a process where the bubble or vapour cavity interacts with boundaries destructively [15]. There are two different mechanisms by which cavitation has been observed to cause damage to a solid surface [16]. These are the emission of the shock wave(s) and the generation of a high-speed liquid jet. This jet develops on the side of the bubble opposite to the solid wall. On bubble collapse the jet travels through the bubble and impacts on the solid surface.

When cavitation damage occurs, it usually involves a very large bubble population [15]. Hence a complex physical situation is developed with bubble-bubble, bubble-boundary and bubble-shock wave interactions occurring simultaneously. Hence, it is difficult to perform a quantitative analysis for multibubble cavitation as there are so many unknown parameters. These include the bubble size distribution, number of active bubbles and the acoustic pressure acting in each bubble [17]. Therefore, in order to understand the

overall mechanism of cavitation erosion, it is necessary to study single bubbles and their effect on a solid/liquid boundary.

In addition to acoustical and hydraulic cavitation there is another form of cavitation called optical cavitation where the cavitation bubble is generated by focusing an intense laser pulse into liquid [18-21]. When a laser pulse is focused into water, beyond a certain threshold of power density, dielectric breakdown occurs and a luminous plasma may be formed. This leads to the emission of shock wave(s) and the generation of a cavitation bubble. This has been applied to study the interaction between single bubbles and a nearby solid boundary in an effort to understand the cavitation erosion process [18,20,22,23].

The implementation of lasers to generate cavitation bubbles has many benefits [22-24]. The conditions such as location, time, dimension and number of bubbles are well controlled. The reproducibility is therefore reported to be good and highly spherical bubbles are generated.

The aim of the work presented in this thesis was to design, construct and employ an experimental set-up to study laser-induced cavitation. Electrochemical and high-speed photographic methods are applied to study the damage caused to a solid boundary by laser-induced cavitation bubbles.

1.1 Laser light and optical breakdown

1.1.1 Nature of light and laser radiation

Light can be defined as an electromagnetic wave that is composed of both electronic and magnetic fields. These fields oscillate perpendicular to each other and to the direction in which the light wave is travelling. The waves can be identified by certain characteristics, ie. wavelength λ and frequency ν. The wavelength is inversely proportional to frequency, and can be defined with a simple calculation

$$\lambda = \frac{c}{\nu}, \qquad (1)$$

where c is the speed of light that is a constant in a vacuum. In addition to exhibiting properties of an electromagnetic wave, light also behaves as if it consisted of discrete particles called photons. Photon energy E_{ph} is related to frequency (and thus to the wavelength) by the formula

$$E_{ph} = h\nu, \tag{2}$$

where h is Planck's constant [25-27].

The term laser is an acronym for *light amplification by the stimulated emission of radiation*. Ordinary light such as that from a light bulb is emitted spontaneously, when material release their excess energy in the form of photons without outside stimulus. Laser light on the other hand, as its name suggests, is different. It occurs when an atom or molecule that is holding excess energy is stimulated to emit that energy as light. This process is discussed in more detail in chapter 2. The laser light has some characteristics that make it very useful and different from ordinary light sources [25-29].

- *Monochromaticity*: Most lasers only emit one wave-length (single colour) or a range of wavelengths
- *Coherence*: The emitted waves are in phase with one another
- *Short pulse duration* (pulsed lasers): Pulses come in various duration and repetition rates; ranging from milliseconds to femtoseconds
- *Directionality*: Laser beams have a very small divergence. Because of this, the brightness of a laser beam is much higher than that of ordinary light sources even at low powers.

1.1.2 Focussing geometry

When a light ray passes through one transparent medium to another, it bends. This process is known as refraction of light and the degree of refraction depends on the refractive indices of the two materials. It was stated earlier that the speed of light, c, is constant in a vacuum. However, when the light travels through matter, its speed becomes slower. Refractive index, n, can be defined as the ratio of the speed of light in a vacuum, c, to the speed of light in a material, c_{mat} [25-27].

$$n = \frac{c}{c_{mat}}, \tag{3}$$

Refraction at curved surfaces can bring light rays together or spread them out, depending on the curvature [25,26]. When a light ray travels through a convex lens, it is focussed into a small region within a medium, i.e. focal point. A laser beam can be considered as a set of parallel light rays which are coherent, monochromatic and have a specific divergence that depends on the nature of the laser resonator, the size of the output aperture and diffraction [29]. However, the laser beam cannot be focussed down to a perfect point of zero diameter. The outer parts of the lens have a slightly shorter focal length than the central zone and therefore the positive lens focuses the parallel light rays to a small spot at its focal point [25].

In this project, a high-power laser beam is focussed into a liquid. As a result of this, the liquid breaks down and a plasma is formed. The formation of the plasma is followed by the formation of a cavitation bubble. In order to generate the small plasma required to generate single bubbles at optical breakdown in a liquid, the size of this focal spot should be as small as possible. [30]

There are a few experimental parameters to be considered when single bubbles are generated. According to Philipp [30], the longitudinal aberration at the beam waist should be minimal. The distance, s' between the lens and the focal point should be maximal to avoid the effect of cell wall and lens to the bubble dynamics. The cone angle, 2θ, should be maximal in order that the eccentricity of the plasma is small. Also, small focusing angles can lead to self-focussing which can be seen as filament and continuum formation [31-33]. Other optimising parameters are the thickness and radius of the lenses, lens material and the lens distances. Figure 1.1 presents the aforementioned parameters when a laser beam is focussed into water through a lens attached to the cell wall. Figure 1.2 present a photo taken by Vogel *et al.* [35] which shows the formation of filament-like plasmas (multiple small breakdown sites next to or at small distances from one another along the beam waist) small focussing angles (1.7°and 1.8°). Tomita *et al.* have also studied the optimisation of focussing optics both in theory and practice [20].

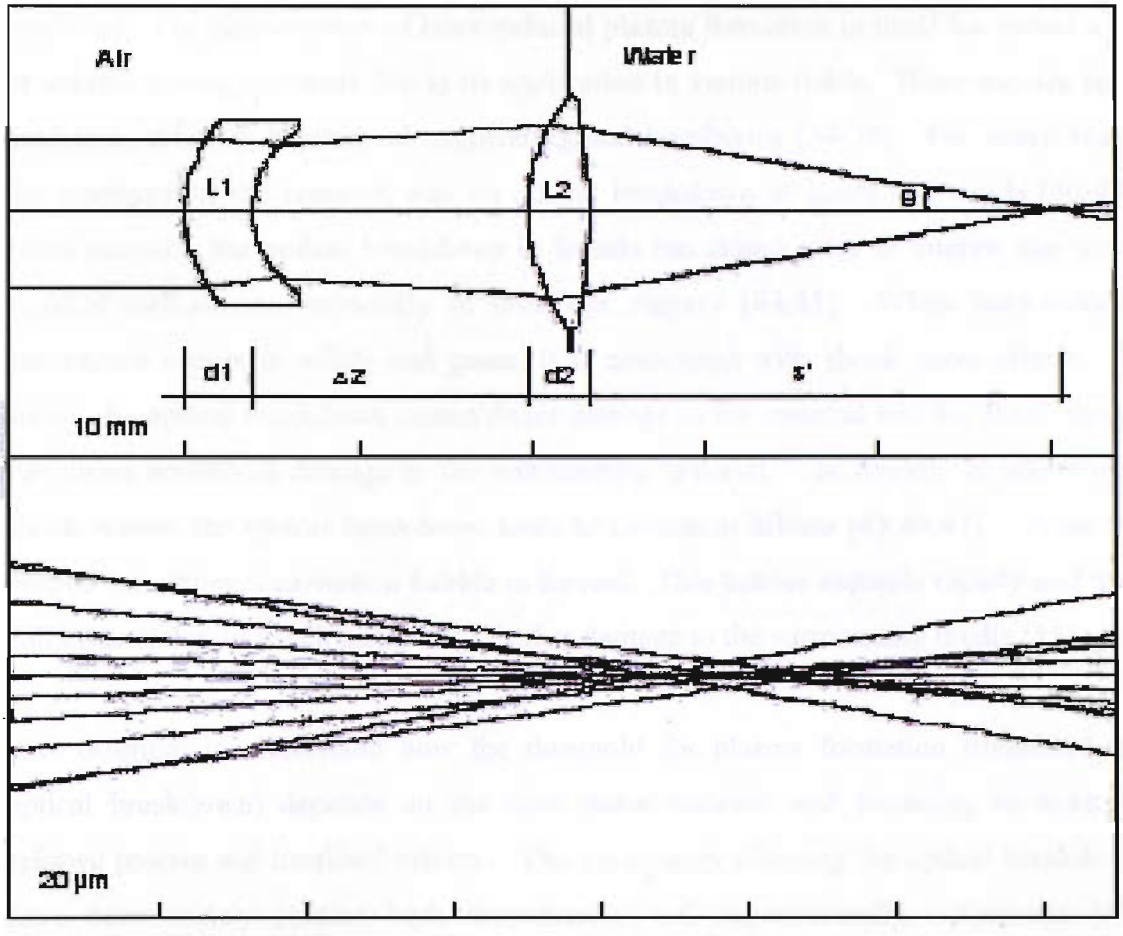

Figure1.1 The parameters when the focusing is optimised. L1 is a converging lens, L2 focusing lens, Δz the distance between the lenses, s' distance between the focusing lens and focal point in water and θ the focussing angle. The length aberration ds' in beam waist is presented in the lower image [30].

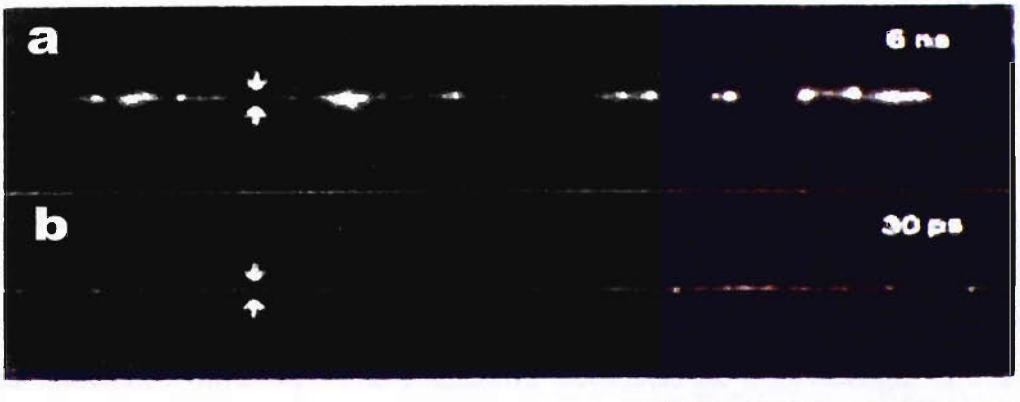

Figure 1.2 Formation of multiple small plasmas (seen as bright spots) at small focussing angles for 6 ns pulse (a) and 30 ps pulse (b). For the 6 ns pulse the focussing angle was 1.8° and for the 30 ps pulse 1.7 °. The focal spot is indicated by arrows [35].

1.1.3 Optical Breakdown

When a laser beam with a very high intensity is focussed into a matter, a plasma can be produced. The phenomenon of laser-induced plasma formation in itself has raised a lot of interest among scientists due to its application in various fields. These include laser medicine, ablation, biomedical engineering and biophysics [34-39]. For many years, the emphasis of the research was on optical breakdown in gases and solids [40-43]. More recently, the optical breakdown in liquids has raised a lot of interest due to its medical applications, especially in laser eye surgery [44,45]. When laser-induced breakdown occurs in solids and gases, it is associated with shock wave effects. In solids, the optical breakdown causes direct damage to the material and the shock waves can cause additional damage to the surrounding material. In liquids, in addition to shock waves, the optical breakdown leads to cavitation effects [43,46,47]. After the plasma formation, a cavitation bubble is formed. This bubble expands rapidly and then collapses violently which can lead to further damage to the surrounding media [23].

It is essential to understand how the threshold for plasma formation (threshold for optical breakdown) depends on the laser pulse duration and focussing in order to achieve precise and localised effects. The parameters affecting the optical breakdown have been widely studied both theoretically and experimentally. Kennedy [48] developed an analytic first-order computational model to calculate laser-induced breakdown thresholds in condensed media, including aqueous and ocular media. Docchio *et al.* [49,50] published theoretical and experimental data to analyse the plasma starting times as a function of the irradiance parameters and of the medium properties in distilled and tap water. Docchio *et al.*[51] also investigated the affect of pulse duration on optical breakdown thresholds and Sacchi [52] the plasma formation theoretically and experimentally for very small focussing angles (up to 1.7°). Vogel *et al.* [35] investigated the optical breakdown thresholds and plasma lengths for a wider range of focussing angles to cover those applied clinically. In most cases the wavelength λ = 1064 nm has been applied in these investigations. This wavelength is employed because it is optimally suited for intraocular surgery, it has a low absorption at the retina and the radiation is invisible. The breakdown thresholds for a wavelength of 532 nm are slightly lower than at 1064 nm because with increasing wavelength more photons are needed to provide the energy necessary for ionisation [35]. In this project the

wavelength of 532 nm is applied in the experiments mainly due to its visibility and therefore easier employment.

1.1.3.1 Breakdown Mechanisms

Dielectric breakdown can be defined as partial or complete ionisation of a solid, liquid or gas through absorption of thermal or electromagnetic energy. In distilled water plasma formation occurs at irradiance above approximately 10^{10} W cm^{-2} [30,35]. Two mechanisms can lead to plasma formation; direct ionisation of the medium by multiphoton absorption and cascade ionisation, also known as avalanche or impact ionisation [36,37]. Both mechanisms can occur in solids, liquids and gases. If the free electron density $\rho = 10^{18}$ cm^{-3} is exceeded during a laser pulse, the ionisation process is called optical breakdown [35].

Cascade ionisation requires one or more free ions to be present in the focal volume at the beginning of the laser pulse [41,53]. If the medium is impure, these seed electrons are most likely to come from ionisation of impurities by heating. In a pure medium seed electrons must be generated by multiphoton absorption [40,53]. Multiphoton initiation of cascade breakdown requires high irradiances (note the calculated value for a 6 ns pulse (1064 nm) is 2.3×10^{12} W cm^{-2}) and therefore seed electrons provided by impurities can significantly lower the breakdown threshold [35,36].

In cascade ionisation the process begins when the seed electrons absorb laser photons during collisions with heavy particles, which can be molecules or ions. This is also known as inverse bremsstrahlung absorption [54]. If the free electrons sustain enough favourable collisions, they can achieve enough energy (energy greater than the ionisation potential) to ionise a bound electron by collision and produce two free electrons of lower energy. When this process is repeated an electron cascade leading to optical breakdown and plasma is generated. The free electrons of the plasma strongly absorb the laser radiation. This leads to rapid heating of the plasma to the temperatures on the order of 10^{40} K producing a visible plasma emission and plasma pressures as high as 10^4-10^5 bar [36,55]. The high temperatures and pressures lead to plasma expansion at supersonic velocities, producing an audible acoustic signal, shock waves and cavitation effects. [30,35-37]. It was stated in the previous paragraph, that if the medium where optical breakdown is impure, these impurities are the likely source of the initial seed

electrons. Docchio [48] *et al.* noticed significant differences between plasmas generated in distilled and tap water. They observed dissimilarities in structure of the plasma column, irregularities in the plasma starting time, wandering of the 'spark' with respect to the focal plane at threshold, existence of multiple and distinct breakdown sites in the plasma column which could all be explained by presence of impurities that were randomly located within the focal volume which acted as preferential sites for optical breakdown. To avoid these problems, it is essential that all the impurities are removed from the medium before the beginning of the experiments.

In pure multiphoton breakdown each electron is independently ionised by simultaneous absorption of multiple photons. Therefore, no seed electrons, collisions or particle-particle interactions are required [36,53]. The process is much faster than cascade build-up and can therefore occur even for the shortest of laser pulses [36,37].

Multiphoton ionisation process is significant at very high irradiances and the threshold for multiphoton breakdown is typically higher than for cascade breakdown. Therefore, cascade ionisation is the most common of the two breakdown mechanisms [36]. Multiphoton ionisation is dominant in the femtosecond pulse regime, where the field may not be present long enough for cascade ionisation. However, the breakdown mechanisms are different at 1064 nm and 532 nm. In the visible range, multiphoton ionisation plays a larger role than in the infrared and both mechanisms contribute the breakdown of liquid [35,36].

1.1.3.2 Plasma Expansion Mechanism - Moving Breakdown Model

After its initial generation, the formed plasma grows as it absorbs more laser energy. The plasma formation starts at the focus of the laser beam, and the plasma expands towards the incoming laser beam. Over the years, three models have been suggested to explain the expansion of the plasma. The first model interprets the plasma growth as a radiation supported detonation wave [56]. According to this model, a shock wave is generated at the point where the optical breakdown first occurs. This shock wave then expands isotropically and gains energy at the expense of the incoming laser beam. This model can be valid in gases, but is not applicable for liquids [35]. The recorded plasma expansion velocities are much higher than that of shock waves. Vogel *et al.* [57]

reported shock wave velocities of 4.5 km/s, whereas plasma front velocities between 12 km/s and 76 000 km/s have been recorded [35]. The second model, so called ionisation wave model, suggest that at the focal point the light interacts with free electrons and the formed plasma expands from that region by diffusion. However, the velocity of particles in liquids is also limited; velocities of the order 10^4 m/s have been reported which is not enough to explain that plasma expansion rate [58]. The third model is called the moving breakdown model and this model is now widely accepted to explain the plasma expansion mechanism. This model was first suggested by Razier [59] and further developed by Docchio *et al.* [49]. This model suggests that optical breakdown occurs independently at different locations along the beam axis provided that the irradiance of the electric field equals the breakdown threshold value.

Figure 1.3 presents a diagram that illustrates the moving breakdown model [49]. The geometrical structure of a (half) Gaussian beam is presented in figure 1.3 a), where $z = 0$ is the beam focus. The shaded areas illustrate the spatial distribution of the power at two different locations along the beam axis. The temporal shape of a laser pulse at some axial locations is presented in figure 1.3 b). The left edge of each shaded area illustrates the instant when breakdown occurs at t_i corresponding to the axial location z_i. At t_0 the peak power is twice the value of threshold irradiance (indicated by a line labelled I_{th}). The irradiance reaches its threshold value before the pulse reaches its peak. For later values of t, the threshold breakdown values are met at distances further away from the focal point as the power of the pulse increases. When $z = z_{max}$, breakdown only occurs at the peak of the pulse. Beyond that point, the breakdown no longer occurs.

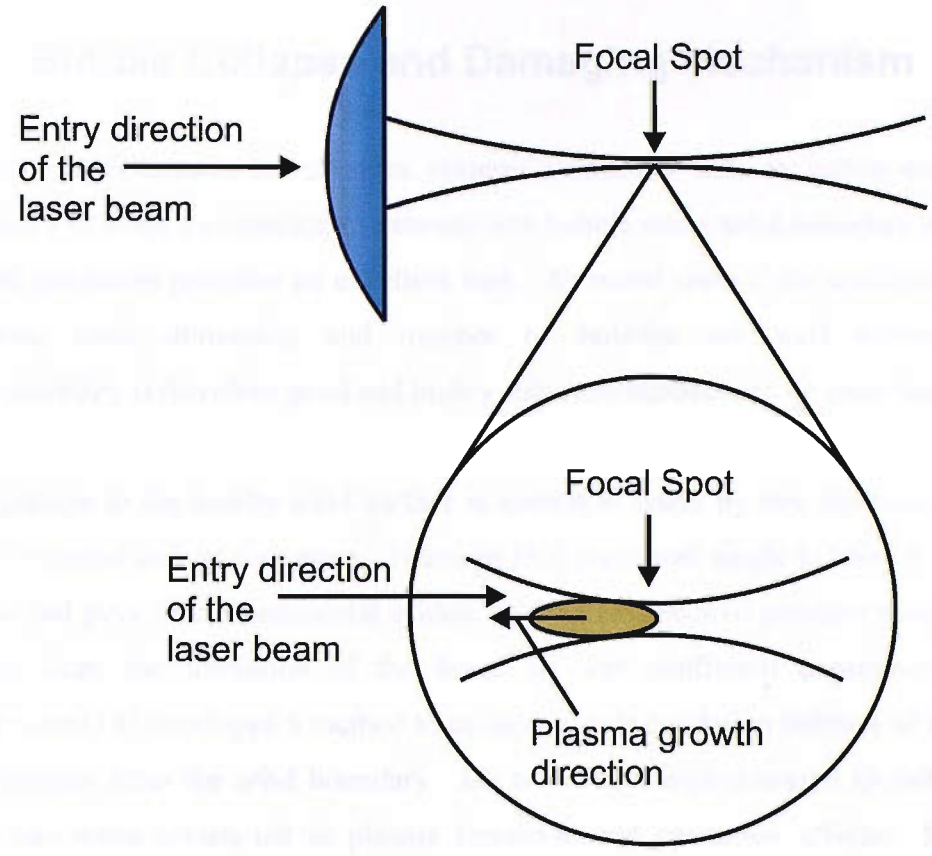

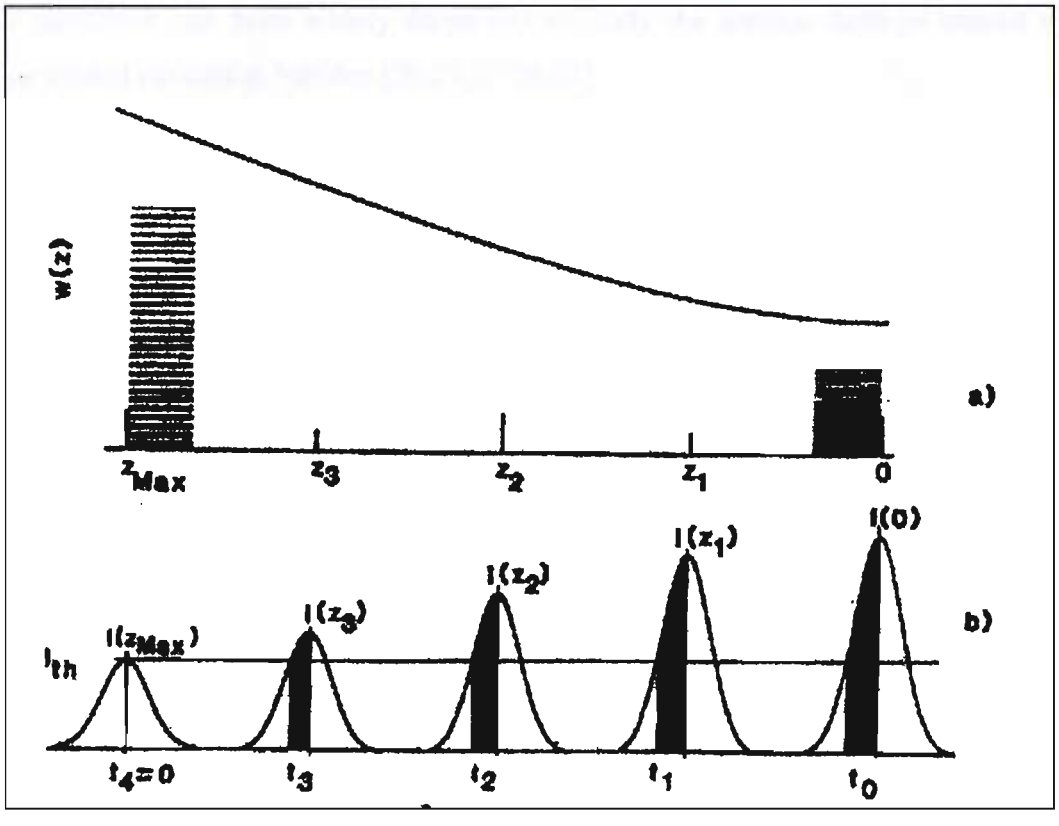

Figure 1.3 Illustration of the moving breakdown in liquids when the plasma grows towards the entry direction of the laser beam as the laser energy increases during a Gaussian pulse. z is the location along the beam waist, $w(z)$ the radius of the beam waist at the location, I_{th} the threshold irradiance for the optical breakdown, t is time and I is irradiance [49].

1.2 Bubble Collapse and Damaging Mechanism

In order to understand the complex systems associated with cavitation erosion, it is necessary to study the interaction between one bubble and a solid boundary and for this optical cavitation provides an excellent tool. As stated earlier, the conditions such as location, time, dimension and number of bubbles are well controlled. The reproducibility is therefore good and highly spherical bubbles can be generated.

The damage to the nearby solid surface is known to occur by two mechanisms, shock wave emission and jet formation. Harrison [60] generated single bubbles by a venture nozzle and gave first experimental evidence of the existence of pressure pulses. Over a decade later, the formation of the liquid jet was confirmed experimentally [61]. Lauterborn [18] developed a method to produce single cavitation bubbles of known size and distance from the solid boundary. He focussed a high-powered Q-switched ruby laser into water which led to plasma formation and cavitation effects. Since then, optical cavitation has been widely employed to study the surface damage caused by laser-generated cavitation bubbles [20,21,23,24,62].

When the optical breakdown occurs in a liquid and a plasma is formed, very high temperatures and pressures are present (10^{40} K, 10^{4}-10^{5} bar [36]). These high temperatures and pressures lead to the fast expansion of the plasma, shock waves and cavitation bubble formation. Since the pressure inside the bubble is higher than the pressure of the fluid that surrounds the bubble, the bubble expands rapidly. When the volume of the bubble increases, the pressure inside the cavity decreases until the maximum bubble volume is reached. The bubble begins to collapse as the pressure inside the bubble is now much lower than the static ambient pressure surrounding the bubble due to the rapid expansion. Shock waves that can have amplitude of up to 1 GPa are emitted when the bubble collapses. If this process takes place near a solid boundary the surface can be eroded. After this primary collapse the bubble rebounds and collapses again, this cycle can be repeated several times [20,21,23,24,62].

As well as the shock wave erosion, damage to a solid interface has been observed as the result of microjet impact [63,64]. The microjet is formed when the bubble collapses near a solid boundary. The uneven collapse is a result of pressures differences on each side of the bubble. The pressure is lower at the side of the bubble that is closest to the

solid surface. The jet is seen as a funnel shape protrusion directed towards the solid boundary. The microjet is caused by uneven collapse speeds on either side of the bubble driven by the differences in pressure; the bubble surface closest to the solid/liquid boundary collapsing slower than the bubble surface far from the same boundary. The jet formation has been investigated extensively by means of high-speed imaging, microscopy and pressure transducers [21,65-69]. Jet velocities of the order of 120 m s^{-1} have been observed experimentally [21,30]. Theoretical and experimental bubble shapes on collapse are presented in figure 1.4 and figure 1.5 shows the outstanding photograph of a microjet. [21,23,70-73].

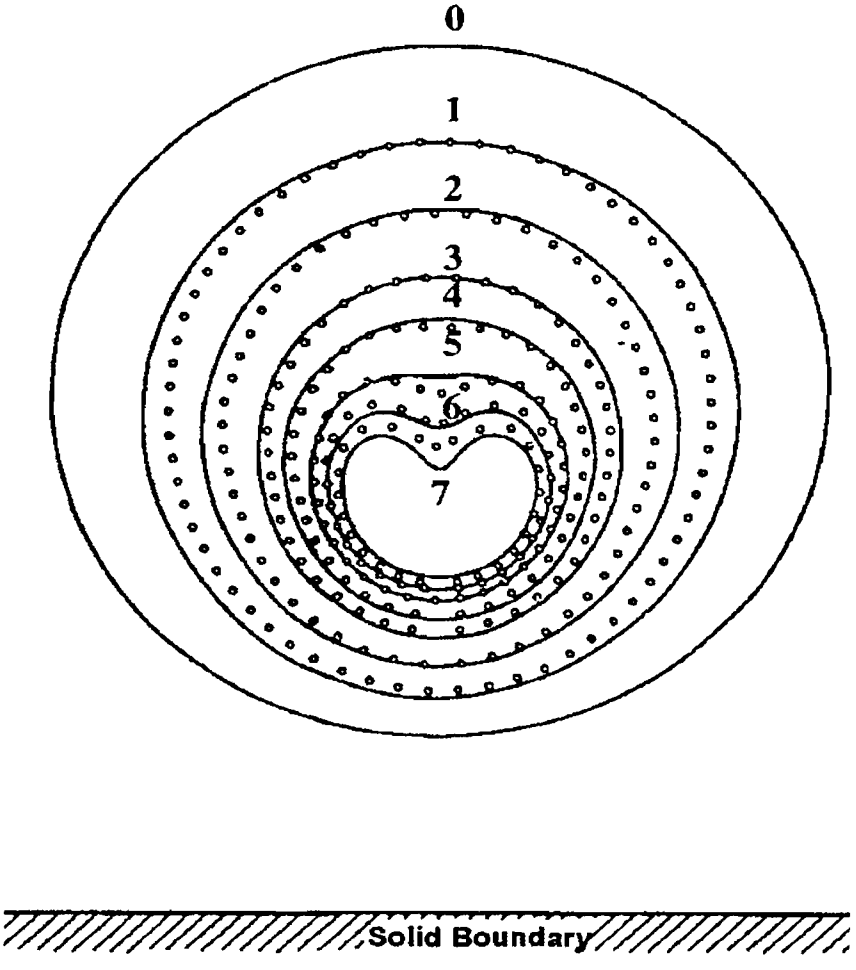

Figure 1.4 Comparison of experimentally determined bubble shapes on collapse (o) of a spherical bubble near a plane solid wall with theoretical curves (—). The framing rate is 300 000 frames/s, initial bubble radius 2.6 mm and the distance of the bubble centre from the wall 3.9 mm [73].

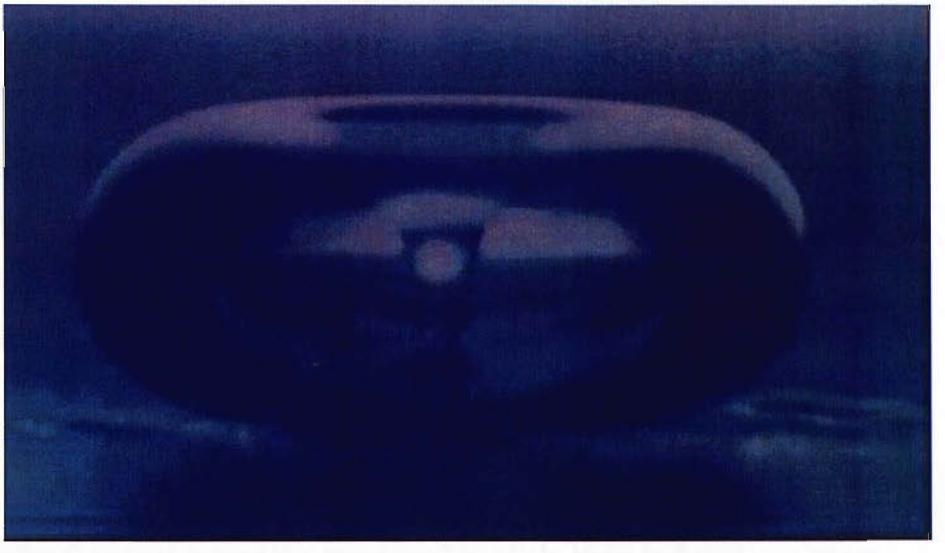

Figure 1.5 The formation of a jet at the collapse phase of an oscillating bubble at low pressure (4-5 kPa) in a 60 Hz sound field [70].

In the absence of the solid boundary, the size of the generated bubble R_{max} can be calculated using Rayleigh's formula

$$R_{\max} = 1.09\sqrt{\frac{p - p_v}{\rho}}t_c, \qquad (1)$$

where p is the ambient pressure, p_v the vapour pressure, ρ density of the liquid and t_c the collapse time for undisturbed, spherical bubble. The damage mechanism depends on the dimensionless distance, γ, between the bubble and the solid liquid interface

$$\gamma = \frac{d}{R_{\max}} \qquad (2)$$

where d is the distance of the bubble centre from the wall at the moment of formation. Damage to a solid surface can be observed when the bubble is generated at a distance less than twice its maximum radius from the solid boundary (γ= 2). If the jet alone was responsible for the damage caused to the surface, one would expect a single indentation below the centre of the bubble. However, the liquid jet has only a minor part in the erosion process, it is significant only when bubbles are formed very close to the solid surface (γ= 0.7). Most of the damage to the surface is thought to originate from shock wave emission during the collapse phase of the bubble [21,74]. Philipp *et al.* [21] also

reported that the bubble touches the surface during its second collapse if $\gamma < 1.9$ and during its first collapse if $\gamma < 0.9$. Thus, the high pressures and temperatures that are present during the violent collapse of the bubble can affect the surface destructively. Largest damage was created by bubbles that were in the range $\gamma < 0.3$ and $\gamma = 1.2$ to 1.4, under these circumstances, the diameter of the damaged area was proportional to observed bubble size.

1.3 Effect of Bubbles on Electrochemistry

In this project, electrochemical means are employed to study laser induced cavitation. These methods can be divided into two categories, those to detect mass transfer events and those that detect surface erosion. When a material is exposed to cavitation for a long period of time, different forms of material damage occurs such as void formation. In most cases, the erosion damage to a surface has been observed as loss of mass or volume by employing photographic means to record the surface damage caused by cavitation effects [21].

The phenomena of cavitation erosion has been investigated in a multidisciplined research effort [75]. The cavitation of a liquid can generally be defined as the activation of pre-existing nuclei to form stable or transient bubbles or voids in the liquid structure. The most commonly employed technique to generate transient cavitation is the application of power ultrasound to a solution. The power ultrasound can create localised transient high temperatures and pressures, as a result of cavitation, in solutions with relatively low bulk temperature. For short periods of time temperatures of ca. 5000 K and pressures of 500 atmospheres have been observed in the interior of the cavitation void [14,76]. These 'hot spots' contain approximately 500 molecules and the associated liquid sphere (ca. 200 nm thick at 1900 K) are thought to be the source of the beneficial effects of ultrasound on chemical reactions [14,77]. Under certain physical conditions, irradiation of a liquid with ultrasound can destroy the homogeneous nature of the liquid which results in cavitation phenomenon. Ultrasound can therefore be employed in chemistry in many systems, some of which are advantageous, such as improved yields and altered product distribution [76,78,79].

The study of the effect of acoustic cavitation on electrochemical processes is widespread and dates back to the 1930s [75]. Ultrasound was employed as a mass transfer enhancement tool by Bard in 1963 [80]. The mass transfer enhancements as the result of ultrasound can be attributed to a variety of mechanisms produced as a result of the exposure of the liquid to an acoustic field. These include transient collapse of cavitation bubbles near the solid surface to produce microjets directed at the surface, transient bubble motion, microstreaming and acoustic streaming [16]. Several authors have reported the effects of ultrasound on mass transfer to an electrode [75,81-84]. The surface effects on the other hand, can only be associated with shock wave impact and microjet [85]. Electrochemical investigations of the effects of ultrasound on surface erosion processes have also been reported. These include studies on the effects of high intensity ultrasound on metal oxide films, glassy carbon, platinum and aluminium and on polymer films deposited on to the electrode surfaces [86-91]. In these studies, the investigation was partly performed *ex-situ* with the effects of erosion studied after the material had been exposed to cavitation. Worth mentioning is work completed by Perusich *et al.* who developed a method for testing the hardness of an oxide film on an iron or cast iron electrode exposed to ultrasound [86,87]. This work demonstrated the effect of ultrasound on an electrode covered by an oxide film, but the individual effects of single bubbles were not covered. However, it is possible to detect single cavitation bubbles by electrochemical means [92]. Macroelectrodes do not have sufficient spatial resolution to detect individual cavitation events, but microelectrodes (also known as ultramicroelectrodes, electrodes that usually have a diameter <50 μm) provide an excellent tool for this purpose [92-95] Microelectrodes are small in size compared to macroelectrodes and therefore individual cavitation effects can be recorded. Additionally, due to the diffusional characteristics of microelectrodes, the compressed diffusion field relaxes back to a steady state situation relatively fast in comparison to macroelectrodes. This enables the microelectrode to be prepared for the next cavitation event.

1.3.1 Mass Transfer

When an electrochemical process occurs on the surface of a microelectrode under steady state conditions (e.g. stagnant solution and mass transfer limited potential), the rate at which species travel to and from the electrode is diffusion-controlled and a hemispherical diffusion field is built around the electrode. If the diffusion hemisphere

is disturbed then the depleted layer around the electrode becomes refreshed. Therefore, any fluid flow in the vicinity of the microdisc, such as that caused by bubble motion or microjetting following the bubble collapse, can be detected as transient current peaks. Figure 1.6 presents a schematic diagram for the events on microelectrode surface. In figure 1.6 a) the hemispherical diffusion field (yellow) is present on the electrode surface. At this state, a steady state current is recorded. In figure 1.6 b) a bubble is formed but is still outside the diffusion field and the current remains at steady state. In figure 1.6 c) the situation changes. The growing bubble now disturbs the diffusion field which is seen as an increased current. This current is further increased in figure 1.6 d) when the bubble expands further. After the cavitation events are finished, the diffusion field surrounding the electrode is reformed and this is seen as the current slowly returning to the steady state level.

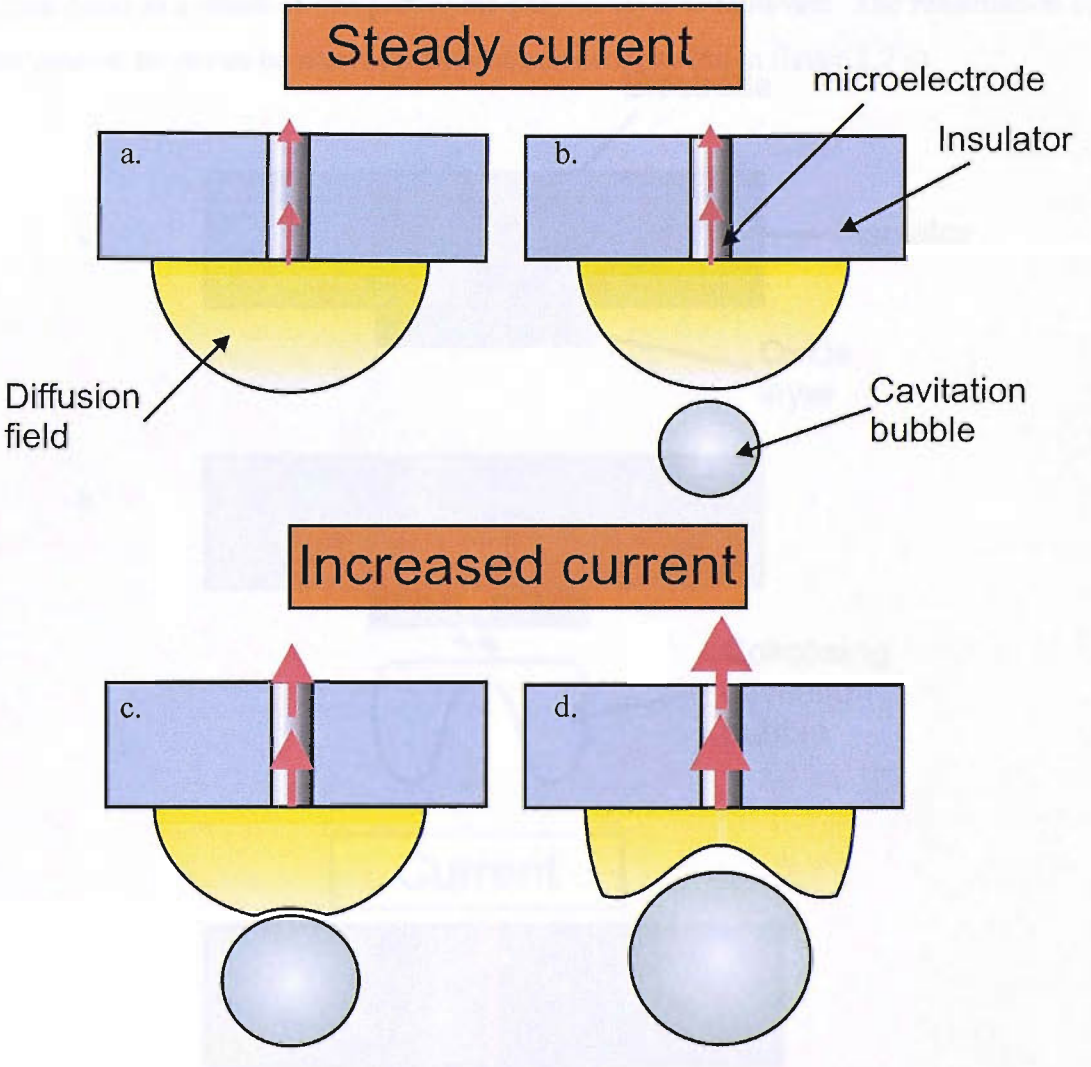

1.6. Mass transfer enhancement on a microelectrode caused by cavitation bubble formation. Red arrows show electron flow (considering $R \rightarrow O + e^-$).

1.3.2 Erosion

Cavitation erosion has been widely investigated due to the damage it can cause to hydrodynamic devices such as propellers and turbines. However, only a few examples of employment of electrochemistry to study it exist. As stated earlier, erosion can only be caused by microjets and shockwaves whereas mass transfer enhancement is sensitive to many different mechanisms. First, single cavitation events were recorded by Birkin *et al.* when they employed passivated electrode surfaces of lead and aluminium to investigate erosion events produced by ultrasound [81]. Figure 1.7 presents a schematic diagram for the events on the surface of an erosion sensor when a bubble collapses. In figure 1.7 a), the electrode surface is passivated (the electrode is held at a certain potential where its surface becomes passivated) and no current is observed. In figure 1.7 b) a bubble collapses near the surface and as a result of this part of the passive layer is removed. The reformation of the passive layer can be seen as a current transient as seen in figure 1.7 c).

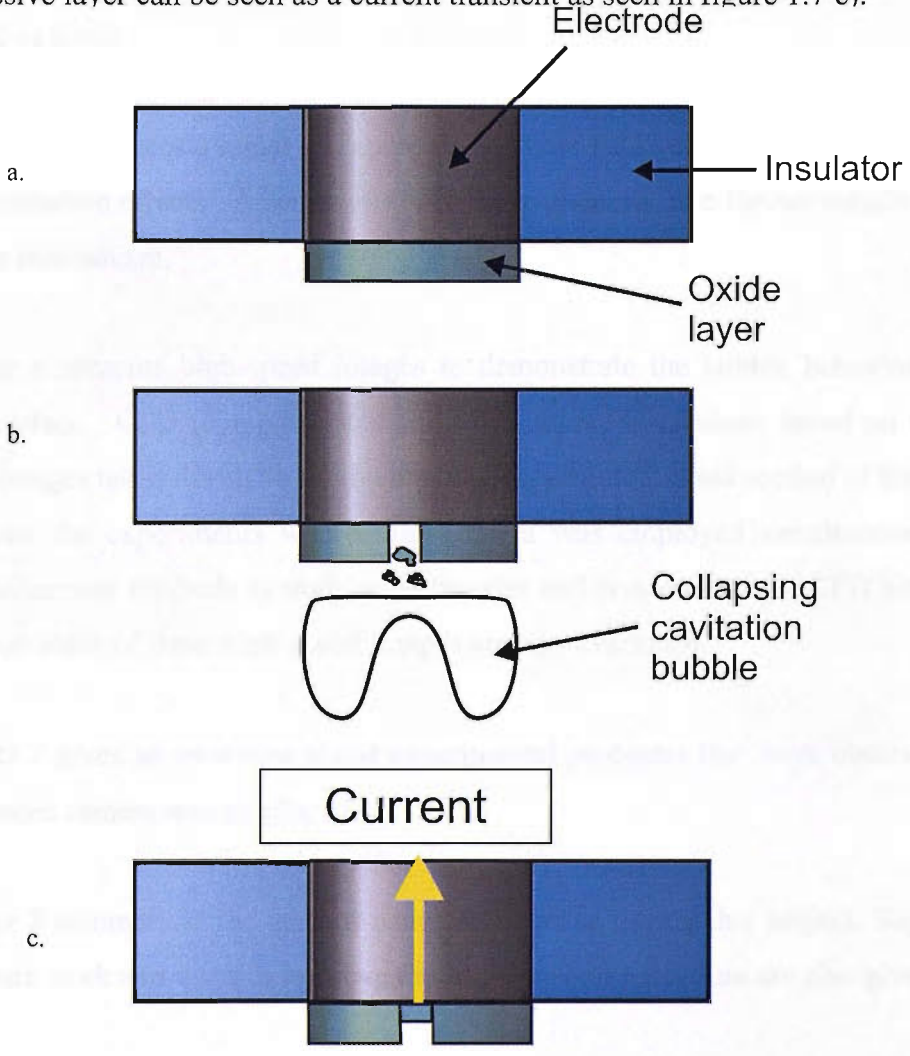

1.7. Employment of a passivated electrode to detect surface erosion events.

1.4 Summary of the work presented

The primary aim of this project was to develop and construct an experimental set up that used electrochemical, acoustical and high-speed photographic techniques to study laser cavitation and employ this system to run experiments.

Chapter 2 gives the details about the experimental techniques and procedures that are employed throughout this project.

Chapter 3 discusses the initial experiments where Pb/Pt microelectrode was employed to study mass transfer and erosion simultaneously with high speed imaging.

Chapter 4 concentrates on mass transfer studies on Au microelectrode in the absence of the erosion sensor. The effect of the distance between the bubble and electrode is studied in detail.

Chapter 5 introduces a range of experiments where Pt/Al electrode was used to study laser cavitation effects. A series of detailed experiments give further insights into the erosion mechanism.

Chapter 6 presents high-speed images to demonstrate the bubble behaviour near a solid surface. CFD (computational fluid dynamics) simulations based on the high-speed images taken during this project are also presented. Final section of this chapter discusses the experiments where high-camera was employed simultaneously with electrochemical methods to study mass transfer and erosion events. CFD simulations based on some of these high-speed images are also examined.

Chapter 7 gives an overview about experimental problems that were observed when high-speed camera was employed.

Chapter 8 summarises the general conclusions made during this project. Suggestions for future work and ways to improve the experimental procedure are also given.

Chapter 2

Experimental

This chapter contains a detailed description of the experimental equipment and techniques that were used to study the optical cavitation. Electrochemical and acoustic techniques in conjunction with high-speed imaging were employed to obtain the results presented in this thesis. The experimental set-up was developed at Southampton and improved throughout this project. Figure 2.1 presents the final experimental set-up employed. This system produced one large cavitation bubble by focussing an intense laser pulse into a liquid. Before entering the cell, the laser beam travelled through a lens system (labelled as L_3, L_2, L_1, see figure 2.1). The activation of the laser Q-switch triggered the electrochemical and high-speed imaging equipment required to capture the cavitation events and record their local effects on mass transfer and erosion of an electrode surface (see chapters 3, 4 and 5).

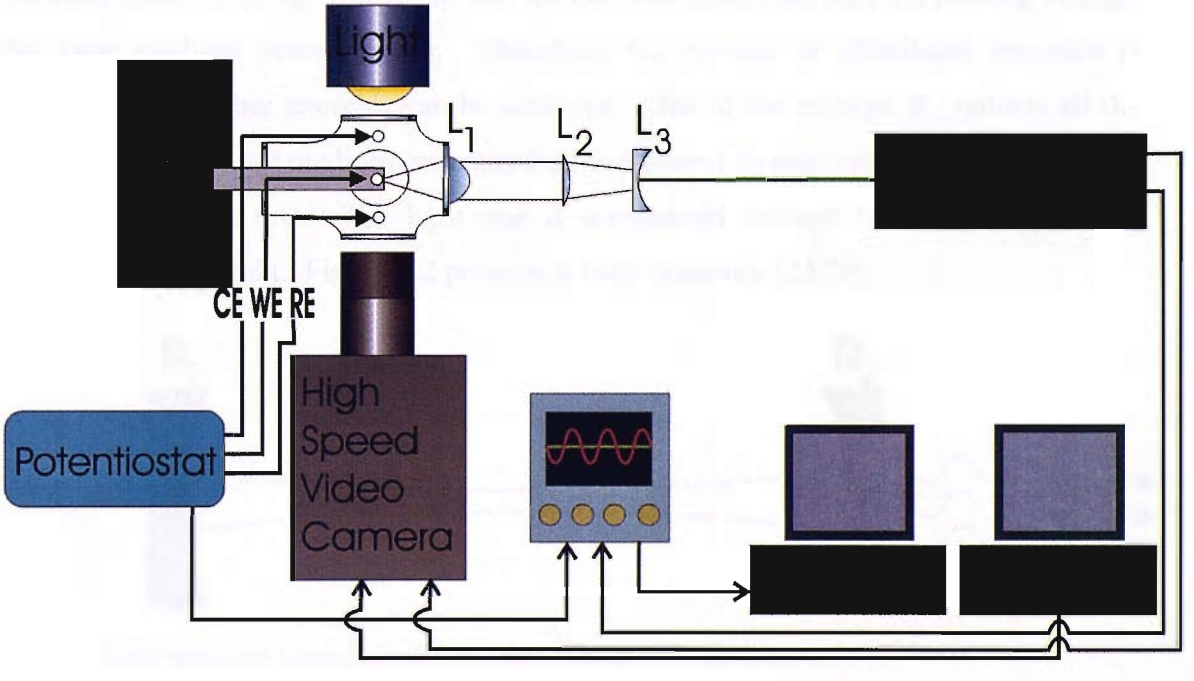

Figure 2.1 Experimental set-up for electrochemical experiments, where CE is the counter electrode, WE working electrode, RE reference electrode and L lens. Two computers were employed as one was used to control the camera and one to control the rest of the equipment.

2.1 Optical equipment

2.1.1 Laser

Cavitation bubbles were generated by focussing an electro-optically Q-switched frequency-doubled Nd:YAG (532 nm) laser into an electrochemical cell.

The atoms of the active medium inside the laser are pumped into a higher level where they are in an excited state. The atoms in the excited state sustain more energy than the atoms in the non-excited state. If more atoms are in the higher level than in the lower level (non-excited state), a population inversion is generated. Some of these atoms emit photons when they return to the non-excited state. Some of these photons run in a direction parallel to the axis of the active medium. As they pass through it, they stimulate emission in other atoms. These photons all have the same wavelength and they are in-phase with one another [25,26].

Inside the laser, there is a pair of mirrors R_1 and R_2 with the active laser medium between them. The light moves to and fro between these two mirrors, passing through the laser medium several times. Therefore, the amount of stimulated emission is increased and higher energies can be achieved. One of the mirrors, R_1 reflects all the light back to the laser medium, whereas the other mirror R_2 only reflects part of the light and transmits the rest. The light that is transmitted through the output mirror R_2 emerges as laser light. Figure 2.2 presents a laser resonator [25,26].

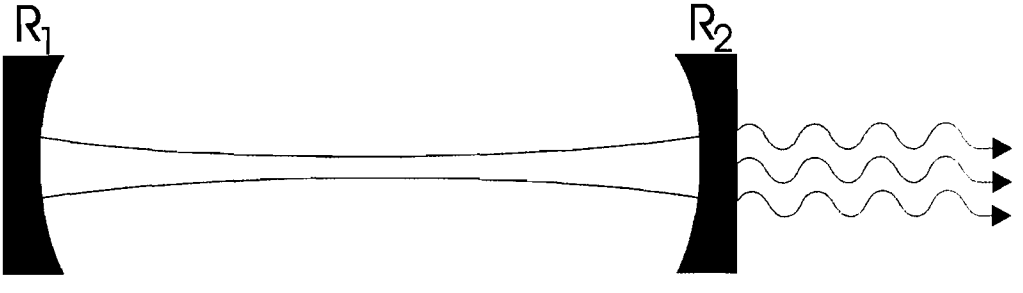

2.2 Laser resonator, where R_1 is the rear mirror and R_2 the output mirror.

In this project a Nd:YAG laser is employed. This is a solid-state 4-level laser, where the active medium is Neodymium (Nd^{3+}) that is doped in Yttrium-Aluminium Garnet ($Y_3Al_5O_{12}$) host crystal. The laser is pumped optically, where the neodymium atoms are

excited from the ground (level 1) to upper laser (level 4) by flashlamp pulses. Level 4 is a very short-lived high-energy level, therefore the atoms drop quickly to level 3 which is metastable and has a much longer life-time and therefore, a population inversion is generated. From level 3 the laser transition transfers the Nd^{3+} atoms to short-lived level 2, from where they return to the ground level 1 [25]. Figure 2.3 presents a 4-level laser.

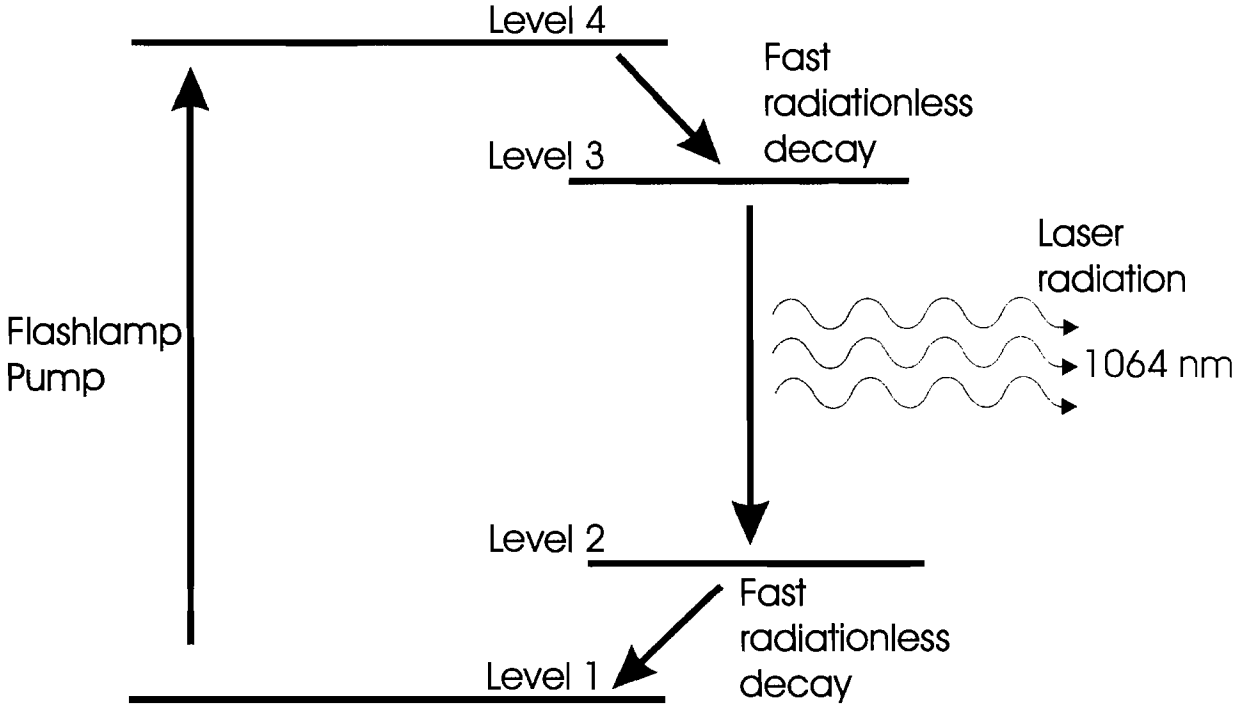

Figure 2.3 The operation of a 4-level Nd:YAG laser. The arrows represent movement of electrons between molecular energy levels that are represented by the horizontal lines.

Laser Q-switching enables the generation of short, high energy pulses. When the laser is Q-switched, the beam is allowed to travel back and forth between the mirrors only for a short time, whilst the pumping action is continuous and therefore a large population inversion is created. Q-switching is achieved by employing a device called a Pockels cell, where a combination of an electro-optical switch and a polarizer does not transmit the radiation. During Q-switching, a voltage pulse is applied which rotates the plane of polarisation by 90° and allows the light to pass. When the switch is triggered the polarizer now transmits the radiation and lasing takes place, and as the population inversion is large, the gain is large and a large pulse is produced quickly [25-27].

The fundamental oscillator output of all the employed lasers was λ = 1064 nm. The frequency was doubled by passing through a KD*P (KD_2PO_4) second harmonic crystal

to give a wavelength of 532 nm, which was used as the fundamental operating wavelength for the laser in all the experiments reported in this thesis.

Three different lasers were employed in this project due to malfunctions with the first laser (see table 2.1). The first laser employed was a Continuum Surelite NY61. The second laser used in the experiments was a Continuum Surelite-II with a type II doubler that was temporarily borrowed from the Photonics Solutions PLC when the Continuum Surelite NY61 broke down. The third laser that was employed in the experiments was a Continuum Inlite II-10 bought from Photonics Solutions PLC. This laser was operated with software provided by the manufacturer which was used to start, stop, flash and open the Q-switch. The shutter, voltage adjustment, flash repetition rate and the Q-switch firing time and frequency were also controlled with the software. The software also monitored and updated the laser system status including faults, conditions and errors. Table 2.1 presents the pulse length, beam diameter, operation frequencies and maximum energy for each laser employed in this project.

Laser	**Pulse duration/ ns**	**Beam diameter/ mm**	**Repetition rate/Hz**	**Maximum Energy at 532 nm mJ/pulse**	**Sections used**	**Comment**
Continuum Surelite NY 61	6-8	6	5, 10, 20	83* 260** 120***	Chapter 3	*) Bad beam shape due to cracked amplifier rod. **) Rod replaced by a rod from another laser, polariser and other inner optics optimised. ***) Satellites observed next to the beam. Coupling mirror damaged, rod damaged too. Laser replaced.
Continuum Surelite SL –II	5	6	1-20 Option for single shots.	170	Chapter 4,6,7	Temporary laser borrowed from Photonics Solutions PLC.
Continuum Inlite II-10	6.5	6	1-20	140	Chapter 5,6,7	Laser bought from Photonics solutions PLC to replace the broken Continuum Surelite NY 61.

Table 2.1. Pulse length, beam diameter, operation frequencies, maximum energy, chapters where certain laser used and comments for each laser employed in this project. The *-symbols indicate the problems encountered with this laser at different times throughout the project.

2.1.2 Development of the optical arrangement

In order to generate cavitation from a focussed laser beam it is necessary to create optical breakdown. In this case the laser beam has to be focussed into the liquid (for details about optical breakdown, see Chapter 1). Therefore, before entering the cell, the beam was directed through a lens system. The original optical arrangement was altered gradually after initial experiments to find the optimal lens system. The first attempt to generate cavitation events was performed by focussing the beam by a planoconvex lens with a focal length of 100 mm. The beam was directed into the electrochemical cell by two mirrors and before entering the lens system it also travelled through a number of irises to improve its shape. This initial experimental arrangement is presented in Figure 2.4. Later on in the project, when the Continuum Inlite laser was employed, the mirrors and iris were removed and the beam was directed straight into the electrochemical cell, as reflecting from mirrors along with a long optical path can diminish the quality of the beam and the beam shape no longer needed improvement.

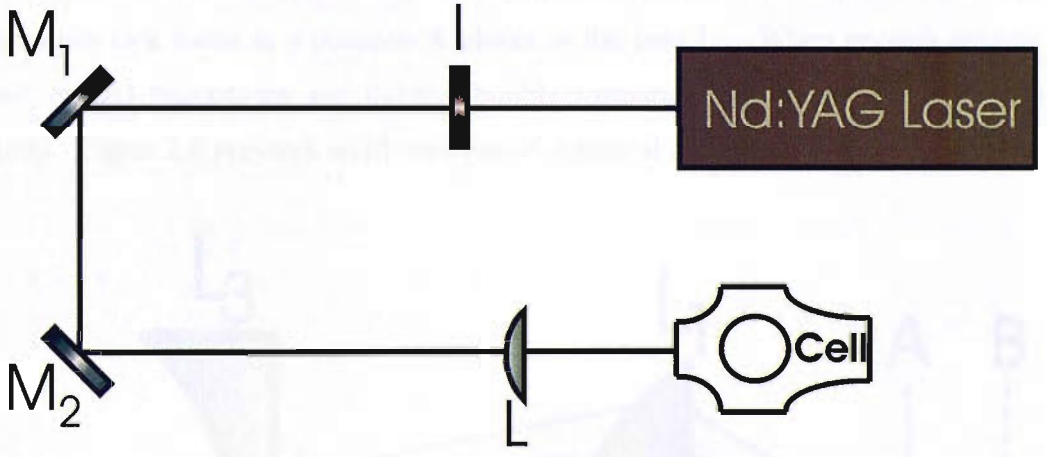

Figure 2.4 The optical arrangement when the cavitation bubbles were first attempted to generate with a laser.

Even though cavitation events occurred with the arrangement shown in Figure 2.4, this lens system was not ideal. Multiple bubbles were formed due to the shallow focussing angle as illustrated in Figure 2.5. In this case, self-focussing and filament formation is also possible due to a long beam waist [35].

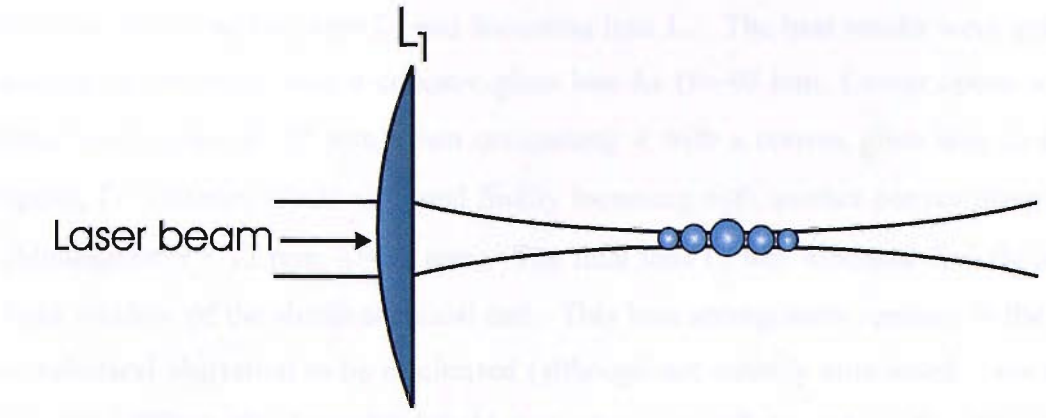

Figure 2.5 Multiple bubble formation when the focussing angle is too shallow.

Therefore, it was necessary to employ a concave lens to expand the beam before it enters the focussing lens to give a larger focussing angle. However, this lens arrangement can also cause multiple bubble formation. This is caused by spherical aberration demonstrated in figure 2.6. It shows that light that hits the lens close to the optical axis is focussed at position B. However, the light that hits the lens closer to its edges comes to a focus at a position A closer to the lens L_1. When enough energy is applied, optical breakdown and thereby bubble formation can occur at each of these positions. Figure 2.6 presents an illustration of spherical aberration [26].

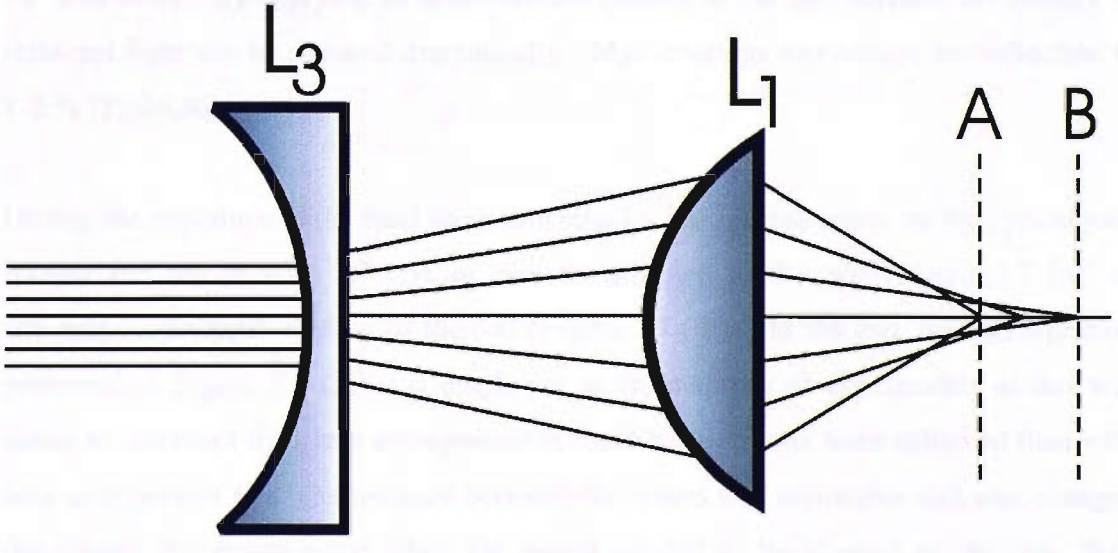

Figure 2.6 Illustration of spherical aberration, where the margins of the lens have a shorter focal length than the centre.

As spherical aberration is more likely to occur when the beam enters the focussing lens L_1 in an expanding angle, it was necessary to employ a collimating convex lens L_2

between the expanding lens L_3 and focussing lens L_1. The best results were gained by expanding the beam with a concave glass lens L_3 (f=-40 mm, Comar optics or f=-25 mm, Mellesgriot, ∅=25 mm), then collimating it with a convex glass lens L_2 (Comar optics, f = 150 mm, ∅=25 mm) and finally focussing with another convex glass lens L_1 (Mellesgriot, f = 12 mm, ∅=18 mm). The final lens L_1 was mounted directly onto the front window of the electrochemical cell. This lens arrangement resulted in the effects of spherical aberration to be minimised (although not entirely eliminated – see chapter 7). In addition the focussing angle was steep enough to reduce the formation of multiple bubbles. Generation of only one bubble was desired, as in that case only the interaction between the bubble and the surface could be studied. If many bubbles are formed, they interact with each other and therefore affect the results.

All lenses were coated with MgF in order to reduce reflections and increase the resistance to mechanical damage on the lens surface. When a laser beam is incident on the boundary between two media (in this case from the air into a glass lens) some light is reflected and some is transmitted into the second medium. The amount reflected depends on the angle of incidence, surface quality, and refraction index of the two media. For a typical uncoated lens, the amount of light reflected at each surface can be ~4 % or more. By applying an antireflection coating to the lens surface, the amount of reflected light can be reduced dramatically. MgF coatings can reduce the reflection to 1-2 % [25,26,96].

During the experiments the final focussing lens L_1 was located either on the optical path outside the cell (Figure 2.7 (i)), or directly attached to the cell (Figure 2.7 (ii)) or attached to the front window of the cell (Figure 2.7 (iii)). In the end, lens arrangement presented in Figure 2.7 (iii) was employed in the majority of experiments as this was easier to construct than lens arrangement (ii) and better results were achieved than with lens arrangement (i). The distance between the lenses was adjustable and was changed throughout the experiments when the optics needed to be aligned to optimise their performance. It is normally recommended, that when focussing a planar beam, the beam should enter the focussing planoconvex lens from its plane side [30]. However, this experimental arrangement is more difficult to construct, and therefore the beam entered the lens from the curved side as this arrangement worked fine.

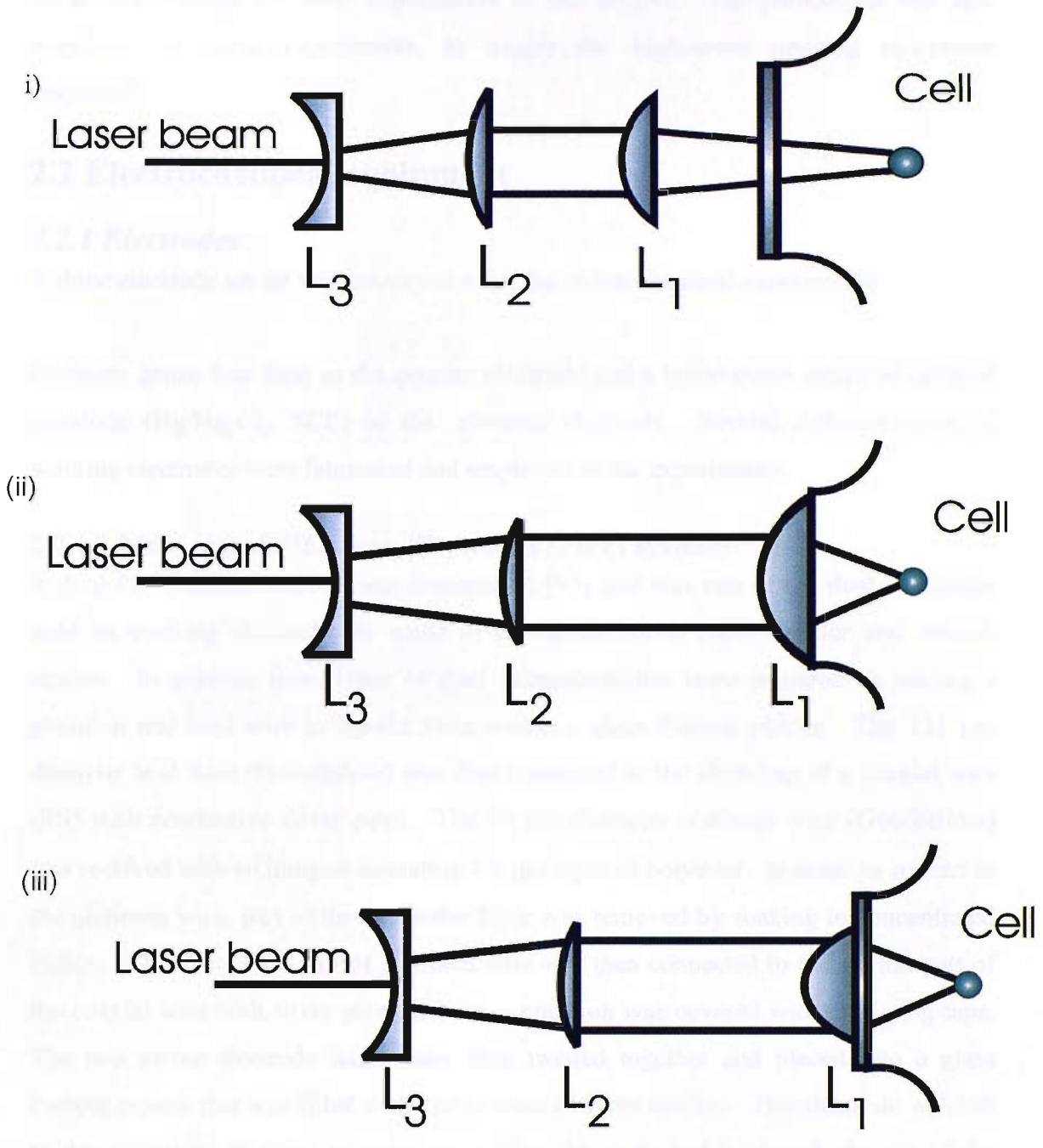

Figure 2.7 The options for lens arrangements for laser cavitation experiments.

Posts and postholders (Thorlabs) were employed to mount the mirrors and lenses. A beam stop was designed and constructed in-house and employed in the experiments after the beam exited the electrochemical cell.

A photodiode (Thorlabs 201/579-7227) was placed close to the optical path of the laser beam and was used to trigger the capture of the electrochemical and hydrophone signals

on an oscilloscope for most experiments in this project. The photodiode was also employed, in some experiments, to trigger the high-speed imaging equipment employed.

2.2 Electrochemical equipment

2.2.1 Electrodes

A three electrode set-up was employed in all the electrochemical experiments.

Platinum gauze was used as the counter electrode and a home-made saturated calomel electrode (Hg/Hg_2Cl_2, SCE) as the reference electrode. Several different types of working electrodes were fabricated and employed in the experiments.

2.2.1.1 Mass transfer/Erosion Electrodes (Pb/Pt system)

A dual Pb/Pt microelectrode was constructed [95] and was one of the dual electrodes used as working electrode for some of the simultaneous mass transfer and erosion studies. In general, these types of dual microelectrodes were prepared by sealing a platinum and lead wire in Epofix resin within a glass Pasteur pipette. The 125 μm diameter lead wire (Goodfellow) was first connected to the shielding of a coaxial wire (RS) with conductive silver paint. The 50 μm diameter platinum wire (Goodfellow) was received with an integral insulating 7.5 μm layer of polyester. In order to contact to the platinum wire, part of this polyester layer was removed by soaking in concentrated H_2SO_4. The uncovered part of platinum wire was then connected to the central part of the coaxial wire with silver paint and the connection was covered with insulating tape. The two active electrode wires were then twisted together and placed into a glass Pasteur pipette that was filled with epoxy resin (Struers epofix). The electrode was left to dry overnight at room temperature. After the resin had hardened, the tip of the electrode was polished with silicon carbide paper and aqueous alumina slurries (1.0 μm and 0.3 μm) to a mirror like finish.

Figure 2.8 presents a schematic picture of a dual microelectrode. The projection of the tip of the electrode presents the SEM image of the Pb and Pt discs.

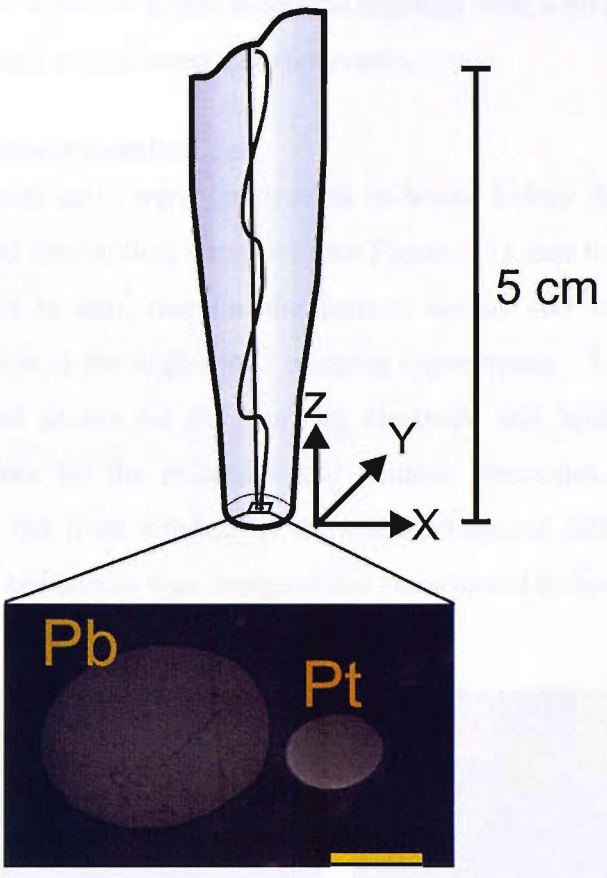

Figure 2.8 The electrode design for a dual microelectrode and a SEM picture of the Pb/Pt dual electrode tip [95].

2.2.1.2 Mass transfer electrodes

Other working electrodes were employed in mass transfer experiments. These consisted of a 25 μm diameter gold microelectrode or a 50 μm diameter Pt microelectrode that was constructed in a similar manner to that described above. However, electrical connection to the electroactive materials was achieved through the use of conductive silver paint between the microelectrode wire and a standard multicore wire (2 mm, Rapid Electronics).

2.2.1.3 Mass transfer/Erosion Electrodes (Al/Pt system)

Another type of dual electrode that was employed in the laser generated cavitation experiments was manufactured in a similar way as the Pb/Pt microelectrode by replacing the lead wire with aluminium. In this case a 250 μm or 0.5 mm diameter aluminium (99.5 %, Goodfellow) electrode was employed (see appropriate figure legend for precise electrode used in the experiments) for erosion experiments either on

their own or as a part of a dual electrode together with a 50 μm diameter platinum wire to simultaneously record mass transfer events.

2.2.2 The electrochemical cell

Several different cells were constructed in-house before the ideal design was found. These cells had four optical windows (see Figure 2.1), one for the beam to enter the cell, and one for it to exit, one for the camera access and one for the illumination of electrode/bubble in the high-speed imaging experiments. The final cell design seen in Figure 2.9 had access for the working electrode and hydrophone from the top and separate holders for the reference and counter electrodes. The focussing lens was attached onto the front window of the electrochemical cell by transparent nail polish (Rimmel). A cell holder was designed and constructed in-house.

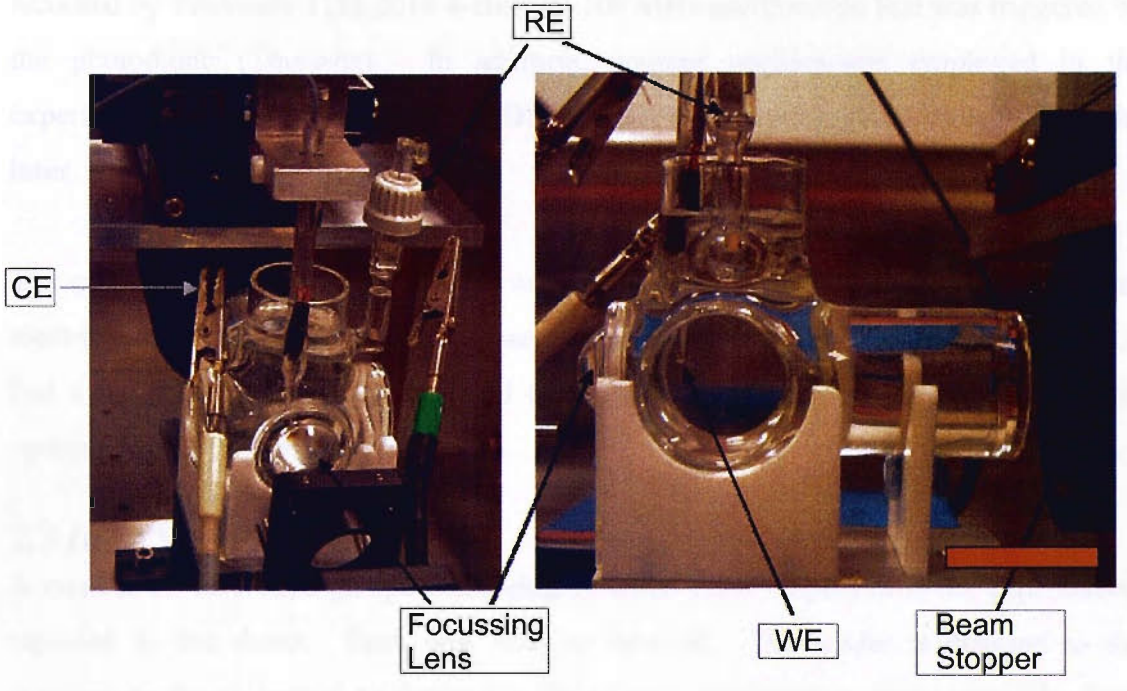

2.9 The electrochemical cell, working electrode (WE), reference electrode (RE) and counter electrode (CE). The scale bar in the figure is 4 cm.

2.2.3 Associated Equipment

An in-house built potentiostat was interfaced to a computer through an ADC card (Talisman electronics, PCI-DAS6040). This system was employed for the electrochemical experiments. Current voltage curves for cyclic voltammetry were recorded by in-house written software (Visual basic 6). Details of the program can be found in Appendix I. In addition a two channel in-house constructed current follower

(gains from 1 x 10^4 V A^{-1} to 1 x 10^8 V A^{-1}) was employed to measure the currents passed at the working electrode(s).

The position of the working electrode was controlled by a micropositioner (Time and Precision). The micropositioner had manual 25 mm X and Y stages and a motorised 50 mm Z stage, all with 10 μm resolution*. The stepper motor was controlled by stepper drive (Parker automation) and in-house written software (see Appendix I). The micropositioner was placed on a home built stand and a metal holder for the working electrode was designed and attached to the positioner.

The current time traces produced by the electrochemical experiments could also be recorded by Tektronix TDS 2014 4-channel 100 MHz oscilloscope that was triggered by the photodiode (Thorlabs). In addition, another oscilloscope employed in the experiments was a 100 MHz Gould (DSO) 465. This was triggered directly from the laser.

The cell, current follower and optics were covered with an aluminium box to reduce electrical noise and prevent possible laser radiation exposure to the user. The metal box had a window for camera access and a lid that could be removed. The lid had an opening for the XY micropositioner.

2.3 High Speed Imaging

A number of different high-speed imaging systems where employed in the experiments reported in this thesis. Each will now be detailed. The reader is directed to the appropriate figure legend to determine the system employed in each case. The final experimental-set up is depicted in figure 2.1.

A DRS Hadland Imacon 468 high speed camera was borrowed from the EPSRC instrument pool and employed in the combined electrochemistry/laser/imaging experiments. The camera took pictures at the rates from 1000 fps (frames per second) to 100 million fps and captured 8 images at the time. Each picture could be individually set so that the exposure time of each channel and the inter-frame time between each channel were independent of each other. A 55 mm Nikon lens was fitted to the camera

* Technically a higher resolution of up to 5 μm could be achieved with the Z stage.

together with one 21 mm extension and two 31 mm extensions to enable the camera to be focussed on the objected. An electrode was used as the object to help focussing. A flashlight was mounted on the opposite side of the cell than the camera and was triggered from the camera. A photodiode (Thorlabs) was used to detect the passing laser pulse and to trigger the camera and flashlight. A 266 MHz computer running Windows 95 controlled the system. The images were analysed using the dedicated DRS Hadland's software and then downloaded in TIFF format to CD via the CD writer fitted to the PC.

A Photosonics Phantom v7 high speed video camera (borrowed from EPSRC instrument pool) was also employed in the experiments. The camera recorded images with the maximum speed 150 000 fps and used SR-CMOS sensors with a maximum resolution of 800 x 600 (21μm) pixels at up to 4,800 fps giving 1.2 seconds of recording time. The resolution decreases as the recording speed increases, giving the resolution of 32 x 32 pixels at the highest recording speed. A Pentium 4 PC was connected to camera processor via 10/100 Ethernet controlled the camera. The camera recorded continuously and therefore both pre and post-trigger images were available. An F2.8 macrozoom lens was used to focus the camera on the target. The images could be saved in a CIN-form and they could be converted with the Cineview-software provided. In many of the laser cavitation experiments presented in this thesis, this high-speed camera was triggered from a photodiode placed close to the beam path. However, the photodiode generated a positive voltage spike while this camera required a negative TTL trigger signal. Hence a PC was used as a trigger relay (see time line explanations) which employed in-house written software that sent a converted digital 5 V signal to the camera at the appropriate time. Further details of this software can be found in appendix 1.

A Photron APX-RS high speed video camera was the third camera employed in the experiments. It provided full megapixel resolution for 3000 fps and the fastest top speed was 250 000 fps. As for the Phantom v7 camera, the resolution decreased when the recording speed was increased. The fastest available shutter speed for the camera was 2 μs. The camera was controlled with Photron's PFV software that was linked to the camera with a FireWire or Ethernet cable. In this case the camera was triggered directly from the laser.

A photodiode was used to trigger the DRS Hadland Imacon and Photosonics Phantom v7 high-speed camera and video camera. Hence, the time when the laser beam fired (and therefore detected by the photodiode which in turn triggered the recording devices) is assigned to 0 s for most experiments. Figure 2.10 presents a typical photodiode output signal. A Coherent Fieldmaster powermeter was employed to measure the average power for the laser radiation.

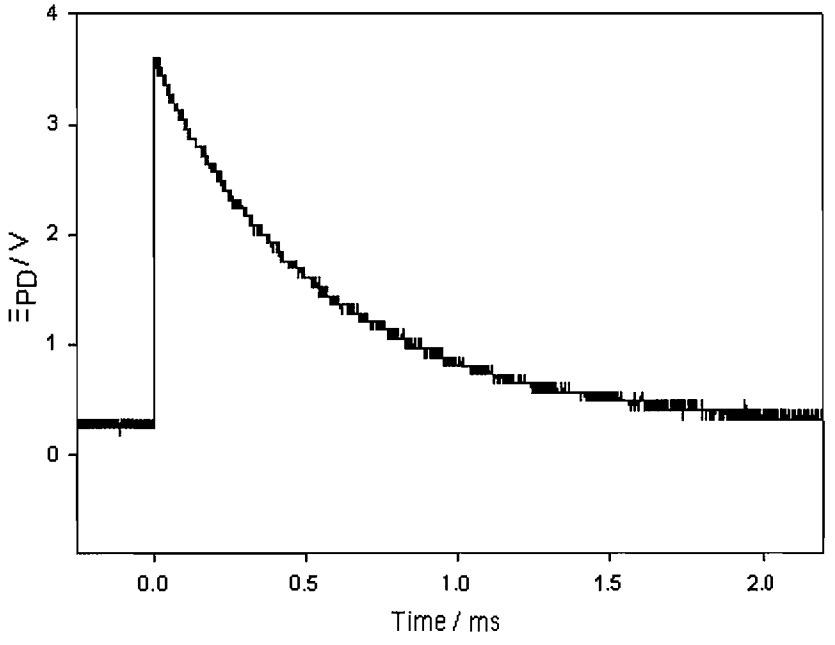

Figure 2.10 Plot showing a typical voltage time trace obtained from the photodiode used to trigger the capture of the electrochemical, acoustic and high-speed images.

Each camera employed required different experimental set-ups due to different triggering and photo capturing properties. When the DRS Hadland Imacon high speed camera was employed to record the events, the camera was triggered directly with the photodiode. The laser employed at this point of the project was the Continuum Surelite NY 61 which did not have the option to generate single shots, and therefore it was necessary to place a beam stopper on the optical path before the photodiode. The beam stopper was attached to a solenoid that was controlled by in-house written software (see appendix I) through an ADC card (Talisman electronics, PCI-DAS 6040). Once the beam stopper was removed, the photodiode detected the first passing laser pulse and triggered the equipment. The experimental set-up and the sequence of events for this set of experiments are presented in Figure 2.11.

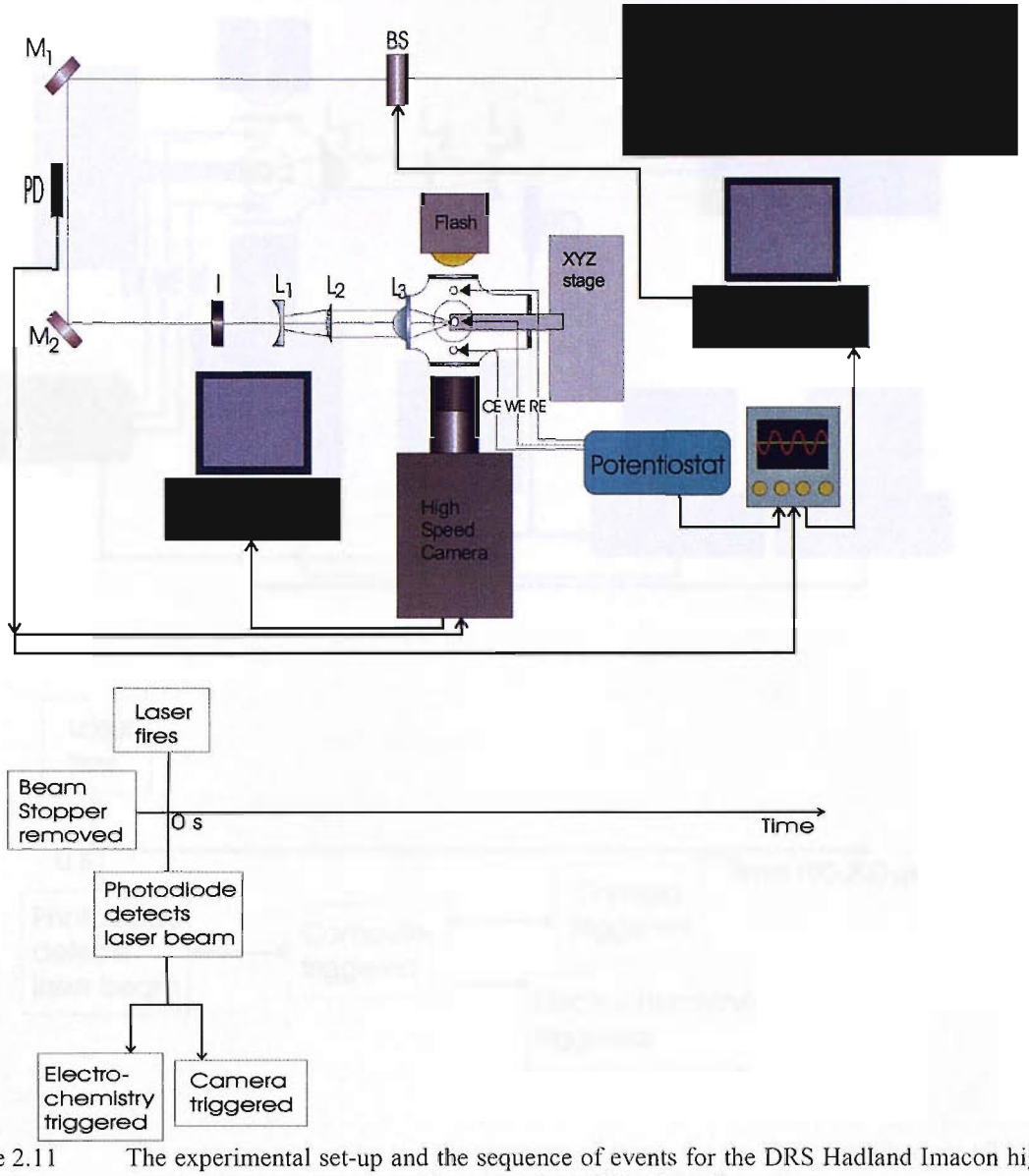

Figure 2.11 The experimental set-up and the sequence of events for the DRS Hadland Imacon high speed camera was employed to record the bubble formation.

When the Photosonics Phantom v7 high speed video camera video camera was employed, the photodiode was used to trigger the computer, which then generated a digital -5 V pulse to trigger the camera. This pulse was also used to trigger the electrochemistry to enable the simultaneous capturing of high-speed images and electrochemical events. It was no longer necessary to employ the beam stopper on the optical path, as the lasers that were used with this camera (Continuum Surelite SL-II and Continuum Inlite II-10) had an option for single shots. The experimental set-up and the sequence of events for this set of experiments are presented in Figure 2.12.

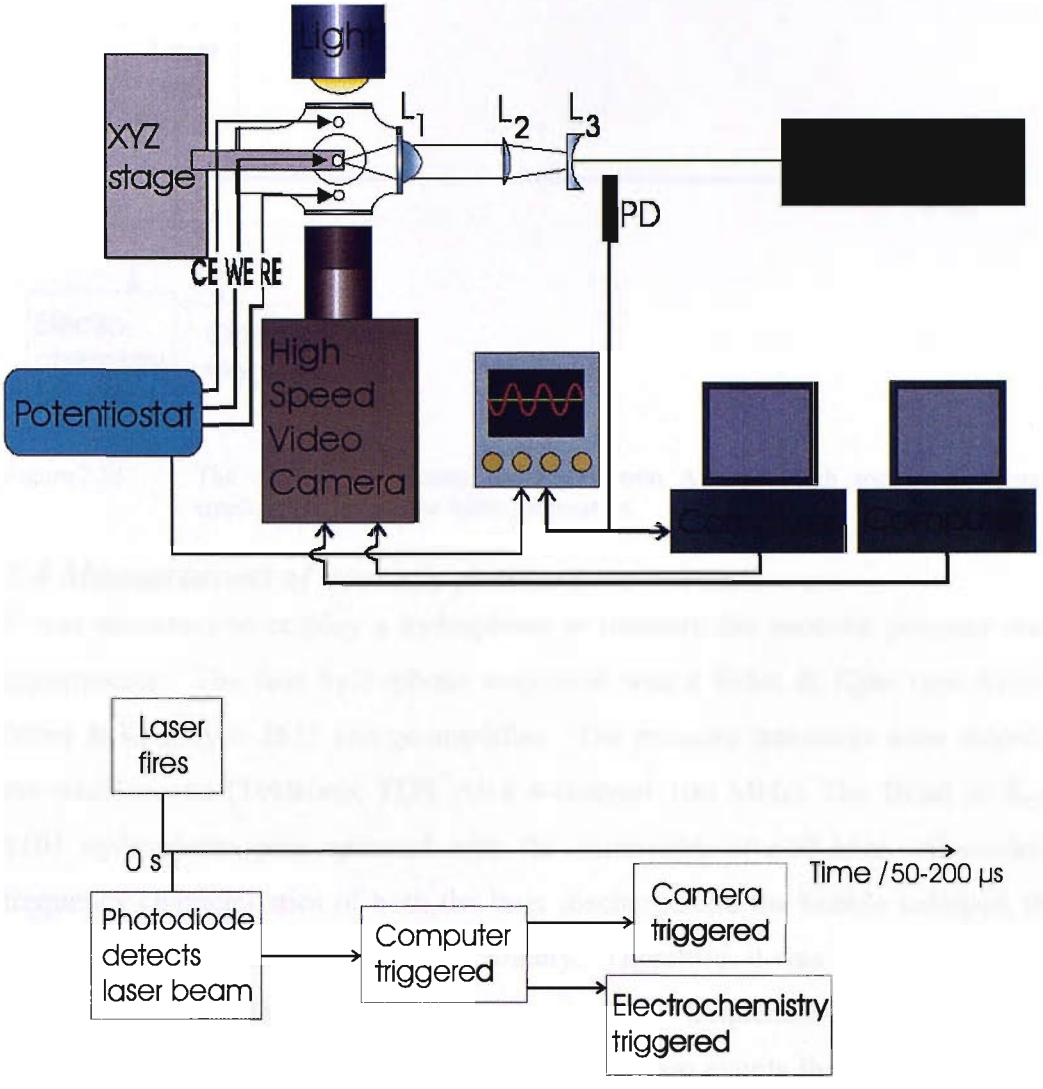

Figure 2.12 The experimental set-up and the sequence of events for the Photonics Phantom v7 high speed video camera was employed to record the bubble formation.

In the final set of experiments when the Photron APX-RS high speed video camera was used, the activation of the laser Q-switch was employed to trigger the recording of electrochemistry and high-speed imaging. This arrangement could only be achieved when the Continuum Inlite laser was used. By employing the Q-switch, the delay between the triggering and recording was practically eliminated, as it no longer was necessary to employ a computer to trigger the electrochemistry and high-speed imaging. This experimental set-up is seen in figure 2.1 and the sequence of events in figure 2.13.

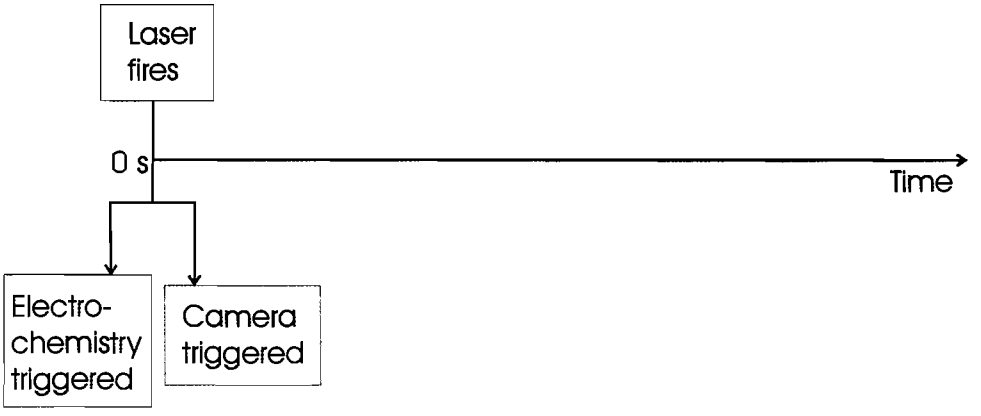

Figure 2.13 The sequence of events for the Photron APX-RS high speed video camera was employed to record the bubble formation.

2.4 Measurement of acoustic pressure

It was necessary to employ a hydrophone to measure the acoustic pressure during the experiments. The first hydrophone employed was a Brüel & Kjær type 8103 with a Brüel & Kjær type 2635 charge amplifier. The pressure transients were recorded with the oscilloscope (Tektronix TDS 2014 4-channel 100 MHz) The Brüel & Kjær type 8103 hydrophone only operated with the bandwidth of 180 kHz. Considering the frequency characteristics of both the laser discharge and the bubble collapse, the 8103 was unable to measure the signal accurately. Therefore, it was replaced by a G.R.A.S. DB10 needle hydrophone that measures high frequencies (0.5-20 MHz, 1 V corresponded to 5012531 Pa) to detect the cavitation events that were recorded by the oscilloscope. The hydrophone was placed at least 3 mm away from the focal spot of the laser beam where the bubbles were generated; placing the hydrophone too close to the beam could damage to it (see later discussion and pressure pulses).

2.5 Chemicals

The solutions were made up using water from an USF Elga Purelab Option E10 water purification system. Water purified in this manner had a conductivity of below 0.06 μS cm^{-1} and a low organic content (TOC < 30 ppb)[†]. The water was filtered and degassed before the majority of the experiments. The chemicals used in the experiments are presented in the table below and were used as received.

[†] manufacturer quoted figure

Chemical	Supplier	Purity/Grade
Epofix Epoxy Resin	Struers	-
H_2SO_4	BDH	98 %
$K_4Fe(CN)_6$	Aldrich	99 %
KI	Aldrich	Analytical
Na_2SO_4	BDH	AnalaR
$Sr(NO_3)_2$	Aldrich	99+ %

Table 2.2 Employed chemicals, supplier and purity.

Chapter 3

Initial experiments with Pb/Pt dual electrode to design the experimental-set-up

This thesis investigates the surface damage and mass transfer enhancement caused by single laser induced cavitation bubble. An experimental set-up is designed and a series of experiments performed for the study of laser cavitation and its effects on surfaces by electrochemical means. The initial experiments involved employing a dual Pb/Pt microelectrode which had previously been used as a sensor to study acoustoelectrochemistry [95]. This electrode consists of lead and platinum wires sealed together in close proximity (for details see figure 2.8 in chapter 2). They are sealed within an insulator so that only the circular cross-sectional end of each wire is showing. Hence, each of the two wires generates an embedded disk electrode. The employment of these electrodes has many advantages owing to their fast electrochemical response times and their small size in relation to the cavitation bubble which is formed (the bubble attains the maximum diameter ~ 1 mm) while the electrodes have a diameter of 50 μm (Pt) and 125 μm (Pb). These are discussed in more detail in Chapter 1. Use of a dual Pb/Pt microelectrode enables the simultaneous study of mass transfer and erosion effects in a relatively small space (~100 μm centre to centre separation). The dual electrode is designed to measure surface erosion and local mass transfer enhancements as a result of forced convection through bubble action. However, it is important to understand the function of the electrodes which enables these processes to be studied simultaneously. The two electrode materials chosen (here Pb and Pt) exhibit very different electrochemical properties. For example, under the conditions employed (such as in a solution containing Na_2SO_4 whilst the potential is held at 0.6 V vs. SCE) an insoluble $PbSO_4$ layer is formed on the Pb electrode surface. Erosion of this interface is followed by an anodic signal as the surface returns to its passive state. This makes it suitable for erosion studies in the presence of cavitation. However, platinum under the same conditions and in the presence of a suitable redox system is able to detect changes in local mass transfer.

3.1 Voltammetric characterisation of Pb/Pt electrode

A cyclic voltammogram of a platinum disc of a dual electrode in a solution of 5 mM $K_4Fe(CN)_6$ in 0.2 M Na_2SO_4 is presented in figure 3.1. The choice of Na_2SO_4 as background electrolyte was based on its suitability for erosion experiments. The plateau at potential positive of +0.35 V vs. SCE on the Pt electrode (– – –) signal corresponds to the mass transfer limited oxidation of the $Fe(CN)_6^{4-}$ species. Here a steady state current of 30 nA was observed. Considering the dimensions of the electrode, redox species concentration reaction, it is possible to calculate (through $i_{MTL}=4n_eaFDc_b$, where a is the radius of the electrode, F is the Faraday's constant, D is the diffusion coefficient and c_b is the bulk concentration of the electroactive species) a diffusion coefficient of the $Fe(CN)_6^{4-}$ species of 6.22×10^{-6} cm^2 s^{-1}. On the other hand, figure 3.1 shows that the surface of the Pb electrode (——) passivates at potentials positive of -0.45 V vs. SCE due to fast formation of an insoluble $PbSO_4$ layer. This can be seen as the anodic peak labelled A. This layer enables the employment of Pb disc as an erosion sensor. An associated stripping peak (B) of this layer can be seen at -0.74 V vs. SCE. Integrating peak A enables the definition of charge 1 μC. By using the Faraday's law ($Q = n_e mF$, where Q is electric charge, n_e the number of electrons, m mass and F Faraday's constant), it is possible to estimate the amount of $PbSO_4$, 0.5×10^{-11} moles. As the radius of the electrode is known (62.5 μm), the thickness of the $PbSO_4$ layer can be estimated as ~ 0.02 μm.

Under these conditions, if the potential of both electrodes is maintained at +0.7 V *vs.* SCE then both mass transfer events and surface erosion events can be detected on the Pt and Pb electrodes respectively. The dual electrode is able to monitor these processes because, at this potential, the oxidation of the ferrocyanide ions on the Pt disc is mass transfer limited, and any movement of the liquid can be detected as an increase in current. This increased current is due to forced convection as a result of fluid motion caused by any bubble close to the electrode surface. In addition at +0.7 V vs SCE, an insoluble $PbSO_4$ layer is present on the Pb electrode surface. In previous studies this passivated surface has been exposed to inertial cavitation and transient anodic current time transients have been observed [93]. These events are caused by the repassivation of the electrode surface after erosion of the passive layer by cavitation. As a result of its successful employment in acoustoelectrochemistry studies [95], a Pb/Pt dual electrode

was employed as an electrochemical sensor for the first set of experiments when laser cavitation was studied by electrochemical means. The following section describes the initial approach to the study of laser induced cavitation using both electrochemical mass transfer and erosion sensors.

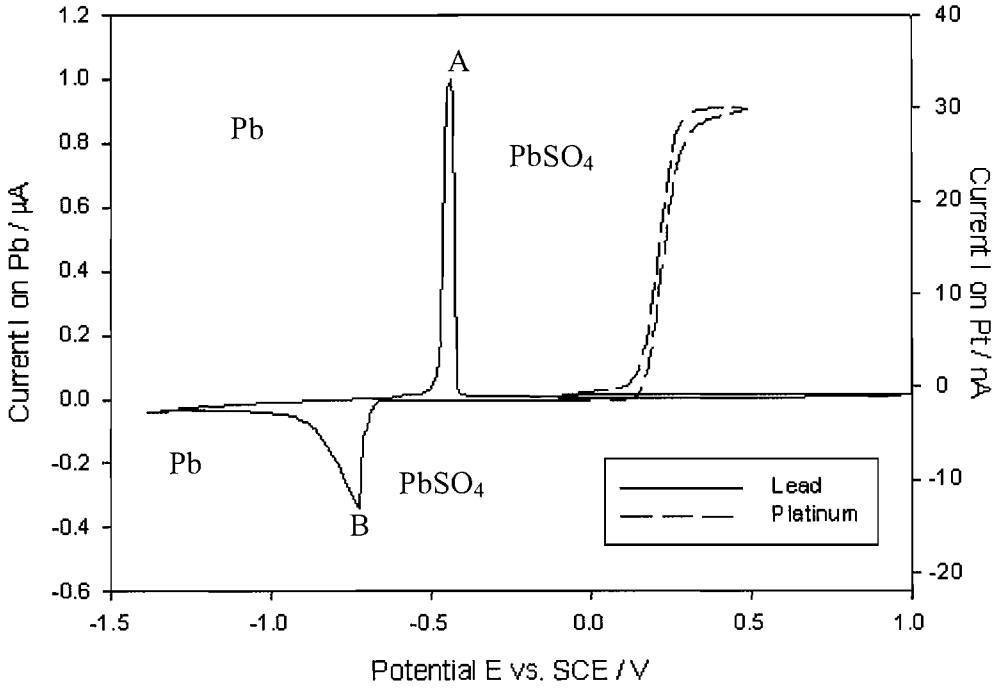

Figure 3.1 Cyclic voltammetry of a 125 µm diameter lead disc of a dual electrode (—) in 0.2 M Na_2SO_4 containing 5 mM $K_4Fe(CN)_6$. The sweep rate was 50 mVs^{-1}. Cyclic voltammetry of a 50 µm diameter platinum disc of a dual electrode (--) in 0.2 M Na_2SO_4 containing 5 mM $K_4Fe(CN)_6$ at room temperature (20°C) and anaerobic conditions. The sweep rate was 5 mV s^{-1}.

3.2 Pt microelectrode as sensor for laser cavitation

In preliminary experiments the effects of laser discharge on mass transfer alone was investigated. The laser employed in these experiments was the Continuum Surelite NY 61. Figure 3.2 shows the current recorded as a function of time at a 50 µm diameter platinum electrode held at +0.7 V *vs.* SCE in the presence of $Fe(CN)_6^{4-}$ when the repetition rate of the laser was 5 Hz. Five separate current peaks can be seen which indicates that each laser pulse causes an event. This is a result of enhanced mass transfer to the electrode surface as a result of forced convection within the solution. This enhancement is seen as individual anodic current time transients. It was also observed that an audible "crack" was heard when the laser fired. This is characteristic of liquid breakdown and cavitation bubble formation. The current time transients are

not constant in time, suggesting that they are caused by different types of event or, more likely, they are caused by the same event but that the characteristics of the event (location, magnitude etc.) are not invariant. However, the mass transfer enhancements are still relatively small (here $k_m \sim 0.05$ cm s^{-1}) whereas in other studies employing ultrasonically induced cavitation mass transfer values of up to 1 cm s^{-1} have been observed [97]

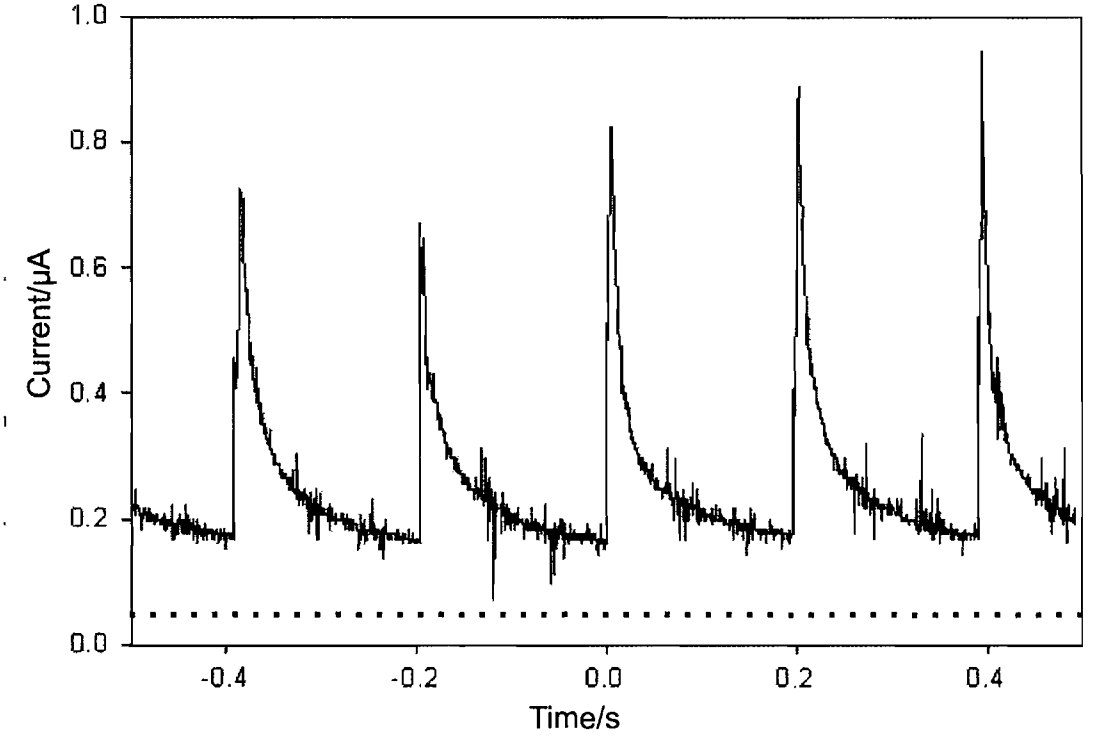

Figure 3.2 Current time transients showing the mass transfer of ferrocyanide to a 50 μm diameter Pt disc in a solution containing 10 mM $K_4Fe(CN)_6$ and 0.75 M Na_2SO_4 The potential of the electrode was held at +0.7 V vs. SCE. The repetition rate of the laser was 5 Hz. The dotted line represents the steady state current.

In order to investigate the locations and sizes of the bubbles generated by the laser, and possibility that a single laser pulse might generate more than one bubble, the enhancement in mass transfer was mapped by measuring the current at 100 positions at the 5 x 5 mm plane located around the visually detected focal spot of the laser. The separation between the tip of the electrode and the focus was estimated to be approximately 1.5 mm. The electrode was held at each position for 5 s to measure the average current. The laser was firing at the repetition rate 10 Hz and therefore, over the 5 s recording time, some 50 laser pulses are generated. The current generated by each laser pulse was detected, and the average normalised current recorded at each point is mapped in figure 3.3. The current is normalised to the highest value of the current

detected (which of course occurs on the map at a value of 1 and given a red coloration). Figure 3.3 reveals that the area of high current does not have one obvious hot spot, but it is spread diagonally. It was suggested earlier that these result supports the suggested existence of multiple bubbles. However, the current was monitored during repetitive laser discharge as single shot mode was not available at this time. Hence seeding effects due to previous laser discharge are to be expected. This will cause some spreading in the mapping data.

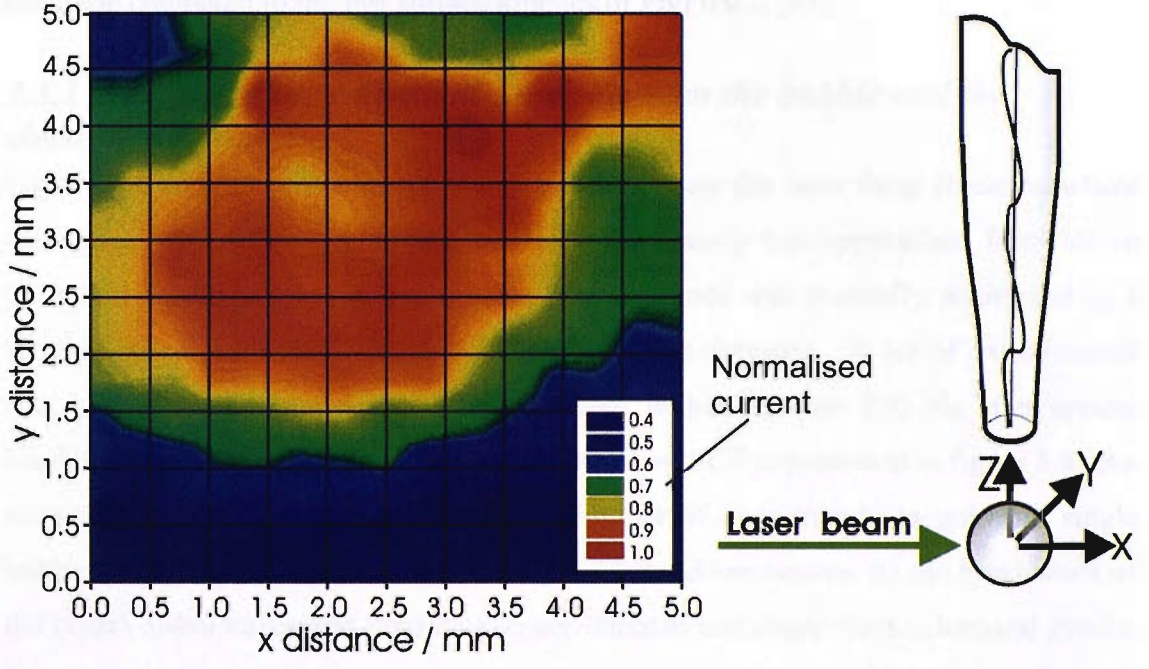

Figure 3.3 Mapping showing the current normalised to maximum at mass transfer limited oxidation of $Fe(CN)_6^{4-}$ in the presence of laser induced cavitation. The tip of the electrode was held approximately 1.5 mm (z) from the focus.

3.3 Employment of Pb/Pt dual microelectrode for simultaneous mass transfer and erosion studies

The results presented thus far suggest that mass transfer enhancement is produced by laser induced cavitation as expected. Hence it is desirable to measure the effects of mass transfer simultaneously with erosion. In order to do this, a dual microelectrode was employed to monitor both the mass transfer and surface effects of the single bubble events generated. Both electrodes were held at +0.7 V *vs.* SCE. In addition a high-speed camera was employed. The capture of the electrochemical and photographic data

was triggered with a photodiode. This enabled both the electrochemical response of both electrodes and the actual bubble produced and its position to be recorded.

This section demonstrates, for the first time, that it is possible to record surface erosion and the associated mass transfer from a single laser induced cavitation event. However, it should be noted that the electrochemical signal from the $Pt/Fe(CN)_6^{4-}$ system is relatively slow compared to the erosion signal from the $Pb/PbSO_4$ system. This is due to the intrinsically slower relaxation of the convection/diffusion field around the Pt electrode compared to the fast surface kinetics of $Pb/PbSO_4$ [95].

3.3.1 Varying of the vertical distance between the bubble and the electrode surface

Figures 3.4 and 3.5 present a set of experiments where the laser focus (location where the optical breakdown occurs and bubble is generated) was approached from above (direction described as z in figure 3.3). The electrode was manually positioned in a location where both mass transfer and erosion were detected. A set of experimental data was obtained from a single bubble event within the first 100 ms after optical breakdown when the potential was held at +0.7 V *vs.* SCE is presented in figure 3.4. An external beam stopper was employed in this set of experiments to generate single bubbles. The laser fires at 0 s, and the optical breakdown occurs. At the breakdown of the liquid, shockwaves and fluid motion are initiated and cause electrochemical events. For example, the emitted pressure pulses remove some of the insoluble $PbSO_4$ layer on the electrode surface. The repassivation of this layer is seen as a fast transient on the lead disc, an anodic current 1.9 μA is detected before the i_{Pb} signal decays back to zero. The signal for mass transfer has a sharp transient at 0 s which could be caused by shock wave emission, laser electronics or possibly coupling with the Pb electrode. This initial small transient is followed by a slower response when the hemispherical diffusion field is disturbed by fluid motion. After the bubble collapses, the diffusion field slowly recovers and returns to steady state conditions as seen in figure 3.4.

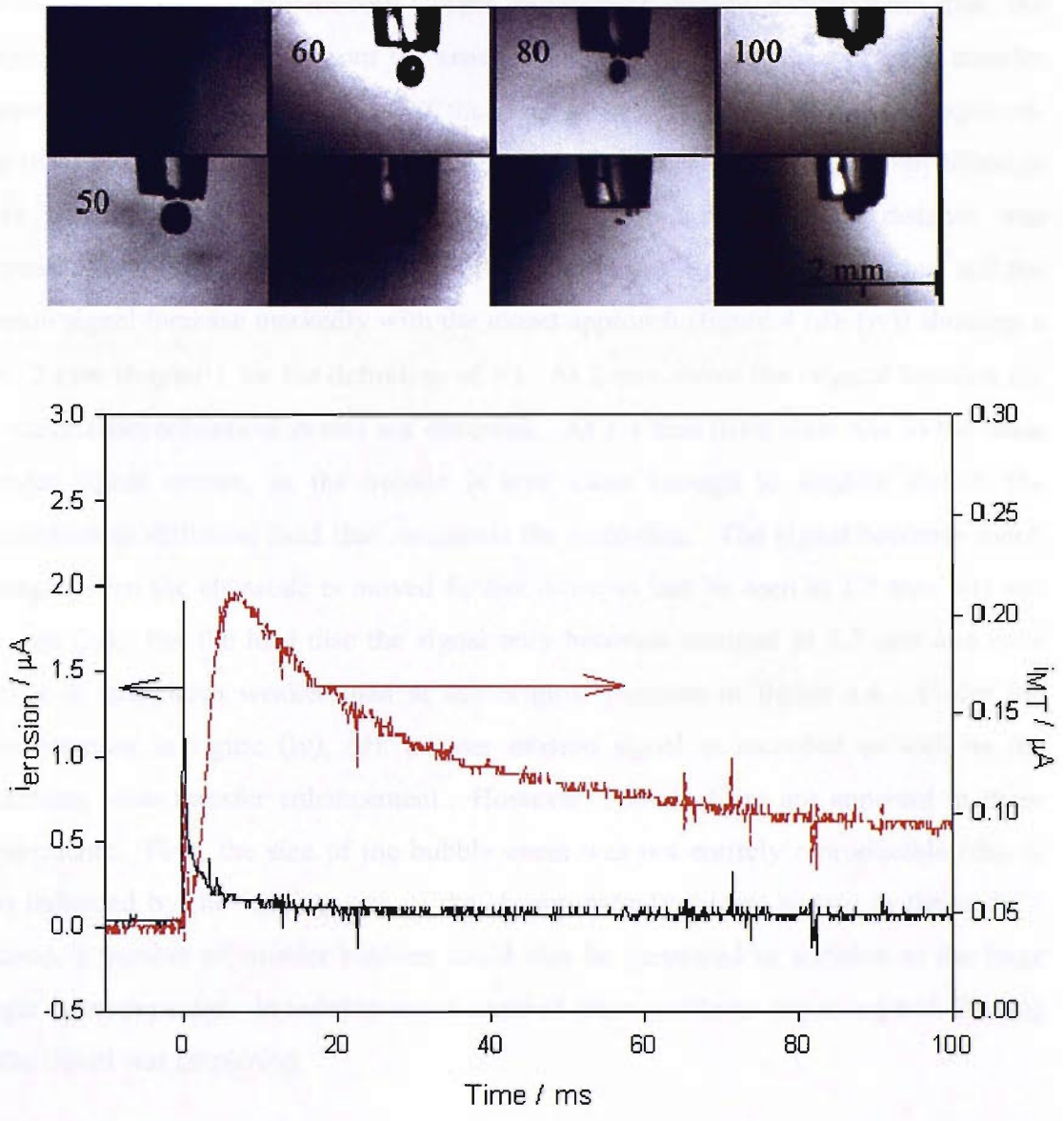

Figure 3.4 Images of laser bubble and the corresponding electrochemical signal for erosion on lead and mass transfer on platinum disc microelectrode in 5 mM $K_4Fe(CN)_6$ and 0.2 M Na_2SO_4 when the potential was held at 0.7 V *vs.* SCE. The unit for the times given in the images is μs and the delay time between the images was 10 μs, and 5 μs between the last two images. The laser energy was approximately 66 mJ/pulse. The time scales for the images and the electrochemical transients are not comparable.

In order to investigate the effect of distance between the bubble centre and the electrode, the dual electrode was moved with respect to the laser focus. At each position selected, the current transients detected at the dual electrode were monitored as a function of time while high-speed imaging recorded the size and location of the bubble with respect to the dual electrode. Figure 3.5 (i) 1.4 mm, figure 3.5 (ii) 1.2 mm and figure 3.5 (iii) 0.8 mm from the original position in figure 3.5 (iv). Figures 3.5 (a)-(d) correspond to the response of the dual electrode to the individual bubble events

shown in (i) to (iv) respectively. This experiment clearly demonstrates that the electrochemical signal both from the erosion sensor (the Pb) and the Pt mass transfer sensor are dependent on the range of the laser focus from the electrode, as expected. The maximum diameter of the bubbles created in each experiment was ~1 mm although there was some variability in this parameter (see images). As the distance was decreased between the bubble centre and the electrodes, the mass transfer signal and the erosion signal increase markedly with the closet approach (figure 4 (d), (iv)) showing a $\gamma < 2$ (see chapter 1 for the definition of γ). At 2 mm above the original location (i), no major electrochemical events are observed. At 1.4 mm (ii) a slow rise in the mass transfer signal occurs, as the bubble is now close enough to slightly disturb the hemispherical diffusion field that surrounds the microdisc. The signal becomes much stronger when the electrode is moved further down as can be seen at 1.2 mm (iii) and 0.8 mm (iv). For the lead disc the signal only becomes stronger at 1.2 mm and even then it is still much weaker than at the original position in figure 3.4. Under the circumstances in figure (iv), (d), a clear erosion signal is recorded as well as the maximum mass transfer enhancement. However, non-idealities are apparent in these experiments. First, the size of the bubble event was not entirely reproducible (this is also indicated by the varying size of the current time transients shown in figure 5.2). Second, a number of smaller bubbles could also be generated in addition to the large single event expected. In order to avoid some of these problems degassing and filtering of the liquid was employed.

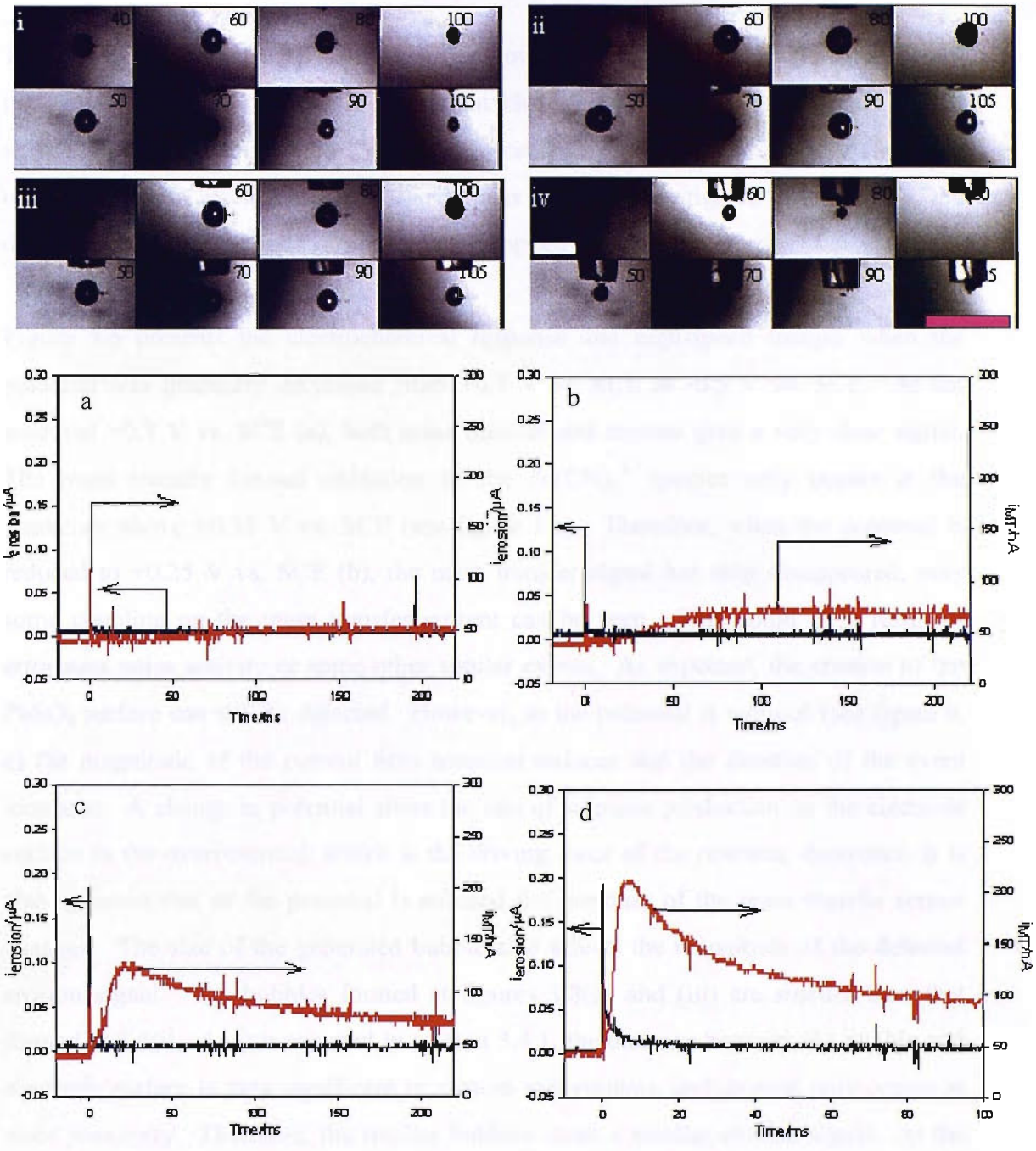

Figure 3.5. High-speed images and electrochemical signal for mass transfer (—) and erosion (—)in a 5 mM $K_4Fe(CN)_6$/0.2 M Na_2SO_4 solution. The potential of the electrodes were held at +0.7 V *vs.* SCE. The distance from the original position (iv) was 1.4 mm, 1.2 mm and 0.8 mm further away from the bubble centre for frames (i), (ii) and (iii) respectively. The time of each image relative to the laser pulse is shown in μs. The scale bar represents 2 mm. The laser energy was approximately 66 mJ/pulse.The electrochemical data shown in (a) – (d) corresponds to images (i) – (iv) respectively. The time scales for the images and the electrochemical transients are not comparable.

3.3.2 Changing the potential

The results in section 3.3.1 indicated that both the mass transfer and erosion signal increased when the electrode was brought closer to the bubble as expected. This verified that the electrochemical events were caused by laser/bubble activity. Accuracy of the detected electrochemical signals was further investigated by studying the dependence of the electrode response on the applied electrochemical potential.

Figure 3.6 presents the electrochemical response and high-speed images when the potential was gradually decreased from +0.7 V *vs.* SCE to -0.5 V vs. SCE. At the potential +0.7 V vs. SCE (a), both mass transfer and erosion give a very clear signal. The mass transfer limited oxidation of the $Fe(CN)_6^{4-}$ species only occurs at the potentials above +0.35 V vs. SCE (see figure 3.1). Therefore, when the potential is reduced to +0.25 V vs. SCE (b), the mass transfer signal has now disappeared, only some coupling on the mass transfer current can be seen. This could be a result of erroneous noise activity or some other similar events. As expected, the erosion of the $PbSO_4$ surface can still be detected. However, as the potential is reduced (see figure b, c) the magnitude of the current time transient reduces and the duration of the event increases. A change in potential alters the rate of sulphate production on the electrode surface as the overpotential, which is the driving force of the reaction, decreases. It is also apparent that as the potential is reduced the response of the mass transfer sensor changes. The size of the generated bubble also affects the magnitude of the detected erosion signal. The bubbles formed at figures 3.8(ii) and (iii) are smaller than that formed at 3.6(i). As it was stated in section 3.4.1, the distance between the bubble and electrode surface is very significant in erosion experiments, and erosion only occurs at close proximity. Therefore, the smaller bubbles cause a smaller erosion signal. At the same time figure 3.6(c) shows only a fast cathodic response can be seen on the Pt disc, which could be attributed to shock wave events, electronics or some photochemical activity as there is no redox electrochemistry occurring at this potential. At -0.5 V vs. SCE (iv) the erosion peak has disappeared as the $PbSO_4$ layer no longer exists on the Pb surface. On the other hand a large current is seen on the Pt electrode, which could be a result of formation of oxygen at this potential.

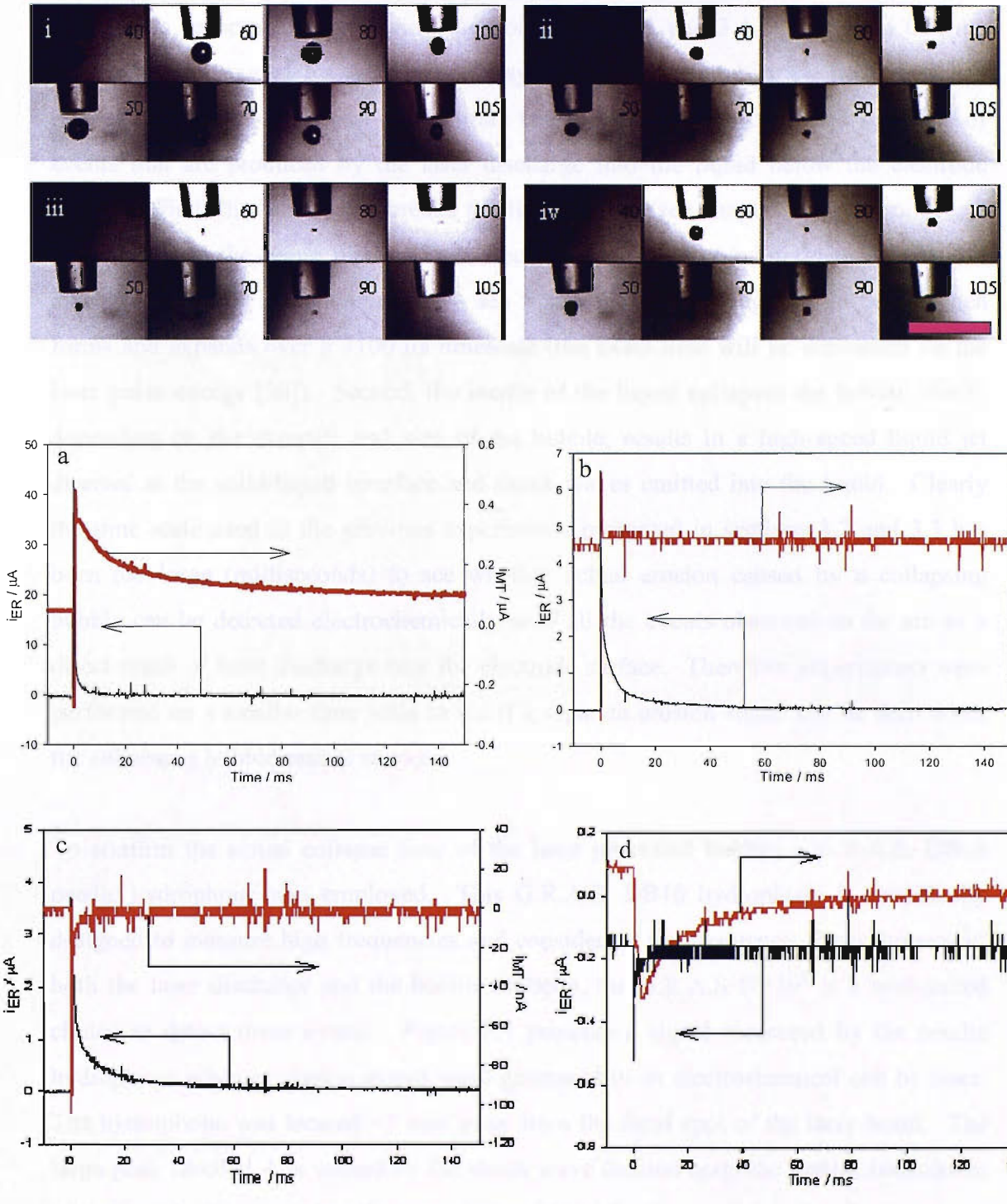

Figure 3.6 High-speed images and electrochemical signal for mass transfer (—) and erosion (—)in a 5 mM $K_4Fe(CN)_6$/0.2 M Na_2SO_4 solution when the potential was changed. The potential was a) 0.7 V vs.SCE, b) 0.25 V vs. SCE, c) 0 V vs. SCE and d) -0.5 V vs. SCE. The time of each image relative to the laser pulse is shown in µs. The scale bar represents 2 mm. The laser energy was approximately 66 mJ/pulse.The high speed images shown in (i) – (iv) corresponds to figures (a) – (d) respectively. The laser energy was approximately 66 mJ/pulse. The time scales for the images and the electrochemical transients are not comparable.

3.4 Experiments on a smaller time scale

The results reported in the previous sections (see 3.4.1 and 3.4.2), indicated that the electrochemical signal for the $Pb/PbSO_4$ system is detected when the laser fires and optical breakdown occurs. It is important to consider the timescales and sequence of events that are produced by the laser discharge into the liquid below the electrode surface. First, the laser pulse breaks the liquid down (see chapter 1) and produces a shock wave in the liquid phase. This occurs at time t = 0 s (as defined by the laser discharge detected by a photodiode – see figure 2.11). A single large bubble then forms and expands over a ~100 μs timescale (the exact time will be dependent on the laser pulse energy [20]). Second, the inertia of the liquid collapses the bubble which, depending on the distance and size of the bubble, results in a high-speed liquid jet directed at the solid/liquid interface and shock waves emitted into the liquid. Clearly the time scale used in the previous experiments presented in sections 3.2 and 3.3 has been too large (milliseconds) to see whether actual erosion caused by a collapsing bubble can be detected electrochemically or if all the events observed so far are as a direct result of laser discharge near the electrode surface. Therefore experiments were performed on a smaller time scale to see if a separate erosion signal can be seen when the collapsing bubble causes erosion.

To confirm the actual collapse time of the laser generated bubble, a G.R.A.S. DB10 needle hydrophone was employed. This G.R.A.S. DB10 hydrophone is specifically designed to measure high frequencies and considering the frequency characteristics of both the laser discharge and the bubble collapse, the G.R.A.S DB10[†] is a well-suited choice to detect these events. Figure 3.7 presents a signal measured by the needle hydrophone when cavitation events were generated in an electrochemical cell by laser. The hydrophone was located ~3 mm away from the focal spot of the laser beam. The large peak labelled A is caused by the shock wave emitted upon the optical breakdown of the liquid. This peak has the magnitude of 250 kPa. The peak labelled B that occurs 165 μs after the peak A, is the signal resulting from the shock wave induced by the bubble collapse and has a similar magnitude. The insertion in figure 3.7 shows this region of interest in more detail. The smaller signals in the time zones labelled as C and D are either smaller bubbles generated next to the bigger one [18,67], or the residuals of

[†] G.R.A.S. DB10 needle hydrophone can measure high frequencies (0.5-20 MHz, 1 V corresponded to 5,012,531 Pa) and is therefore suitable for laser cavitation experiments.

the bigger shock wave A or B that are bouncing back and forth within the electrochemical cell. The transient seen at 184 μs labelled E is thought to be caused by the bubble rebound and has the magnitude of 92 kPa. These are clearly significant pressure pulses (>2 bar) considering that the pressure from such an event will rapidly dissipate (due to radial spreading) away from laser focus.

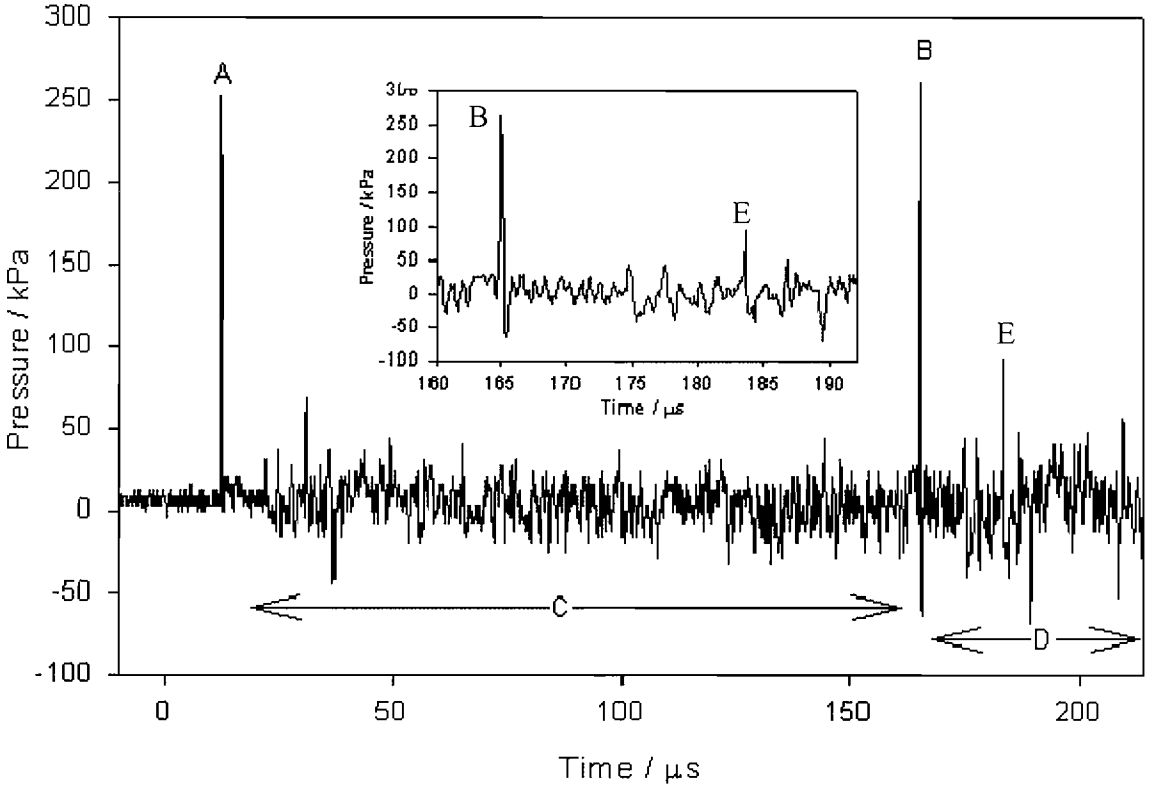

Figure 3.7. The G.R.A.S. DB10 hydrophone signal for laser cavitation in a solution of 1 mM KI in 0.2 M Na_2SO_4 in the absence of the electrode at room temperature when the solution was degassed before the experiments. The off-set of peak A is caused by problems with triggering.

Figure 3.8 details the erosion caused by a single cavitation event. It shows the current time trace recorded at a passivated Pb electrode for a single laser pulse.

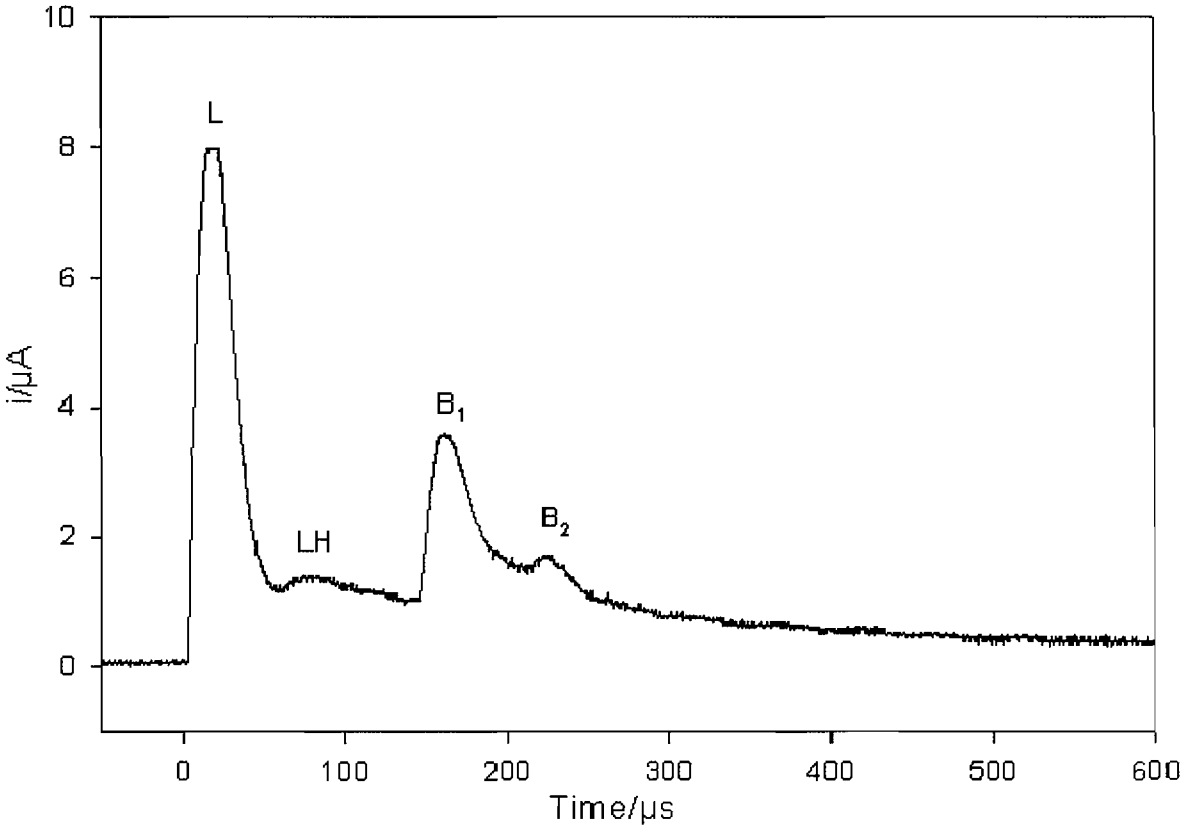

Figure 3.8. Plot showing the erosion signal recorded for 125 μm diameter Pb electrode exposed to a single laser generated bubble event. The laser was fired at t = 0 s. The solution contained 1 mM KI and 0.2 M Na_2SO_4. The potential of the electrode was held at +0.6 V vs. SCE.

The transients in figure 3.8 were recorded with increased time resolution in comparison to figures 3.4-3.6. The electrochemical arrangement was also optimised. A number of transients are apparent. First, at time t = 0 s a large anodic current time transient was observed (labelled L). The hydrophone signal in figure 3.7 showed a large transient when the optical breakdown occurred. Therefore it can be concluded that the peak A in figure 3.8 is also a result of laser action. This coincides with the formation of a shock wave as the result of liquid breakdown[‡]. In addition two further transients are observed (labelled B_1 and B_2). Similar transients were also observed in figure 3.7 150 μs after the transient observed at optical breakdown. These are assigned to a bubble collapse process in close proximity to the electrode surface. It is also interesting to note that there are two distinct events shown here which are possibly assigned to the erosion of the surface from primary bubble collapse (B_1) and secondary bubble collapse after rebound (B_2). In addition, the size of the erosion events indicates that erosion of the

[‡] Note due to the short distances (< 1 mm) some laser ablation may occur.

surface as a result of liquid breakdown is at least twice as high as the erosion of the surface by bubble action. This poses an interesting question as to the validity of cavitation erosion studies performed through this laser generation method. The electrochemical data presented here suggests that a significant proportion of the damage caused to a solid surface is a result of liquid breakdown through the action of the laser itself rather than bubble action. This conclusion would not be possible with *ex-situ* investigation of the surface which is commonly employed [21]. However, the electrochemical experiment has the temporal resolution necessary to distinguish between these events and is an *in-situ* technique. Finally the baseline for the electrochemical signal has been shifted away from zero in the time interval between laser shock erosion (L) and the bubble processes (labelled $B_{1,2}$). In this region a small anodic current can be observed (labelled LH). The origin of this event is unclear, but it is possible that heating of the liquid due to the laser pulse are responsible. It must be remembered that the ~15 mJ pulse of laser energy is focussed to < 1 mm from the surface of the salt passivated Pb solid/liquid interface. Clearly some of this energy results in solution heating. The passivation of the Pb surface relies on the insolubility of the $PbSO_4$ layer. The solubility product, K_{sp}, of $PbSO_4$ is 1.82×10^{-8} at 25 °C. Hence it is possible to calculate the solubility product as a function of temperature (and hence the concentration of Pb^{2+} at the solid liquid interface) using equation (1)

$$\ln K_{sp} = -\frac{\Delta G^o}{RT} \qquad (1)$$

here ΔG^0 is the Gibbs free energy associated with the process, T the temperature and R the gas constant. This calculation suggests that the solubility of the $PbSO_4$ increases with temperature. However, equating this to the actual local temperature is a non-trivial matter as a number of temperature dependent parameters (e.g. the mass transfer coefficient of the Pb^{2+} ion as a function of temperature and solution flow) as well as the contribution of direct laser heating of the surface need to be known directly. Clearly without supporting experimental evidence a local temperature prediction is difficult to achieve from the data. Nevertheless the presence of the transient labelled 'LH' in figure 3.8 does suggest that local temperature may be important. Indeed electrochemical experiments using direct focussing of laser energy onto electrode surfaces to induce rapid temperature changes (but with lower intensities) have been reported in the

literature [98,99]. These provide supporting evidence for the consideration of thermal effects within the experimental environment employed here.

3.5 Conclusions

In this chapter a Pb/Pt microelectrode was employed to study laser cavitation. The purpose of these initial experiments was to establish whether this electrode system was suitable for mass transfer and erosion studies. Many encouraging results were achieved and it was demonstrated that electrochemical methods were suitable to study laser generated cavitation. When a lead disc was employed to study erosion, a very strong signal always occurred at time $t = 0$ s. This could be a result of laser ablation, where material is removed by laser heating effects [100,101]. A separate electrochemical signal was detected on the lead disc of the microelectrode as a result of cavitation erosion on bubble collapse. However, the first transient at $t = 0$ s decays relatively slowly, which could be caused by heating effects. This implies that the response of the lead electrode is actually too slow to detect cavitation erosion caused by a laser. It was also noted, that some coupling might be happening between the two electrodes.

Therefore, it was necessary to introduce a new sensor for erosion studies and mass transfer and erosion should be studied separately. These results are discussed in the next chapters.

Chapter 4

Mass transfer studies on Au microelectrode

This chapter presents a more detailed study of the effects of laser generated cavitation bubbles on mass transfer to an electrode surface. A gold microelectrode has been employed to record cavitation events that are produced as a consequence of laser radiation in a solution containing a suitable redox probe. These events are detected on the microelectrode as current-time transients caused by a single laser generated cavitation bubble. An enhancement is detected in mass transfer of material to an electrode surface. This enhancement was associated with the forced convection, ie. bubble motion, resulting from laser discharge near the electrode surface. The effects of electrode potential, laser energy and the position of the electrode with respect to the bubble are presented. The shapes and magnitudes of current-time transients are discussed.

In the previous experiments, a platinum disc electrode was chosen to study mass transfer effects of laser cavitation. Chapter 3 presented the results for experiments where a Pb/Pt dual microelectrode was employed. It was noticed that some coupling of the electrodes was present (for details see chapter 3 section 3.3). Hence to investigate the origin of this effect and to isolate mass transfer only, it was necessary to investigate mass transfer separately from erosion.

The influence of laser energy and therefore bubble size [20] on mass transfer to a microelectrode was investigated. In addition, experiments were completed with low laser energies (5-7 mJ/pulse), where no bubbles were formed. This was to investigate the effects of laser action, in the absence of bubble formation, on the electrochemical and instrument response of the systems employed. In addition, the affect of an increase in the applied energy above that required to generate a cavitation bubble was studied. Finally, the effect of the position of the electrode was also investigated. These results are presented here.

4.1 Electrochemical characterisation of gold microelectrode

An inlaid gold micro disc electrode (from hence referred to as a microelectrode) of diameter 25 μm was employed as an electrochemical sensor for these mass transfer studies. Figure 4.1 presents the cyclic voltammogram of a 25 μm diameter gold microelectrode in a solution containing 5 mM $K_4Fe(CN)_6$ in 0.2 M $Sr(NO_3)_2$. The choice of $Sr(NO_3)_2$ as an inert background electrolyte was based on its ability to enable the electrochemistry of the ferro/ferricyanide system to be reproducible. The plateau in the current potential response of this electrode at potentials >+0.3 V vs. SCE corresponds to the mass transfer limited oxidation of the $Fe(CN)_6^{4-}$ species at the microelectrode surface. At this potential, a steady state oxidation current of ~12 nA is applied on the electrode surface. It is possible to calculate the diffusion coefficient of the $Fe(CN)_6^{4-}$ species from this steady state current[§]. In this case a value of 5.0×10^{-6} $cm^2\ s^{-1}$ is obtained [97]. The sigmoidal shape of the current potential curve shown in figure 4.1 is produced by the hemispherical diffusion field prevalent for electrodes of this dimension and geometry. In the absence of other forces and if the electrode potential is maintained >0.3 V vs. SCE, then a steady current of ~ 12 nA is observed. However, any perturbation of this diffusion field, produced through, for example, the forced convection of fluid due to bubble motion will be detected as an enhanced current at the microelectrode.

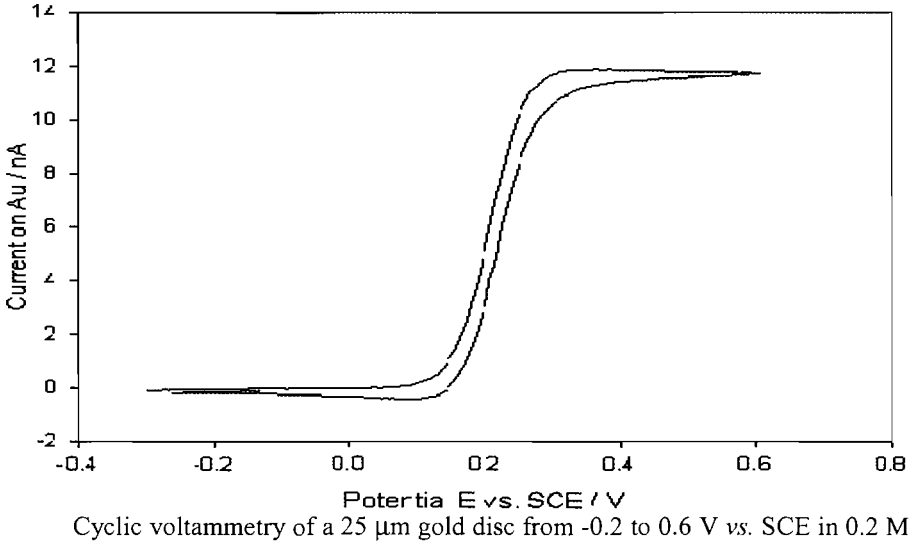

Figure 4.1 Cyclic voltammetry of a 25 μm gold disc from -0.2 to 0.6 V *vs.* SCE in 0.2 M $Sr(NO_3)_2$ containing 5 mM $K_4Fe(CN)_6$ at room temperature in aerobic conditions. The sweep rate was 20 mV s^{-1}.

[§] $i_{MTL}=4n_eaFDc$, where a is the radius of the electrode, F is the Faraday's constant, D is the diffusion coefficient and c is the bulk concentration of the electroactive species.

4.2 The effect of applied laser energy on mass transfer

In order to discriminate between processes that are associated with the laser discharge and its possible effects on the electrode surface, a number of experiments were performed to investigate the effect of laser power on the electrochemical current time transients recorded. It had been noted that a strong audible acoustic signature (a distinct 'cracking' sound) could be observed only above certain critical laser energies. Considering the nature of the experimental arrangement employed, it is likely that this observation is associated with a threshold for the formation of a large cavity within the liquid and its subsequent collapse. This hypothesis was supported by observation of high-speed video images recorded above and below this critical threshold.

Figure 4.2 presents a typical series of images of a bubble collapsing near an electrode surface in a solution of 1 mM KI in Na_2SO_4.

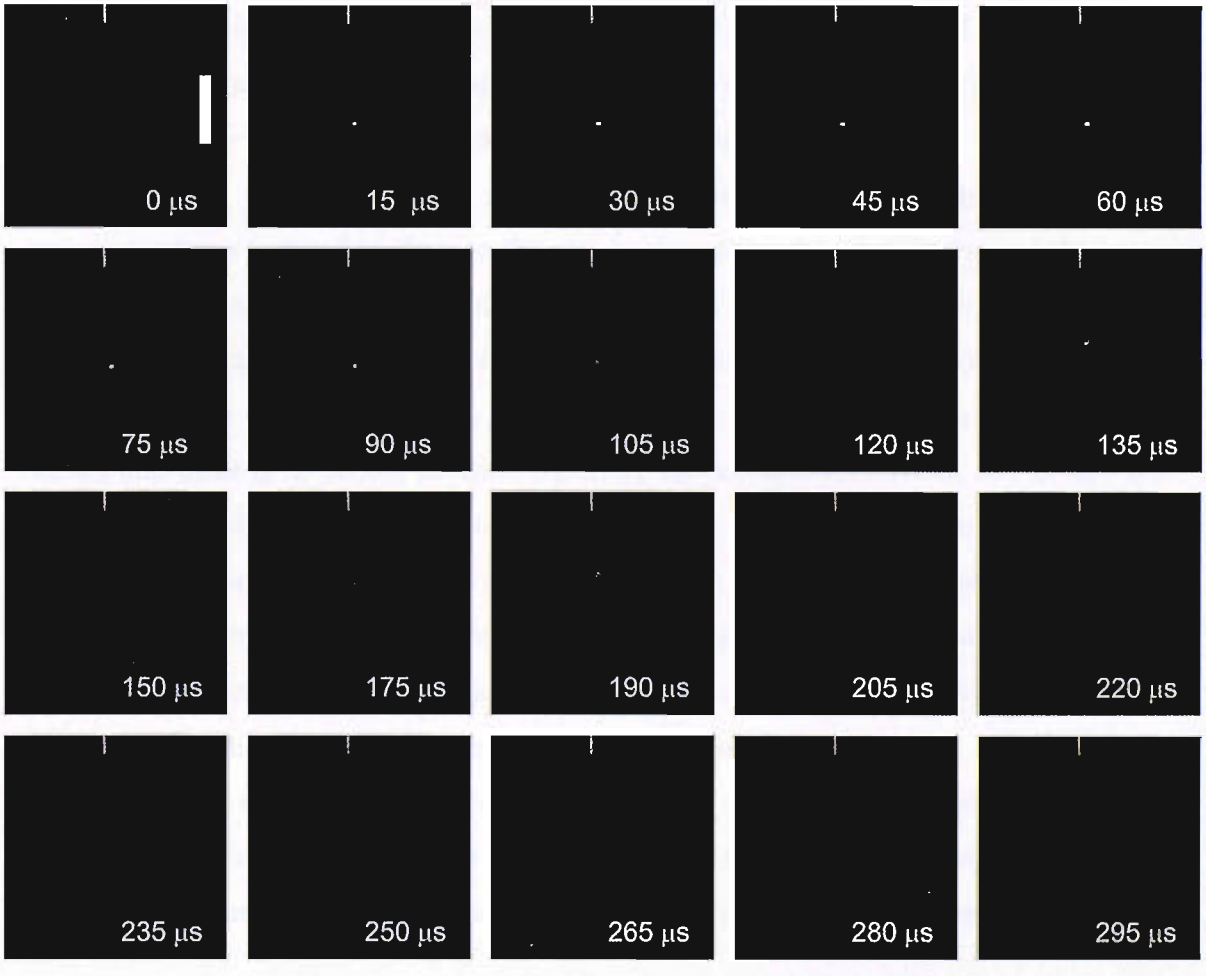

Figure 4.2 Formation of a cavitation bubble in a liquid containing 1 mM KI in Na_2SO_4 recorded at 64 000 fps. Scale bar in the figure is 1 mm.

Below the threshold for formation of the acoustic signature from the cell, no bubble formation was detected by either electrochemical or high-speed imaging means. For example figure 4.3 (a) shows the effect of laser discharge focussed into the liquid directly below a 25 μm diameter Au microelectrode held in a solution containing potassium ferrocyanide. In this case the electrode was held under mass transfer limiting conditions (+0.4 V *vs.* SCE). Hence any perturbation in the diffusion field, caused by forced convection processes, will be detected as a positive current enhancement at the microelectrode. In the absence of such mechanisms, a steady state oxidation current of ~12 nA corresponding to the conversion of ferrocyanide to ferricyanide species is detected at the electrode surface. This was observed at times < -120 μs with respect to the laser discharge (the negative sign indicating that the event was prior to laser discharge). It should be noted that the data acquisition was triggered by a photodiode which recorded the discharge of the laser at time t = 0 s. In the experiments presented in here, a Continuum Surelite SL-II was employed. The laser energy was controlled by the Q-switch delay time, which for Continuum SL-II was at the range of 110-140 μs in these experiments. In this experimental setup (gain, electrode and laser) the operation of the Q-switch and the laser discharge causes a number of transients which operate over time from -120 μs to ~+220 μs. However, after this period the electrochemical response returns to a value close to the steady state current in the absence of the laser event. The origin of these transients can be linked to the laser discharge. For example the positive transient prior to time t = 0 s corresponds to the laser Q-switch delay. The events after t = 0 s also appear to be a result of the laser discharge as figure 4.3 (b) shows that there is no strong acoustic signature for solution breakdown and in turn no associated bubble emission. However, after ~200 μs the current returns to a value 26 nA which is close to, but in excess of, the steady state current. In the absence of shocks and bubble events, one could postulate that this slight increase in current is a result of local solution heating as a consequence of laser discharge into the liquid. However, an accurate estimation of this effect is difficult to give as the exact energy lost as heat in the locality of the laser focal point is not known under the conditions employed. Nevertheless, the electrochemical data suggests that the perturbation of the mass transfer environment around the microelectrode is minimal under these conditions.

Figure 4.4 shows the effect of increasing the laser energy (by changing the Q-switch delay) on both the electrochemistry and the acoustic emission within the liquid. In this

case a strong audible acoustic emission was observed. In turn the data recorded from the hydrophone suggests that liquid breakdown as the result of laser action occurs (see figure 4.4 (b) LS_1). No simultaneous high speed imaging was employed in the electrochemical experiments presented in this chapter, but the distance between the electrode surface and the bubble centre was estimated to be <1500 μm.

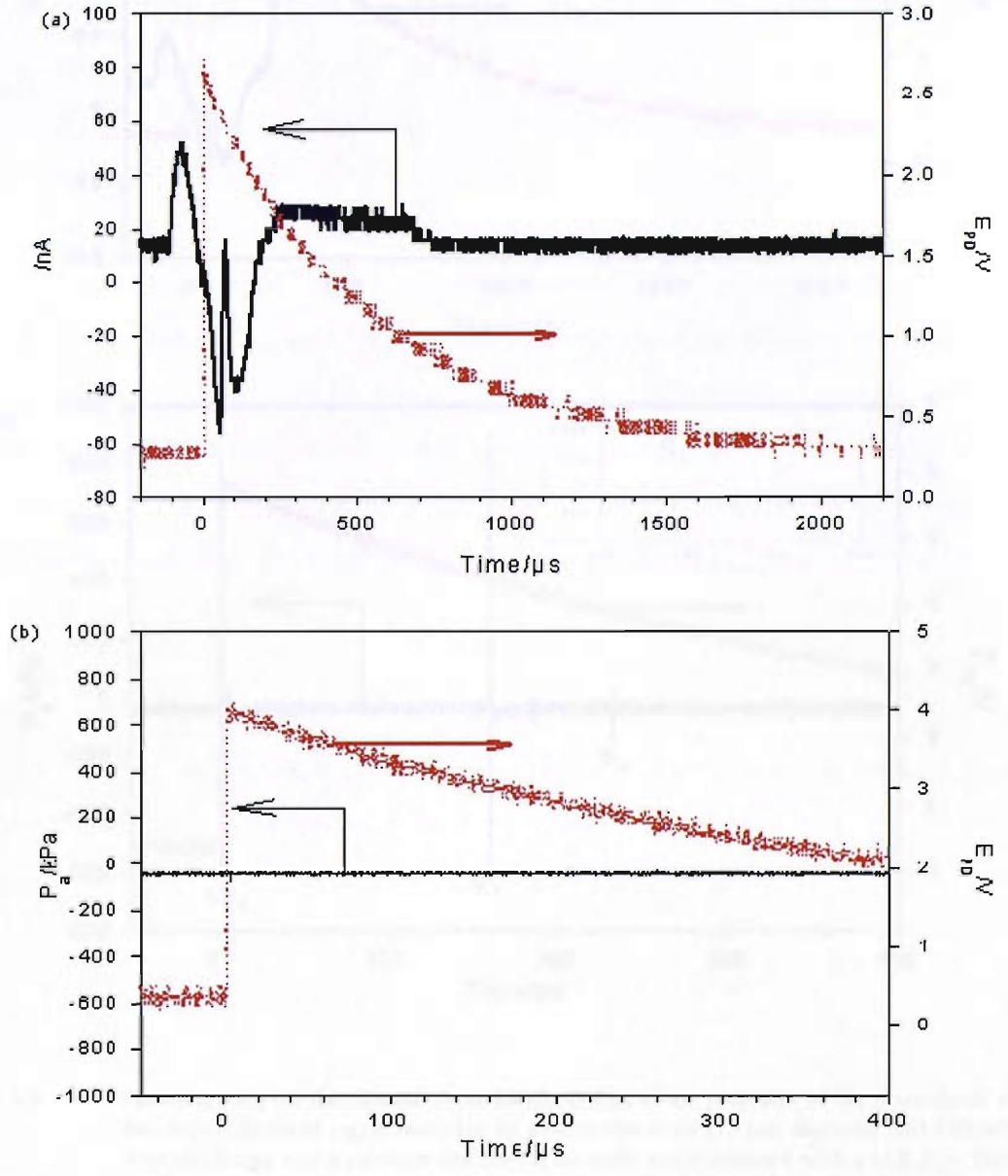

Figure 4.3 Plots showing (a) the simultaneous measurement of the response of the photodiode and the electrochemical signal recorded by a microelectrode (25 μm diameter Au) following laser discharge into a solution and (b) the acoustic trace detected with a G.R.A.S. DB10 needle hydrophone in comparison to the laser discharge (shown as the photodiode output, E_{PD}). The laser energy was ~7 mJ. The electrolyte consisted of 5 mM $K_4Fe(CN)_6$/0.1 M $Sr(NO_3)_2$ solution. The microelectrode was positioned ~1.5 mm from the focal point of the laser. The experiments were performed at room temperature (~20 °C).

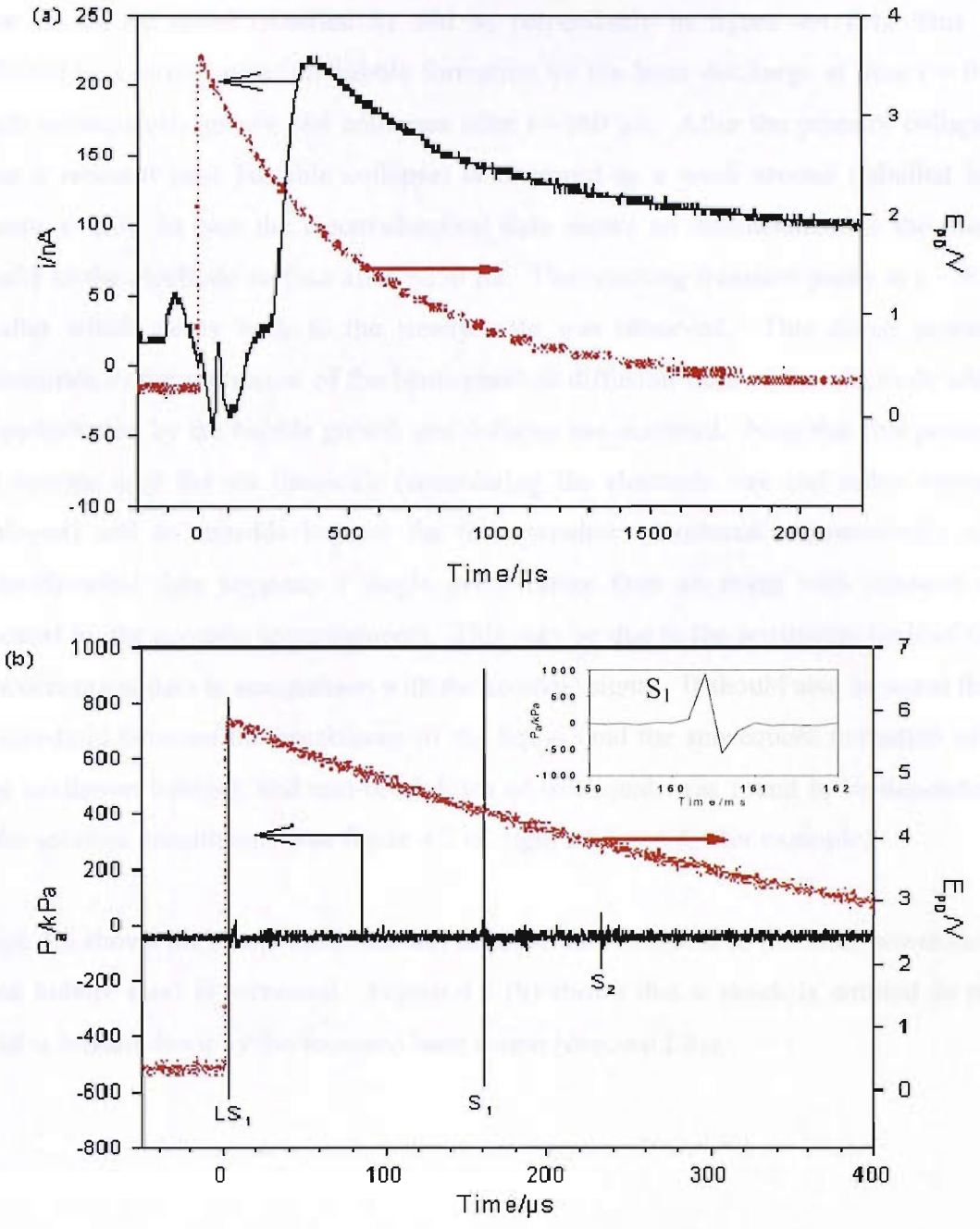

Figure 4.4 Plots showing (a) the simultaneous measurement of the response of the photodiode and the electrochemical signal recorded by a microelectrode (25 μm diameter Au) following laser discharge into a solution and (b) the acoustic trace detected with a G.R.A.S. DB10 needle hydrophone in comparison to the laser discharge (shown as the photodiode output, E_{PD}). LS_1 is the acoustic transient generated when the laser fires, S_1 is caused by the bubble collapse and the S_2 is caused by the secondary collapse. The laser energy was ~23 mJ. The electrolyte consisted of 5 mM $K_4Fe(CN)_6$/0.1 M $Sr(NO_3)_2$ solution. The microelectrode was positioned ~1.5 mm from the focal point of the laser. The experiments were performed at room temperature (~20 °C). The insert in figure 4.4 (b) represents a blow-up of the peak S_1.

In addition to the shock generated by laser discharge LS_1, a second and third acoustic event should be noted (labelled S_1 and S_2 respectively in figure 4.4 (b)). This is attributed to a large cavitation bubble formation by the laser discharge at time t = 0 s which subsequently grows and collapses after t ~160 μs. After the primary collapse phase a rebound (and possible collapse) is observed as a weak second (labelled S_2) acoustic event. In turn the electrochemical data shows an enhancement in the mass transfer to the electrode surface after ~250 μs. The resulting transient peaks at t ~ 400 μs after which decay back to the steady state was observed. This decay process corresponds to the relaxation of the hemispherical diffusion field of the electrode after the perturbation by the bubble growth and collapse has occurred. Note that this process will operate over the ms timescale (considering the electrode size and redox system employed) and so extends beyond the time window monitored. Interestingly the electrochemical data suggests a single event rather than an event with rebound as indicated by the acoustic measurements. This may be due to the sensitivity limit of the electrochemical data in comparison with the acoustic signal. It should also be noted that the threshold between the breakdown of the liquid (and the subsequent formation of a large cavitation bubble), and non-breakdown of the liquid, was found to be dependent on the solution constituents (see figure 4.2 *vs.* figure 4.3 and 4.4 for example).

Figure 4.5 shows the electrochemical and acoustic data recorded as the laser power (and hence bubble size) is increased. Figure 4.5 (b) shows that a shock is emitted as the liquid is broken down by the focussed laser action (denoted LS_2).

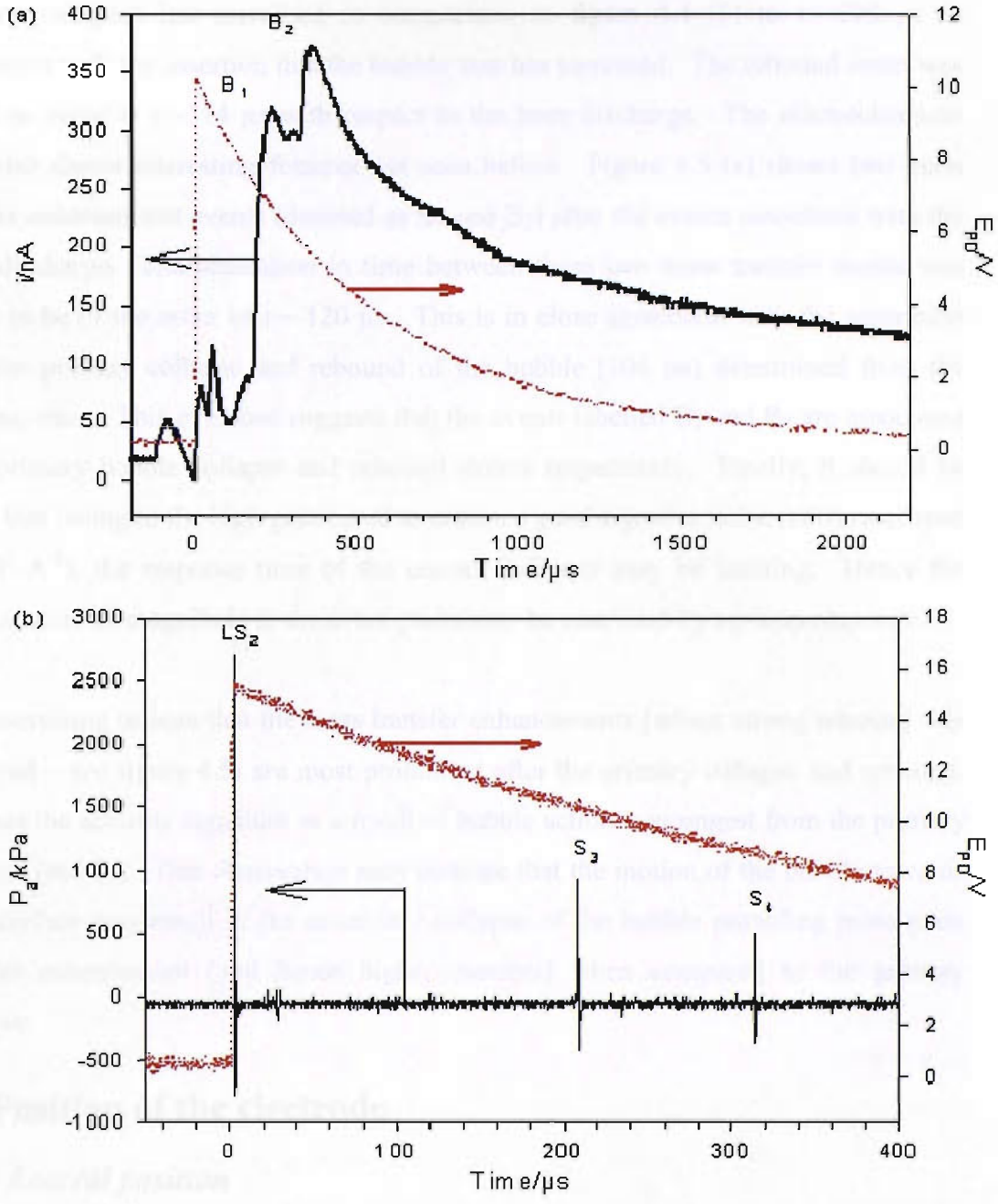

Figure 4.5 (a) Plots showing the simultaneous measurement of the response of the photodiode and the electrochemical signal recorded by a microelectrode (25 μm diameter Au) following laser discharge into a solution. (b) Plots showing the acoustic trace detected with a G.R.A.S. DB10 needle hydrophone in comparison to the laser discharge (shown as the photodiode output, E_{PD}). The laser energy was ~44 mJ. The electrolyte consisted of 5 mM $K_4Fe(CN)_6$/0.1 M $Sr(NO_3)_2$ solution. The microelectrode was positioned ~1.5 mm from the focal point of the laser. The experiments were performed at room temperature (~20 °C).

In this case the magnitude of the LS_2 is considerably bigger (>2.5 MPa) than that shown in figure 4.4 (b) (LS_1 ~ 0.8 MPa). In addition the signal from the bubble collapse is also considerable (S_3 ~0.9 MPa) and the rebound signal (S_4 ~0.55 MPa) is clearly defined.

Interestingly the bubble lifetime (defined here as the time taken from laser discharge to primary collapse) has increased in comparison to figure 4.4 (b) to t ~208 μs in agreement with the assertion that the bubble size has increased. The rebound event was found to occur at t ~314 μs with respect to the laser discharge. The electrochemical data also shows interesting features not seen before. Figure 4.5 (a) shows two mass transfer enhancement events (denoted as B_1 and B_2) after the events associated with the laser discharge. The separation in time between these two mass transfer events was found to be of the order of $t \sim 120$ μs. This is in close agreement with the separation between primary collapse and rebound of the bubble (106 μs) determined from the acoustic trace. This evidence suggests that the events labelled B_1 and B_2 are associated with primary bubble collapse and rebound events respectively. Finally, it should be noted that owing to the high gain (used to ensure a good signal to noise ratio) employed (10^7 V A^{-1}), the response time of the current follower may be limiting. Hence the absolute current magnitude at the event peaks may be restricted by op-amp response.

It is interesting to note that the mass transfer enhancements (where strong rebound was observed – see figure 4.5) are most prominent after the primary collapse and rebound: whereas the acoustic signature as a result of bubble action is strongest from the primary collapse (see S_3). This observation may indicate that the motion of the bubble towards the interface may result in the secondary collapse of the bubble providing more mass transfer enhancement (and hence higher currents) when compared to the primary collapse.

4.3 Position of the electrode

4.3.1 Lateral position

The mass transfer effects of laser induced cavitation were further investigated by varying the position of a 25 μm diameter Au electrode in a solution of 5 mM $K_4Fe(CN)_6$ in 0.1 M $Sr(NO_3)_2$ laterally and the mass transfer current recorded. The plasma and thereby also the cavitation bubble are formed at the focus of the laser beam. Therefore, the highest current is expected to be found near this position. If the detected current transients are actually caused by cavitation events, a smaller current is expected when the electrode is moved further away from the focal spot of the beam. A position of the electrode where a strong mass transfer current was detected was chosen as a starting position for the experiments and was marked as position (0,0). From this position the

electrode was then moved laterally at 0.2 mm steps on a *x,y*–plane. The directions are illustrated in the figure 4.6. The potential of the electrode was held under mass transfer limiting conditions (+0.4 V *vs.* SCE) for each experiment. Any perturbation in the hemispherical diffusion field, caused by forced convection processes, will be detected as a positive current at the microelectrode. In the absence of such mechanisms, a steady state oxidation current of ~12 nA corresponding to the conversion of ferrocyanide to ferricyanide species at the electrode surface was observed. This is in agreement with the currents reported in figure 4.1 where a steady state current of 12 nA was observed whe the potential was +0.4 V *vs.* SCE.

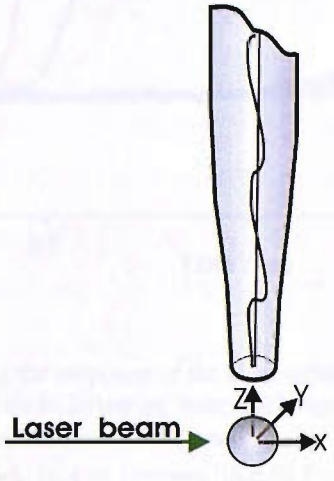

Figure 4.6 Experimental set-up for the experiments where the electrode was moved in *x,y,z*-directions.

In these experiments, no high-speed camera was employed (employing a high-speed camera would have been very beneficial, but unfortunately no camera was available at this time). However, the distance between the electrode surface and the bubble centre was thought to be <1000 μm from these and previous experiments. Figure 4.7 presents the current time mass transfer signal recorded at six different positions of the electrode. The choice of the starting position was arbitrarily assigned to (0,0) and the electrode moved in the positive *x*-direction at 0.2 mm steps. Each transient represents the current recorded at each position employed.

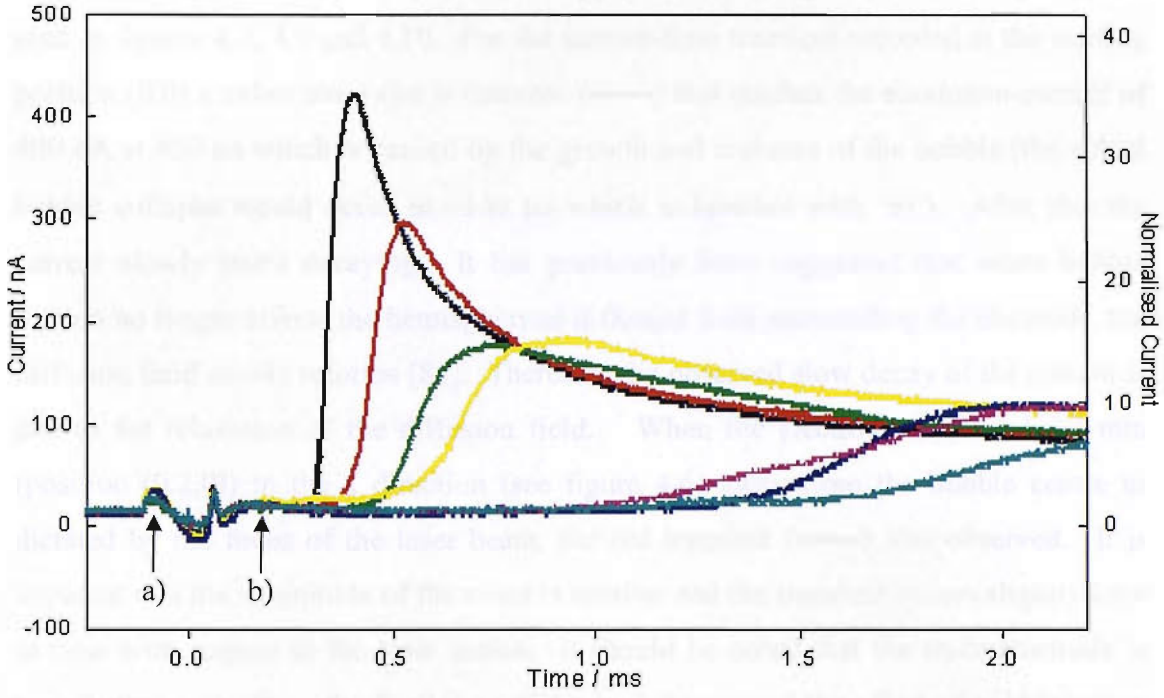

Figure 4.7 Plots showing the response of the electrochemical signal recorded by a 25 µm diameter Au microelectrode following laser discharge into a solution of 5 mM $K_4Fe(CN)_6$ in 0.1 M $Sr(NO_3)_2$ when the electrode was moved laterally. The positions were (0,0) (——), (0.2,0) (——), (0.4,0) (——), (0.6,0) (——), (0.8,0) (——), (1.0,0) (——) and (1.2,0) (——). The potential of the electrode was held at +0.5 V vs. SCE and the laser energy was ca. 25 mJ/pulse. The distances do not represent the accurate distances from the focal spot but the distances from position (0,0) where the strongest electrochemical transient was detected. The arrow labelled a) indicates the activation of the Q-switch and b) indicates the actual collapse time of the bubble.

For each transient in figure 4.7, a steady state current of 12 ± 4 nA was detected on the electrode at the beginning of the experiment. At about -130 µs (labelled 'a)'), a small transient is detected for each trace. This was thought to assigned to the activation of the laser Q-switch. For these experiments, the laser Q-switch delay was set to 125 µs which would mean the activation of the Q-switch would occur at –125 µs. This clearly proves that the transient detected for each trace at -130 µs was caused by laser activity. The chosen Q-switch delay 125 µs corresponded to laser energy of 25 ± 3 mJ/pulse. Another small transient was seen at 50 µs. The transient does not change as the electrode moves and the distances are too small for the shock and can therefore be attributed to laser action. At 50 µs, the shock moves 50 mm which is way past the electrode.

The mass transfer events of interest take place after 300 μs. These time scales and the transients observed are reproducible and expected for this experimental arrangement as seen in figures 4.7, 4.9 and 4.10. For the current-time transient recorded at the starting position (0,0) a rather steep rise is detected (——) that reaches the maximum current of 400 nA at 450 μs which is caused by the growth and collapse of the bubble (the actual bubble collapse would occur at ~150 μs which is labelled with 'b)'). After this the current slowly starts decaying. It has previously been suggested that when bubble motion no longer affects the hemispherical diffusion field surrounding the electrode, the diffusion field slowly reforms [81]. Therefore the observed slow decay of the current is due to the relaxation of the diffusion field. When the electrode is moved 0.2 mm (position (0.2,0)) in the x direction (see figure 4.6) away from the bubble centre as dictated by the focus of the laser beam, the red transient (——) was observed. It is apparent that the magnitude of the event is smaller and the transient occurs slightly later in time with respect to the laser action. It should be noted that the microelectrode is now further away from the focal spot of the laser beam, and the effect of bubble action on the hemispherical diffusion field is therefore smaller. Thus, the maximum current recorded for the red trace is 300 nA, 100 nA less than for the black trace. In addition the electrochemical response is slower through the forced convection/diffusion response of the electrode. Note that for a linear diffusion model[**] alone the time response over this length scale can be estimated with the relationship $t = l^2/D$ (where l = distance and D the diffusion coefficient). For these dimensions, and a typical diffusion coefficient, a diffusion only response would take an estimated 80 s. Hence this time difference is related to the convection/diffusion response of the electrode as expected.

Figure 4.7 shows that when the microelectrode is moved even away further away, to 0.4 mm (——) and 0.6 mm (——) from the starting position (0,0), the observed current is further reduced and the response time of the current time transient extends to longer times. Figure 4.7 also shows that these two currents have a similar magnitude, but the trace recorded for position (0.6,0) appears later than the trace for (0.4,0). The bubble at (0.6, 0) is further away from the microelectrode and therefore the fluid motion caused by it is observed later. The next three current transients ((0.8,0), (1.0,0) and (1.2,0)) appear much later, at 1.0-1.5 ms. However, it should be noted that the microelectrode

[**] As a first approximation

is no longer directly above the bubble as the maximum bubble radius (R_m) in these experiments is of the order of 0.5-0.8 mm. Hence under these conditions the electrode has been moved a distance greater than R_m. Note that while some variation in the sizes of the bubbles is expected (which can lead to differences in the magnitude of the detected currents) the observed changes in the current time transients are greater than can be attributed to this effect. Hence a physical model related to the size and position of the bubble must be invoked. In order to illustrate the effects Figure 4.8 presents a schematic demonstrating the position of the bubble with respect to the electrode. At location (0,0) the bubble is assumed to be directly above the electrode and hence have the maximum effect on the current time signal recorded by the electrode. At location (0.6,0) part of the bubble is still above the electrode whereas at location (1.0,0) the bubble is no longer in the direct vicinity of the electrode. This explains the shift in the positions of the electrochemical transients in figure 4.7. For example for the transient at (0.6,0) (——) the bubble is still partially above the electrode. However, for the transient at (1.0,0) (——) the distance between the electrode and bubble centre is so great that the whole bubble is outside the vicinity of the electrode. Consequently the effect of the bubble on the hemispherical diffusion profile and hence the current time transient recorded is expected to be significantly less. This is indeed what is observed. Clearly as the x distance increases the time to current maximum also increases. Again there also appears to be a demarcation at ~ 0.6 mm which is likely to be the effect of the bubble radius.

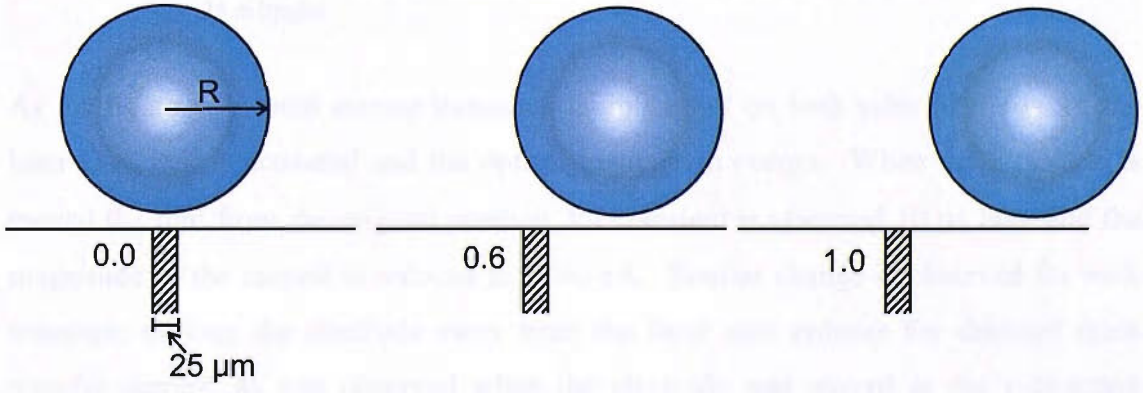

Figure 4.8 Illustrations demonstrating the location of the bubble with respect to the electrode. R is the radius of the bubble which is approximately 0.5 mm. At (0,0), the bubble is almost directly above the electrode. When the location is (0.6,0), only part of the bubble is directly above the electrode and at location (1.0,0) the bubble is completely outside the vicinity of the electrode.

Figure 4.9 presents the current-time transients recorded when the electrode was moved along the positive y-direction. The original position was the same as for figure 4.7, (0,0), and the electrode was moved 0.2 mm at each time. Again, the effect of the distance can be seen in the events recorded between 0.3 mm and 0.6 mm when a shift is seen in the position of the transients as explained in previous paragraph and figure 4.8.

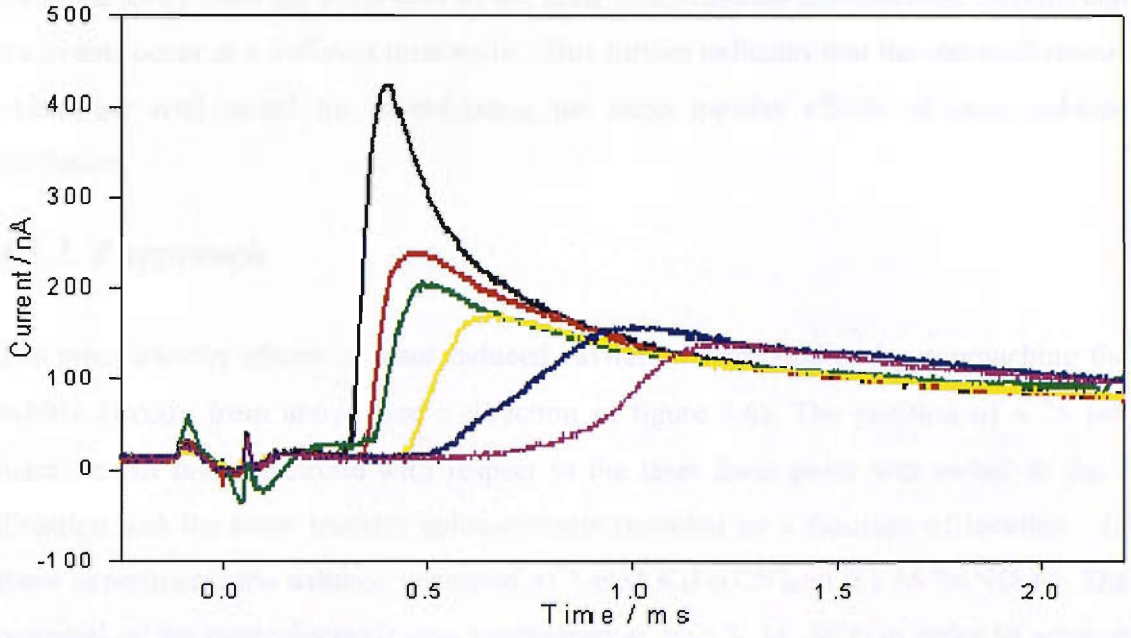

Figure 4.9 Plots showing the response of the electrochemical signal recorded by a 25 μm diameter Au microelectrode following laser discharge into a solution of 5 mM $K_4Fe(CN)_6$ in 0.1 M $Sr(NO_3)_2$ when the electrode was moved laterally. The positions were (0,0) (—), (0,0.2) (—), (0,0.4) (—), (0,0.6) (—), (0,0.8) (—) and (0,1.0) (—). The potential of the electrode was held at +0.5 V vs. SCE and the laser energy was ca. 25 mJ/pulse.

As for figure 4.7, small current transients are observed on both sides of 0 s when the laser Q-switch is activated and the optical breakdown occurs. When the electrode is moved 0.2 mm from the original position, the transient is observed 50 μs later and the magnitude of the current is reduced to ~240 nA. Similar change is observed for each transient; moving the electrode away from the focal spot reduces the detected mass transfer current, as was observed when the electrode was moved at the *y*-direction (figure 4.6). Figures 4.7 and 4.9 both indicate that under these conditions the maximum current observed in the current time transient was of the order of 400 nA. This indicated that in this position (where the bubble is estimated to be still ~1 mm away from the solid/liquid interface of the microelectrode) the enhancement in the mass

transfer coefficient is relatively small (of the order of 0.17 cm s^{-1}) but was found to be reproducible.

It is clear that the mass transfer effects of the cavitation bubble are strongly dependent on the range of the electrode from the bubble, as both the time scale and the magnitude of transients alter when the lateral position of the electrode is changed. Moving the electrode away from the focal spot of the laser beam reduces the observed current, and the events occur at a different time scale. This further indicates that the electrochemical means are well suited for investigating the mass transfer effects of laser induced cavitation.

4.3.2. Z approach

The mass transfer effects of laser induced cavitation were studied by approaching the bubble directly from above (see z direction in figure 4.6). The position of a 25 μm diameter Au microelectrode with respect to the laser focal point was varied in the *z* direction and the mass transfer enhancements recorded as a function of location. In these experiments the solution consisted of 5 mM $K_4Fe(CN)_6$ in 0.1 M $Sr(NO_3)_2$. The potential of the microelectrode was maintained at +0.5 V vs. SCE in order to achieve mass transfer limited conditions. Hence when the liquid breaks down, and a cavitation bubble is formed at the focus of the laser beam the disruption of the hemispherical diffusion field by fluid motion will again be detected as an anodic current enhancement. In this experiment when the bubble is approached from above, at a distance far above the bubble, so that no perturbation of the diffusion field should be observed. However, when the microelectrode is at a suitable distance to detect the fluid flow generated as a result of bubble motion, the perturbation of the diffusion field should be seen as an increasing current (for more detailed description, see chapter 1).

Figure 4.10 presents the electrochemical traces recorded at five different distances above the bubble. The current time signal shown as a black trace (——), represents the situation when the bubble is generated at a sufficient distance below the electrode surface, where the diffusion field is not affected by the bubble related fluid motion. Hence, on the time scale represented, no increase in steady state mass transfer current was observed. It should be noted that the small transients observed in the black trace

are associated with the laser operation (e.g. Q-switching and electronic pickup). Figure 4.10 shows that as the electrode is moved down towards the bubble centre by steps of 0.2 mm (red trace etc.), a significant increase in current is observed. The effects of the bubble on the diffusion field of the microelectrode are apparent as an increase in the mass transfer to the electrode surface (i_{max} = 100 nA). Figure 4.10 also shows that moving the microelectrode downwards to 0.4 mm (—), 0.8 mm (—) and 1 mm (—) below the original starting position (black), increases the observed current for each position as a larger portion of the diffusion field is replaced by the bubble. In addition to this increase in mass transfer perturbation, the response time of the signal decreases. This may be understood as an increased perturbation of the diffusion sphere of the microelectrode as the microelectrode approaches the bubble centre. This results in both an increase in the observed current and a decrease in the response time of the current time transient as shown in figure 4.10. Finally, at the closest z distance (—), evidence of primary and secondary bubble events were observed (indicated with arrows). Also, the noise that is seen on both sides of t = 0 ms (circled in figure 4.10) remain the same for each trace. This indicates that these are not a result of shock/laser action but electronics.

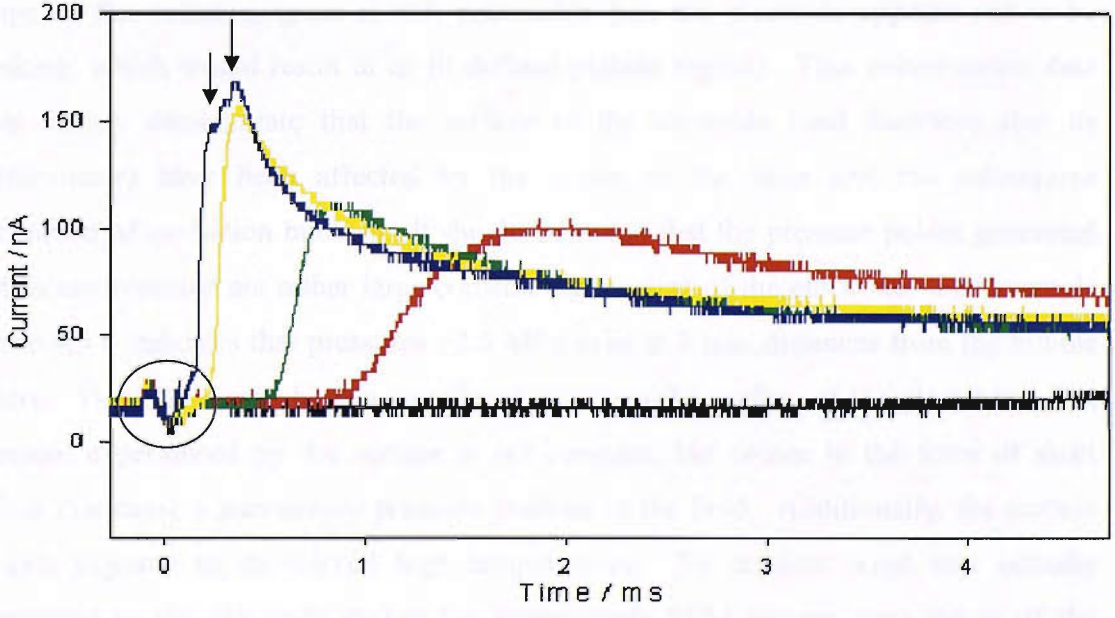

Figure 4.10 Plots showing the response of the electrochemical signal recorded by a 25 µm diameter Au microelectrode following laser discharge into a solution of 5 mM $K_4Fe(CN)_6$ in 0.1 M $Sr(NO_3)_2$ when the electrode was gradually moved towards (on z axis) the bubble. The starting position is the black trace (—), and the distances from this position are 0.2 mm (—), 0.4 mm (—), 0.8 mm (—) and 1 mm (—). The potential of the electrode was held at +0.5 V vs. SCE and the laser energy was ca. 25 mJ/pulse. The arrows indicate the primary and the secondary collapse of the bubble. The circle indicates the transients associated with the laser operation.

4.3.3 Damage caused to the electrode surface

Clearly the results presented thus far in this chapter indicate that this experimental approach is able to detect the presence of the cavitation bubble and its associated effects on the mass transfer to a microelectrode. However, in these experiments the ultimate distance between the bubble centre and the electrode was maintained at ~1000 μm in an attempt to extend the lifetime of the microelectrode in this environment. Nevertheless, it was observed that the steady state signal on the Au electrode changed over the course of the experiments. It was believed that, even though the surface of the microelectrode was ~1000 μm away from the laser focal point, the laser damaged the electrode during the experiments. Hence the absolute value of the steady state current became more unreliable with time. Figure 4.11 shows the cyclic voltammogram for the 25 μm gold in a solution containing 5 mM $K_4Fe(CN)_6$ in 0.2 M $Sr(NO_3)_2$ before a series of experiments (—) and after being exposed to the laser radiation (– – –). Before the experiments involving the generation of laser induced cavitation close to the microelectrode surface, the polished electrode has a plateau current of ~ 12 nA. After the microelectrode has been exposed to the laser radiation a number of time (estimated to be 100's of cavitation bubbles) this plateau has shifted to ~ 22 nA. Interestingly the shape of the voltammogram is still reasonable (i.e. the electrode appears not to be 'leaking' which would result in an ill defined plateau region). This voltammetric data does clearly demonstrate that the surface of the electrode (and therefore also its performance) have been affected by the action of the laser and the subsequent generation of cavitation bubbles. It should be noted that the pressure pulses generated in this environment are rather large considering the size of the electrode. For example figure 4.5 b indicates that pressures >2.5 MPa exist at 3 mm distances from the bubble centre. These appear to have a significant effect on the surface of the electrode. The pressure experienced by the surface is not constant, but comes in the form of short pulses that cause a momentary pressure gradient in the field. Additionally, the surface is also exposed to short-lived high temperatures. To confirm what was actually happening to the electrode during the experiments SEM images were taken of the electrode surface. Figure 4.12 presents an SEM image of a 25 μm microelectrode that has been exposed to laser cavitation. Some rather dramatic events have occurred on the electrode surface. The gold wire has actually been pulled out of the epoxy. The reason for this is uncertain, but could have something to do with the physical properties of

gold. One of the most notable characteristic features of gold is its ductility [102]. The pressure waves emitted at the optical breakdown and bubble collapse affect the gold disc and surrounding epoxy, and the varying pressure in some alternating pushing and pulling activity on the surface results. Owing to its ductility the gold wire does not return to its original shape, but becomes stretched which looks like as if it has been dragged out of the epoxy bedding.

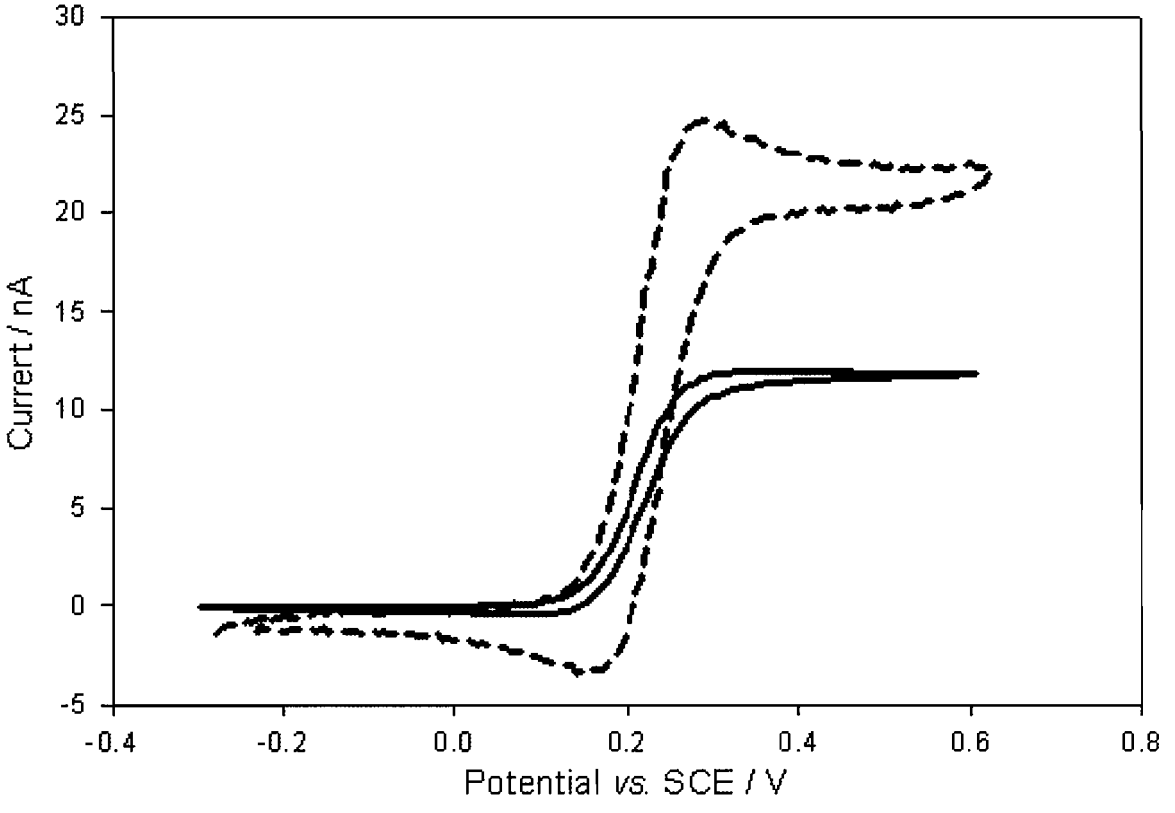

Figure 4.11 Cyclic voltammetry of a 25 μm gold disc in 0.2 M $Sr(NO_3)_2$ containing 5 mM $K_4Fe(CN)_6$ at room temperature before (———) and after (– – – –) being exposed to laser radiation during the experiments. The sweep rate was 20 mV s^{-1}.

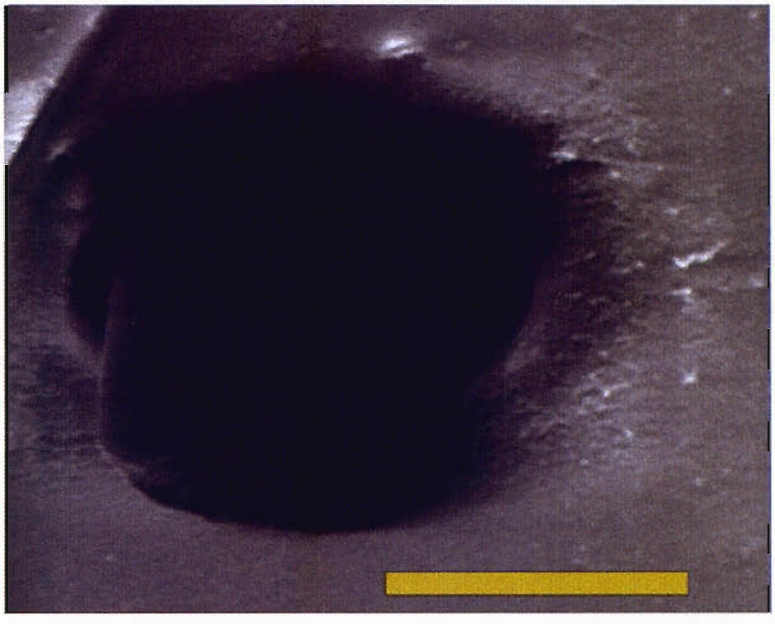

Figure 4.12 SEM image of a 25 μm microelectrode after being exposed to laser cavitation effects. The scale bar in the image is 20 μm.

4.4 Conclusions

This chapter presented the results when mass transfer enhancement from a single large cavitation bubble was measured using a microelectrochemical technique. A 25 μm gold microelectrode was employed. Significant enhancements in mass transfer were demonstrated when single bubbles were generated by laser discharge close to the electrode surface. The events were only detected when the laser energy exceeded the threshold energy for optical breakdown, and could not therefore be caused by laser heating or electronics alone. Evidence for bubble growth and rebound has been gained from electrochemical, acoustic and high-speed video footage. A threshold in electrolyte solutions for the formation of large cavitation bubbles has been noted from both electrochemical and acoustic data. It was also noted, that the mass transfer enhancement was very distance dependent, as expected. Moving the electrode further away from the forming bubble decreased the magnitude of recorded electrochemical events. It was also noted that during the experiment, significant damage was caused to the electrode; the cyclic voltammograms recorded before and after the experiments showed a significant increase in the mass transfer limiting current. The SEM-images taken after the experiment provided an explanation for this; the electrode is pulled out from the epoxy during the experiments. The reason for this was unclear, but was

thought to have something to do with the ductility properties of gold. Therefore, gold was not an ideal choice as an electrode material in the experiments where electrochemical means have been employed to study optical cavitation, even though good results have been achieved in the past when this material has been employed to study acoustic cavitation. It was necessary to employ another electrode material for the mass transfer studies to establish whether improvement in the endurance could be obtained. Also, it would be necessary to employ a high-speed camera to see whether the events presented are actually caused by laser activity.

Chapter 5

Employment of a Pt/Al dual electrode for simultaneous mass transfer and erosion studies

Chapter 3 reported the results of initial experiments to study the mass transfer and erosion simultaneously when a single cavitation bubble was generated with a laser. Some very promising results were presented but, it was also noted that the erosion sensor used in these experiments was not ideal. The response of the Pb-electrode was too slow and an additional current time transient (possibly associated with heating effects) was observed. Also the Au electrode employed in Chapter 4 showed poor durability. Therefore, a Pt/Al dual electrode was employed to replace the Pt/Pb electrode. Aluminium was chosen for the erosion experiments as it has been used previously with cavitation erosion experiments and found to exhibit fast repassivation transients [93]. In addition, as a material, aluminium is harder than lead, and has under appropriate potential/pH conditions a permanent oxide layer. Therefore Al is more resistant against possible laser heating effects. The hardness of metal can be defined as its resistance to plastic formation, which is usually done by indentation tests [101]. Brinell hardness values of 38.3 MN m^{-2} for lead and 245 MN m^{-2} for aluminium have been reported [102]. In addition, in the experiments presented in chapter 3, it was not pure lead but the insoluble $PbSO_4$ layer that was eroded which has a temperature dependant solubility.

Metallic aluminium is very reactive with oxygen, and a thin passivation layer of aluminium oxide quickly forms on any exposed aluminium surface. This oxide layer is responsible for metallic aluminium's resistance to wearing and protects the metal from further oxidation.

In an aqueous electrolyte and under appropriate potential control, an oxide layer is present on the surface of the aluminium. The nature and type of the oxide will be dependent on the conditions and potential of the electrode surface. It is convenient to represent the thermodynamic state of the surface of the aluminium electrode by the Pourbaix diagram [103]. The relevant information is shown in figures 5.1 and 5.2.

Figure 5.1 shows that under the pH and potential conditions employed in the following experiments, a layer of $Al_2O_3.3H_2O$ (hydrargillite) will be present on the electrode surface. It can be seen from the diagram that in potentials such as those employed in the experiments presented in this chapter, the hydrargillite layer is present on the surface of the electrode. Another axis is added to the diagram to represent the relation between SCE (used in the experiments in this chapter) and SHE (standard hydrogen electrode; potential originally presented in diagram 5.1) reference electrodes. Figure 5.2 shows the passive and corrosive regions (with differing aluminium oxide forms) for aluminium at 25 °C when no substances with which aluminium forms soluble complexes or insoluble salts are present. In the potentials employed in the experiments in this chapter the hydrargillite layer is passive.

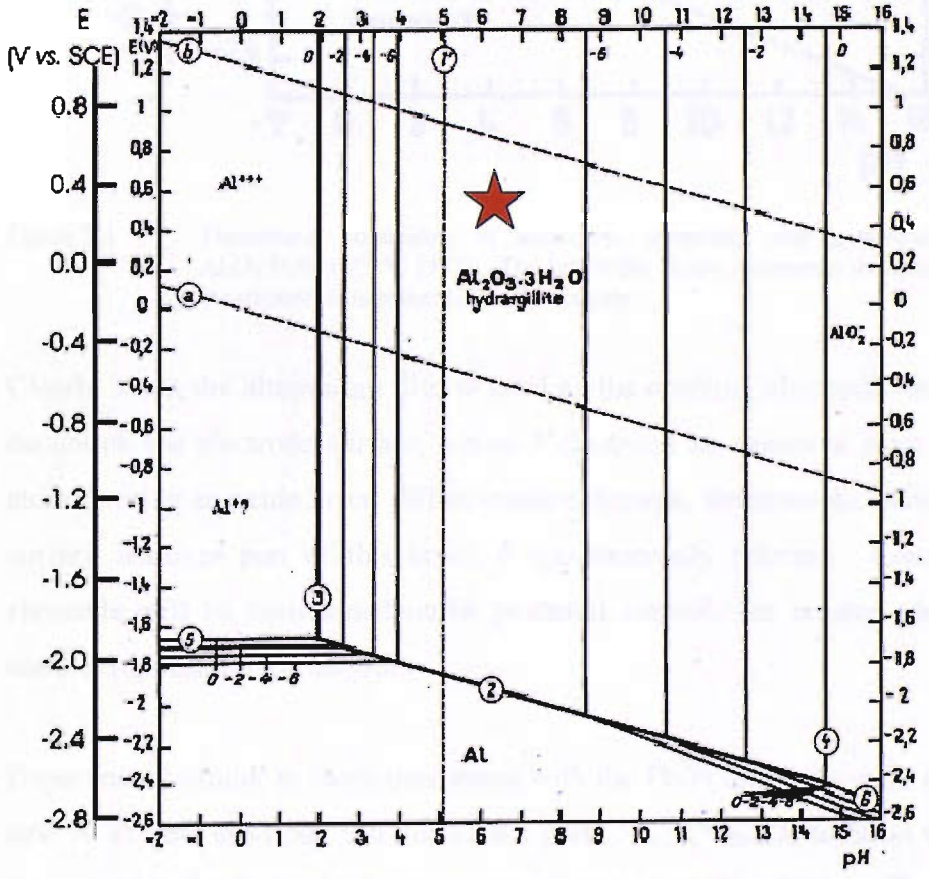

Figure 5.1 Potential-pH diagram for aluminium in water at 25 °C [103]. The red star indicates the conditions employed for experiments presented in this chapter

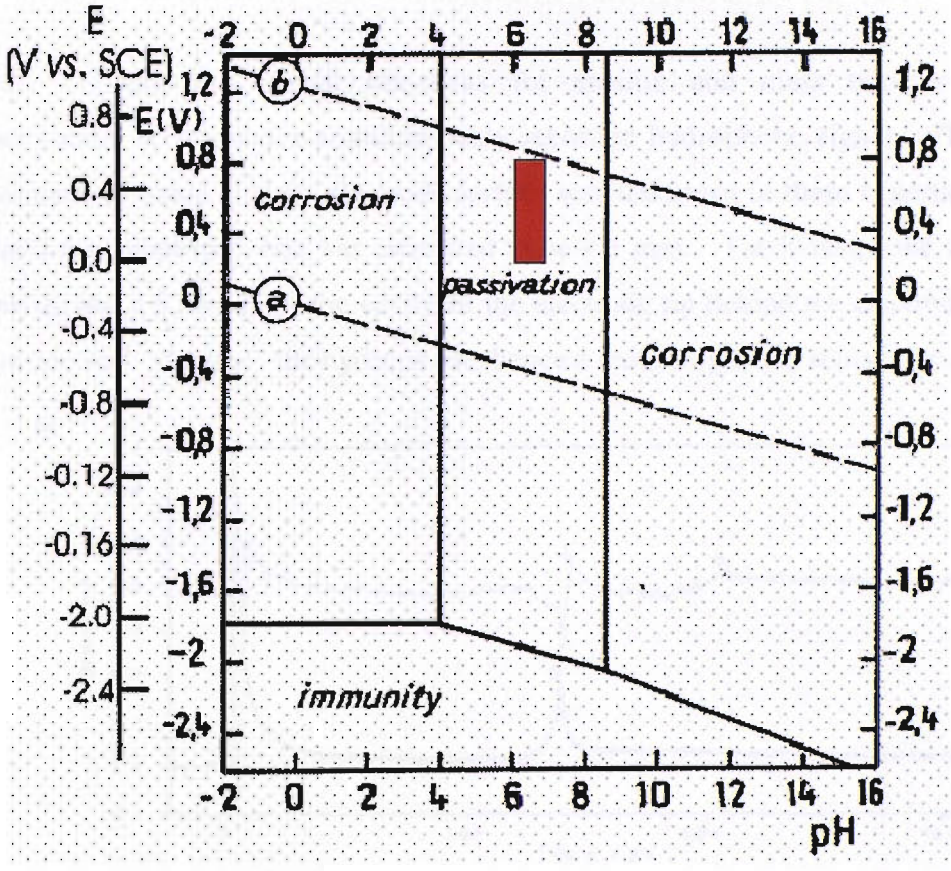

Figure 5.2 Theoretical conditions of corrosion, immunity and passivation of hydrargillite $Al_2O_3 \cdot H_20$ at 25 °C [103]. The bar in the figure represents the conditions employed in the experiments presented in the chapter.

Clearly when the aluminium disc is used as the working electrode, an anodic reaction occurs on the electrode surface, where 3 electrons are removed from each aluminium atom forming an oxide layer. When erosion through, for example, bubble action, of this surface removes part of this layer, it spontaneously reforms. Considering that the electrode will be maintained under potential control, the erosion should be seen as anodic response on the current.

Experiments similar to those performed with the Pb/Pt electrode were repeated with the new Al/Pt dual electrode. In this case a $[Fe(CN)_6]^{4-}/Na_2SO_4$ solution was employed as electrolyte in the first set of experiments presented in this chapter. The electrochemical behaviour of the Pt microelectrode in this solution was explained in chapter 3. For all experiments presented in section 5.1 the Q-switch delay of the laser was 130 μs which corresponds to the energy of ca. 40 mJ per pulse.

5.1 Initial experiments on Pt/Al electrode in ferrocyanide

Figure 5.3 presents typical transients for erosion and mass transfer with this experimental set-up and a simultaneously recorded hydrophone signal. The distance between the bubble and the electrode surface was unknown in these experiments as no camera was employed, but was estimated to be < 1 mm. The hydrophone was located approximately 5 mm from the centre of the electrode tip behind the electrode (note the electrode will "shadow" the hydrophone, hence a reduced growth signal is expected)[††].

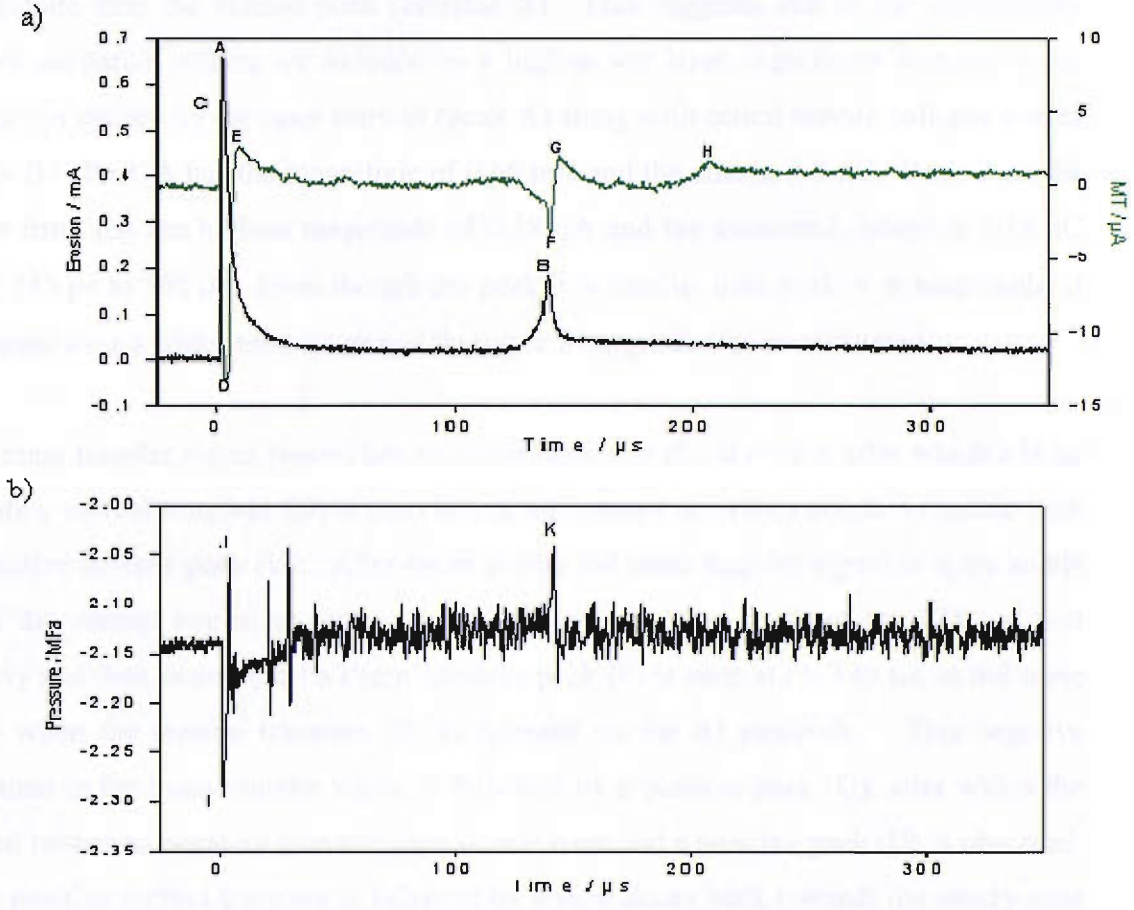

Figure 5.3 Plots showing the electrochemical transients (a) for 0.5 mm diameter Al (——)and 50 µm diameter Pt (——) electrode when a Al/Pt dual electrode was employed to study laser cavitation in a solution of 5 mM $K_4Fe(CN)_6$, 0.2 M Na_2SO_4. The potential was held at +0.5 V *vs.* SCE and the simultaneously recorded hydrophone signal (b).

In figure 5.3a, a set of large erosion/corrosion transients (——) are seen. Peak A occurs at time, t = 0 s which corresponds to the laser-induced breakdown of the liquid. This peak has a fast decay, even though the current does not decay all the way back to the 0

[††] The negative offset of the hydrophone in all figures presented in this chapter is caused by the interaction of the hydrophone with the electrolyte ($Fe(CN)_6^{3-/4-}$). The offset is small and the hydrophone still indicates the time frames for the optical breakdown and bubble collapse correctly.

A (due to limitations of the oxide kinetics and the timescale of the experiments). Nevertheless, the response is still faster than when the Pb microdisc was used to detect erosion events (see Chapter 3). Another erosion/corrosion transient (peak B) appears at approximately $t \sim 140$ μs. This is attributed to cavitation bubble collapse. The collapse time is related to the bubble size and so is a convenient way of estimating the size of the bubble [20]. It should be noted that the results are similar to (but with with more clarity as a result of the faster corrosion kinetics of the Al electrode) those obtained with the Pb electrode. Again the first peak observed (labelled A in figure 5.3a) is larger in magnitude than the second peak (labelled B). This suggests that in the experiments where cavitation effects are induced by a high-power laser, significant damage to the surface is caused by the laser activity (peak A) along with actual bubble collapse events (peak B). Peak A has the magnitude of 0.66 mA and the charge 5-6 nC. Peak B on the other hand has the highest magnitude of 0.18 μA and the measured charge is 8-14 nC over 145 μs to 350 μs. Even though the peak B is smaller than peak A in magnitude, it is spread over a wider time range and therefore a bigger charge is calculated.

The mass transfer signal (——) has an initial rapid rise (C) at $t \sim 0$ s, after which a large negative current transient (D) is seen before the current reverts to anodic in nature with a positive current peak (E). After these events the mass transfer signal is quite stable until the current begins to revert to the negative direction at about $t = 125$ μs, first slowly and then faster, until a sharp negative peak (F) is seen at $t = 140$ μs, at the same time when the erosion transient (B) is detected on the Al electrode. This negative transient in the mass transfer signal is followed by a positive peak (G), after which the signal reverts to negative side and then slowly rises and a positive peak (H) is observed. This positive current transient is followed by a slow decay back towards the steady state current. Clearly these events detected on the Pt microdisc are very different from the results achieved on Au in microdisc in Chapter 4 as no negative current transients were detected when Au electrode was employed under similar conditions but with the bubble further away from the solid/liquid interface. In addition no negative current time transients were detected in Chapter 3 when a Pt microdisc was employed simultaneously with the Pb 125 μm diameter electrode again in conditions similar to the experiments presented here. It should also be noted that the current time transient (F,G) appears to mirror the current time transient observed in the erosion signal (B) (see the

blow up in figure 5.4). These observations imply that the unusual current time transient (note negative mass transfer currents are not possible in this system under potential control) on the Pt microdisc, hence these are most likely caused by some form of coupling between the electrodes. This seems to be present when the erosion current time transients are particularly large (note mA scale). These coupling transients are superimposed on the mass transfer signal produced by the optical breakdown of the liquid (and bubble growth) and cavitation collapse effects (see $t \sim 150$ μs). It is apparent that the negative current transients appear at the same time with the peaks on the Al electrode, and seem to be their mirror images. Whether all the positive transients on the Pt signal are caused by laser discharge and cavitation events is unclear from figure 5.3. However, the mass transfer event (H) has no associated erosion signal and is associated with bubble rebound and secondary collapse (see chapter 4). One should also note that the events detected on Pt have an unusually high magnitude, reaching the maximum current of ca. 3-4 μA, whereas the results presented in Chapters 3 and 4 had the maximum current of 400 nA. This suggests that at these low γ values extremely high mass transfer rates can be generated (here in the range 1.2-1.7 cm s^{-1}). Mass transfer trace was also monitored in the absence of the aluminium electrode. The signal recorded is presented in figure 5.5. The trace is still very noisy and unstable, but the negative transients have completely disappeared which indicates they have been caused by interference with the aluminium electrode and its current time response.

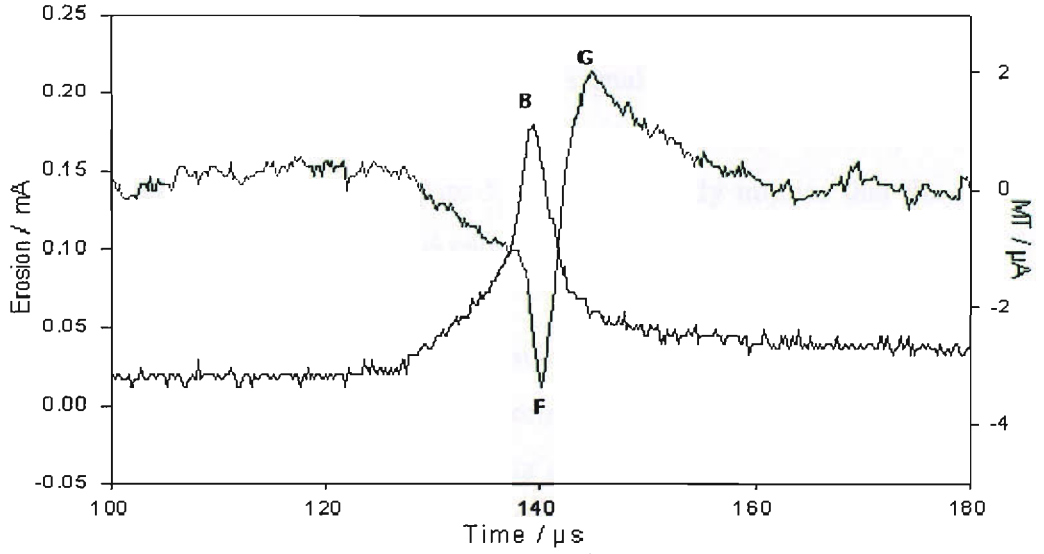

Figure 5.4 Plots showing the electrochemical transients for 0.5 mm diameter Al (——) and 50 μm diameter Pt (——) electrode when a Al/Pt dual electrode was employed to study laser cavitation in a solution of 5 mM $K_4Fe(CN)_6$, 0.2 M Na_2SO_4. The potential was held at +0.5 V *vs.* SCE.

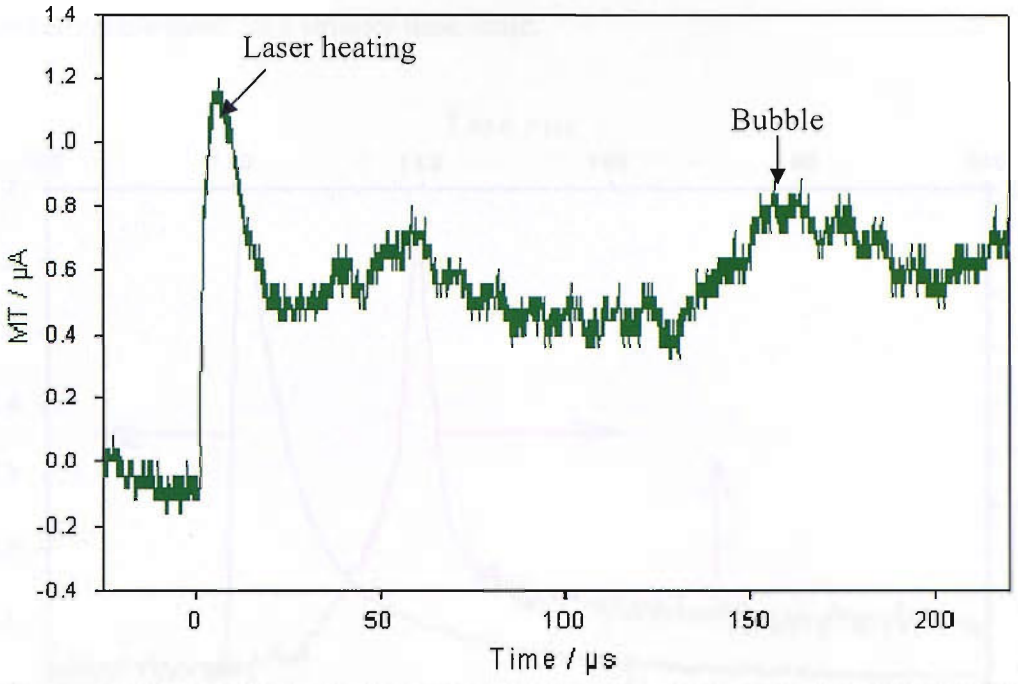

Figure 5.5 Plot showing the electrochemical transient for a 50 µm diameter Pt microdisc in a solution of 5 mM $K_4Fe(CN)_6$, 0.2 M $Na_2SO_4$when aluminium disc of a Al/Pt dual electrode was disconnected. The potential was held at +0.5 V *vs.* SCE.

Figure 5.3b shows the hydrophone signal that is recorded simultaneously with the electrochemical signal in figure 5.3a. Even though the overall signal is quite noisy, it is apparent that at $t \sim 0$ s optical breakdown occurs. This is predominantly a negative pressure spike followed by positive peaks (I) and (J). Further events can also be detected within the first 50 µs after the optical breakdown. These could be caused by the original pressure wave caused by optical breakdown bouncing back and forth in the electrochemical cell. After 50 µs the hydrophone signal is similar to that before 0 s, until another large peak (K) appears at 140 µs, at the same time when activity was also seen on the electrochemical signal in figure 5.3a. This clearly implies that the signal detected on the Pt/Al electrode at 140 µs is caused by bubble collapse.

It should be noted that the erosion transients shown in figure 5.3a have differing shape. For example when the transients are further examined, peak (A) in figure 5.3a at $t \sim 0$ s shows a rapid rise in current followed by a slower decay. This is similar to "scratch" or fracture transients recorded for aluminium [104]. However, the smaller erosion peak (B) which is associated with bubble collapse has a very different appearance (see figure 5.6 for a blow up of the transients recorded on the Al electrode). The initial rise of the current transient (B) is much slower, and therefore the peak (B) has a completely

different shape from the initial optical breakdown peak (A). The shape of each transient was further investigated on a smaller time scale.

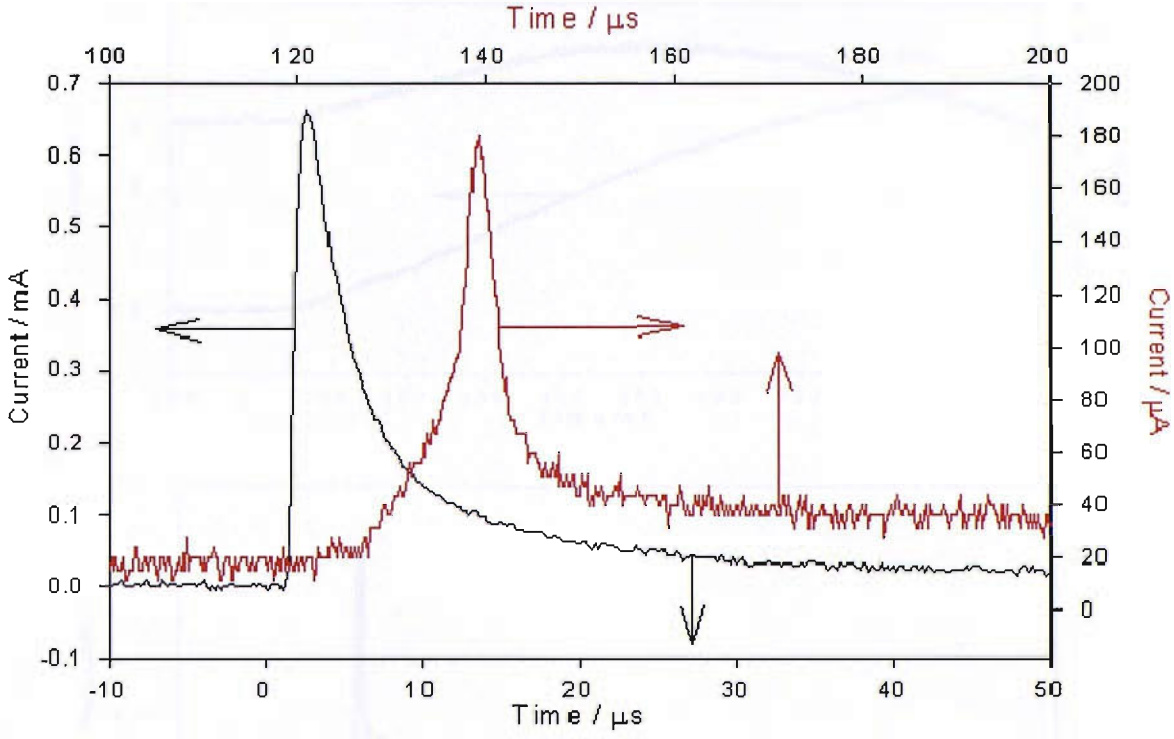

Figure 5.6 Plots showing the electrochemical transients recorded for 0.5 mm diameter Al electrode at optical breakdown (——) and bubble collapse (——) when an Al/Pt dual electrode was employed to study laser cavitation in a solution of 5 mM $K_4Fe(CN)_6$, 0.2 M Na_2SO_4. The potential was held at +0.5 V *vs.* SCE.

In order to investigate the shape and timing of the events recorded the experiment was repeated and the electrochemical response within the first few microseconds after the optical breakdown was investigated. Figure 5.7a shows both the mass transfer (——) and erosion (——) signal recorded in the region around $t \sim 0$ s (as the laser is discharged into the liquid[†]). The initial gradient for the erosion is 550 A s^{-1} and 106 A s^{-1} for the mass transfer sensor. This initial gradient for mass transfer is very fast, faster than could be expected from a mass transfer sensor. Normally one could expect a small delay between the optical breakdown and the response on mass transfer sensor due to the diffusional response of the electrode. After the initial rise the signal starts descending at only 0.5 μs after reaching the maximum current of 4 μA. This early rise could be a result of the effect of the laser action (for example solution/electrode heating). The fast decay seen on the mass transfer sensor is likely to happen because of

[†] Note that the scope is triggered at $t = 0$ s by the laser action.

electrical coupling between the two electrodes; the response on mass transfer is affected by the erosion transient (see earlier discussion).

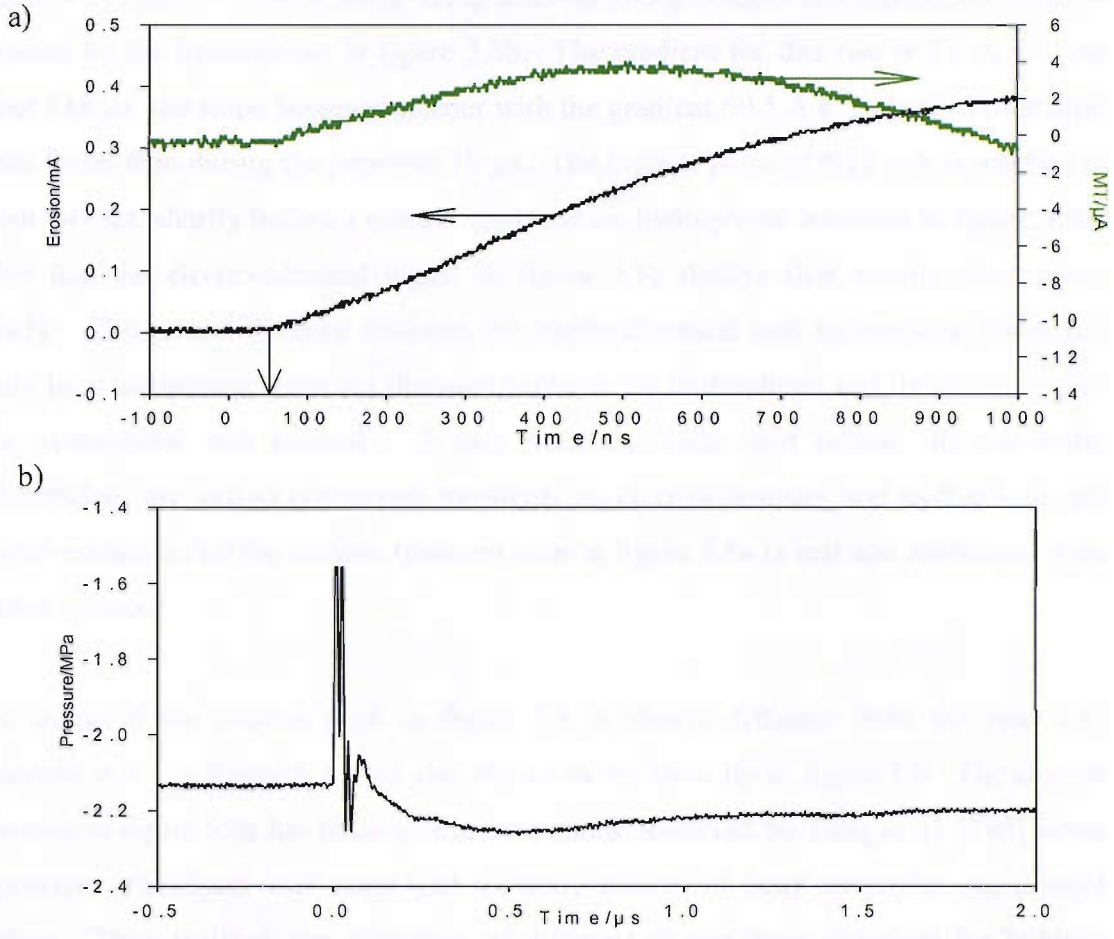

Figure 5.7 Plots showing (a) the electrochemical transient at optical breakdown for 0.5 mm diameter Al (——) and 50 μm Pt (——) when a Al/Pt dual electrode was employed to study laser cavitation in a solution of 5 mm $K_4Fe(CN)_6$, 0.2 M Na_2SO_4 and the potential was held at +0.5 V *vs.* SCE and the simultaneously recorded hydrophone signal (b).

It is also interesting to comment on the time scale of the response of the electrodes. The electrochemical response occurs ~ 50 ns after the laser has fired. If this represents the distance that the shock generated by the laser induced breakdown has to travel, the distance between the focal point of the laser and the surface of the electrode was estimated to be of the order of 75 - 100 μm. This considers a shock speed of 1500 - 2000 m s^{-1} [21,57]. This is consistent with the distance between the bubble creation point (e.g. the laser focus).

Clearly an interesting feature of these results are the events observed as a result of bubble collapse. The experiment was repeated and the events occurring upon bubble

collapse at ~140 μs studied in more detail. The results are presented in figure 5.8. When the erosion on aluminium is investigated, it was observed that the erosion transient in figure 5.8a first starts rising at about 135 μs before any significant event is detected by the hydrophone in figure 5.8b. The gradient for this rise is 7.5 A s^{-1}. At about 146 μs, the slope becomes steeper with the gradient 69.5 A s^{-1}, which is over nine times faster than during the previous 10 μs. The highest point of 0.21 mA is reached at about 147 μs, shortly before a peak is observed on hydrophone transient in figure 5.8b. After this the electrochemical signal in figure 5.8a decays first steeply, then more slowly. The time difference between the electrochemical and hydrophone transients could be a component from the distance between the hydrophone and the event origin. The hydrophone was located ~ 5 mm from the focal spot behind the electrode. Nevertheless the almost concurrent transients on electrochemistry and hydrophone are further evidence that the erosion transient seen in figure 5.8a is real and associated with bubble collapse.

The shape of the erosion peak in figure 5.8 is clearly different from the peak (A) observed at 0 s in figure 5.3a and also shown in the blow up in figure 5.6. The current transient in figure 5.8a has features similar to those observed by Tong *et al.* [105] when a pressure transducer was employed to study effects of laser cavitation on a solid surface. They realised that transients of different shapes were observed for bubbles collapsing at different distances from the solid surface. However, at each distance the recorded trace never had just one sharp and clear peak, quite often a smaller peak was observed before the dominant peak of largest magnitude. They suggested this smaller peak was due to "splash"-impact at the base of the liquid jet and it is associated with the emission of a shock wave. Tong *et al.* proposed that the larger peak is a result of subsequent acceleration of the flow through the torus and the start of the re-expansion of the cavity. The smaller peak is only observable at certain values of γ, where a thin liquid layer is sandwiched between the bubble and the surface. When erosion is studied by means of pressure applied to a metal surface by a micro indenter, high plastic deformation volumes have been observed [106]. It is proposed here that plastic formation is a probable cause of the erosion peak B in figure 5.3a as a result of bubble collapse.

Interestingly the transient for mass transfer enhancement to the platinum electrode in figure 5.8 starts rising at ~120 μs which could be a result of higher solution velocities associated with the bubble collapse process. This rise is interrupted when the peak at the Al electrode appears, again indicating interaction between the two electrodes. A negative peak is seen on Pt at the same time the sharp rise on Al is detected in ~147 μs. After the events on Al electrode decay the current on Pt returns to the value it had before being affected by the possible coupling of electrodes. However, even after this the mass transfer seems very noisy and unstable, which could be caused by other unknown processes such as bubble fragments changing the environment (local flow) close to the electrode surface (see chapter 6).

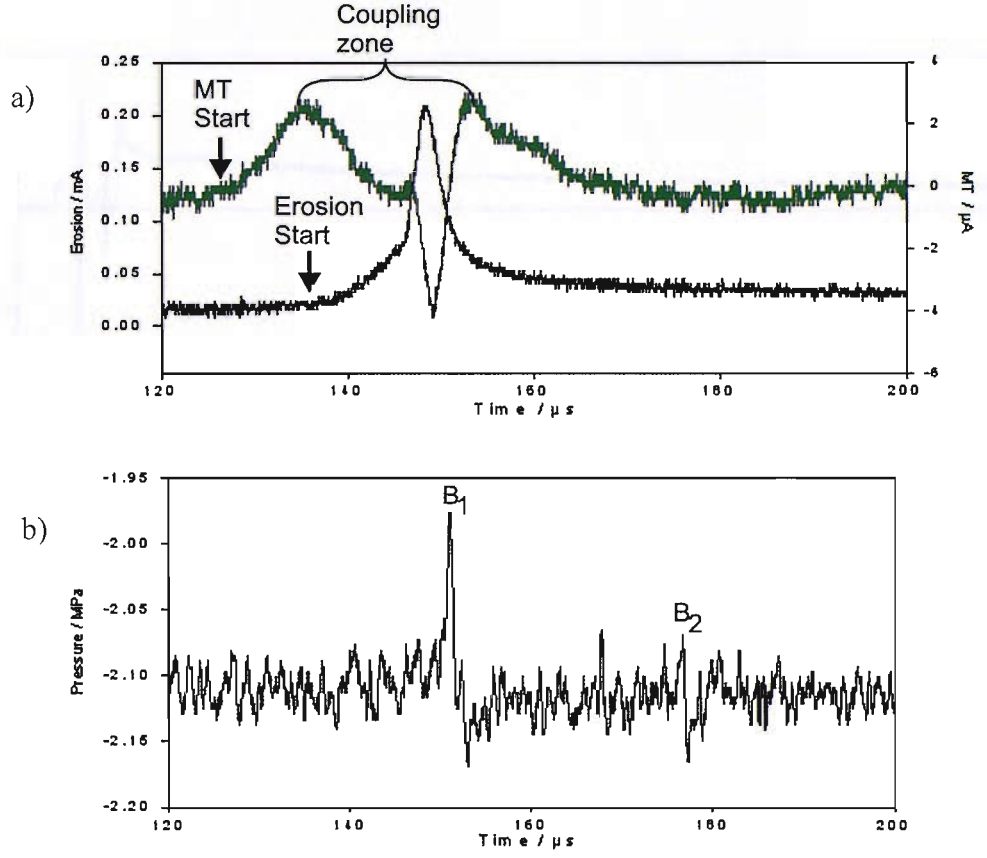

Figure 5.8 Plots showing a) the electrochemical transient at bubble collapse for 0.5 mm diameter Al (——) and 50 μm Pt (——) when a Al/Pt dual electrode was employed to study laser cavitation in a solution of 5 mm $K_4Fe(CN)_6$, 0.2 M Na_2SO_4 and the potential was held at +0.5 *vs.* SCE and b) the simultaneously recorded hydrophone signal.

When the electrochemical response is studied on a longer time scale, in this case several milliseconds as seen in figure 5.9, the signals for erosion on Al appears right at the beginning of the time scale, and the current returns back to 0 mA within the first 300 μs. The signal detected on the platinum microelectrode bounces up and down for the first

300-400 μs, after which there is a sharp peak before the signal starts decaying back towards the steady state current. The steady state current is marked in figure 5.9 with a red line. This decay is likely to be a result of relaxation of the diffusion field, and therefore a real mass transfer signal. It can be concluded that the actual mass transfer signal is disturbed by laser electronics and interaction with the Al electrode and therefore the signal is moving up and down for the first few hundred microseconds, and after no more erosion is detected on the aluminium electrode, the real mass transfer transient is seen as a slow decay when the current returns back towards the steady state conditions when the diffusion field is reformed. This time history is expected for the differing processes at the two electrodes.

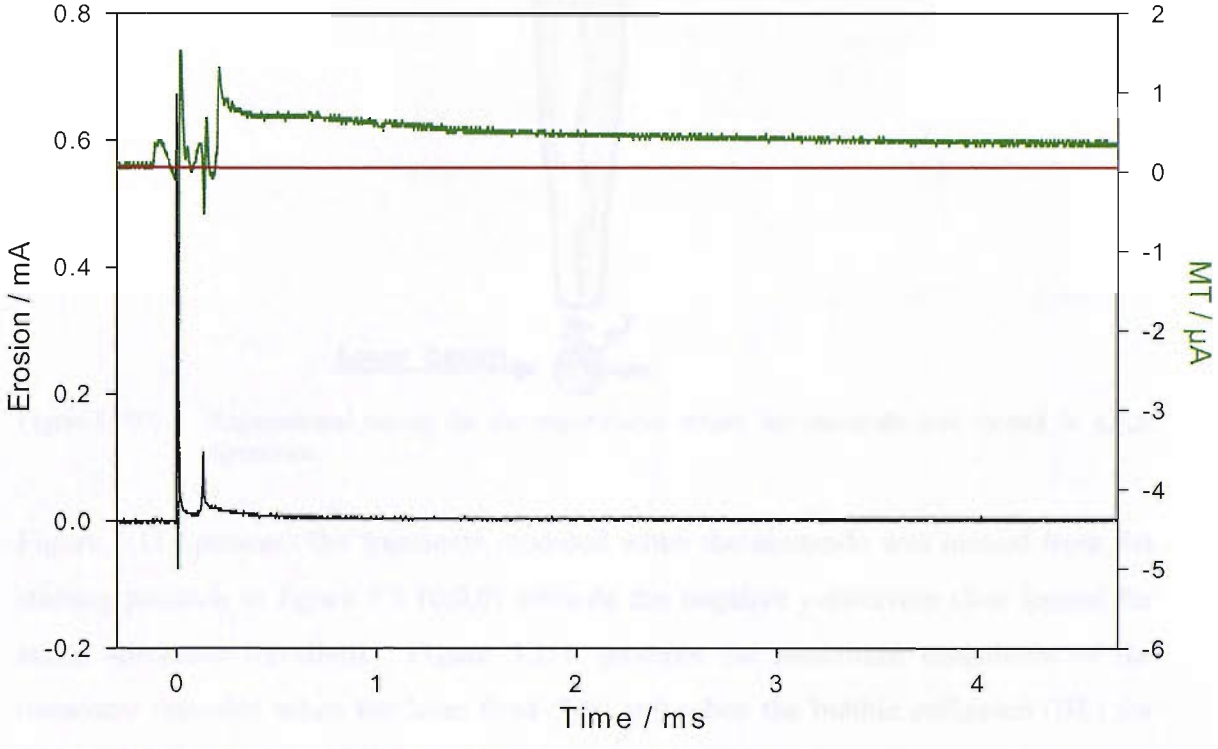

Figure 5.9 Plots showing the electrochemical transient at bubble collapse for 0.5 mm diameter Al (black) and 50 μm Pt (green) when a Al/Pt dual electrode was employed to study laser cavitation in a solution of 5 mm $K_4Fe(CN)_6$, 0.2 M Na_2SO_4 and the potential was held at +0.5 V *vs.* SCE.

From the results seen in figures 5.3-5.9 it was apparent that some problems were encountered with the Pt mass transfer sensor. Nevertheless, further experiments employing this electrode system were completed with the emphasis on results produced by the Al erosion sensor alone.

5.2 *x,y,z*-position in ferrocyanide with simultaneous hydrophone measurements

5.2.1 Moving the electrode horizontally

In the first set of experiments, the position of the electrode was varied with respect to the bubble. The directions of electrode movement are demonstrated in figure 5.10. The time scale chosen for this set of experiments was from -20 to 220 μs to enable good temporal resolution for the erosion transients. The horizontal position of the electrode with respect to the bubble was varied first by moving the electrode along the x- and y-axis. The transients recorded at starting position (0,0,0) are shown in figure 5.3.

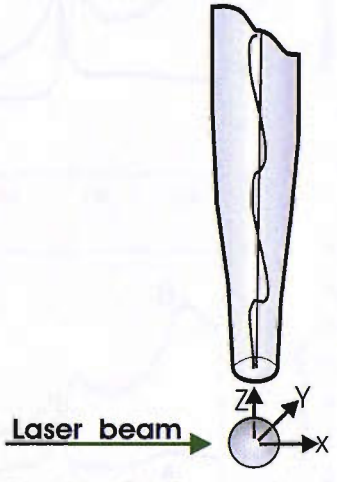

Figure 5.10 Experimental set-up for the experiments where the electrode was moved in x,y,z-directions.

Figure 5.11a presents the transients recorded when the electrode was moved from the starting position in figure 5.3 (0,0,0) towards the negative *y*-direction (See legend for actual distances travelled). Figure 5.11b presents the maximum magnitude of the transients recorded when the laser fired (LE) and when the bubble collapsed (BE) for different distances from the position in figure 5.3 (0,0,0).

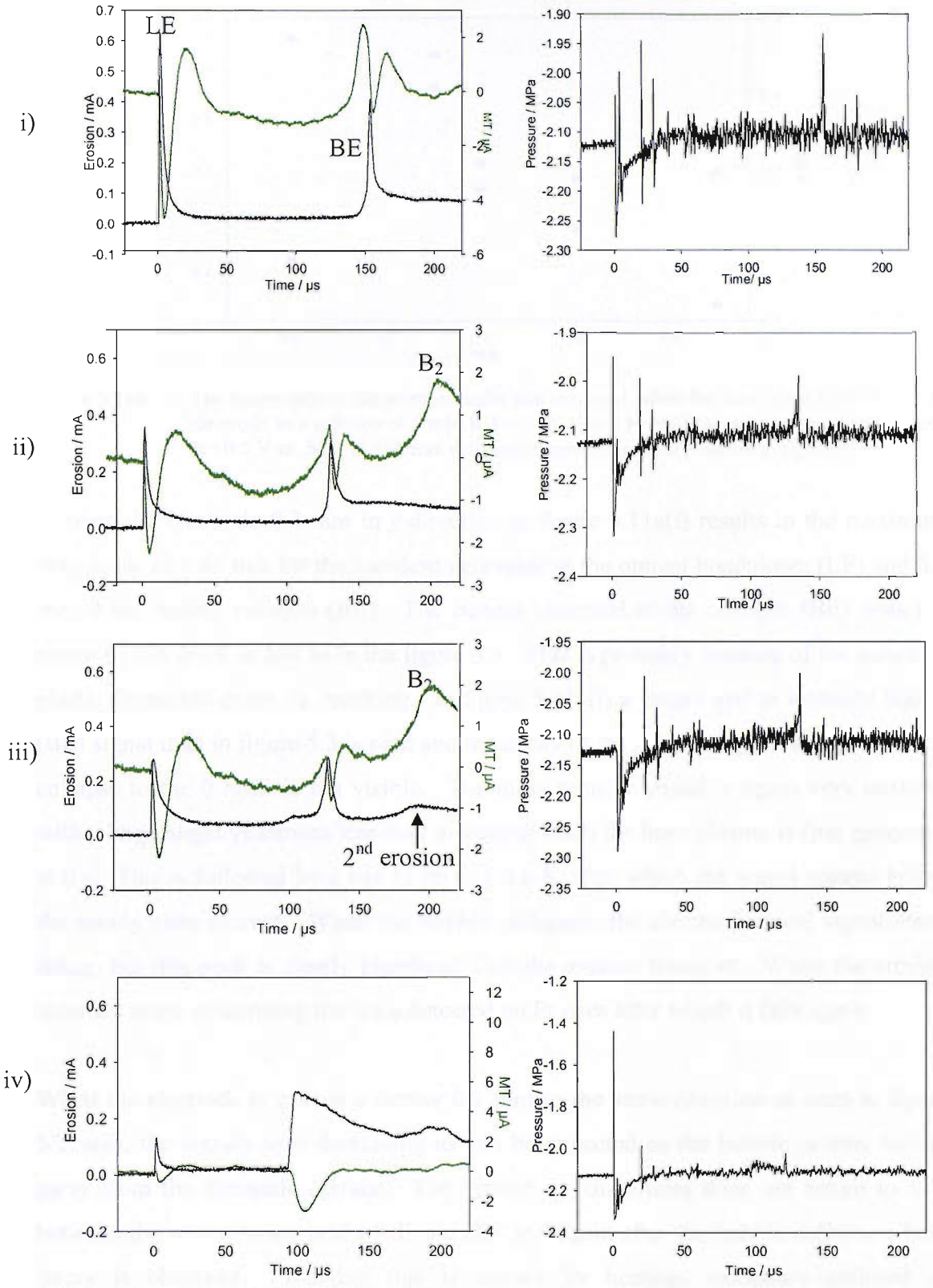

Figure 5.11a. Plots showing the erosion on Al, mass transfer on Pt and simultaneously recorded hydrophone transient in a solution of 5 mM $K_4Fe(CN)_6$, 0.2 M Na_2SO_4 and the potential was held at +0.5 V *vs.* SCE. The locations of the electrode are i) (0,-0.3,0), ii) (0,-0.4,0), iii) (0,-0.6,0) and iv) (0,-0.9,0) from the original starting position presented in figure 5.3. LE indicated erosion caused by laser and BE erosion caused by bubble. B_2 is the transient caused by the secondary collapse.

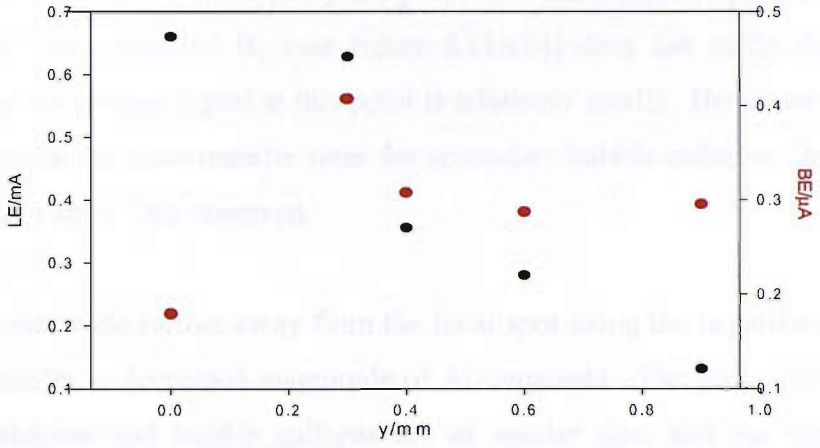

Figure 5.11b. The magnitude of the erosion peaks that occurred when the laser fired (LE) on the Al electrode in a solution of 5 mM $K_4Fe(CN)_6$ in 0.2 M Na_2SO_4 and the potential was held at +0.5 V *vs.* SCE at different distances from the orginial position in figure 5.3.

Moving the electrode 0.3 mm in *y*-direction in figure 5.11a(i) results in the maximum magnitude of 0.65 mA for the transient generated at the optical breakdown (LE) and 0.8 mA at the bubble collapse (BE). The current observed at the collapse (BE) does not return to 0 A level as fast as in the figure 5.3. This is probably because of the nature of plastic formation event vs. cracking. In figure 5.11a(i) a longer and in intensity higher (BE) signal than in figure 5.3 is seen and the decay of the transient generated by the first collapse to the 0 level is not visible. The mass transfer signal is again very unstable with a large negative current transient occurring when the laser plasma is first generated at 0 s. This is followed by a rise to up to 1.8 µA, after which the signal returns below the steady state current. When the bubble collapses, the electrochemical signal starts rising, but this peak is clearly interfered with the erosion transient. When the erosion transient starts descending the trace detected on Pt rises after which it falls again.

When the electrode is moved a further 0.1 mm to the same direction as seen in figure 5.11a(ii), the signals start decreasing as can be expected as the bubble is now further away from the electrode surface. The current on aluminium does not return to 0 A between the two separate peaks (LE and BE) and again after the bubble collapse a long decay is observed. Whether this is caused by heating, secondary collapse or interference with the Pt electrode is uncertain. No secondary collapse is detected by the hydrophone, although this could also be due to a greater distance between the bubble centre and the hydrophone tip. The signal detected on the Pt disc is quite similar to that in figure 5.11a(i), the only difference is the large positive current transient that appears

after 200 μs. This peak is most likely the positive Pt trace caused by the rebound of the bubble. The peak labelled B_2 (see figure 5.11a(ii)) does not suffer from coupling problems (as the erosion signal at this point is relatively small). Hence we may use this peak to estimate the mass transfer rates for secondary bubble collapse. In this case k_m values of 0.211 cm s^{-1} are observed.

Moving the electrode further away from the focal spot along the negative y-axis (figure 5.11a(iii)) results in decreased magnitude of Al-transients. The peaks generated in the optical breakdown and bubble collapse are of similar size, and the current is quite unstable between them. The collapse transient is followed by another event that could be caused by secondary collapse.

In figure 5.11a(iv) the transient recorded for bubble collapse is huge in comparison to the peak that appears at optical breakdown. However, the collapse event detected by the hydrophone is rather small in magnitude which could also mean that the hydrophone is too far to detect the collapse properly. The signal recorded by the Pt electrode is very unstable, and a very large negative transient is seen when the bubble collapses. Clearly the bubble formation is affecting the electrochemistry at these close distances presented in figures 5.11a(iii) and (iv).

Figure 5.12 presents the results from the experiments when the electrode was moved to a direction opposite to that in figure 5.11. The starting position was still the one presented in figure 5.3. The electrode was first moved in this direction by 0.1 mm. The magnitude of the peak generated at the optical breakdown in figure 5.12(i) falls by 0.2 mA but it takes the signal just as long as in figure 5.3 to return to 0 mA. Like in figure 5.3, smaller peak caused by cavitation erosion is induced at 147 μs. A small transient is seen at the same time by the hydrophone. Negative events are again monitored by the Pt-electrode at the same time when the events occur on the erosion sensor.

In figures 5.12(ii) and (iii) moving the electrode to 0.2 mm and 0.3 mm from the starting position, respectively, results in further decrease on both transients recorded by the erosion sensor. The negative events observed on the Pt-electrode have also become smaller. Clearly the sensor performance is extremely dependent on the distance between the bubble centre and the electrode. In the final experiment presented in figure

5.12(iv), the distance is 0.5 mm from the starting position. The bubble erosion event is no longer observable but the laser at $t = 0$ s still damages the surface. Similar transients are recorded by the hydrophone; rather large events after the initial optical breakdown but no events at ~150 μs where the bubble collapse is expected to take place. Also, no significant negative event is detected by the mass transfer transient when the bubble collapses.

In the final set of experiments presented in this section in figure 5.13 where the horizontal (x,y) position of the electrode was varied, the electrode was moved towards the negative x-direction from the starting position in figure 5.3 (position 0,0,0). When the electrode is moved -0.1 mm from the starting position on the x-axis in figure 5.13(i), the magnitude of the transients decrease significantly. Moving the electrode further to the same direction in 0.1 mm steps in figures 5.13(i)-(iv) reduces the sizes of the transients. Also, throughout this experiment presented in figure 5.13 the electrochemical signal has been very noisy. At this point it was obvious, that the electrode surface had been either significantly eroded or the electrode was leaking. Therefore, to guarantee good quality of results it was necessary to remove and polish the electrode before continuing the experiments.

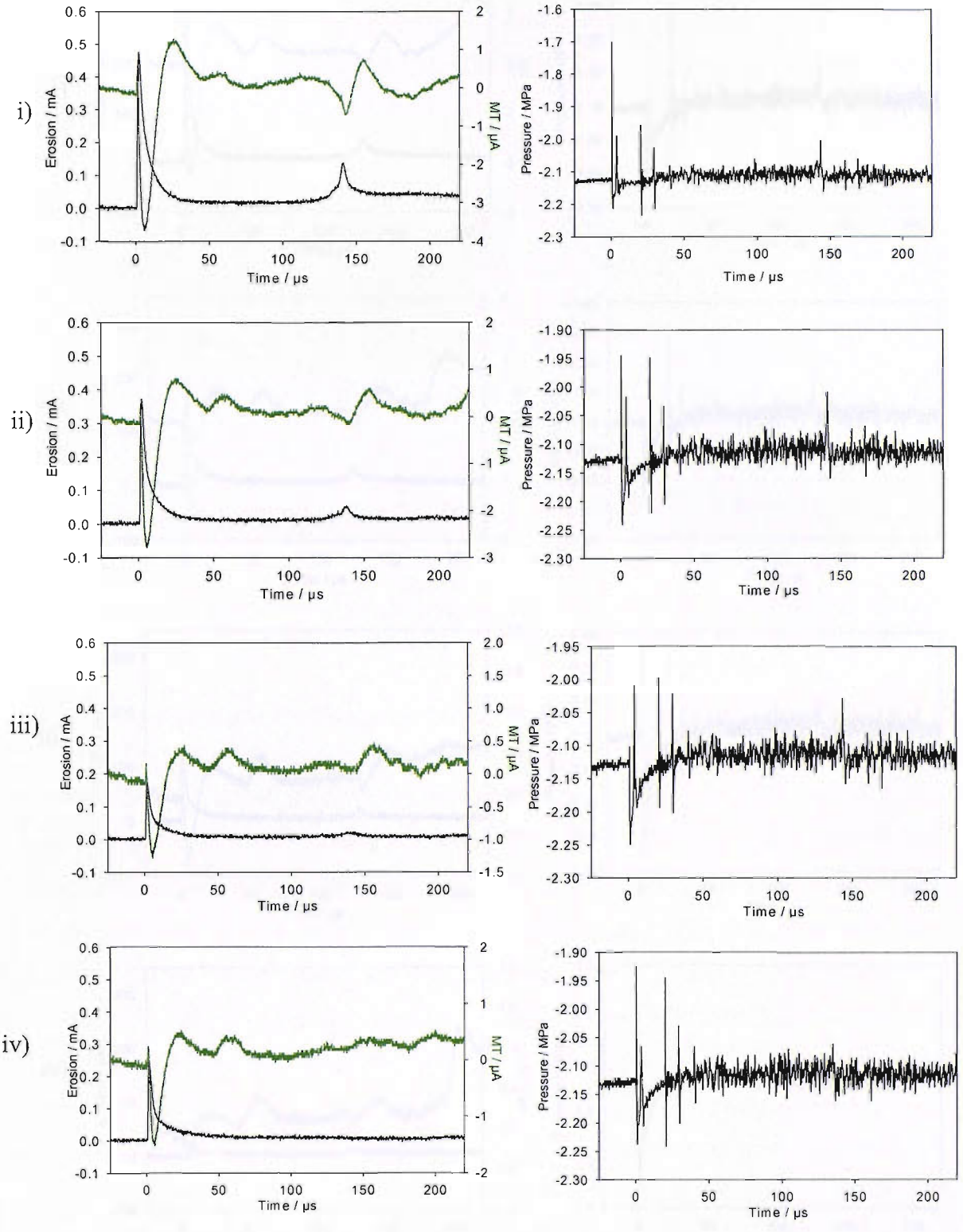

Figure 5.12. Plots showing the erosion on Al, mass transfer on Pt and simultaneously recorded hydrophone transient in a solution of 5 mM $K_4Fe(CN)_6$, 0.2 M Na_2SO_4 and the potential was held at +0.5 V vs. SCE. The locations of the electrode are i)(0,0.1,0), ii) (0,0.2,0), iii) (0,0.3,0) and iv) (0,0.5,0) from the original starting position presented in figure 5.1. Note the presence of electrode "shadows" the hydrophone hence the acoustic signal is much smaller than previously observed.

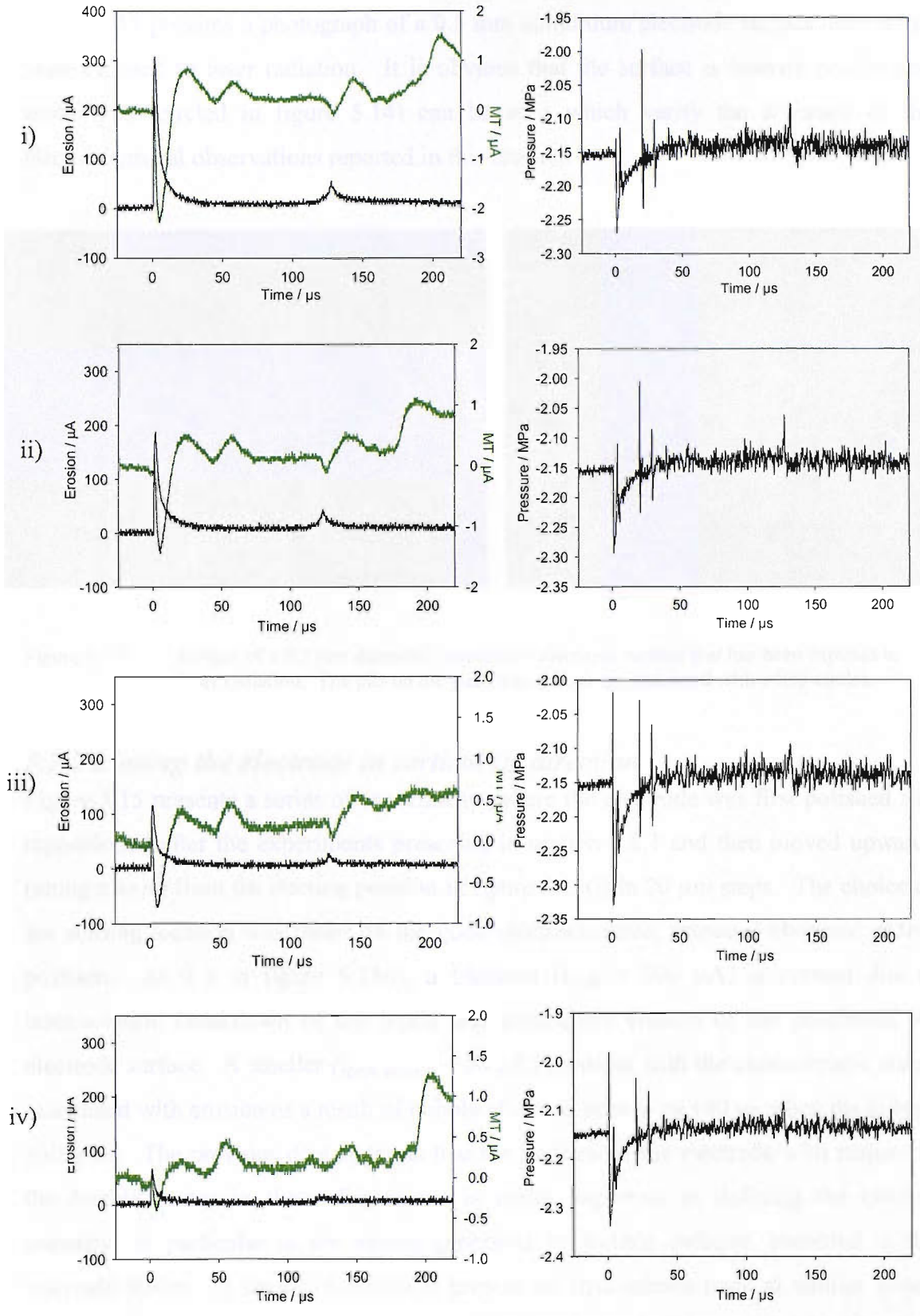

Figure 5.13. Plots showing the erosion on Al, mass transfer on Pt and simultaneously recorded hydrophone transient in a solution of 5 mM $K_4Fe(CN)_6$, 0.2 M Na_2SO_4 and the potential was held at +0.5 V vs. SCE. The locations of the electrode are i)(-0.1,0,0), ii) (-0.2,0,0), iii) (-0.3,0,0) and iv) (-0.4,0,0) from the original starting position presented in figure 5.1.

Figure 5.14 presents a photograph of a 0.5 mm aluminium electrode surface after it has been exposed to laser radiation. It is obvious that the surface is heavily eroded and actual pits (circled in figure 5.14) can be seen which verify the accuracy of the electrochemical observations reported in this chapter.

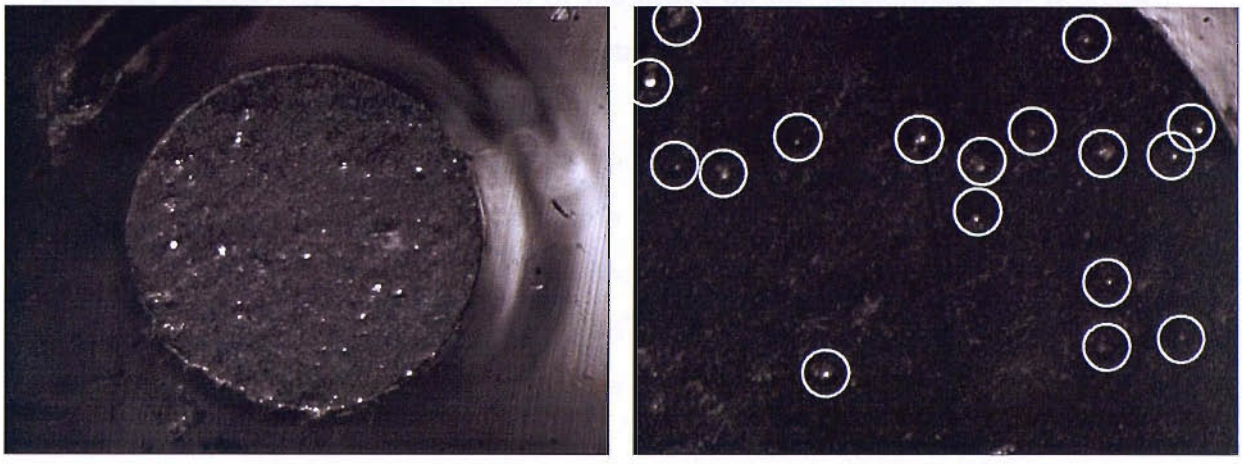

Figure 5.14 Images of a 0.5 mm diameter aluminium electrode surface that has been exposed to laser radiation. The pits on the electrode surface are indicated with white circles.

5.2.2 Moving the electrode in vertical (z) direction

Figure 5.15 presents a series of experiments where the electrode was first polished and repositioned after the experiments presented in section 5.2.1 and then moved upwards (along z-axis) from the starting position in figure 5.15(i) in 20 μm steps. The choice of the starting location was based on the good electrochemical response observed at this position. At 0 s in figure 5.15(i), a transient (i_{peak} = 300 μA) is present due to laser/solution breakdown of the liquid and subsequent erosion of the passivated Al electrode surface. A smaller ($i_{peak\ erosion}$ ~ 50 μA) transient with the characteristic shape associated with erosion as a result of bubble effects is seen at ca.140 μs when the bubble collapses. The previous data suggests that the position of the electrode with respect to the bubble centre in three dimensions is really important in defining the erosion transient, in particular to the events generated by bubble collapse, recorded at the microelectrodes. A series of events is present on hydrophone trace at similar times. The signal for mass transfer on Pt shows many events as in figures 5.3-5.9. Negative peaks are present at the same time when activity is displayed on the erosion sensor. These negative events are followed by positive peaks. Also, one large positive event

appears after 200 μs which could be the actual mass transfer event (similar to that labelled H in figure 5.3).

In figure 5.15(ii) the electrode has been moved 20 μm upwards from the position in figure 5.15(i). As expected, a slight reduction in the magnitude of transients on the Al-electrode is observed. Also the size of the peaks on the Pt-electrode has decreased. Similar effects were detected when the electrode was moved upwards along the z-axis by 20 μm steps (see figure 5.15(ii) –(iv)). In figure 5.15(iv) the erosion trace has become very small compared to 5.15(i). Notably the peak caused by bubble collapse has lost its shape and almost disappears into the noise. However, the transient detected on the mass transfer sensor at 200 μs has become clearer than in previous experiments. This could mean that under the reduced influence of coupling with Al-electrode, the ability of the Pt-electrode to monitor mass transfer events has improved. A strong secondary collapse is present on the mass transfer signal but hardly any erosion is detected.

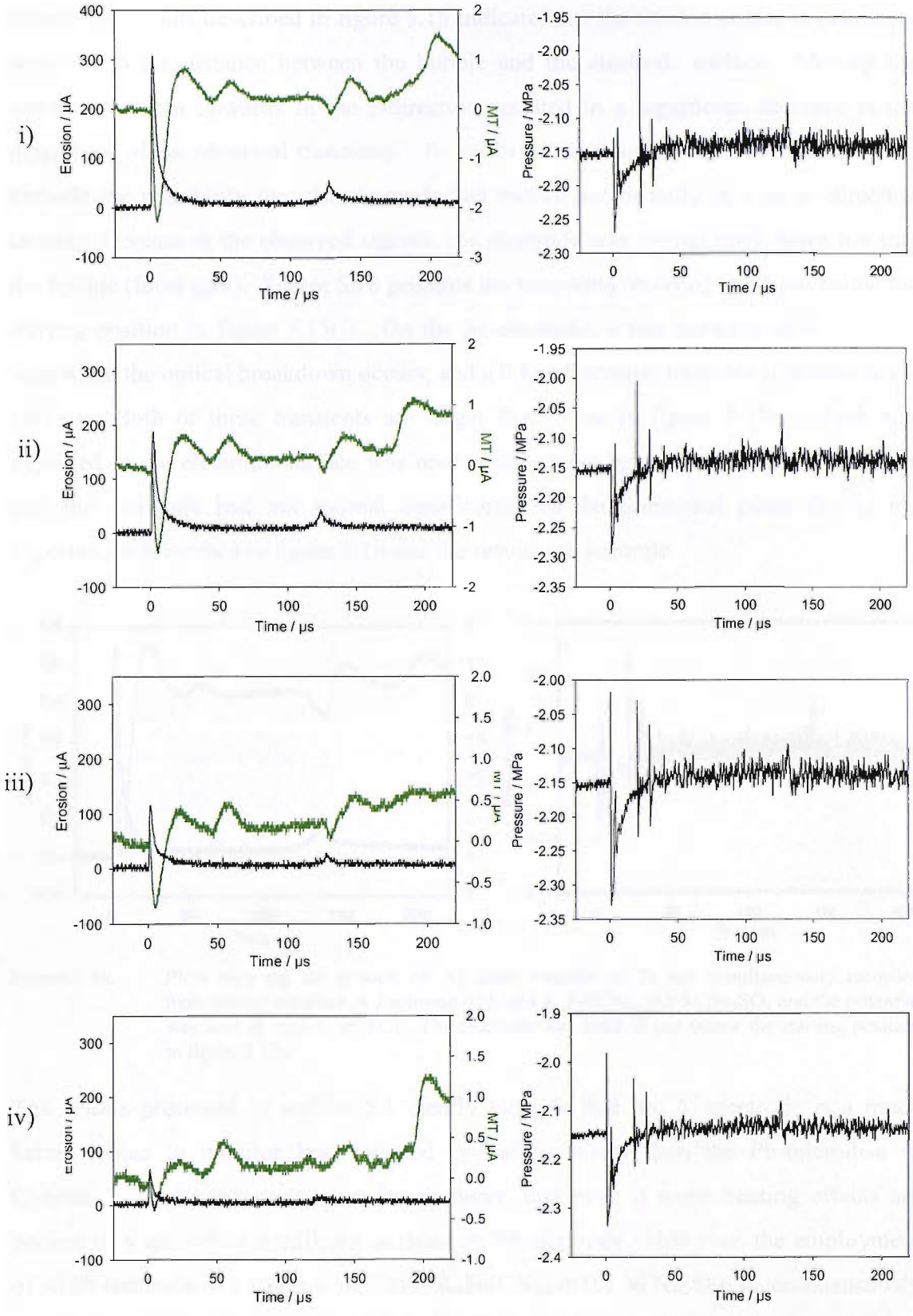

Figure 5.15 Plots showing the erosion on Al, mass transfer on Pt and simultaneously recorded hydrophone transient in a solution of 5 mM $K_4Fe(CN)_6$, 0.2 M Na_2SO_4 and the potential was held at +0.5 V vs. SCE. The locations of the electrode are i) (0,0,0), ii) (0,0,0.02), iii) (0,0,0.04) and iv)(0,0,0.06).

Clearly the results described in figure 5.15 indicate, that the erosion sensor is extremely sensitive to the distance between the bubble and the electrode surface. Moving the electrode 60 μm upwards in the *z*-direction resulted in a significant decrease in the magnitude of the observed transients. To confirm the accuracy of these results and to exclude the possibility that the electrode had moved accidentally in *x* or *y* –direction causing decrease in the observed signals, the electrode was moved back down towards the bubble (focal spot). Figure 5.16 presents the transients recorded at 20 μm below the starting position in figure 5.15(i). On the Al-electrode, a fast transient of 0.65 mA is seen when the optical breakdown occurs, and a 0.1 mA erosion transient is present at ca. 140 μs. Both of these transients are larger than those in figure 5.15(i) which was expected as the electrode surface was now closer to the bubble centre. This indicates that the electrode had not moved significantly in the horizontal plane during the experiments presented in figure 5.16 and the results are accurate.

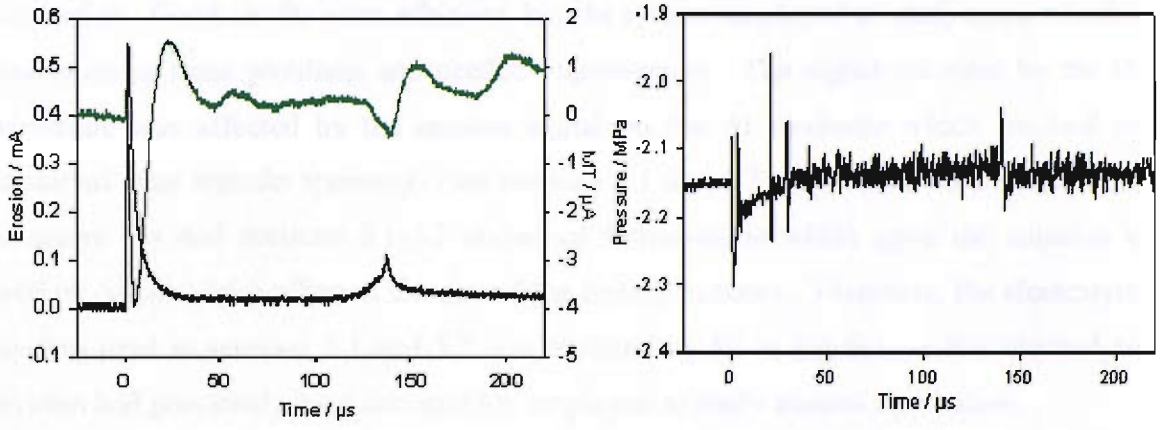

Figure 5.16. Plots showing the erosion on Al, mass transfer on Pt and simultaneously recorded hydrophone transient in a solution of 5 mM $K_4Fe(CN)_6$, 0.2 M Na_2SO_4 and the potential was held at +0.5 V vs. SCE. The electrode was held 20 μm below the starting position in figure 5.15i.

The results presented in section 5.1 clearly indicate that the Al-electrode is a much better choice to monitor laser-induced cavitation events than the Pb-microdisc in Chapter 3. The response time is much faster, and even if some heating effects are present they are not as significant as those on Pb-electrode. However, the employment of Al/Pt-electrode in a solution of 5 mM $K_4Fe(CN)_6$ in 0.2 M Na_2SO_4 to simultaneously study erosion and mass transfer has not been quite as successful due to an unstable and noisy mass transfer signal. Therefore, the system for simultaneous mass transfer and erosion studies had to be improved.

It was also necessary to determine the distance between the bubble and the electrode, the actual bubble size and the time scale with respect to the bubble life cycle where the events occur. Therefore, it was necessary to employ a high-speed camera to determine all these parameters.

The development of the new experimental system for further simultaneous mass transfer and erosion studies and the synchronised electrochemical monitoring and high-speed imaging are presented later on in this chapter.

5.3 Pt/Al dual electrode in KI system

Previous sections 5.1-5.2 presented the initial experiments where Pt/Al dual electrodes were employed to study the mass transfer and erosion effects of laser induced cavitation. Good results were achieved, but the system employed to study mass transfer encountered some problems and needed improvement. The signal recorded by the Pt electrode was affected by the erosion signal on the Al electrode which resulted in distorted mass transfer transients (see sections 5.1 and 5.2). Also, the solution used in chapters 3-4 and sections 5.1-5.2 contained ferrocyanide which gave the solution a yellow colour which affected the size of the formed bubbles. Therefore, the electrolyte system used in sections 5.1 and 5.2 was replaced by KI in Na_2SO_4 as this electrolyte system had previously been successfully employed to study acoustic cavitation.

5.3.1 Potential change for Pt electrode in KI

The effect of the changing the potential of an electrode was studied using a 25 μm diameter Pt microelectrode in the solution containing 1mM KI in 0.2 M Na_2SO_4. The potential was gradually reduced from +0.7 V *vs.* SCE to +0.1 V *vs.* SCE. Chapter 3 described a similar experiment where the potential was shifted for a Pb/Pt dual microelectrode in a solution of $K_4Fe(CN)_6$ in Na_2SO_4. Figure 5.16 presents a cyclic voltammogram for the 25 μm diameter Pt microelectrode in a solution that contains 1 mM KI in 0.2 M Na_2SO_4. From the cyclic voltammetry of this system it should be noted that when the potential of the electrode is held at +0.6 V *vs.* SCE, the oxidation of iodide (I^-) can be detected as a mass transfer limited positive current. Hence the

potential steps shown in figure 5.17 show positive current transients at this potential followed by a steady state oxidation signal. It is possible to calculate the diffusion coefficient for the I^- ion from this steady state current. Here we find that $D_{I^-} \sim 6.22 \times 10^{-6}$ cm^2 s^{-1}. Included on Figure 5.17 are potential step from +0.1 V vs. SCE to +0.65 V *vs.* SCE before (——) and after the exposure of the electrode to laser induced cavitation (——). Before the experiment a 8.3 ± 0.06 nA steady state current is observed when the potential is +0.65 V *vs.* SCE. At +0.1 V vs. SCE the measured current is essentially 0 nA which indicates that no observable electrochemistry takes place on the microelectrode surface at this potential. After exposure of the electrode to > 100 repeated cavitation events the steady state current has shifted to 12.9 ± 0.22 nA and has become noisier. In addition the current at 0 V vs SCE is no longer 0 nA (indeed ~ -3 nA). These observations indicate that the electrode was damaged (in particular the seal between the insulating substrate and the Pt) during the experiments. This is in agreement with results reported in sections 4.3 and 5.2 which are attributed to the damaging effects of cavitation on electrode surfaces.

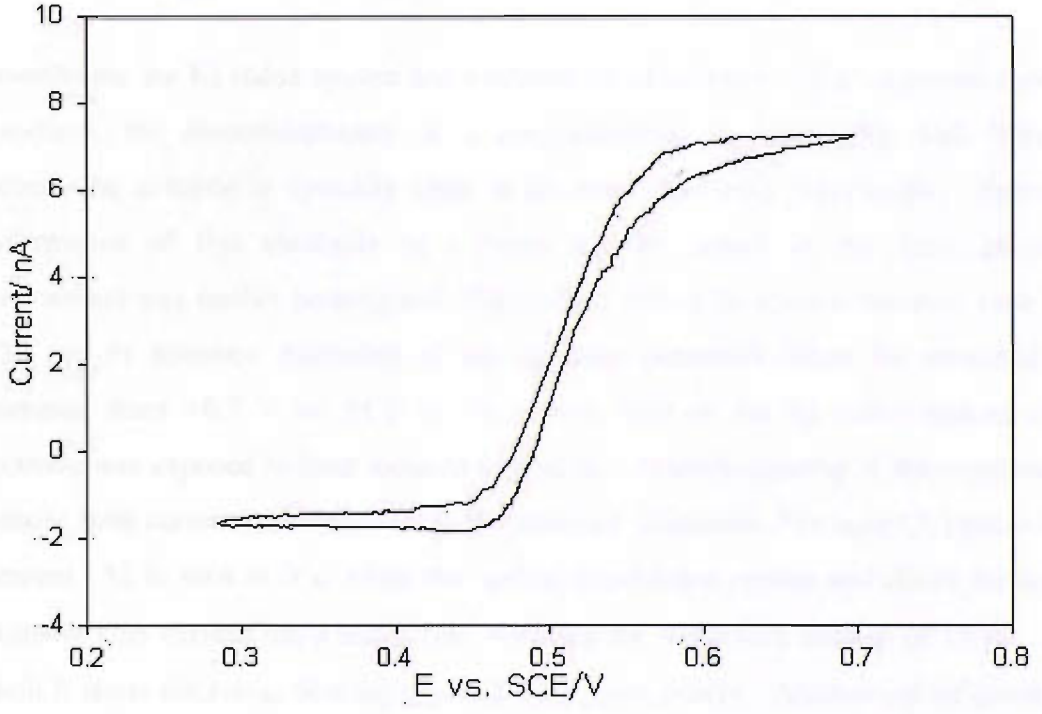

Figure 5.16 Cyclic voltammetry of a 25 µm platinum disc from -0.2 to 0.6 V *vs.* SCE in 0.2 M Na_2SO_4 containing 1 mM KI at room temperature in aerobic conditions. The sweep rate was 20 mV s^{-1}.

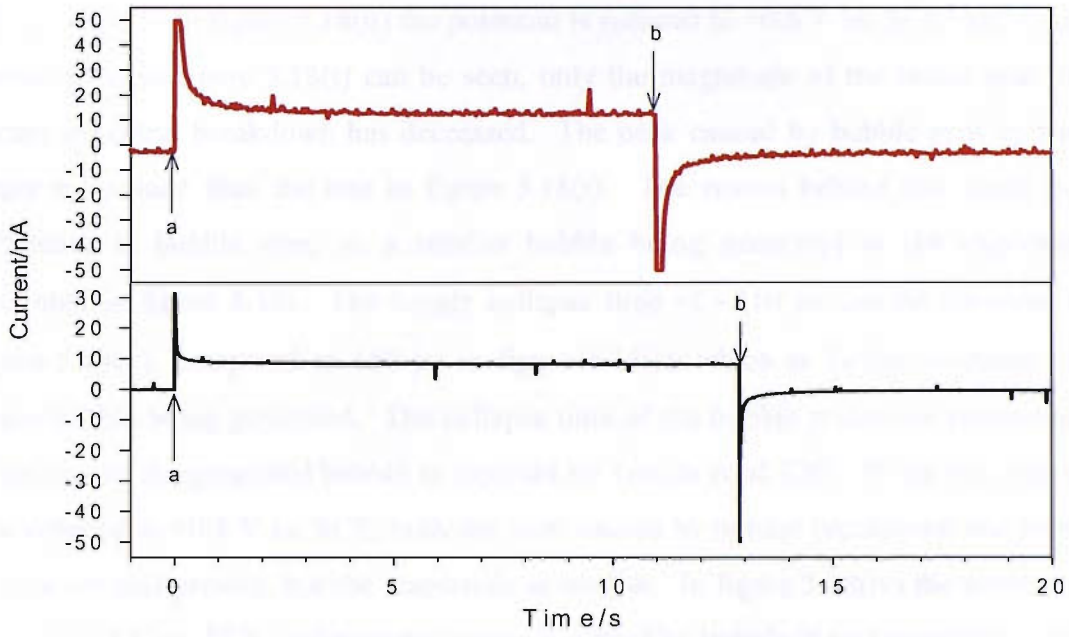

Figure 5.17 Potential step from 0.1 V to 0.65 V *vs.* SCE on a 25 μm diameter platinum disc in 0.2 M Na_2SO_4 containing 1 mM KI before (——) and after (——) the experiment at room temperature (19 °C) in a degassed solution. Note a = 0.1 V *vs.* SCE and b = 0.65 V *vs.* SCE.

Nevertheless the KI redox system has a number of advantages. First, as shown here and elsewhere, the electrochemistry at a microelectrode is reasonably well behaved. Second, the solution is optically clear at the laser (532 nm) wavelength. Hence the performance of this electrode as a mass transfer sensor in the laser cavitation environment was further investigated. Figure 5.18 shows the electrochemical trace from a 25 μm Pt diameter microdisc at six different potentials when the potential was decreased from +0.7 V vs. SCE to +0.2 V *vs.* SCE in the KI redox system as the electrode was exposed to laser induced cavitation. At the beginning of the experiments, a steady state current was observed on the platinum electrode. For figure 5.18(i), a large transient (A) is seen at 0 s, when the optical breakdown occurs and shock waves are emitted. This current has a sharp rise, reaching the maximum current of 19 μA, after which it starts decaying, first rapidly and then more slowly. Another set of events are seen at 180 μs. This is attributed to bubble action and is supported by high-speed imaging and acoustic measurements relating the laser pulse to the primary bubble collapse. This bubble induced event is smaller in magnitude than that observed for the laser breakdown of the liquid, and a sharp peak (B) can be seen initially when the bubble collapses, after which the current slowly returns to steady state. After the second

set of events the current begins to return to the steady state due to the relaxation of the diffusion field. In figure 5.18(ii) the potential is reduced to +0.6 V *vs.* SCE, and similar transients as in figure 5.18(i) can be seen, only the magnitude of the initial peak that occurs at optical breakdown has decreased. The peak caused by bubble activity has a larger magnitude than the one in figure 5.18(i). The reason behind this could be a difference in bubble size, ie. a smaller bubble being generated in the experiment presented in figure 5.18i. The longer collapse time of ~210 μs can be observed for figure 5.18(ii), compared to 180 μs in figure 5.18(i), which is further evidence of a larger bubble being generated. The collapse time of the bubble is directly proportional to the size of the generated bubble as reported by Tomita *et al.* [20]. When the potential was reduced to +0.5 V *vs.* SCE, both the peak caused by optical breakdown and bubble motion are still present, but the magnitude is smaller. In figure 5.18(iv) the potential is held at +0.4 V *vs.* SCE, and now the transient caused by bubble is no longer observable. The transient that occurs at the optical breakdown is present, but disappears almost entirely when the potential is reduced to +0.3 V *vs.* SCE in figure 5.18(v), where a small cathodic transient is seen. This is followed by a small anodic peak which could be attributed to shock wave events, electronics or some photochemical activity. Final figure 5.18(vi) presents the electrochemical signal when the potential is held at +0.2 V *vs.* SCE. This change in behaviour is related to the redox chemistry of the KI system on the Pt surface. At potentials above ~0.3 V the electrochemical oxidation of the I^- species clearly contributes to the electrochemistry observed. However, below this the effects are minimal and could be associated with pressure or laser action effects on the electrochemistry of the Pt electrolyte interface.

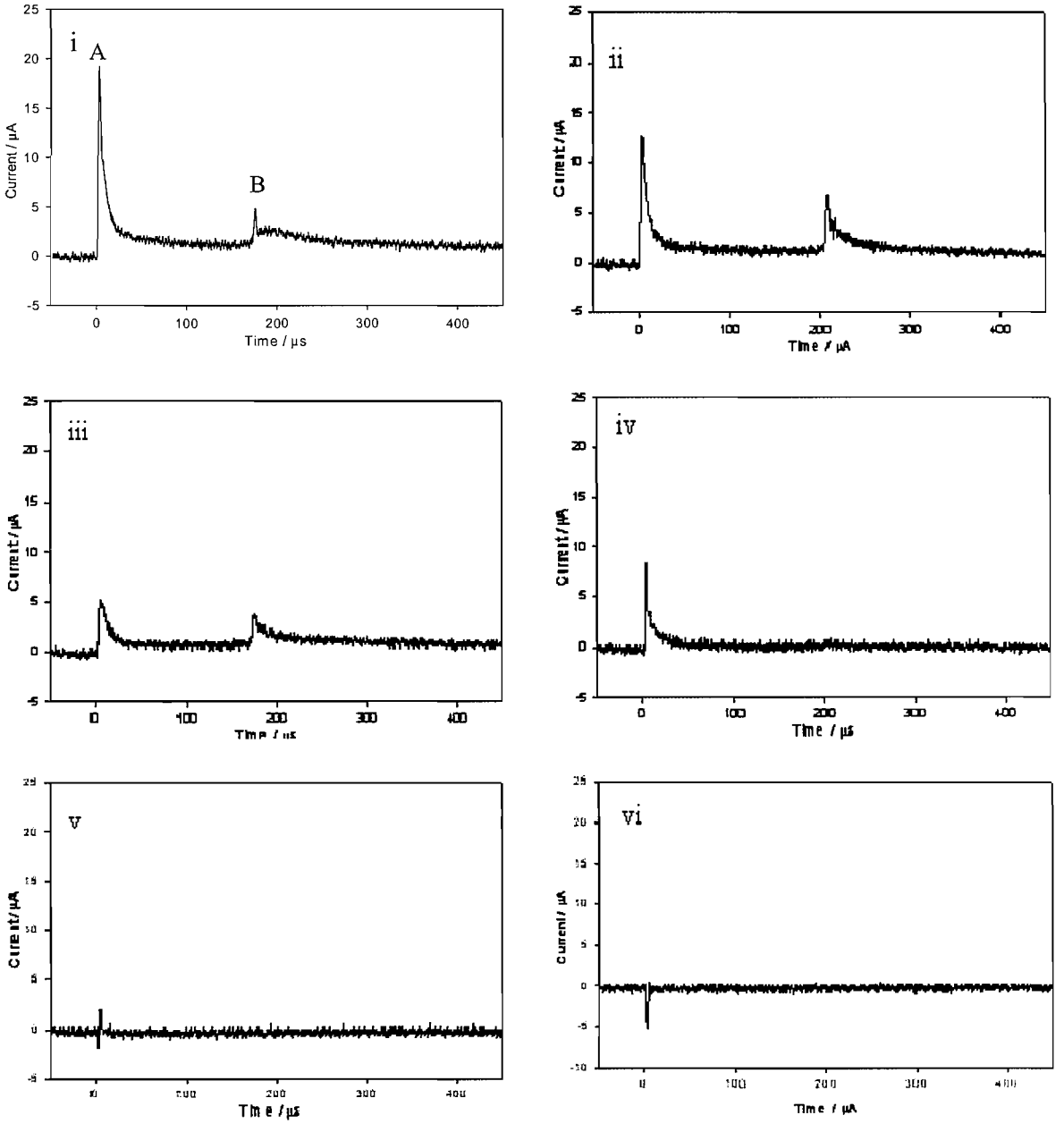

Figure 5.18 Plots showing the electrochemical trace on a Pt 25 µm diameter microdisc in a solution of 1 mM KI in 0.2 M Na_2SO_4 when the electrode was exposed to laser-induced cavitation events and the potential was held at i) 0.7, ii) 0.6, iii) 0.5, iv) 0.4, v) 0.3 and vi) 0.2 V vs. SCE at room temperature.

It should also be noted that the magnitude of the observed mass transfer signal is extremely high in these examples. Steady state currents of the order of 9 nA are expected for the electrodes. However, in the forced convection and possibly pressure effected systems recorded here, currents of the order of 6 µA have been observed (see figure 5.18(i)). This corresponds to a normalised current (I_N, defined as the current maximum/the steady state current) of 2222. In turn the mass transfer coefficient ($k_m = (4D/\pi a)I_N$) of 14.1 cm s^{-1}. This is 1-2 order of magnitude higher than that recorded for

cavitation produced by power ultrasound. Some care must be taken when considering these effects. For example these high currents are seen at solution breakdown as well as at the bubble collapse. This implies that the electrode not only will respond to the mass transfer enhancement due to the forced convection induced by bubble motion, but also responds to the solution breakdown and associated effects. Hence the electrode could also be responding to direct heating from the laser or effects associated with shock wave impingement on to the surface of the solid liquid interface. Unfortunately, the electrochemical traces alone cannot distinguish between these effects. However, it should still be noted that these effects are clearly associated with the electrochemistry of the I^- ion as indicated by the observed potential dependence reported here. Further comments and conclusions will be drawn in subsequent sections (see 5.3.2).

5.3.2 Potential change on Al electrode in Na_2SO_4

Some experiments were completed on Al-electrode with the absence of the system to detect mass transfer to see whether transients similar to those in section 5.1 could be produced. A 250 μm diameter Al-electrode in a solution of 0.2 M Na_2SO_4 was employed. Figure 5.19 presents the affect of potential change on this electrode. The recorded current transients at three different potentials are presented.

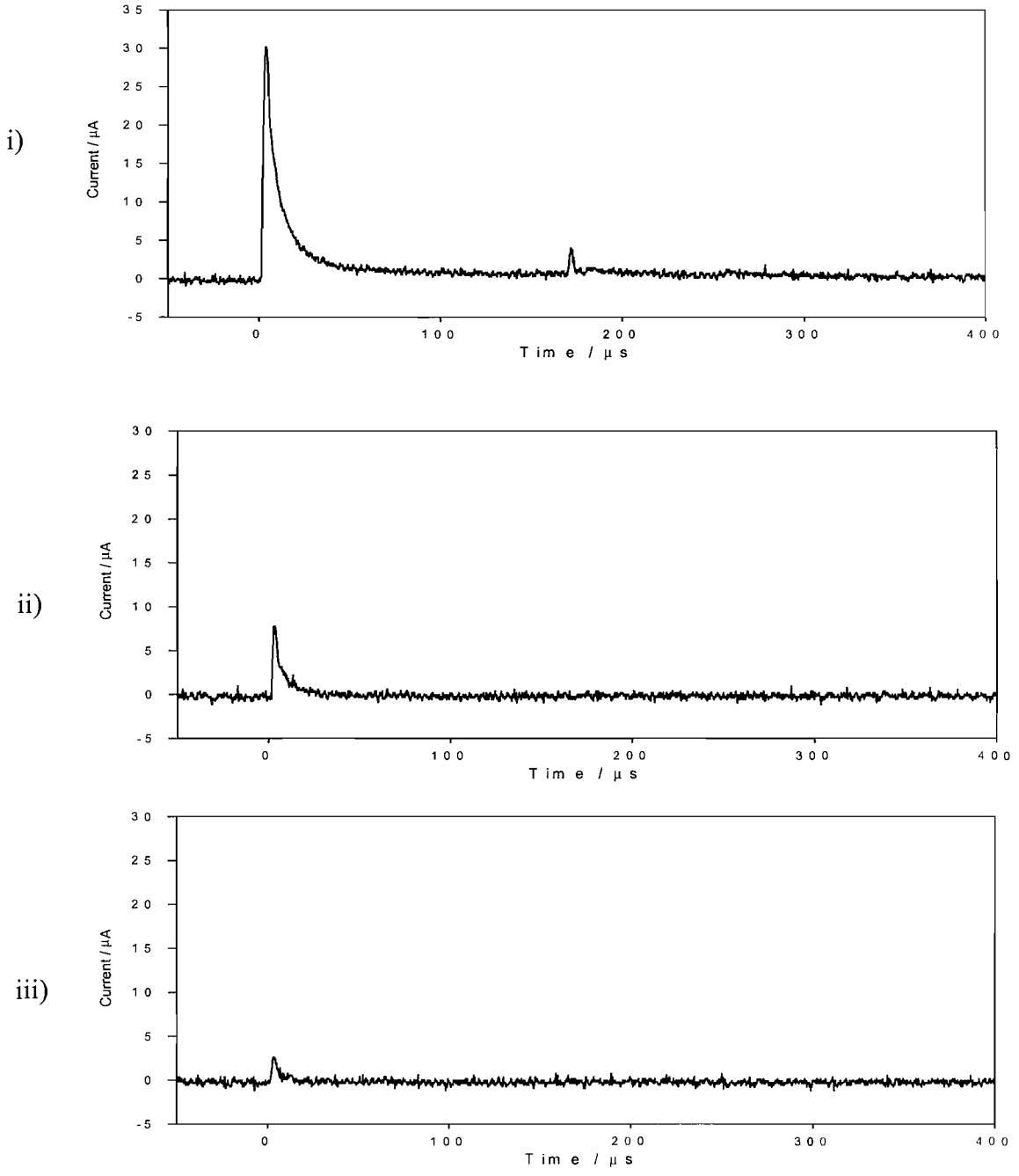

Figure 5.19 Electrochemical trace on a Al electrode in 0.2 M Na_2SO_4 when the electrode was exposed to laser-induced cavitation events and the potential was i) 0.7, iii) 0.3 and iv) 0.1 V vs. SCE. The laser energy was ca. 13 mJ/pulse.

In figure 5.19(i) the potential is held at +0.7 V *vs.* SCE and an oxide layer is present at the Al electrode surface. When exposed to laser cavitation events, part of this layer is removed and reformation of this layer is seen as current transients. First a 30 µA transient is detected when the optical breakdown occurs and the second smaller 4 µA transient is seen at approximately 180 µs when the bubble collapses. When the potential is gradually reduced to +0.5 V *vs.* SCE in figure 5.19(ii) and to +0.3 V *vs.* SCE in figure 5.19(iii), the magnitude of the peak that occurs at optical breakdown has

significantly decreased, and the peak that results from the bubble activity has completely vanished. The passive oxide layer on the surface of the electrode could be thinner at these potentials than at 0.7 V *vs.* SCE and therefore a smaller response is observed. When the potential is reduced to 0.1 V vs. SCE, the magnitude of the electrochemical transient observed when the optical breakdown occurs is further decreased and is now ca. 10 % of the current detected in figure 5.19(i). Clearly the detected events are strongly dependant on the applied potential. Decrease in potential results in decrease in the size of the current transients. The results presented in figure 5.19 were reproducible as the current was measured several times at every potential and similar transients were recorded each time. The transients are a lot smaller than reported previously in this chapter, which is a result of a greater distance between the bubble and the electrode.

The response for aluminium alone was further studied by varying the position of the electrode. The measured currents and a hydrophone response in three different positions when electrode was moved in the z-direction (see figure 5.10 for different dimensions) are presented in following figure 5.20. It was stated previously in chapter 4 and chapter 5 sections 5.1-5.2 that when the electrode is moved towards the bubble centre, the recorded electrochemical transients become larger. The laser energy applied in these experiments was ca. 21 mJ/pulse and considerably smaller than the energy employed in sections 5.1 and 5.2 (40 mJ/pulse). Even though less energy is applied in this section, the collapse time of the bubbles is longer (~ 240 μs) than in section 5.1 (~ 150 μs) [20]. The larger the bubble, the longer it takes it to collapse. The explanation lies within the nature of the employed electrolytes. The solution of KI in Na_2SO_4 is colourless; whereas the solution of ferrocyanide in Na_2SO_4 employed in sections 5.1-5.2 has a light yellow colour. Therefore it could be concluded that the yellow ferrocyanide solution absorbed part of the applied laser energy which resulted in smaller bubble size. In figure 5.20(i) the first peak (A) is saturated and the exact current recorded at the optical breakdown is unknown but in excess of 0.4 mA (estimated based on figures 5.20(ii) and 5.20(iii)). It should be noted that this saturation problem is unavoidable if one requires an accurate measurement of the current for both events (e.g. the transient at laser discharge and the transient due to the bubble collapse). The bubble collapse transient (B) is seen at approximately 250 μs. The charge over the first 250 μs is 0.8-1.4 nC and after the bubble collapse at 250-450 μs 1.5-2.0 nC. In figure 5.20(ii) and

5.20(iii) the position of the electrode is 100 μm and 150 μm below the position in figure 5.20(i), respectively. Figure 5.20 shows that the magnitudes of current transients are larger when the electrode was moved closer to the focal spot of the laser beam. Indeed a significant increase in the current transients from the Al electrodes employed was observed at the point of bubble collapse (labelled B) between figures (ii) and (iii). For these two figures, the charge over the first 250 μs after optical breakdown is 2-2.3 nC for figure 5.19(ii) and 2-3 nC for figure 5.20(iii). However, over the bubble collapse region (250-450 μs) the charge is 2.6-3 nC in figure 5.19(ii) but has risen to 3-9 nC in figure 5.20(iii). This implies that more material is being removed at the bubble collapse than in the optical breakdown process at $t = 0$ μs as the electrode is moved closer to the bubble centre. Indeed this difference increases when the electrode is moved closer to the focal spot of the laser beam.

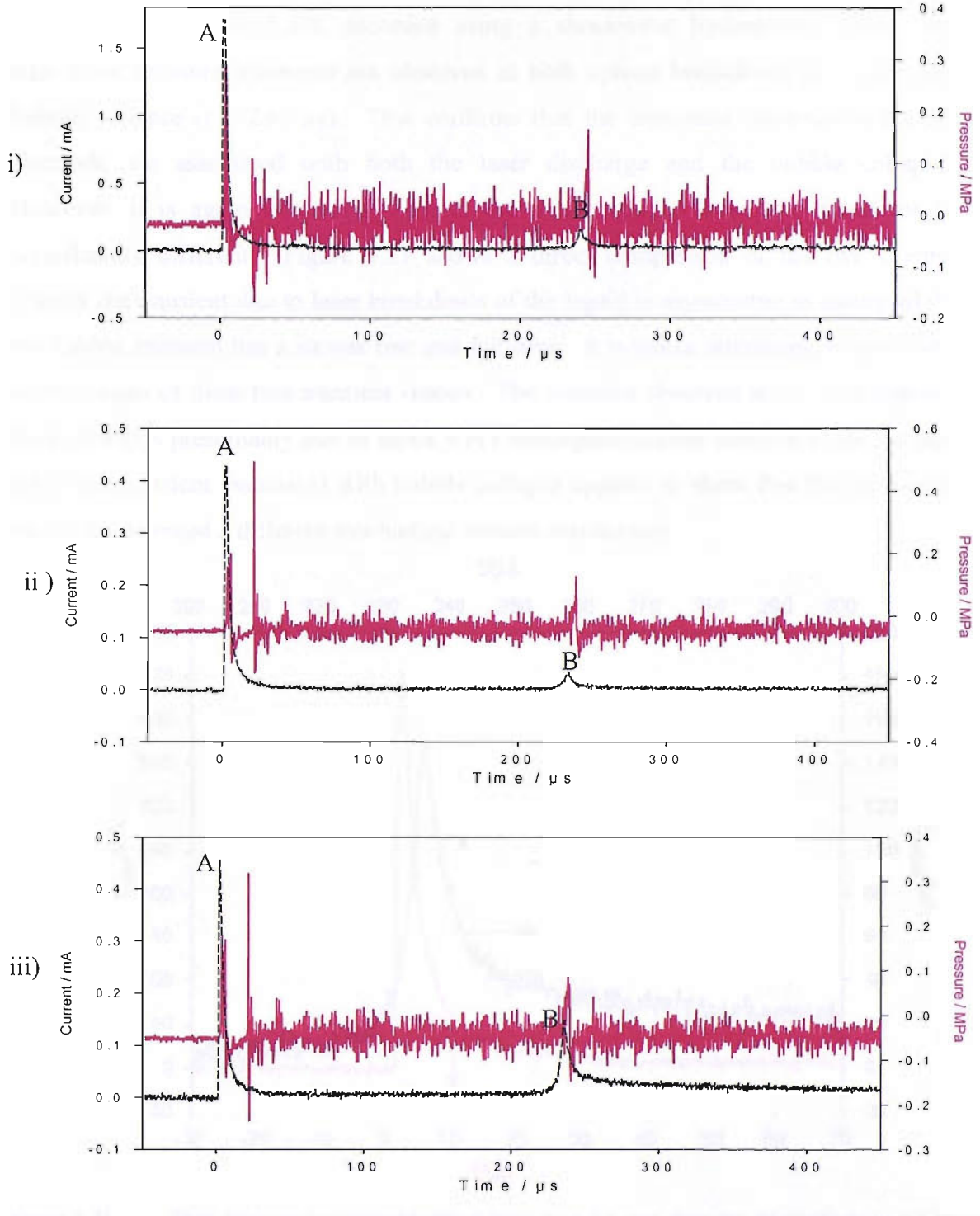

Figure 5.20 Plots showing the electrochemical response for a 0.5 mm diameter Al electrode (—) in 0.2 M Na_2SO_4 when the electrode was exposed to laser-induced cavitation events. The electrode was moved 100 µm in *z* direction for (ii) and 150 µm in *z* for (iii) with respect to the starting position (i). The laser energy was ca. 21 mJ/pulse and the solutions was filtered and degassed before the start of the experiments that were performed at room temperature. Also shown is the response of a hydrophone recorded simultaneously (—).

Further information can be gathered from the results shown in figure 5.21. The acoustic transients (see figure 5.20), recorded using a shockwave hydrophone, show that significant pressure transients are observed at both optical breakdown (t = 0 μs and bubble collapse (t ~ 250 μs). This confirms that the transients observed at the Al electrode are associated with both the laser discharge and the bubble collapse. However, it is again interesting to note that the shape of these two transients is significantly different. Figure 5.21 shows a direct comparison of the two events. Clearly the transient due to laser breakdown of the liquid is asymmetric in nature while the bubble transient has a slower rise and fall time. It is hence interesting to speculate on the origin of these two transient shapes. The transient observed at t = 0 μs (optical breakdown) is presumably due to shock wave impingement/laser ablation of the surface while the transient associated with bubble collapse appears to show that the surface of the Al experienced a different mechanical erosion mechanism.

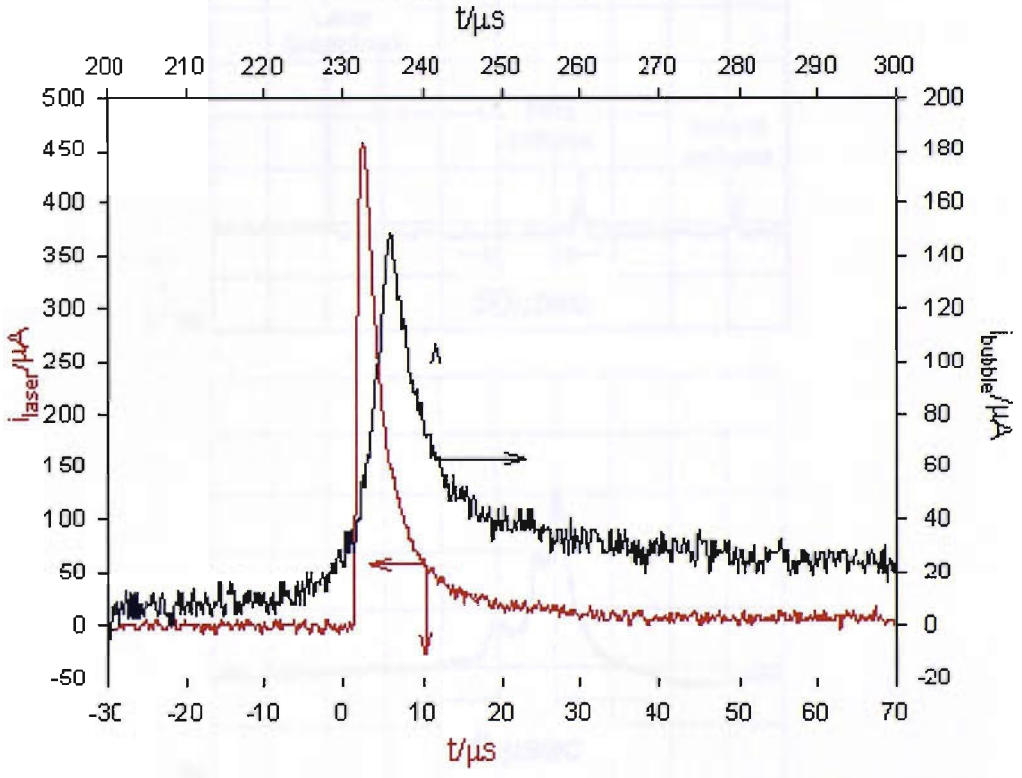

Figure 5.21 Plots showing the electrochemical trace on a 0.5 mm diameter Al electrode in 0.2 M Na_2SO_4 at optical breakdown at t = 0 μs (——)and bubble collapse at t ~ 250 μs (——) when the electrode was exposed to laser-induced cavitation events at room temperature (19°C). The laser energy was ca. 21 mJ/pulse.

Further insight into this mechanism may be gained by analysis of the data obtained by Shaw *et al.* Figure 5.22 shows a pressure time trace taken from [107]. In this example the pressure is measured by a PVDF modified surface. It is interesting to note that

pressure shown in figure 5.22 and the current time transient shown in figure 5.20(iii) are remarkably similar. Hence one possible explanation for the erosion signal observed on the Al electrode is related to the pressure extended on the surface. The erosion at $t = 0$ s caused by the optical breakdown of the media is presumably a result of a sudden fracture of the passivating oxide layer in response to the high positive pressure pulse. However, the pressure extended on the surface by the bubble collapse is longer in duration (~ 15 μs) and similar in shape and duration to the current transient shown in figure 5.21. Hence, it is likely that the pressure extended on the surface by the bubble collapse causes an erosive corrosive mechanism which is different to that caused by the shape pressure transient at $t = 0$ μs. One possible explanation for this effect would be a plastic deformation of the surface as a result of the bubble collapse.

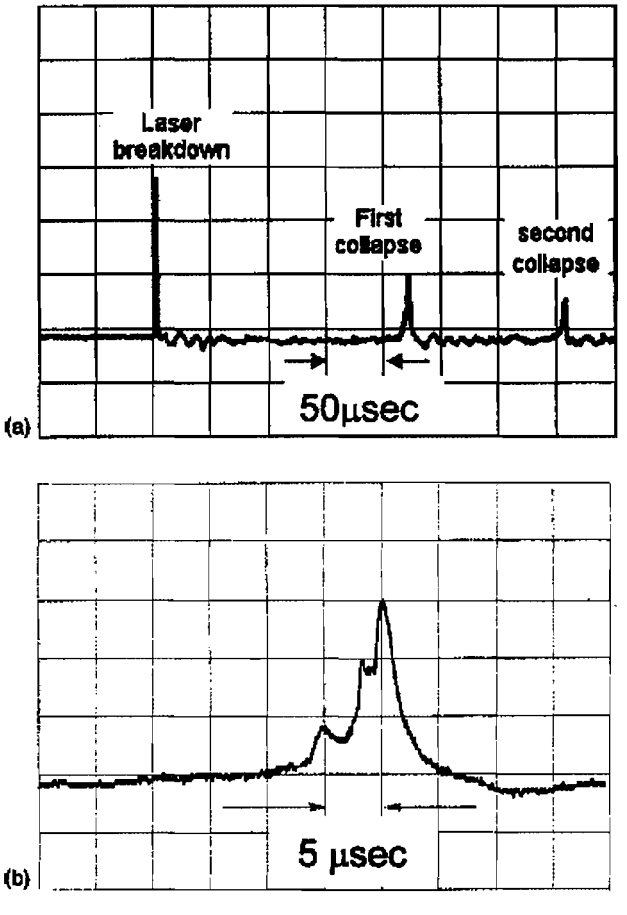

FIG. 2. (a) Transducer plot at low resolution for a typical event. (b) Transducer plot at high resolution of the pressure peak due to the first collapse at $\gamma = 0.72$.

Figure 5.22 Pressure profile for a PVDF (polyvinylidene fluoride) transducer as a function of time [107].

5.3.3 Simultaneous mass transfer and erosion in KI system

The results in figures 5.19 and 5.20 are very similar to those presented in sections 5.1 and 5.2 and it was concluded that the erosion sensor is unaffected by the events on the Pt electrode. In the next set of experiments presented in this chapter, dual Pt/Al electrode was employed to study erosion and mass transfer in a solution of 1 mM KI in Na_2SO_4. Sections 5.1 and 5.2 reported experiments conducted with this same electrode system in a ferrocyanide solution (The comparison of bubble size *vs.* laser energy is presented in chapter 6). The ferrocyanide solution resulted in the partial absorption of the laser energy and therefore some of the experiments reported in those sections are repeated here in a KI system which is transparent. Also, the mass transfer signal in the experiments in sections 5.1 and 5.2 was very unstable. Thus, a KI solution was employed to provide more reliable results. Figure 5.23 presents the currents recorded on Al and Pt electrodes at the original electrode position where a strong electrochemical signal was recorded on both Pt and Al sensors. In all cases the potential of both electrodes was held at +0.6 V *vs.* SCE. This corresponds to the mass transfer limited potential for the oxidation of I^- at the Pt surface while the Al electrode is maintained in a passive state. The pressure transients produced by the laser discharge and subsequent bubble formation where also recorded simultaneously. The Q-switch delay was 130 μs which corresponds to laser energy ~ 40 mJ/pulse.

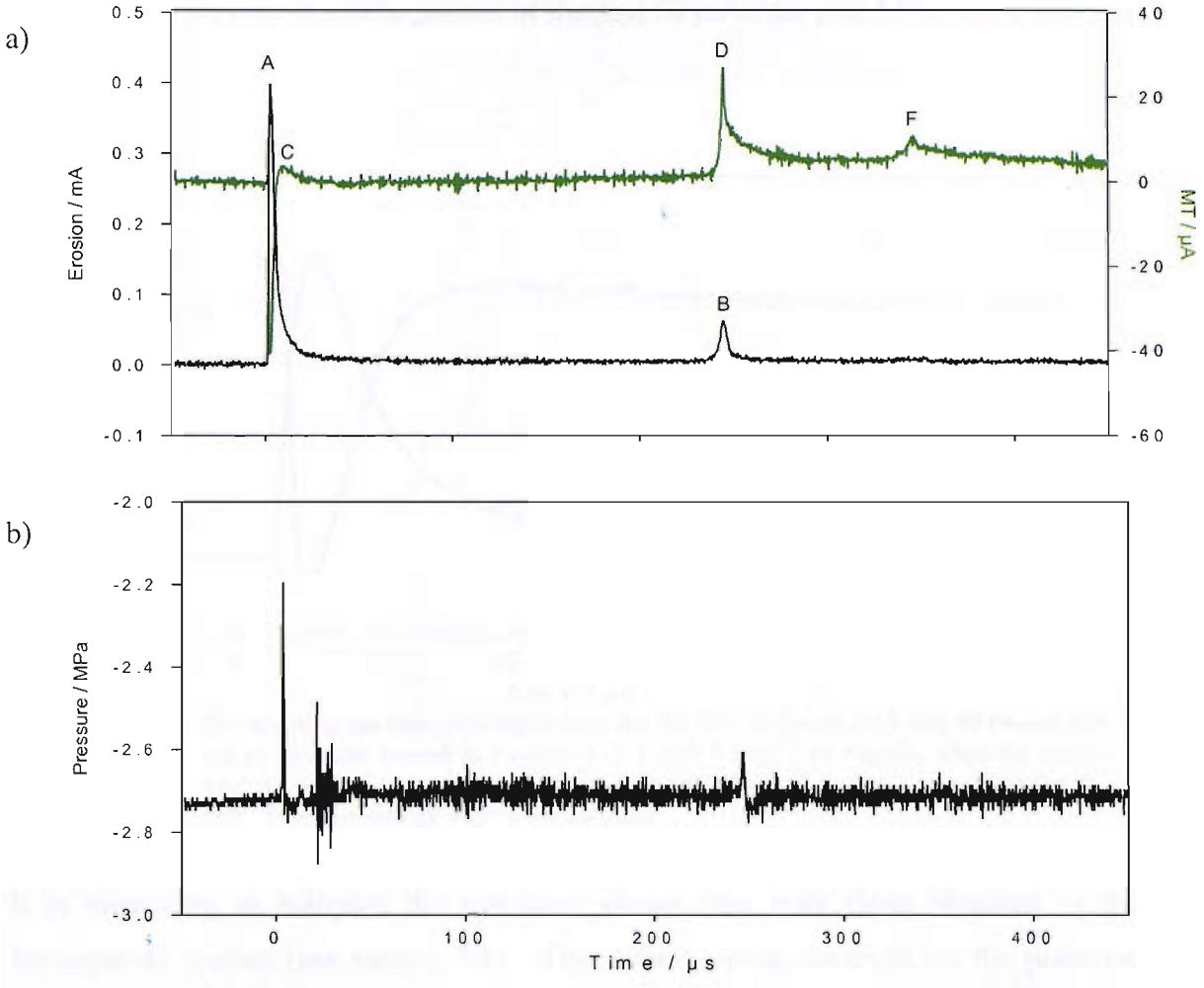

Figure 5.23 Plots showing a) the electrochemical trace on a 0.5 mm Al (——) and 50 µm Pt electrode (——) in a solution of 1 mM KI in 0.2 M Na_2SO_4 when the electrode was exposed to laser-induced cavitation events and the potential of the electrode was held at 0.6 V *vs.* SCE and b) simultaneously recorded hydrophone signal. The laser energy was ca. 40 mJ/pulse.

Two separate events are again detected on the Al electrode (——), first one (A) at $t = 0$ s at optical breakdown, and the second one (B) at ~ 240 µs when the bubble collapses. The shape of the transients is similar to those reported earlier in this chapter (see figure 5.20 (iii)). In turn similar pressure transients are also observed on the hydrophone. The dual electrode employed in this study is designed to monitor fluid flow and hence enhancements in mass transfer as a result of diffusion/convection processes. Indeed a number of events are detected on the trace recorded by the platinum electrode (——). Before the optical breakdown occurs at $t = 0$ s, a steady state current is present on the electrode surface (see the cyclic voltammogram in figure 5.16) At the optical breakdown a small increase is observed (labelled (C)) but this is masked by a large cathodic peak. This is similar to section 5.1 where this same electrode system was

employed in ferrocyanide solution, the negative peak appears simultaneously with the large erosion peak A. An enlargement of the first 30 μs of the plot 5.23a is presented in figure 5.24.

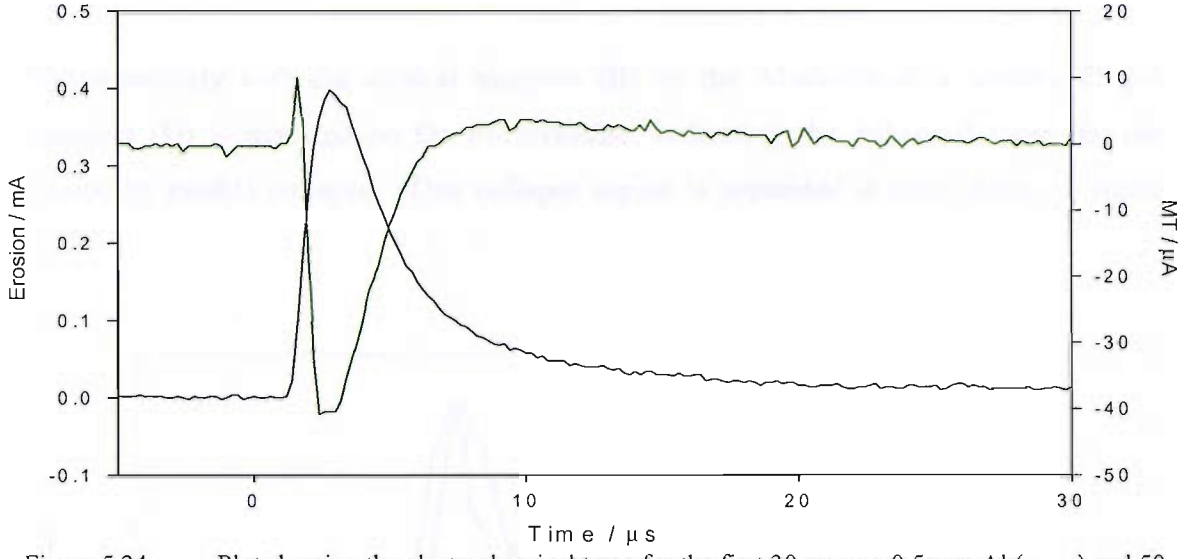

Figure 5.24 Plot showing the electrochemical trace for the first 30 μs on a 0.5 mm Al (——) and 50 μm Pt electrode (——) in a solution of 1 mM KI in0.2 M Na_2SO_4 when the electrode was exposed to laser discharge. The potential of the electrode was held at 0.6 V *vs.* SCE. The laser energy was ca. 40 mJ/pulse.

It is interesting to compare the transients shown here with those obtained in the ferrocyanide system (see section 5.1). The cathodic peak observed on the platinum electrode resembles a mirror image of the anodic peak detected on the aluminium electrode. One should also note that no negative transient was present in figure 5.18i where the transients on platinum electrode were recorded in the absence of aluminium disc. However, when the Pt/Al electrode was employed in ferrocyanide system in section 5.1, cathodic transients were detected on the platinum electrode also at the bubble collapse, when an erosion peak of smaller magnitude appears (labelled as peak (B) in figure 5.23). Interestingly, the mass transfer transient (see D) recorded by platinum electrode in KI when the bubble collapses is unaffected by this event (B). Therefore, it is not clear whether the large negative peak (labelled C) at 0 s is caused by the coupling between the electrodes or another event associated with shock impact on the Pt surface. Hence, the exact reason behind this large cathodic transient is unknown at this time. It is likely that the absence of the coupling signal when the bubble collapses is just a scale effect. It was reported earlier that Pt/$Fe(CN)_6^{4-}$ system only produced ~2 μA from mass transfer detector whereas Pt/I^- system produces ~30 μA. At

t = 0 s, the recorded erosion signal was ~400 μA and the associated coupling signal was ~ 40 μA. When the bubble collapses, the erosion transient is 60 μA, and therefore one could expect a coupling signal ~6 μA. As 6 μA is a lot smaller than the 25 μA mass transfer signal, no negative transient is observed.

Simultaneously with the erosion transient (B) on the Al-electrode, a positive 25 μA transient (D) is detected on the Pt-microdisc, indicating the enhanced mass transfer caused by bubble collapse. This collapse region is presented in more detail in figure 5.25.

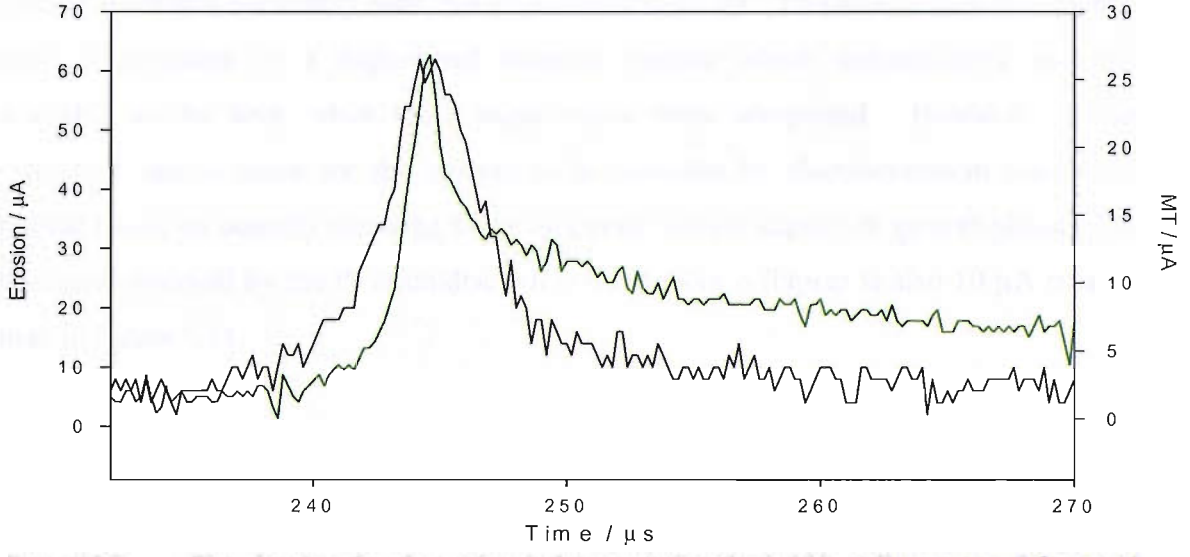

Figure 5.25 Plot showing the electrochemical trace during the bubble collapse on a 0.5 mm Al (——) and 50 μm Pt electrode (——) in a solution of 1 mM KI in0.2 M Na_2SO_4 when the electrode was exposed to laser-induced cavitation events and the potential of the electrode was held at 0.6 V vs. SCE. The laser energy was ca. 40 mJ/pulse.

As it can be seen from figure 5.25, the signal for mass transfer (——) starts rising slightly later than the erosion transient (——). Both mass transfer and erosion signals reach the maximum at approximately the same time. After reaching the maximum (27 μA), the mass transfer trace begins to return towards the steady state current as the diffusion field relaxes. In turn this corresponds to a mass transfer coefficient (k_m = $(4D/\pi a)I_N$) of 1.76 cm s^{-1}. Figure 5.23, also shows another mass transfer events (labelled F) detected at 350 μs. This is attributed to bubble rebound and collapse (see section 5.3.1). Lastly it is interesting to note that surface erosion is only noted at the primary bubble collapse (confirmed by the simultaneous pressure measurements) and not at the rebound collapse.

Figure 5.26 presents the recorded electrochemical transients and hydrophone signal when the electrode was moved 50 μm upwards (see figure 5.10 for details about the different directions) from the position in figure 5.24. The magnitudes of both mass transfer (——) and erosion (——) sensors have now decreased as expected as the distance between the bubble centre and the electrode has increased. The transient detected on Al at optical breakdown is ~one quarter and the transient recorded during the bubble collapse is one third of the size they have in figure 5.23. This implies that the erosion sensor only monitors events when the electrode surface is very close to the bubble. It is impossible to measure the distance between the bubble centre and the electrode surface accurately with this experimental set-up. This would only be possible with employment of a high-speed imaging system which unfortunately was not available at the time when these experiments were completed. However, it was estimated that in order for the erosion to be detected by electrochemical means the bubble has to be actually touching to the electrode surface during its growth phase. The transient observed by the Pt microdisc when the bubble collapses is also 10 μA smaller than in figure 5.23.

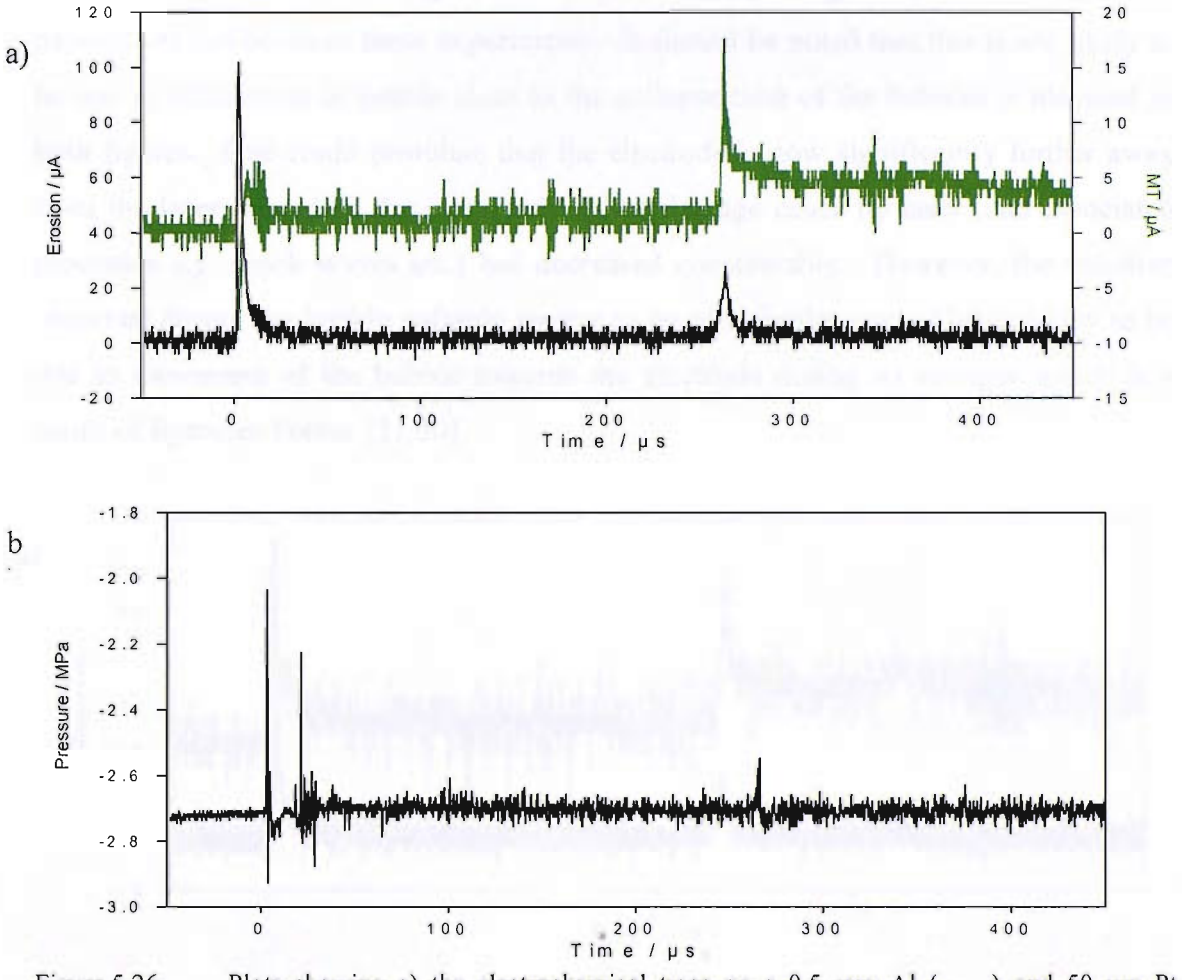

Figure 5.26 Plots showing a) the electrochemical trace on a 0.5 mm Al (——) and 50 µm Pt electrode (——) in a solution of 1 mM KI in 0.2 M Na_2SO_4 50 µm above the position in figure 5.20 when the electrode was exposed to laser-induced cavitation events and the potential of the electrode was held at 0.6 V *vs.* SCE and b) simultaneously recorded hydrophone signal. The laser energy was ca. 40 mJ/pulse.

Figure 5.27 presents the transients recorded 100 µm above the position in figure 5.23. Again as expected a decrease in magnitude is again observed on the erosion sensor (——). Interestingly, a rather significant decrease is also monitored on the mass transfer sensor (——). However, one would not expect such sensitivity from the mass transfer sensor as the diffusion field surrounding the electrode can be estimated to be ~10 times the size of the electrode radius. This observation is further confirmed in figure 5.28 where the electrode is located 200 µm above the position in figure 5.23 and the mass transfer signal has practically disappeared on this current scale. However, it is possible that the mass transfer transients could be observable with a more sensitive gain value. Figure 5.28 also shows that the erosion transients recorded on the Al electrode at optical breakdown and bubble collapse have a similar magnitude to one another. Indeed

the magnitude of the erosion transients recorded at bubble collapse ($t \sim 250$ μs) are approximately the same in figure 5.27 and 5.28 even though the electrode has been moved 100 μm between these experiments. It should be noted that this is not likely to be due to differences in bubble sizes as the collapse time of the bubbles is identical in both figures. One could postulate that the electrode is now significantly further away from the laser focus that the magnitude of the damage cause by laser (and associated processes e.g. shock waves etc.) has decreased considerably. However, the transient observed during the bubble collapse appear to be of a similar size. This is likely to be due to movement of the bubble towards the electrode during its collapse which is a result of Bjerknes Forces [21,30].

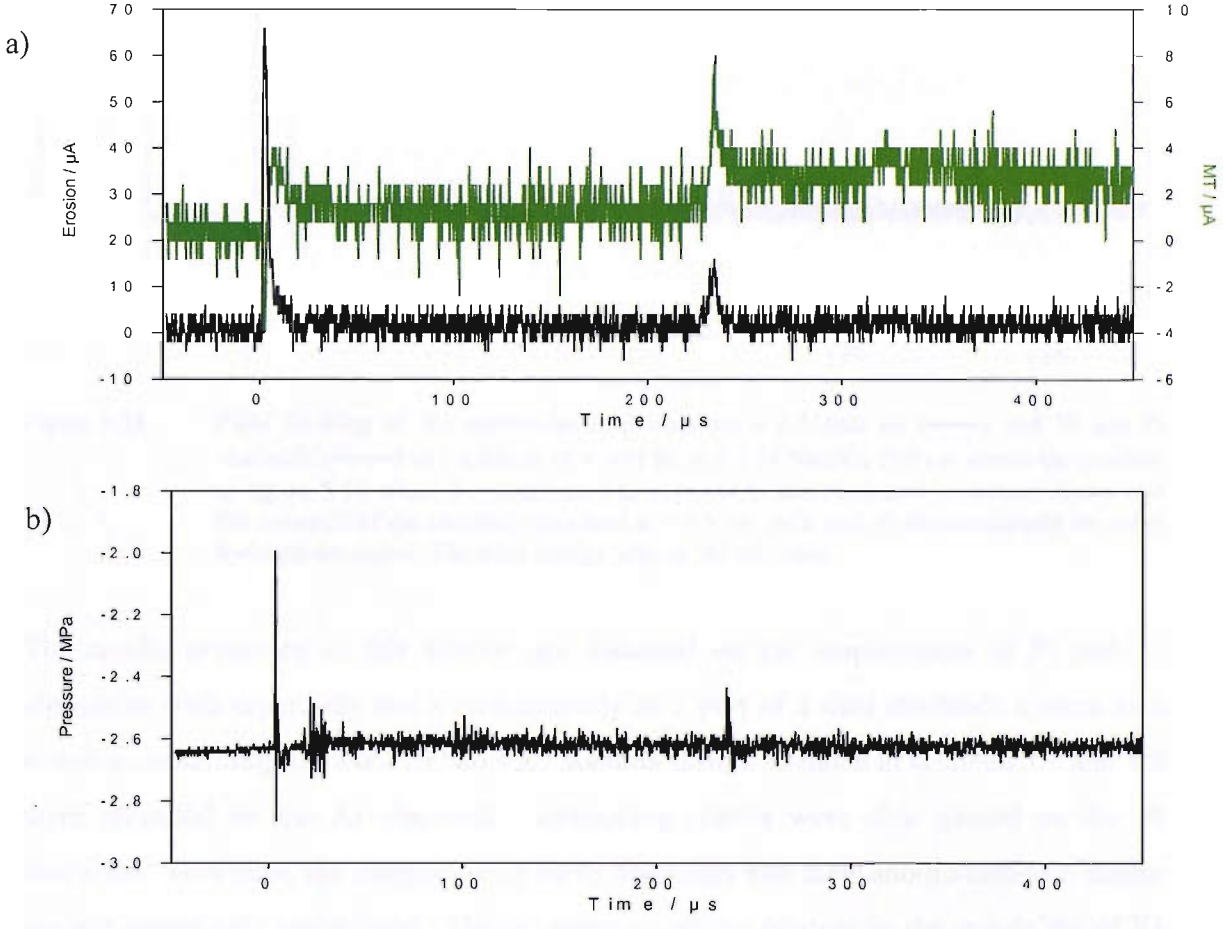

Figure 5.27 Plots showing a) the electrochemical trace on a 0.5 mm Al (——) and 50 μm Pt electrode (——) in a solution of 1 mM KI in 0.2 M Na_2SO_4 100 μm above the position in figure 5.20 when the electrode was exposed to laser-induced cavitation events and the potential of the electrode was held at 0.6 V *vs.* SCE and b) simultaneously recorded hydrophone signal. The laser energy was ca. 40 mJ/pulse.

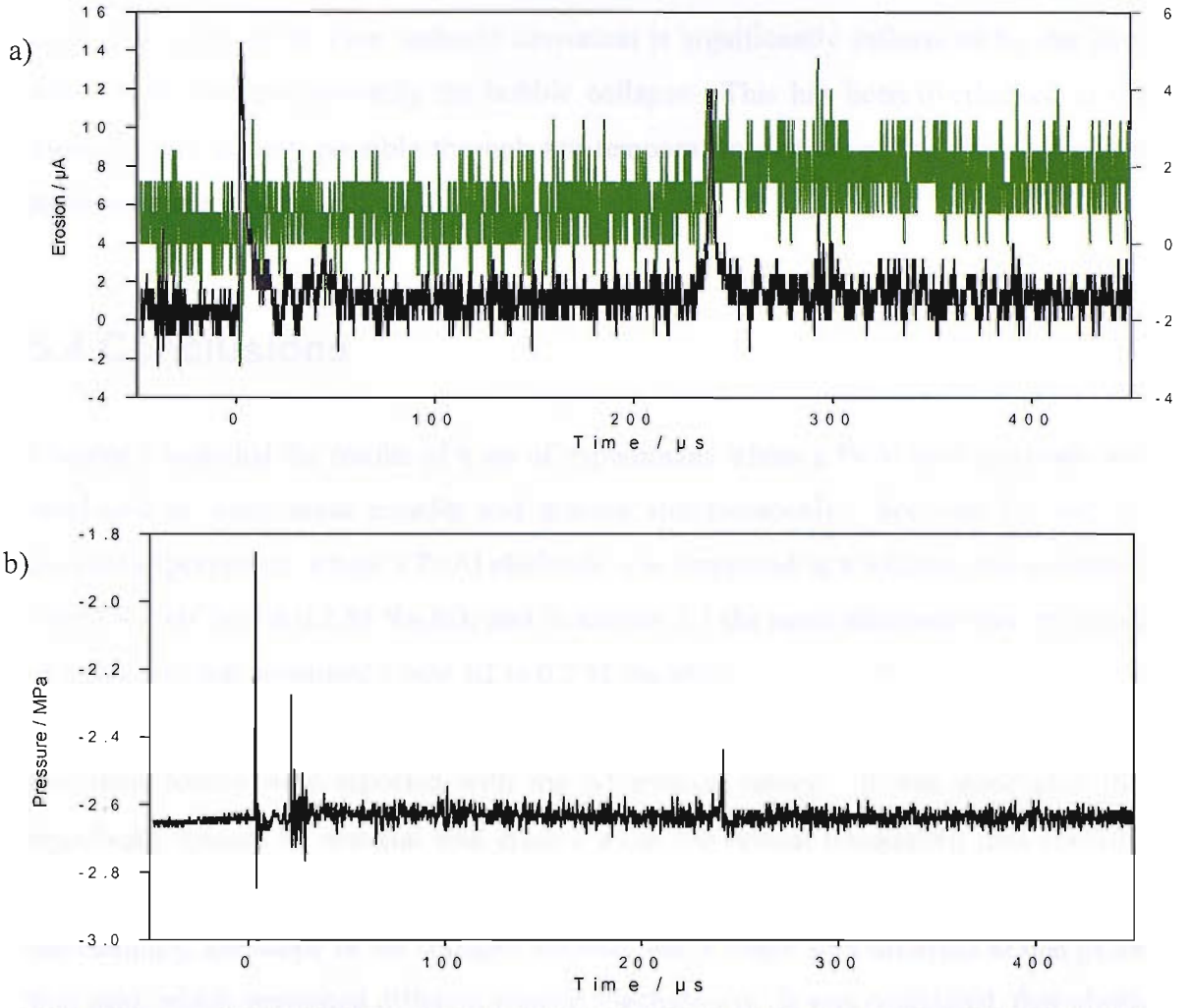

Figure 5.28 Plots showing a) the electrochemical trace on a 0.5 mm Al (——) and 50 µm Pt electrode (——) in a solution of 1 mM KI in 0.2 M Na_2SO_4 200 µm above the position in figure 5.20 when the electrode was exposed to laser-induced cavitation events and the potential of the electrode was held at 0.6 V *vs.* SCE and b) simulatenously recorded hydrophone signal. The laser energy was ca. 40 mJ/pulse.

The results presented in this section are focussed on the employment of Pt and Al electrodes both separately and simultaneously as a part of a dual electrode system in a solution containing KI in 0.2 M Na_2SO_4. Results similar to those in sections 5.1 and 5.2 were recorded on the Al electrode. Interesting results were also gained on the Pt electrode. However, the magnitude of these transients and their anodic/cathodic nature are not completely understood. Hence, some questions relating to the suitability of KI system to study mass transfer events in this environment remain. Nevertheless, significant results relating to the erosion/corrosion mechanisms, bubble rebound and collapse processes have been presented. Lastly, the magnitude and shape of the erosion processes are significantly different when one compares the laser optical breakdown to the bubble collapse phenomena. Indeed one can suggest from these results that the

erosion of surfaces by laser induced cavitation is significantly influenced by the laser action itself and not primarily the bubble collapse. This has been overlooked in the literature and is only possible through the temporal resolution of the electrochemical techniques employed here.

5.4 Conclusions

Chapter 5 included the results of a set of experiments where a Pt/Al dual electrode was employed to study mass transfer and erosion simultaneously. Sections 5.1 and 5.2 covered experiments, where a Pt/Al electrode was employed in a solution that contained 5 mM $K_4Fe(CN)_6$ in 0.2 M Na_2SO_4 and in section 5.3 the same electrode was employed in a solution that contained 1 mM KI in 0.2 M Na_2SO_4.

Excellent results were reported with the Al erosion sensor. It was concluded that significant amount of material was eroded when the optical breakdown first occurred and the plasma was formed. Another peak was observed when the bubble collapsed. Interestingly, the shape of the collapse transient had a shape very different to that of the first peak which suggested different erosion mechanisms. It was postulated, that plastic formation occurred on the electrode surface and was responsible for the observed peak shape.

The attempts to monitor mass transfer events on the Pt microdisc were not quite as successful. The results recorded in the ferrocyanide solution were very unstable and it was noted that the events on Pt electrode mirrored those on the Al erosion sensor, indicating coupling between the electrodes. When the ferrocyanide system was replaced by KI, more stable results were recorded. However, again a large cathodic peak of unknown origin was present when the plasma formation took place. Another, positive peak was recorded when the bubble collapsed, and also a third peak was observed which was thought to be a result of second bubble collapse. Nevertheless significant mass transfer rates ($0.2 \rightarrow 2$ cm s^{-1}) are generated by these events. The explanation for the high mass transfer rates could be related to the electrochemistry of the I^- species ($I^- - e^- \rightarrow \frac{1}{2} I_2$). If I_2 does crash (slowly) out on the electrode then this

species, and its removal, may be responsible for the high i_{MT} when the bubble erosion was observed.

Clearly, the employment of high-speed camera system would have been very beneficial during the experiments presented to confirm some of the observations and postulations done in this chapter. Unfortunately, such equipment was not available at the time when these experiments were conducted. The next chapter will examine the laser induced cavitation events by high-speed photographic means as well as present the CFD simulations based on the high-speed images.

Chapter 6

High-speed imaging and CFD simulations

Throughout this project, three different high-speed cameras were employed to capture the bubble formation and collapse. The employment of high-speed imaging equipment enabled the determination of bubble size and the distance between the bubble and the surface of the electrode. Chapter 3 presented images recorded by a Hadland high-speed camera. In addition, some high-speed images taken by the Photron high-speed video camera were presented in chapter 4.

The images taken on high-speed cameras (in particular those by Photosonics Phantom v7 high-speed video camera) were used for theoretical examination of the bubble collapse. The images taken were the basis for testing of computational simulations of the bubble life from its maximum to its collapse and rebound cycles. The shock waves that cause damage to the nearby surface are emitted when the bubble collapses and therefore it would be interesting to study this collapse region in detail. The high-speed imaging equipment used was not fast enough to capture the events when the bubble reaches its minimum in detail. However, with CFD simulations, detailed data of the events when the bubble collapses can be examined. Some of the results of the simulations are presented in this chapter. The simulations were completed in collaboration with Dr Graham Ball and Kylie Osman from Atomic Weapons Establishment (AWE).

The employment of high-speed cameras enabled the determination of bubble size at different laser energies. Figure 6.1 presents the maximum bubble size observed a function of laser energy. The figure includes bubbles generated by two different lasers and also the results published by Tomita and Shima [20]. For the Continuum NY61 laser the bubble size was determined in both distilled water and ferrocyanide solution. The measured maximum diameter of the bubble is smaller in ferrocyanide solution than in water presumably due to extra absorption processes in this solution. This is one possible reason why the maximum bubble diameters at different laser energies recorded in the experiments in Southampton are less than half of those reported by Tomita and

Shima. Also, the problems encountered with the Continuum NY61 laser are responsible for generation of smaller bubbles next to the primary bubble. This laser had several faults, including bad beam shape, which could result in loss of energy and generation of smaller bubbles (see chapter 2 section 2.1.1 for details). One should also note that a different type of laser was employed by Tomita and Shima and the focussing optics also have a role in the size of generated bubbles. For the Continuum Inlite laser only the bubble size in a solution containing KI in Na_2SO_4 is presented.

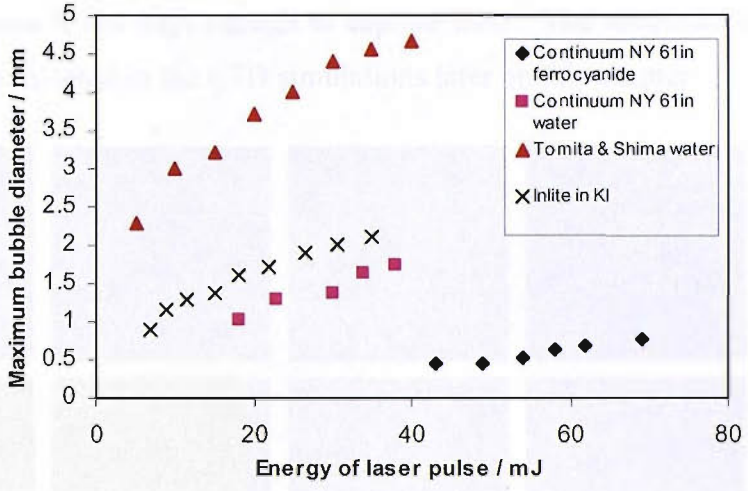

Figure 6.1 The maximum bubble diameter versus the applied laser energy for two different lasers in electrolyte solutions and purified water and as reported by Tomita and Shima [20]. The electrochemical solutions were aerobic 5 mM $K_4Fe(CN)_6$ and 1 mM KI in 0.2 M Na_2SO_4 in room temperature 19 °C.

6.1 The collapse of a bubble at different values of γ detected by high-speed camera

When a bubble is generated near a solid surface, it collapses unevenly (see chapter 1 for details about bubble collapse dynamics). The surface of the bubble furthest away from the solid wall collapses faster than the surface of the bubble closer to the solid/liquid interface. This results in a formation of a liquid jet that travels through the bubble. Chapter 1 stated that the impact of the liquid jet on the surface causes significant erosion when the dimensionless distance between the bubble and the solid-liquid interface, γ, has a value smaller than 0.7 [21]. This means the distance between the bubble and the surface is less than twice the radius of the bubble. In the next section, a sequence of high-speed images captured after laser induced bubble formation, is presented. In each case the γ value of the system is varied and the effects on bubble

formation noted. Note the beam and focussing optics remain fixed while the electrode is moved down from above.

Figure 6.2 presents a typical laser generated bubble in electrochemical solution (KI in Na_2SO_4) that collapses unevenly in the presence of a solid boundary (electrode surface, $\gamma = 3.4$). The camera speed was 68 000 frames per second. The moment when the first bubble minimum is reached is very short–lived and therefore the frame rate employed in these experiments is not high enough to capture this. The minimum of the bubble is studied in more in detail in the CFD simulations later on this chapter.

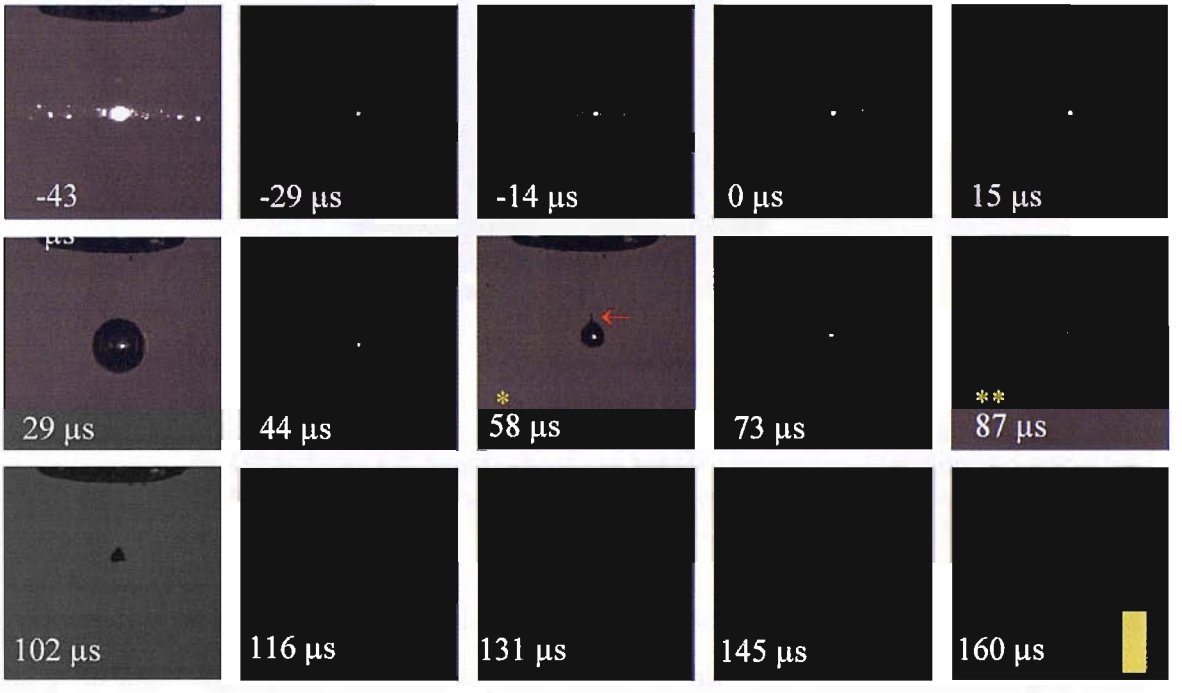

Figure 6.2 Images showing a bubble generated in a solution of 1 mM KI in 0.2 M Na_2SO_4 at room temperature when the applied laser energy was 9 mJ/pulse. The camera speed was 68 000 fps and the γ was 3.4. The scale bar in the figure is 1 mm. Note, the laser fires at -43 µs while bubble maximum is taken at 0 µs. The bubble reaches its first minimum between 44 and 58 µs (also indicated with *) and the second minimum is seen at 87 µs (labelled **). The red arrow indicates the forming jet.

In figure 6.2 the formation of the plasma is seen at -43 µs which is when the optical breakdown takes place and the camera is triggered. After the formation of the plasma the bubble starts growing reaching the maximum at about 0 µs (as the camera recorded pictures only every 14 or 15 µs, the moment of absolute maximum may not have been captured), after which it begins to collapse. The bubble minimum appears between 44 µs and 58 µs (also labelled with a *). After reaching the minimum the bubble rebounds

and a jet (indicated with a red arrow) is formed which can be seen at 58 μs. A blow up of this image is presented in figure 6.3 where the small jet forming on top of the bubble can be seen more clearly. The rebound is followed by a second collapse at 87 μs that is marked with **. A formation of a small counter jet can also be seen at 87 μs. During the series of images the bubble moves towards the solid surface as a result of Bjerknes forces.

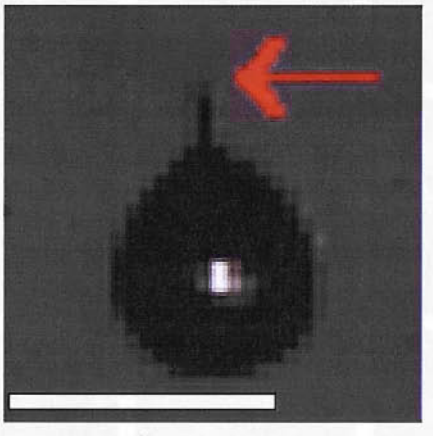

Figure 6.3 Blow up of the image taken at 58 μs (*) where the jet (indicated with the red arrow) is formed in figure 6.2. Images showing a bubble generated in a solution of 1 mM KI in 0.2 M Na_2SO_4 at room temperature when the applied laser energy was 9 mJ/pulse. The camera speed was 68 000 fps and the γ was 3.4. The scale bar in the figure is 0.5 mm.

In figure 6.4 the distance between the bubble and solid surface has been decreased and the γ is 2.0. Again, the moment of maximum bubble size is assigned to 0 μs. The minimum of the bubble is not captured as it is so short-lived. After the first collapse the jet formation (indicated with a red arrow) is clearly visible in the image that is taken at 58 μs (labelled *) and can also be observed at the following two (** and ***) images. The reason for this is the formation of a slightly larger bubble than in figure 6.2. Also, the bubble is now closer to the solid surface but at the same time still too far for the jet to cause any damage to the surface (γ = 2). The formation of the counterjet is also observable (indicated with a green arrow). The bubble collapses for the second time at ~116 μs, after which it quickly rebounds and collapses again (indicated with ◊). Throughout these events the bubble centre moves towards the surface of the electrode. In addition, a small residue of bubbles is observed below the electrode where the bubble has been.

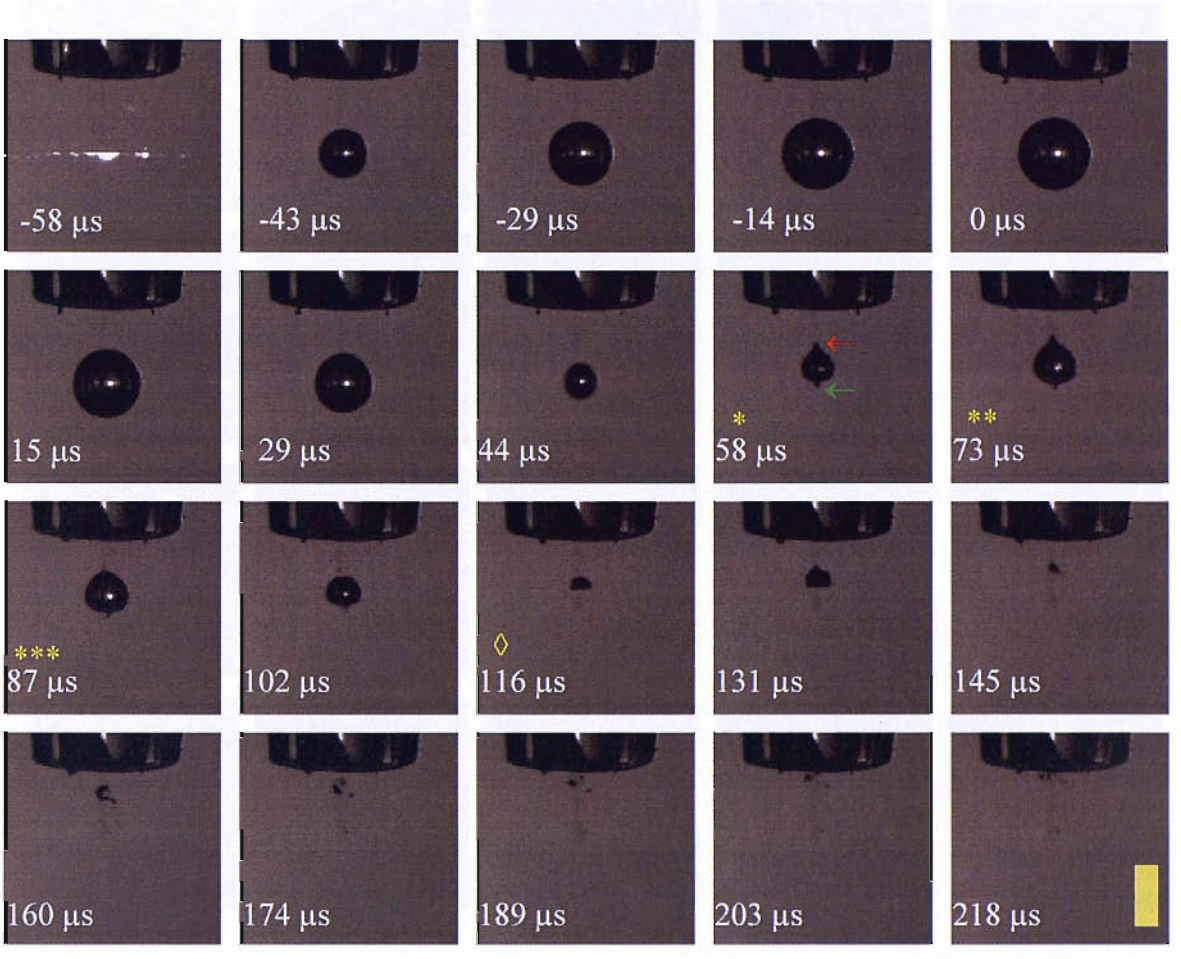

Figure 6.4 Images showing a bubble generated in a solution of 1 mM KI in 0.2 M Na_2SO_4 at room temperature when the applied laser energy was 9 mJ/pulse. The camera speed was 68 000 fps and the γ was 2.0. The scale bar in the figure is 1 mm. The liquid jet can be observed in frames labelled *, ** and *** when the bubble collapses and rebounds for the first time. The jet is also indicated with the red arrow. The green arrow indicates the counter jet forming on the side of the bubble opposite to the electrode surface. The secondary collapse can be seen in figure labelled with ◊.

Figure 6.5 presents the formation of a bubble when the γ is 1.5. The high-speed camera is triggered at -58 µs which is followed by the bubble formation. The bubble quickly grows and reaches its maximum at the image taken at 0 µs. After its maximum it begins to collapse and is seen to become slightly elongated before it collapses at 58 µs (also labelled with *). When the bubble rebounds, the tip of the jet appears to touch the surface of the electrode (indicated with a red arrow) and the bubble appears to be in contact with the electrode for the rest of its lifetime. A counter jet is also observed on the other side of the bubble (indicated with a green arrow). The second collapse occurs at 203 µs and rebounds again after that whilst attached to the surface.

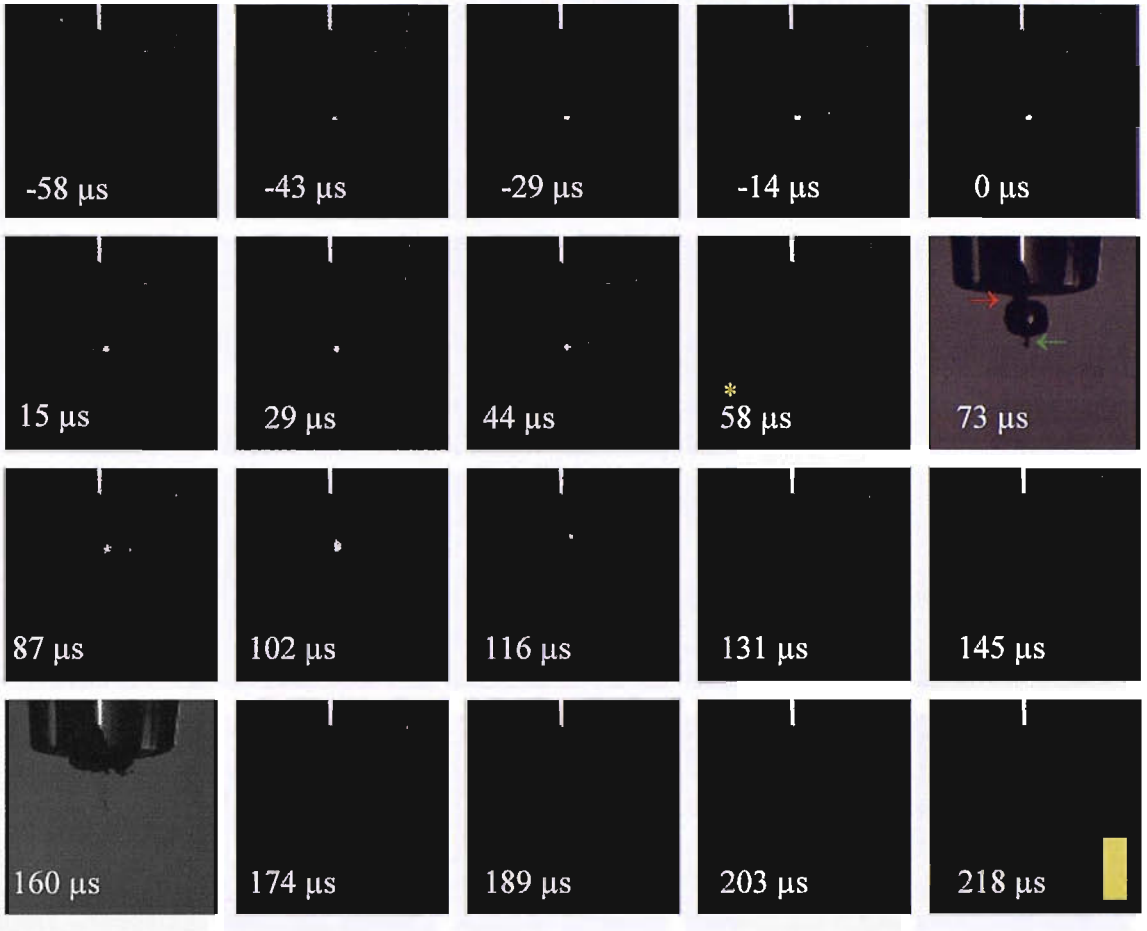

Figure 6.5 Images showing a bubble generated in a solution of 1 mM KI in 0.2 mM Na_2SO_4 at room temperature when the applied laser energy was 9 mJ/pulse. The camera speed was 68 000 fps and the γ was 1.5. The scale bar in the figure is 1 mm. The liquid jet can be observed in the frames labelled with * and it is also indicated with the red arrow. The green arrow indicates the counter jet forming on the side of the bubble opposite to the electrode surface.

The final set of high-speed images presented in section is seen in figure 6.6. For this set of images the γ is 0.5. At this value of the γ (<0.7) the liquid jet is thought to be partially responsible for the damage caused to the surface [21,30]. The bubble is now so close to the electrode that the surface of the bubble nearest to the electrode becomes flat as the bubble grows. A layer of liquid is sandwiched between the bubble and the electrode. When the bubble starts to collapse it becomes elongated and the collapse occurs at 58 µs (marked with *). In this case the formation of the liquid jet is not clearly observable as the bubble is attached to the surface of the electrode when it rebounds. After the first rebound the bubble collapses again, quickly reforms and then disappears leaving a cloud of small bubbles along the electrode surface.

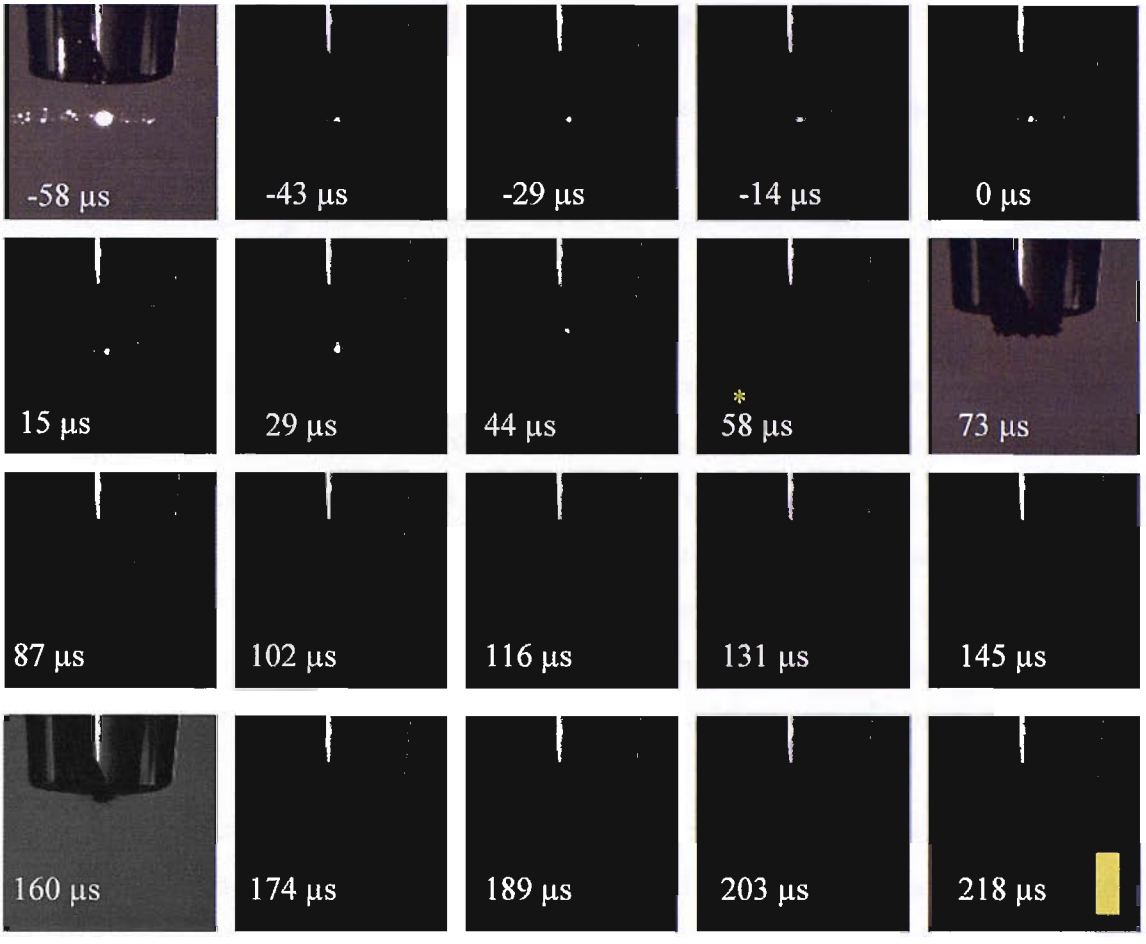

Figure 6.6 Images showing a bubble generated in a solution of 1 mM KI in 0.2 M Na_2SO_4 at room temperature when the applied laser energy was 9 mJ/pulse. The camera speed was 68 000 fps and γ was 0.5. The scale bar in the figure is 1 mm. The first minimum of the bubble is indicated with *.

Figures 6.2-6.6 presented high-speed images taken in a solution of 1 mM KI in 0.2 M Na_2SO_4 when the distance between the bubble centre and the electrode surface was gradually decreased. Very similar bubbles in size and shape were generated in each case and therefore it is easy to compare their behaviour. It can be clearly seen from the figures how value of γ affects the bubble dynamics. In the first set of high-speed images in figure 6.2 the liquid jet that is formed is very small and can only be observed in one image, and the bubble rebound and second collapse are rather symmetric. As the distance between the bubble centre and the solid surface decreases in the following figures, the forming jet becomes more prominent as seen in figures 6.4 and 6.5. It was observed from figures 6.5 and 6.6 that the bubble becomes elongated before collapsing for the first time and appears to be attached to the electrode surface after the collapse. These results aid understanding the electrochemical results reported in previous chapters and are a great basis for the CFD simulations that are presented in the following section.

6.2 CFD simulations for a bubble collapse

A CFD (computational fluid dynamics) code was written by colleagues (Graham Ball and Kylie Osman) to simulate bubble behaviour in the environment next to a solid/liquid surface (eg. the electrode). In CFD, numerical methods are employed to simulate the behaviour and interaction of fluids, gases and surfaces.

For the simulations presented in this chapter, the domain of the calculation went from -1.0cm to 1.56cm in the x direction and 0.0cm to 1.28cm in y. The mesh size was 4096x2048 so the resolution is 0.625um in both directions. The calculation was axisymmetric; the y_{min} boundary (ie. the x axis) was a reflective boundary and the other three boundaries were transmissive. The transmissive boundaries used a relaxing pressure boundary condition. This means that the pressure in the boundary cells is a proportion of the calculated pressure and a proportion of the input pressure.

The liquid water used a polynomial equation of state. The bubble in the calculations is water vapour. The surface as aluminium was modelled using a Balmoral equation of state and the Steinberg-Guinan strength model. The hydro code solves the compressible Euler equations using a lagrangian phase, where the grid is allowed to move with the material motion; and then a remap phase which returns the grid to the original Cartesian topology. A second order predictor-corrector method is used during the lagrangian phase to update the energy, density, velocity and stress fields. During the remap phase a second order upwind method is used except at material interfaces where the method drops to first order but the interface is explicitly tracked to prevent numerical diffusion of the materials. The data is stored on a staggered grid, with densities and energies at cell centres, velocities at cell vertices. To prevent oscillations around shock waves, an artificial viscosity is added to smear the shock waves over a few cells. A collection of relevant results are presented here.

For the CFD simulations, it was assumed that the bubble contained water vapour and the surrounding liquid was water. The initial conditions for the water vapour were pressure, p_v, of 23.744 kPa and density, ρ_v, of 5×10^{-6} g cm^{-3}. The surrounding water was thought to be at standard atmospheric conditions with a hydrodynamic pressure, p_w, of 101.3 kPa and density, ρ_w, of 0.9854 g cm^{-3}. The solid surface in the CFD simulated

was thought to consist entirely of pure aluminium which had the density, ρ_{Al}, of 2.7 g cm^{-3}.

In order to reduce the computing time the simulations were only run for one half of a bubble due to symmetry of the problem. In the first set of images (figures 6.7-6.10) the bubble density was plotted against time. The red colour represents the highest density whereas blue is the lowest (note the scale is valid also for figures 6.8-6.10 and shown in figure 6.7). Figure 6.7 presents an example of a bubble at its maximum. The red bar that has the highest density in the figure represents the solid surface. In the CFD simulations, this is pure aluminium and on the high-speed images the tip of the electrode. A high-speed image of a bubble at its maximum that has been rotated 90° is also presented in the figure. Unlike the rest of the images of simulations, this figure presents the whole bubble. This is the phase in bubble life where all the simulations were started, as the growth phase of the bubble is assumed not to cause damage to the surface and is therefore not significant. Therefore, only the bubble collapse and the associated jet formation were simulated along with the bubble rebound and secondary collapse as the source of damage to the surface are the forming jet and the shock waves emitted during collapse. The letters A and B indicate the different sides of the bubble, A being the side of the bubble furthest from the solid/liquid interface and B the side of the bubble that is closest to the solid/liquid interface. These terms will be used throughout this section to refer to the different bubble sides.

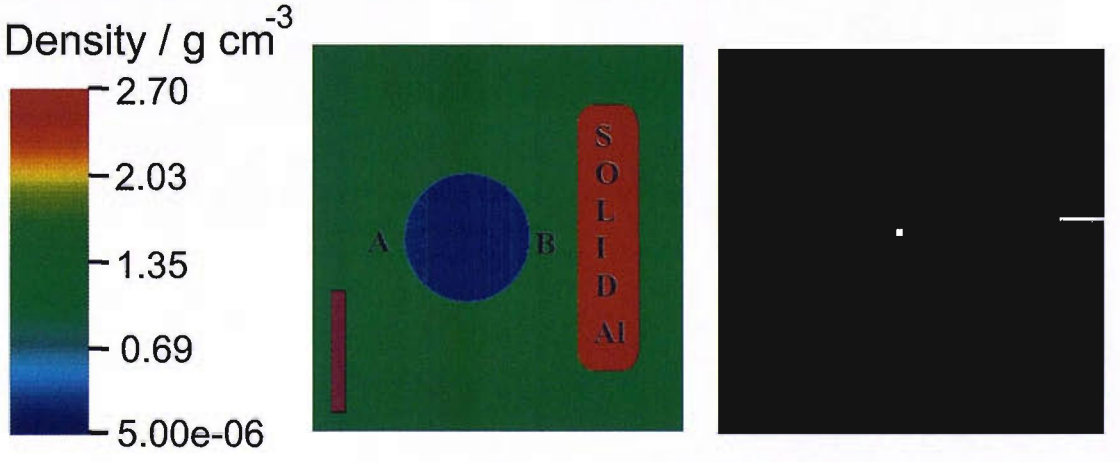

Figure 6.7 A computer simulated cavitation bubble at its maximum when the γ is 1.8 and a high-speed image of a bubble when when the γ is 1.5. The purple scale bar in the figure is 1 mm. A and B indicate the different sides of the bubble.

Figure 6.8 presents the simulation for the bubble from its maximum in figure 6.6 until the first collapse as a function of density. Because $\rho_v << \rho_w$, no variation is seen at the density of the bubble. In all the simulations presented in this chapter time starts when the bubble is at its maximum (see figure 6.6). The first collapse of the bubble in the simulations occurs at the same time as in high-speed images in figures 6.2-6.7, where the bubble reached its minimum between 44 μs and 58 μs (there was always 14-15 μs between each image at the employed camera speed 68 000 fps. Up to 40 μs the simulated images are presented every 10 μs. From 45 μs to the first minimum time between the images is only 1 μs as the motion of the bubble collapse becomes much faster at this stage and this region is of particular interest. The collapse is symmetric and the bubble maintains its spherical shape until 48 μs. From 48 μs onwards, the bubble is no longer a sphere. A liquid jet caused by higher pressure on side A than side B results in the formation of a jet that is seen to travel through the bubble. The jet-like shape is clearly observable when the bubble reaches its minimum at 50 μs in the final image in figure 6.8. The simulations presented here thus far match perfectly with the high-speed images that were presented in figure 6.5.

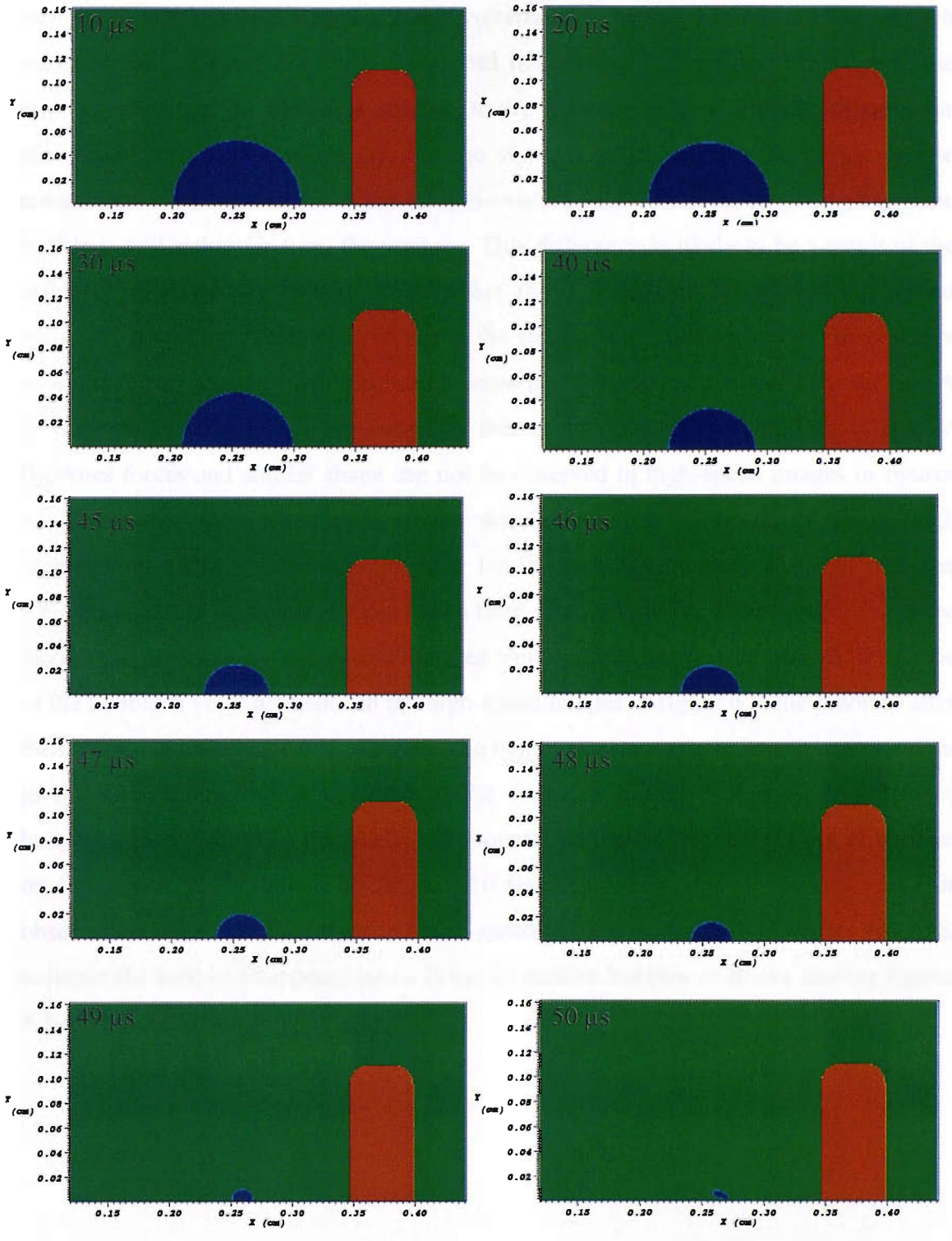

Figure 6.8 Figures showing computer simulated cavitation bubble when density of the bubble was plotted against time from its maximum until the first collapse when the $\gamma$is 1.8.

Figures 6.9 and 6.10 present the events after the first and second collapse of the bubble, respectively. After each collapse the bubble quickly rebounds, and the liquid jet is now visibly approaching the electrode surface (indicated by a yellow arrow in figure 6.9). The tip of the jet moves towards the electrode as the bubble first grows rapidly, finally

touching it at 80 μs, and then the bubble collapses for the second time at 130 μs which matches well with the time-scale high-speed images (see figure 6.5). However, in the high-speed images the bubble is attached to the electrode surface when it collapses for the second time at about 130 μs. In the simulations, the movement of the bubble towards the electrode surface is almost non-existent, and during the second collapse the bubble is still rather far from the surface. This difference is likely to be a result of the influence of buoyancy forces, which affect the experimental (bubble in high-speed images) but was not taken into account in the simulations. Also, from 100 μs onwards in figure 6.9 an anomaly that has been pointed by a pink arrow can bee seen on side A of the simulated bubble. The origin of this is unknown but it could be related to Bjerknes forces and similar shape can not be observed in high-speed images in figures 6.2-6.6. After the second collapse the simulated bubble rebounds in figure 6.10, regaining its shape. The maximum size for this bubble is observed at 170 μs, after which the bubble begins to collapse and a third minimum is simulated at 210 μs. Even though the time scale of the events matches well with the high speed images, the shape of the bubble is very different. In the high-speed images in figure 6.5, the rebound after the collapse is observable at 174 μs, but the bubble does not regain its shape like it does in the simulations, but is flattened to the electrode surface. Again, the effect of buoyancy forces could be responsible. A counter jet can be seen as a string of bubbles on the side A of the bubble in figure 6.10 (indicated with an orange arrow). This observation again matches with the high-speed images in figure 6.5. After the final collapse the bubble disappears into a cloud of smaller bubbles as it was seen in figures 6.2-6.5 but not in the simulations.

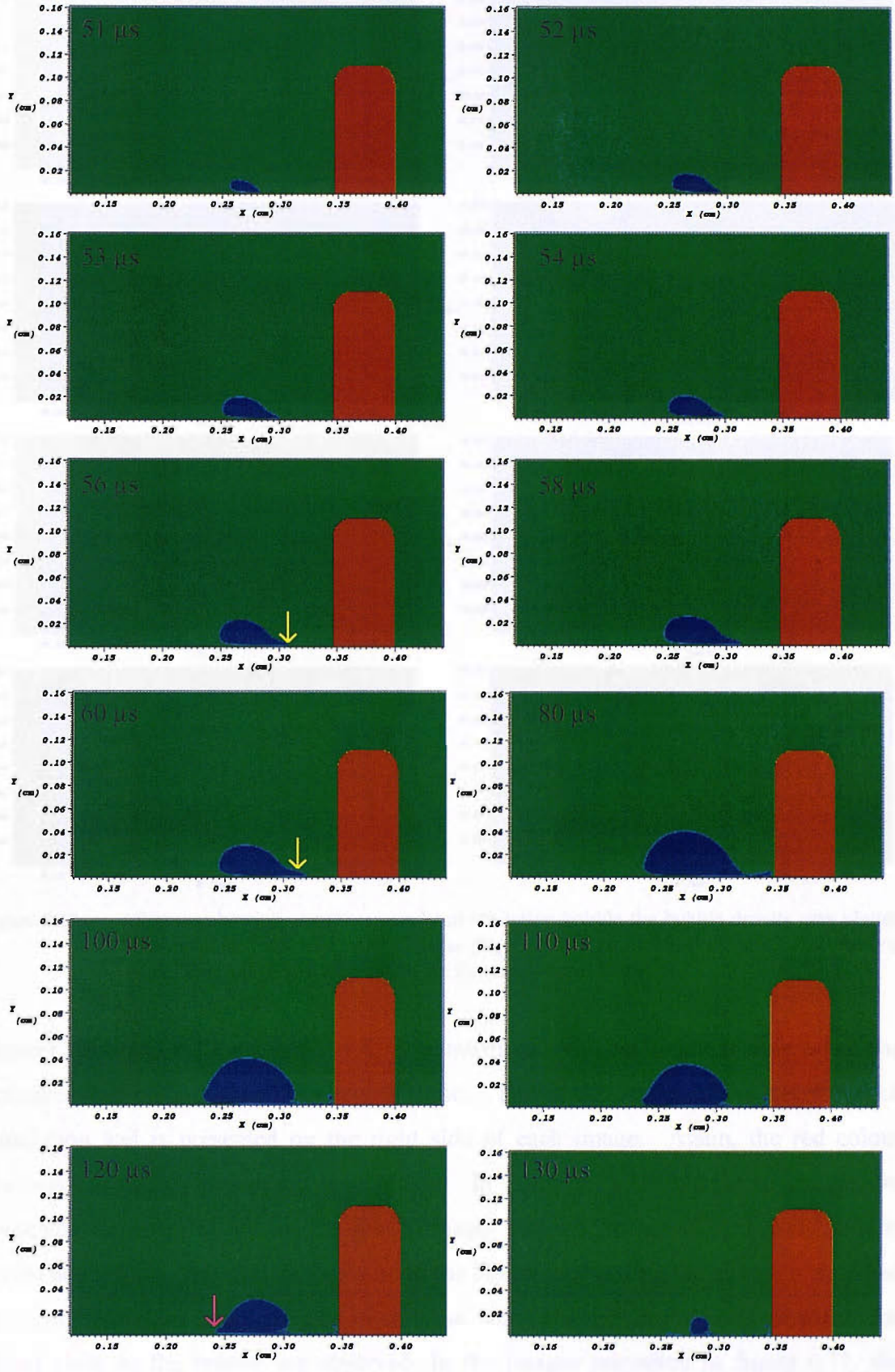

Figure 6.9 Figures showing computer simulated cavitation bubble when the bubble density was plotted against time from its first collapse (figure 6.8) until the second collapse when the γ is 1.8. Then yellow arrow indicates the formation of the liquid jet. The pink arrow indicates the anomaly seen in the bubble shape.

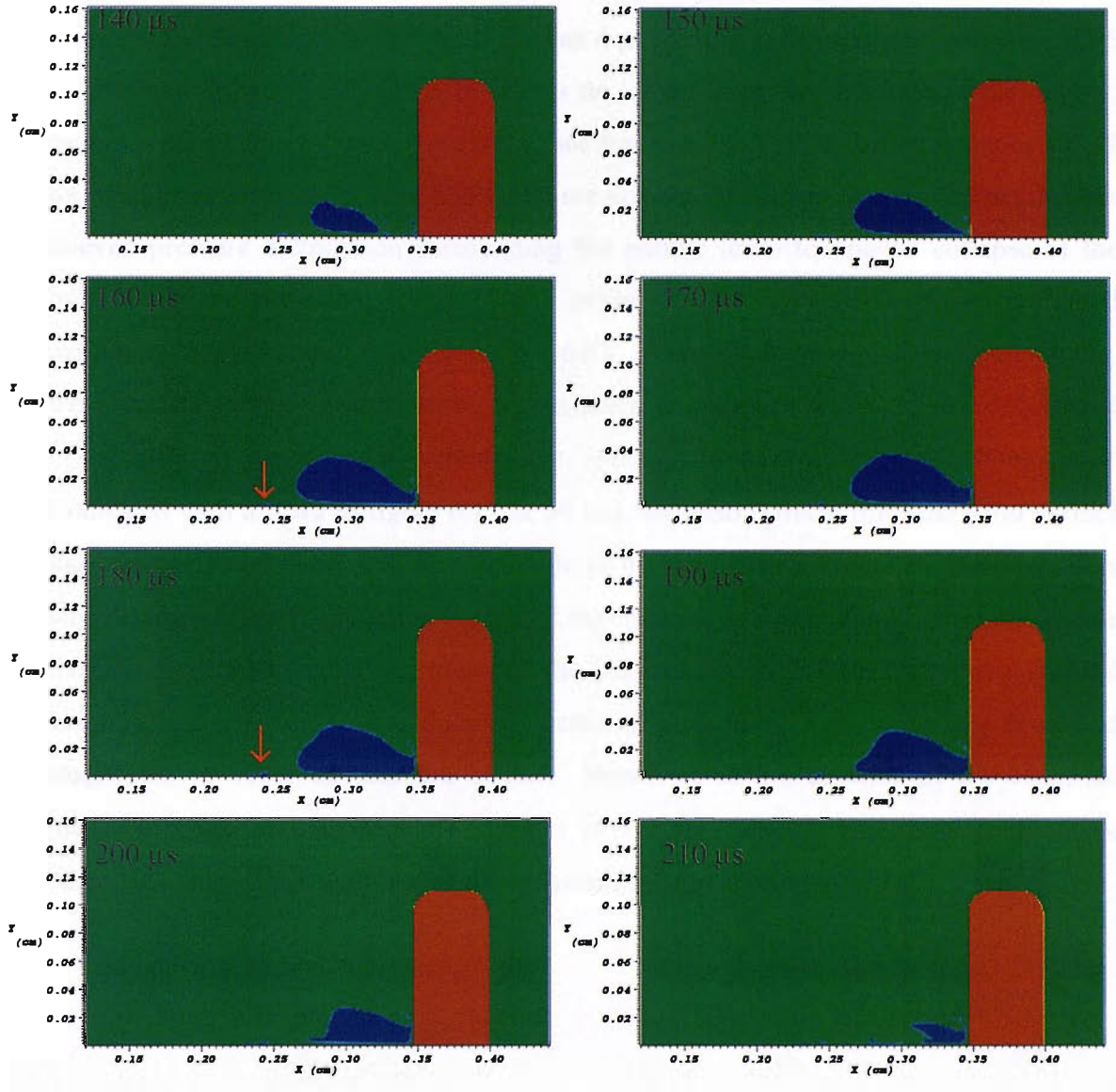

Figure 6.10 Figures showing computer simulated cavitation bubble the bubble density was plotted against time from its second collapse (figure 6.8) until the third collapse when the γ is 1.8. The orange arrows indicate the formation of a counter jet.

Figures 6.11 and 6.12 present the CFD simulations of a cavitation bubble when the pressure was plotted as a function of time. The scale bar is individual for each simulation and is presented on the right side of each image. Again, the red colour presents the highest value and blue lowest. In figure 6.11 the simulated images are presented for every 10 µs for the first 5 images and for the last two images the time difference is 5 µs. At 0 µs, the pressure in the liquid surrounding the bubble is assumed uniform. When the bubble begins to collapse, some changes in the pressure within the liquid close to the bubble are observed. In the images presented in figure 6.11, the pressure is even in each direction from the bubble and the bubble collapses symmetrically on each side.

Figure 6.12 presents the pressure for the last 4 μs leading to the primary collapse. At 46 μs the pressure surrounding the bubble is no longer even on each side of the bubble; higher pressure is present on the side A (see figure 6.7). This is further enhanced at 47 μs, where pressures as high as 484.4 kPa are present. As it has been stated before, this uneven pressure distribution surrounding the bubble leads to uneven collapse of the bubble and jet formation, which is also evident in the high-speed images presented earlier on in this chapter (see figures 6.2-6.6). When the bubble reaches its minimum, the simulations also clearly show the existence of pressure waves of up to 4.3 MPa (15.9 MPa in the collapse centre) that spread circularly from the bubble centre (indicated with arrows in figure 6.12 at 50 μs), and also reflects from the solid surface near the collapsed bubble. The magnitude of the simulated pressure of these waves is slightly higher than the pressure measured experimentally in chapter 5. One should note that the hydrophone used to measure the pressure in the experiments was situated behind the electrode and was therefore partially blocked by it resulting in a decreased magnitude of observed pressure events. However, in the absence of the electrode pressure pulses of the order of 2.5 MPa at ~ 4 mm from the collapse centre were detected. This agrees with the implications of these simulations.

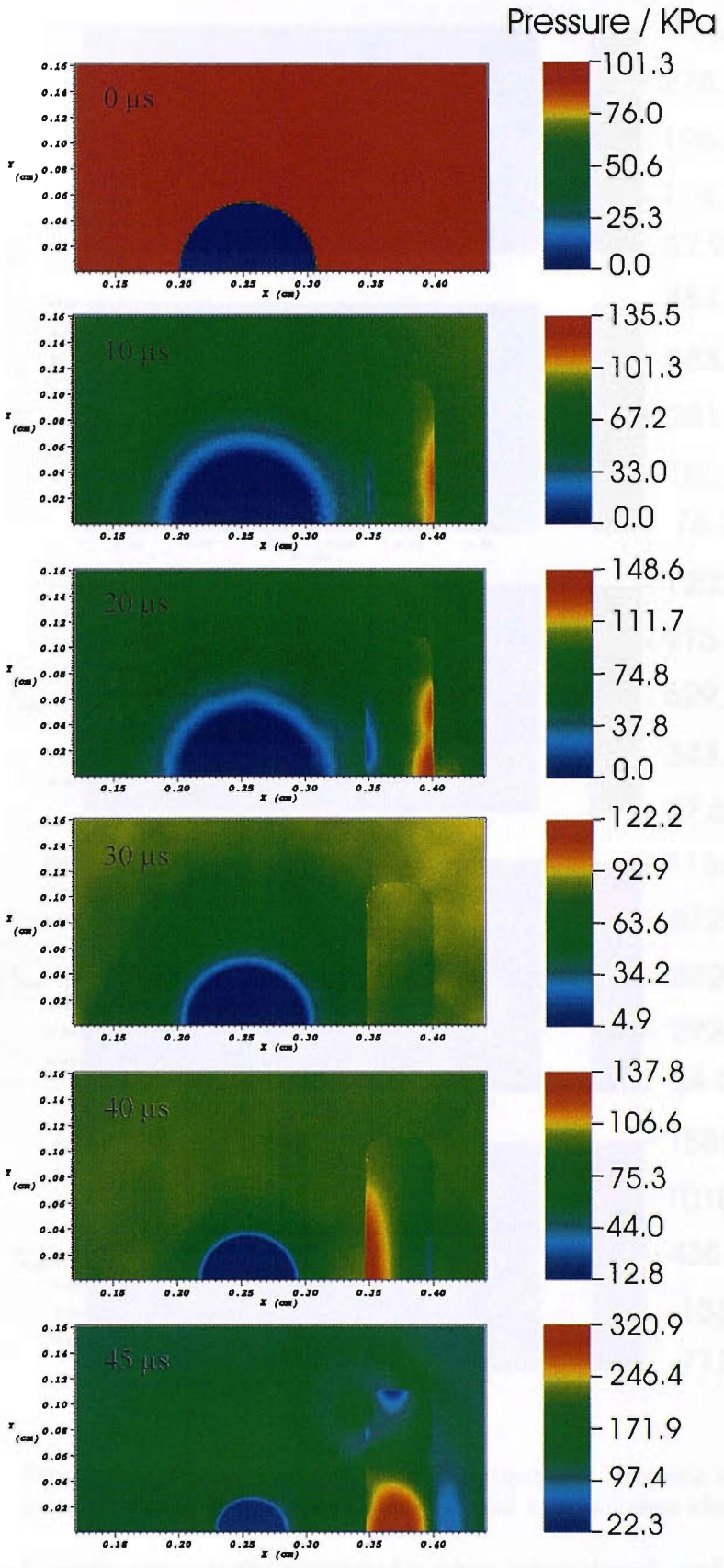

Figure 6.11 Figures showing the computer simulated collapse when the pressure was plotted against time for the first 45 µs after its maximum when the $\gamma$is 1.8.

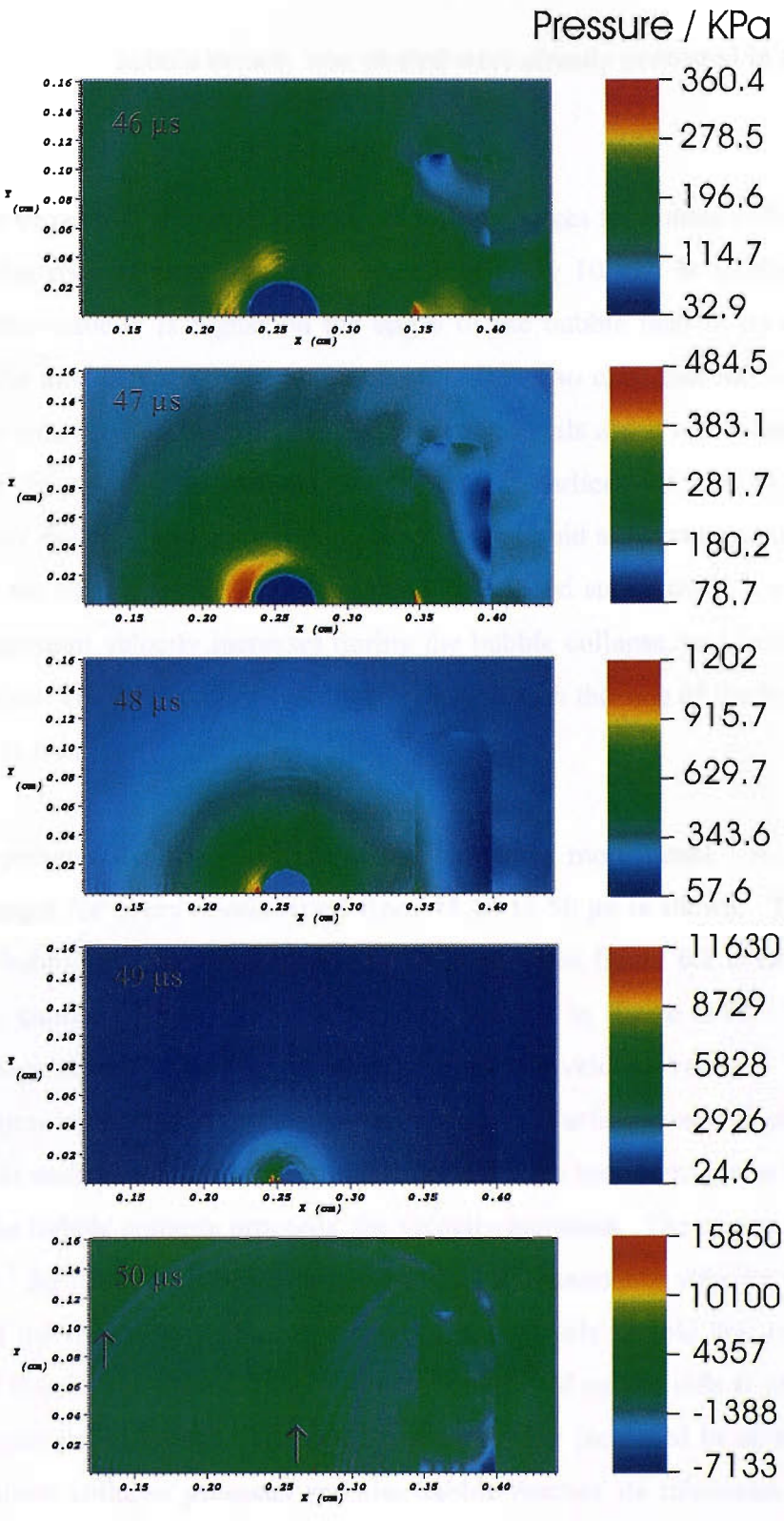

Figure 6.12 Figures showing the computer simulated collapse of a cavitation bubble when the pressure was plotted against time from 46 µs until it first collapses when the $\gamma$is 1.8.

The next set of images presents the simulated bubbles when density and velocity were plotted as a function of time. The velocity is presented as vectors on top of the simulated bubble. The emphasis in these figures lies within the velocity as the

simulations where the bubble density was plotted were already presented in figures 6.7-6.10.

In the first set of simulated images in figure 6.13, the images for bubble collapse for the first 40 μs after its maximum size are presented at every 10 μs. In all the images in figure 6.12, the velocity is higher on the edges of the bubble than in its centre. The direction of the flow is towards the bubble centre. It is also clear that the velocities are greater on the side A of the bubble (see figure 6.7 for details about side A and B) that is furthest away from the solid surface. As was stated earlier, this side of the bubble collapses faster due to higher pressure gradient in the liquid surrounding the bubble on that side. In the first image at 10 μs, the maximum speed simulated is 2 m s^{-1}. This simulated maximum velocity increases during the bubble collapse, and in the image at 40 μs the highest velocity is 15 m s^{-1} which is observed on the side of the bubble where the liquid jet is forming.

Figure 6.14 presents the first collapse of the bubble in more detail. A close-up of simulated images for every microsecond from 45 μs to 50 μs is shown. The distance between the bubble and the solid surface is the same as in figure 6.8 even though the solid surface cannot be seen in these close-up images in figure 6.14. The higher resolution image makes it easier to observe the simulated velocity vectors. Throughout the collapse process the bubble moves towards the solid surface due to Bjerknes forces as was seen in earlier simulated images 6.8-6.12 and high speed images in figures 6.2-6.6. When the bubble collapse proceeds, the velocity increases. The maximum velocity is 30-45 m s^{-1} for the first three images. At 48 μs the maximum velocity increases to 70 m s^{-1} and the direction of the velocity vectors is clearly visible due to the higher resolution of this image. The highest velocity is observed on the side B of the bubble where the liquid jet is formed. The velocities are further increased to up to 200 m s^{-1} when the bubble collapse proceeds and the bubble reaches its minimum. After the minimum the bubble rebounds which is seen in figure 6.15 with the predicted maximum velocity 200 m s^{-1} at 52 μs. However, on average the simulated velocities have the value within the region of 50-100 m s^{-1} with most of the vectors now pointing away from the centre of the bubble towards the direction of the expansion. As the bubble grows further, the velocities drop and the maximum of 25 m s^{-1} is suggested at 110 μs. When the bubble collapses for the second time at 130 μs, the speed of fluid flow

increases again and gains the highest value 100 m s^{-1}. The direction of the flow is towards the centre of the bubble as can be expected with the highest values present on the side A of the bubble.

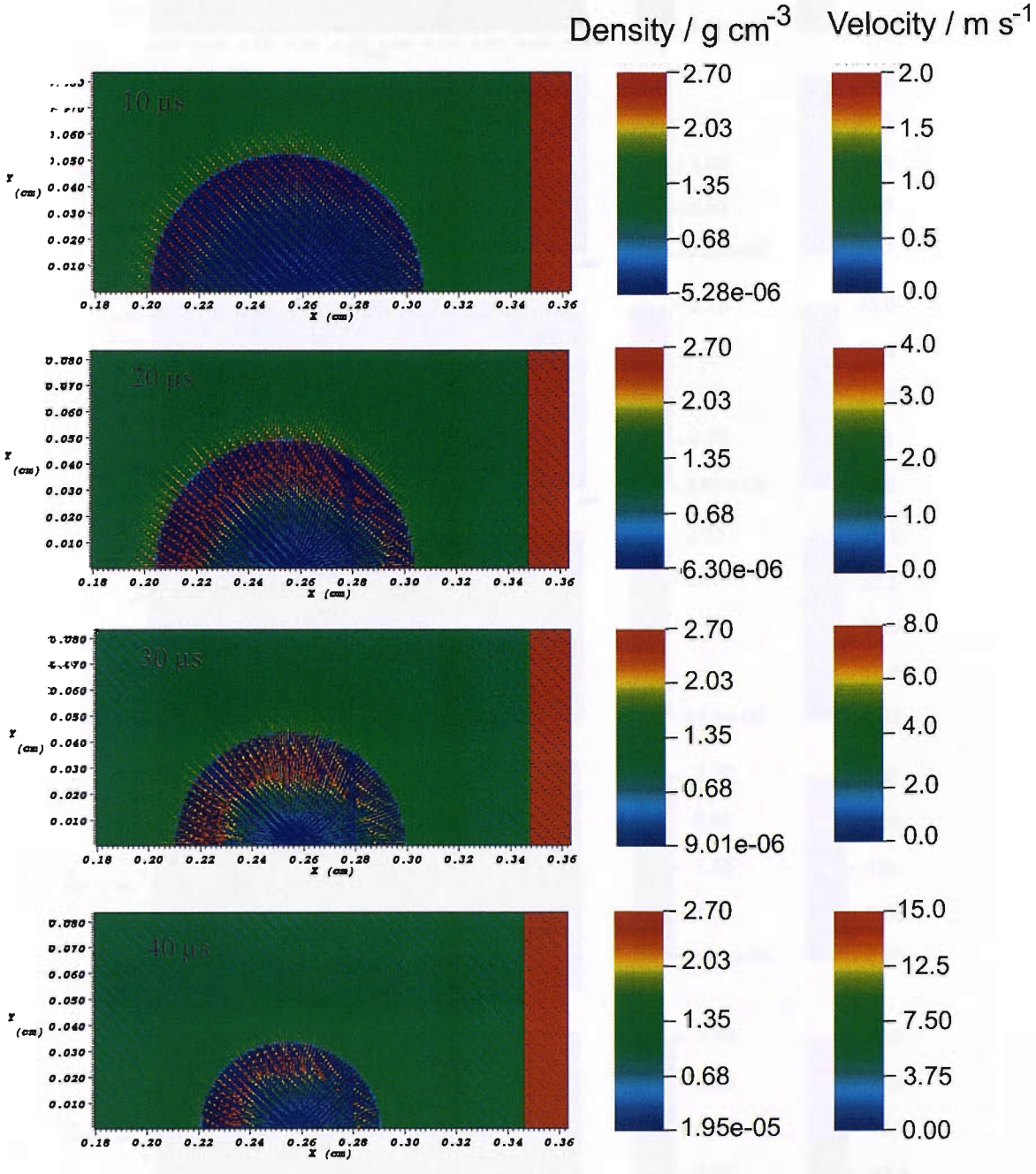

Figure 6.13 Figures showing the computer simulated collapse of a cavitation bubble when density and velocity were plotted from 10 µs to 40 µs when the γ is 1.8.

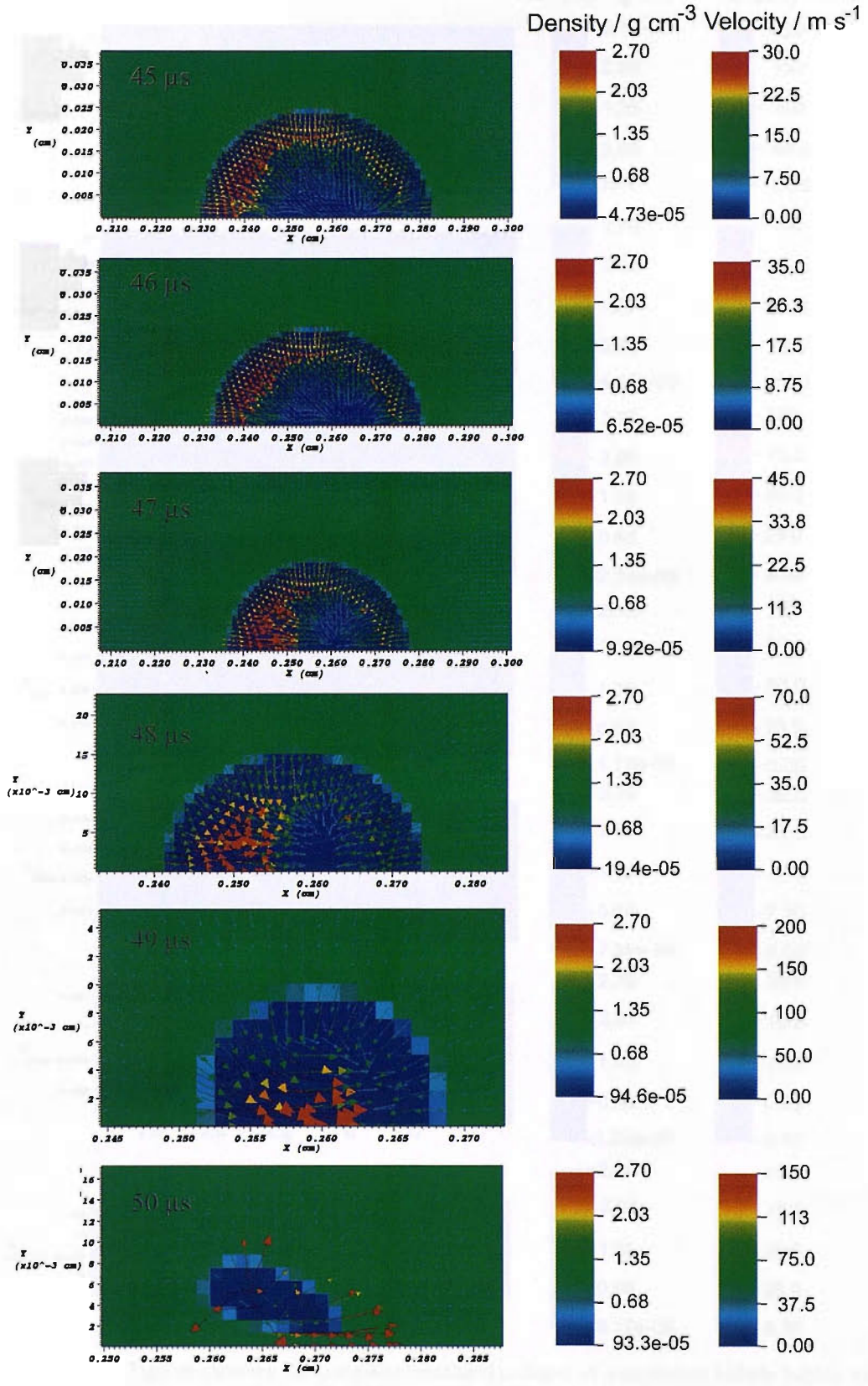

Figure 6.14 Figures showing the computer simulated collapse of a cavitation bubble bubble when density and velocity were plotted from 45 µs until 50 µs where the bubble collapses for the first time when γ is 1.8.

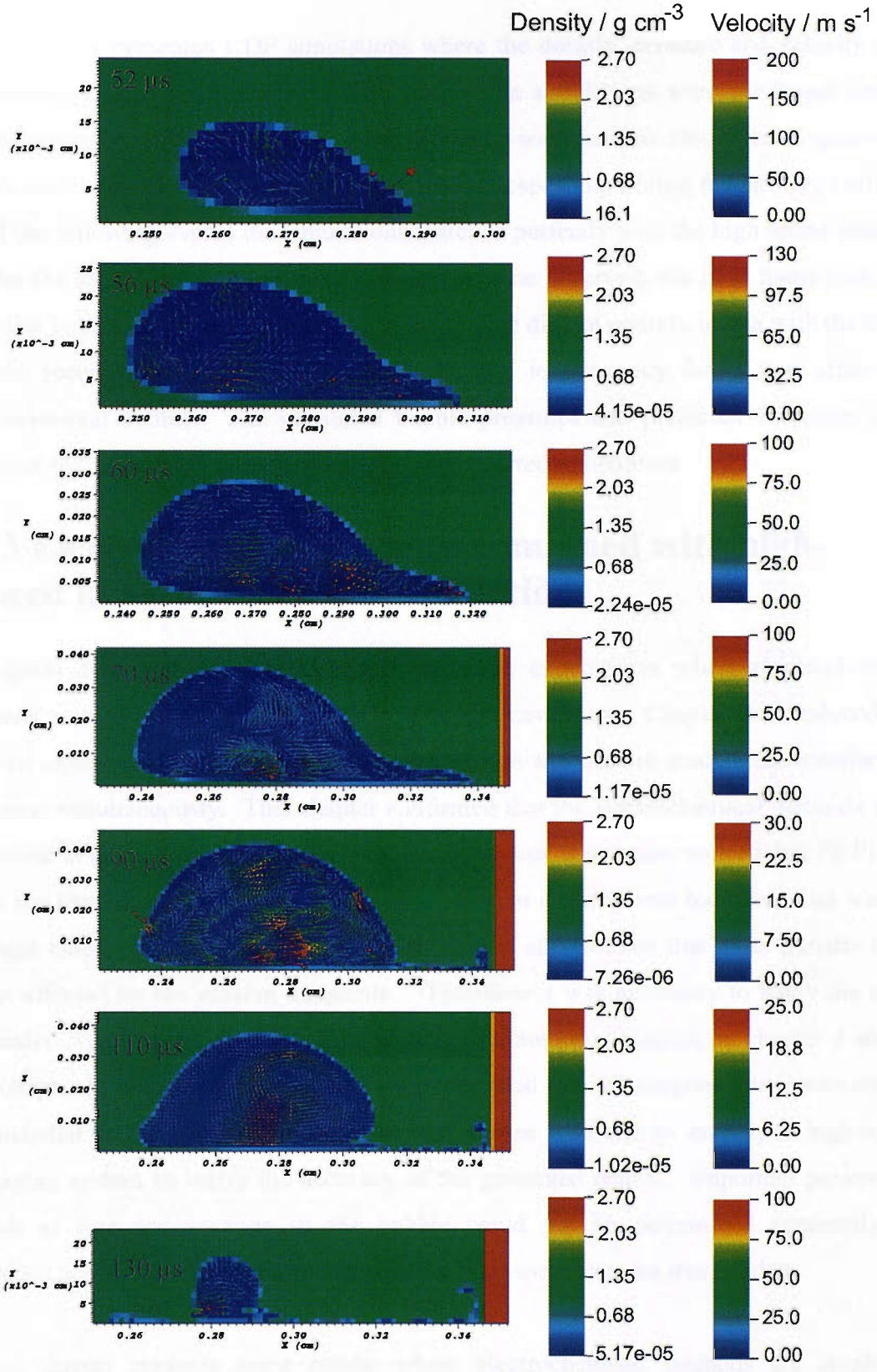

Figure 6.15 Figures showing the computer simulated collapse of a cavitation bubble bubble when density and velocity were plotted from its first collapse until the second collapse when the $\gamma$is 1.8.

This chapter presented CDF simulations where the density, pressure and velocity of a cavitation bubble were plotted against time. The simulations were run based on the experimental results where high-speed imaging was used to record laser generated cavitation events in this thesis. It was noted that especially during the primary collapse and the following events the simulations matched perfectly with the high-speed images. After the secondary collapse some differences were observed; the time frame was still similar but the shape and the location of the bubble did not entirely match with the high-speed recordings. This was thought to be due to buoyancy forces that affect the experimental bubble. The simulated bubble pressures and predicted velocities were similar to those observed experimentally and reported in literature.

6.3 Electrochemical methods combined with high-speed imaging and CFD simulations

Chapters 3, 4 and 5 presented results from the experiments where electrochemical means were employed to study laser generated cavitation. Chapter 3 introduced the initial experiments where the Pb/Pt microelectrode was used to study mass transfer and erosion simultaneously. This chapter confirmed that the electrochemical methods were suitable to study laser generated cavitation. However, it was also noticed that Pb/Pt was not the ideal electrode material (lead as an erosion detector was too slow) and was no longer employed in the in other chapters. It was also noticed that mass transfer trace was affected by the erosion transients. Therefore it was necessary to study the mass transfer events in the absence of the erosion detector (Au electrode in chapter 4 and Pt in chapter 5). Some excellent results were presented in these chapters, but it was always concluded at the end of each chapter that it was essential to employ a high-speed imaging system to verify the accuracy of the presented results. Important parameters such as size and location of the bubble could not be determined accurately by electrochemical means alone and therefore a high-speed camera was needed.

This chapter presents some results where electrochemical methods are employed simultaneously with high-speed imaging. The electrode systems covered are Au in the solution containing 5 mM $K_4Fe(CN)_6$ in 0.2 M $Sr(NO_3)_2$, Pt in a solution containing 1 mM KI in 0.2 Na_2SO_4 and Pt/Al in solutions containing either KI or $K_4Fe(CN)_6$ in Na_2SO_4.

This chapter also presents some CFD simulations that were developed to compare the high-speed photographic images obtained experimentally. The bubble in the images was formed in the solution containing $K_4Fe(CN)_6$ in Na_2SO_4. Simulations where the variable was density, pressure or velocity were plotted against time are presented together with high-speed images and electrochemical data for the bubble in question.

6.3.1 Mass transfer on Au microelectrode with high-speed images

Chapter 4 covered experiments where a 25 μm Au microelectrode was employed to study mass transfer events caused by the growth and collapse of laser induced cavitation bubbles. In the experiments presented in chapter 4 the 25 μm diameter gold microelectrode was employed in a solution containing 5 mM $K_4Fe(CN)_6$ in 0.2 M $Sr(NO_3)_2$. If the potential of the electrode is held at >+0.3 V vs. SCE mass transfer limited oxidation of the $Fe(CN)_6^{4-}$ species occurs at the microelectrode surface. At this potential, a steady state oxidation current of ~12 nA is applied on the electrode surface. Any perturbation of this diffusion field, produced through, for example, the forced convection of fluid due to bubble motion was detected as an enhanced current at the microelectrode. When the electrode was close to the bubble surface, a large 400 nA current was observed (see chapter 4 figure 4.7). Moving the electrode gradually away from the surface resulted in decreased current on each step because the mass transfer enhancement is very distance dependent. When the bubble was far away from the surface of the electrode or a small bubble was generated, the recorded current transient was smaller than when the bubble was close to the surface or a big bubble was formed. Also, when the distance between the bubble and electrode was increased, the response time of the electrode increased. In order to confirm whether all these electrochemical observations were reliable it was necessary to repeat some of them simultaneously with high-speed imaging system.

Figure 6.15 presents the simultaneously recorded high-speed images and electrochemical transient for the mass transfer on a 25 μm Au microelectrode in a

solution that contained 5 mM $K_4Fe(CN)_6$ in 0.2 M $Sr(NO_3)_2$ when γ[‡‡] was 2.9. The recording speed of the high-speed camera was 68 000 fps and the Q-switch delay of the Continuum Inlite laser was set to 330 μs which corresponds to a laser energy of 7 mJ/pulse. The employed high-speed camera (Photosonics Phantom v7) was damaged at the time when the images were taken and only one quarter of the available image size was useful. Therefore, the images are slightly blurry in comparison to the images 6.2-6.6 where the same camera and recording rate were employed.

Figure 6.16 resents the simultaneously recorded high-speed images and mass transfer transient for a bubble in exactly the same conditions as the bubble in figure 6.15 when γ was 1.3.

When the figures are compared, it is clear that the bubble in figure 6.15 is a lot smaller than the bubble in figure 6.16. The bubble in figure 6.15 grows and collapses far from the electrode without ever coming to contact with its surface. However, the bubble is close enough to the electrode for it to affect its collapse pattern and the bubble collapses unevenly forming a jet that travels towards the surface. The surface of the bubble in figure 6.16 on the other hand is only ~0.3 mm from the electrode and during its rebound after the first collapse the bubble is actually attached to it.

The difference in bubble size results in very different electrochemical transients seen in figures 6.15 and 6.16. In figure 6.15, the steady state current is present on the electrode surface before the optical breakdown occurs at 0 μs and also for the next 750 μs after it. This is followed by a slow rise in the recorded current when the fluid motion caused by the bubble activity affects the diffusion field surrounding the electrode. The current reaches its maximum at 1300 μs and remains at this level for the rest of the recorded time. Similar results were reported earlier in chapters 3, 4 and 5 where it was observed that after the bubble activity the mass transfer current slowly decayed back to the steady state level. It was concluded that this happened because of the relaxation of the diffusion field. In figure 6.16 the current starts rising much earlier, at 400 μs. The maximum current has the magnitude of 100 nA and it appears at 500 μs. The current rises more rapidly than in figure 6.15 which indicates that the generated bubble is larger

[‡‡] $\gamma = s/R_{max}$, where s is the distance between the bubble centre and the electrode surface and R_{max} the maximum bubble radius.

and has an increased effect on the diffusion field around the electrode. It should be noted that the microelectrode is now closer to the focal spot of the laser beam, and the effect of the growing bubble on the hemispherical diffusion field is therefore larger.

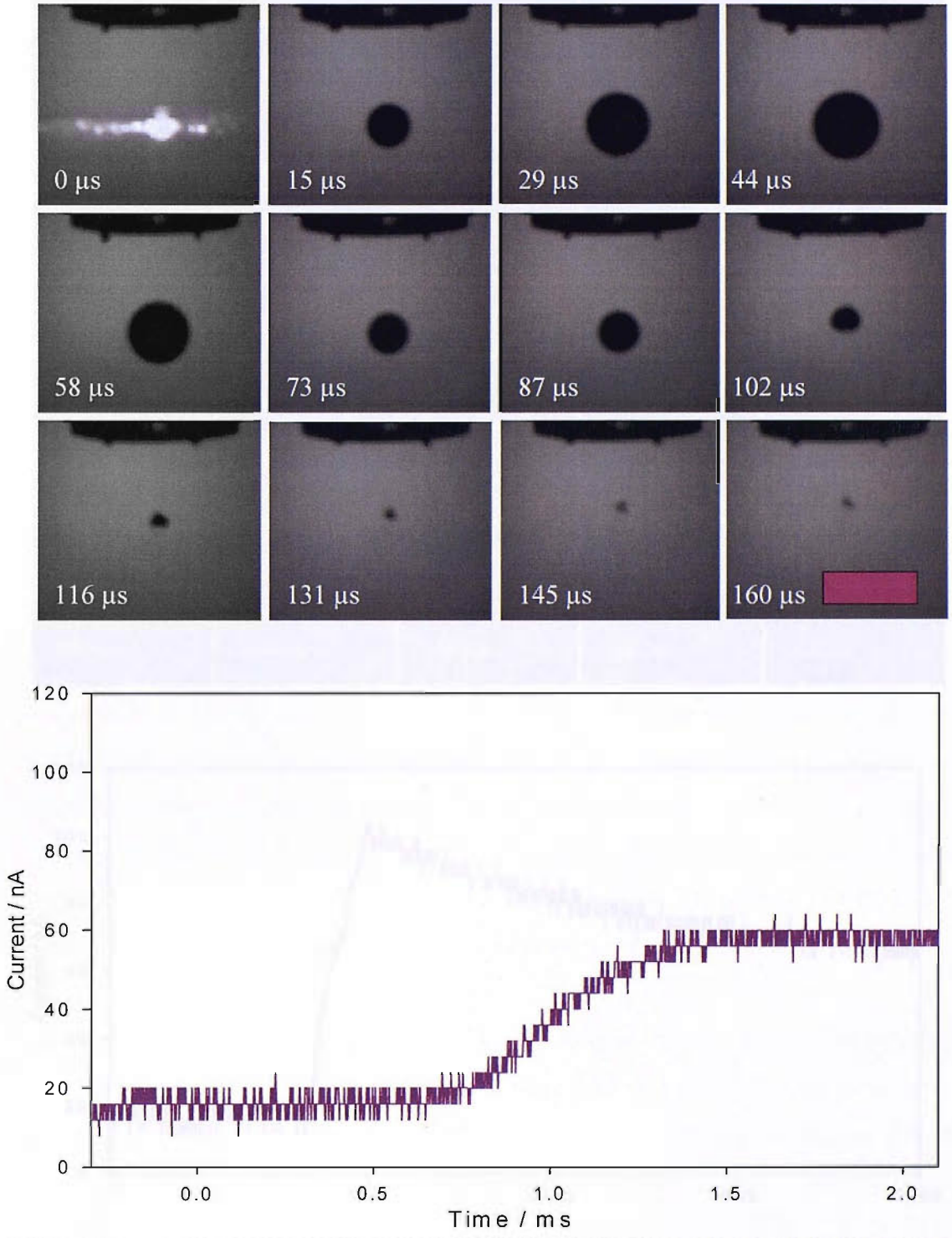

Figure 6.15 Images showing the generated bubble and simultaneously recorded electrochemical transient on 25 µm Au microelectrode in a solution of 5 mM $K_4Fe(CN)_6$ in 0.2 M $Sr(NO_3)_2$ at room temperature when the applied laser energy was 7 mJ/pulse. The camera speed was 68 000 fps. γ is 2.9. The scale bar in the figure is 1 mm.

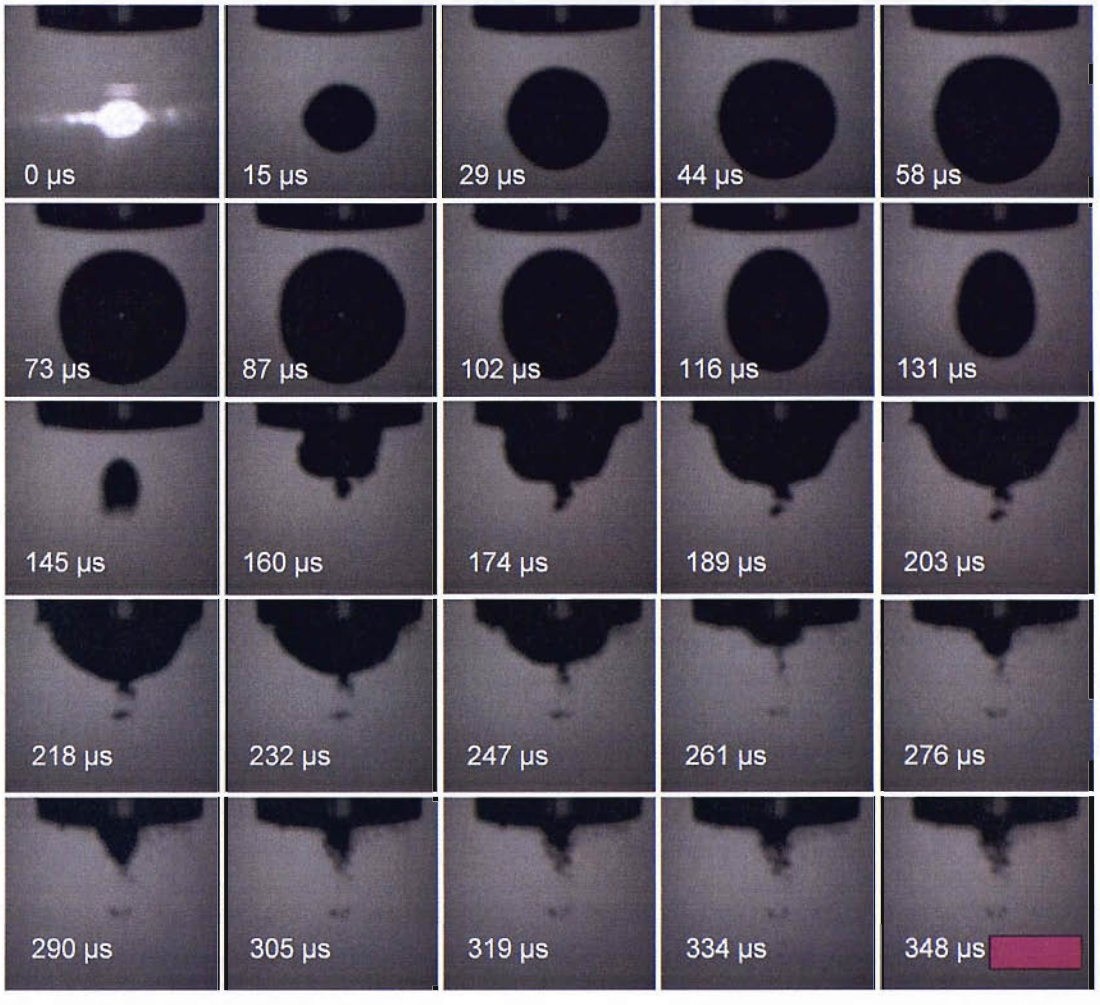

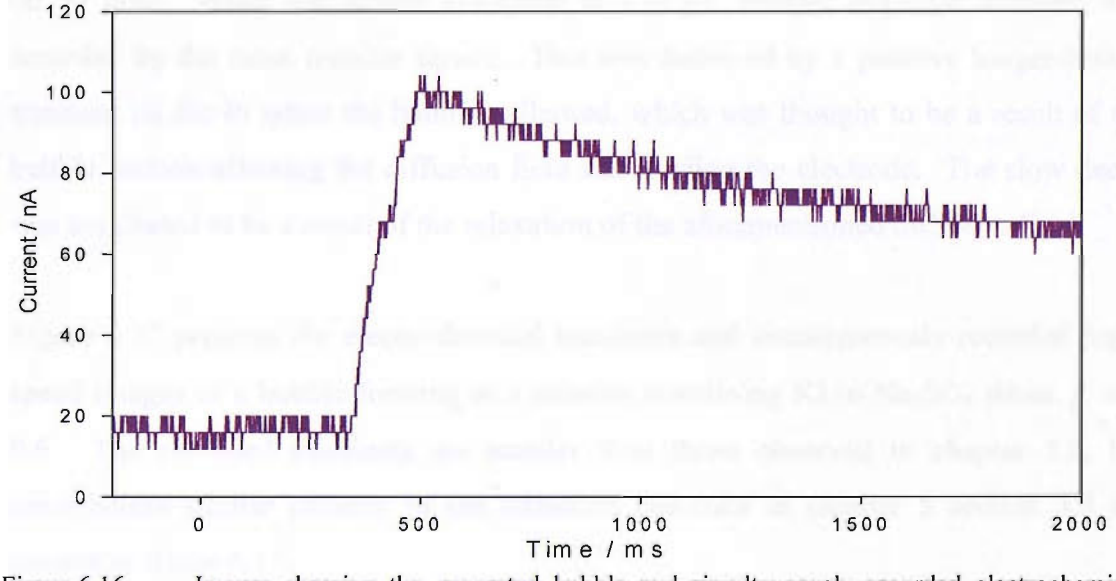

Figure 6.16 Images showing the generated bubble and simultaneously recorded electrochemical transient on 25 µm Au microelectrode in a solution of 5 mM $K_4Fe(CN)_6$ in 0.2 M $Sr(NO_3)_2$ at room temperature when the applied laser energy was 7 mJ/pulse. The camera speed was 68 000 fps and γ is 1.3. The scale bar in the figure is 1 mm.

6.3.2 Mass transfer on Pt and erosion on Al with simultaneous high-speed imaging

Section 5.3 in chapter 5 covered in detail experiments where a Pt/Al dual electrode was employed to simultaneously record mass transfer and cavitation events in a solution containing 1 mM KI in 0.2 M Na_2SO_4. In all cases the potential of both electrodes was held at +0.6 V *vs.* SCE. This corresponds to the mass transfer limited potential for the oxidation of I^- at the Pt surface while the Al electrode is maintained in a passive state (for details, see chapter 5).

When this electrode system was employed, a large positive peak was observed on the erosion sensor when the optical breakdown occurred. Simultaneously, a negative transient was recorded by the mass transfer sensor. When the bubble collapsed, a smaller positive transient was observed on the aluminium electrode detecting the erosion events. This transient had a shape different from the peak that occurred at the optical breakdown; the rise of the second peak was much slower and after reaching its maximum it slowly decayed back to the 0 A level. This was discussed in detail in chapter 5. It was also observed that the mass transfer signal interacted with the simultaneously recorded erosion signal. In section 5.3 a large negative transient was observed on the Pt electrode at the same time when a large positive peak was observed on Al disc. When the bubble collapsed at 150 μs, another negative transient was recorded by the mass transfer sensor. This was followed by a positive longer-lasting transient on the Pt when the bubble collapsed, which was thought to be a result of the bubble motion affecting the diffusion field surrounding the electrode. The slow decay was concluded to be a result of the relaxation of the aforementioned diffusion field.

Figure 6.17 presents the electrochemical transients and simultaneously recorded high-speed images of a bubble forming in a solution containing KI in Na_2SO_4 when γ was 0.6. The recorded transients are smaller than those observed in chapter 5.3, but nevertheless similar patterns to the transients recorded in chapter 5 section 5.3 are present in figure 6.17.

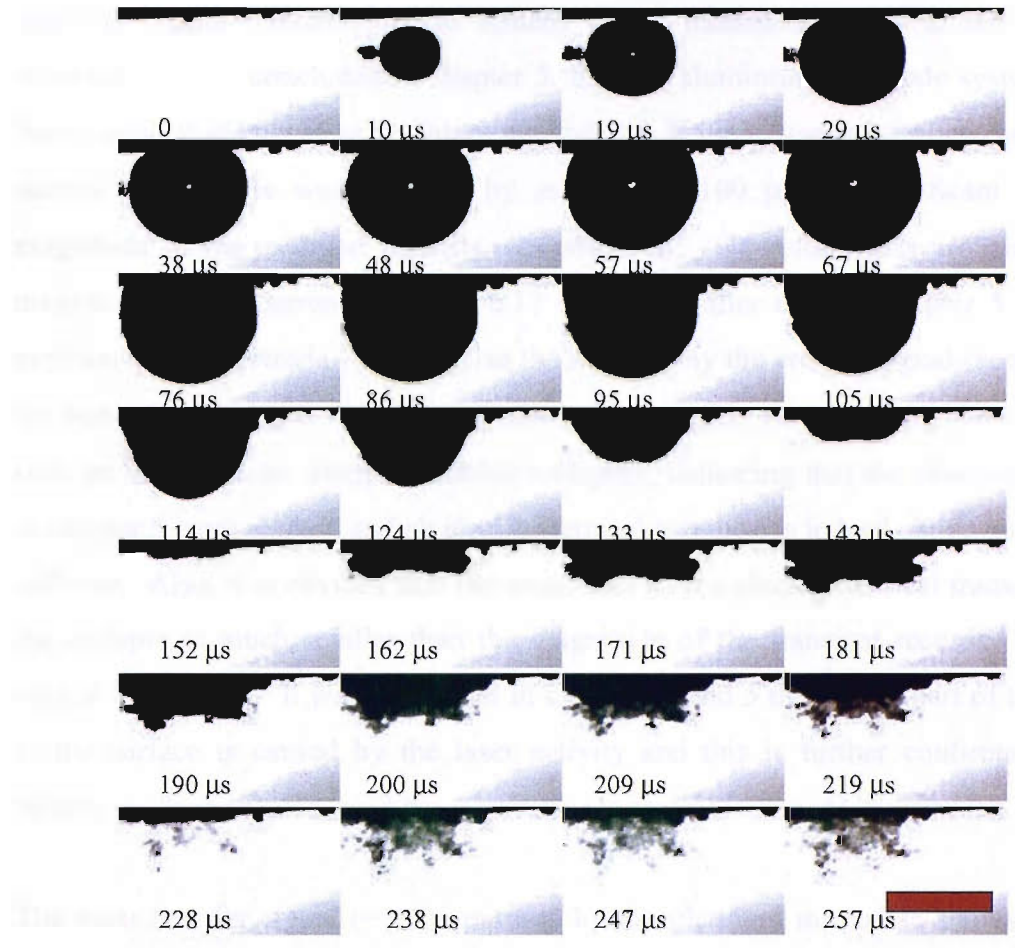

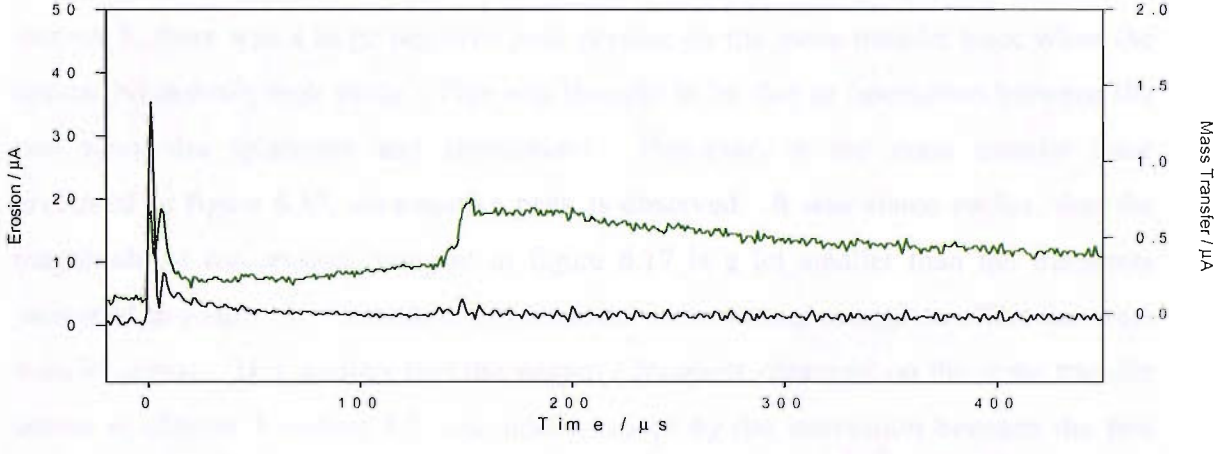

Figure 6.17 Plots showing a) high-speed images when the frame rate was 105 000 fps and b) simultaneously recorded mass transfer on 50 µm Pt (——) and erosion on 250 µm Al (——) electrodes when exposed to laser cavitation events in 0.2 M Na_2SO_4 containing 1 mM KI at room temperature. The laser energy was 11.5 mJ/pulse. Scale bar in the picture is 1 mm.

In figure 6.17, on the aluminium electrode (——), when the optical breakdown takes place at 0 µs, a large positive transient is observed. However, the magnitude of this transient is much smaller (35 µA) than the magnitude of transient observed in chapter 5

with the similar electrochemical system where transients of up to 0.4 mA were recorded. It was concluded in chapter 5, that the aluminium electrode system used to detect erosion events is very distant dependant. If the distance between the electrode surface and bubble was changed by as little as 100 μm, a significant impact on magnitude of the recorded currents was observed. Therefore, it is probable that the magnitude of the current in figure 6.17 is a lot smaller than in chapter 5 due to the position of the electrode. This is also the reason why the erosion signal recorded when the bubble collapses at 150 μs is almost unobservable. Nevertheless, some activity is seen on the electrode when the bubble collapses, indicating that the observations made in chapter 5 were correct, and an electrochemical response is indeed observed during the collapse. Also, it is obvious that the magnitude of the electrochemical transient during the collapse is much smaller than the magnitude of the transient recorded during the optical breakdown. It was concluded in chapters 3 and 5 that a vast part of the damage to the surface is caused by the laser activity and this is further confirmed in these results.

The mass transfer signal (——) monitored by the platinum microdisc shows a positive transient at 0 μs when the optical breakdown occurs. In the experiments presented in chapter 5, there was a large negative peak present on the mass transfer trace when the optical breakdown took place. This was thought to be due to interaction between the two electrodes (platinum and aluminium). However, in the mass transfer trace presented in figure 6.17, no negative peak is observed. It was stated earlier, that the magnitude of the erosion transient in figure 6.17 is a lot smaller than the transients presented in chapter 5. Therefore, this transient is not strong enough to affect the mass transfer signal. This implies that the negative transient observed on the mass transfer sensor in chapter 5 section 5.3 was indeed caused by the interaction between the two electrodes. After the positive events at 0 μs the recorded trace begins to return towards the steady state condition. This process is interrupted when another event is recorded by the mass transfer sensor at 150 μs when the bubble collapses. The signal starts rising reaching its maximum 0.75 μA at the same time when the bubble minimum is recorded by the high-speed camera. After the peak the signal remains above 0.6 μA for another 100 μs before it starts decaying back towards the steady state level. This is due to bubble activity (rebound and further collapse) on the electrode surface. It is only after

these events that the hemispherical diffusion field surrounding the electrode can slowly reform which is seen as the ceasing current in figure 6.17.

In figure 6.18 the position of the electrode is 140 μm above the position in figure 6.17. In previous chapters 3-5 it was reported that the change in the position of the electrode affected the magnitude of the recorded transients significantly. To confirm the accuracy of these results some of the experiments were repeated when the high-speed video camera was present. In figure 6.18 the γ is 0.82. In the high-speed images in figure 6.17 the bubble was touching the surface of the electrode from 29 μs onwards and was attached to it for the rest of its growth and collapse phases. In figure 6.18 the bubble is slightly smaller and further away from the electrode surface and therefore it becomes attached to the surface of the electrode only from 57 μs onwards. This has a direct impact on the electrochemical transients recorded. The transient recorded at the aluminium disc (——) when the laser fires at 0 μs is less than a quarter in magnitude of the transient recorded in figure 6.17. No erosion transients are recorded when the bubble collapses which according to the high-speed images takes place at 130 μs. A small positive transient (——) is recorded by the mass transfer sensor when the laser fires. The influence of the bubble collapse is recorded by the platinum electrode, but just like with the Au disc in chapter 4, the electrochemical transient is present later in time than the actual bubble collapse. The current starts rising at 160 μs, 30 μs after the bubble minimum was recorded by high-speed video camera. The current continues to rise up until the maximum 0.5 μA until 205 μs, after which it decays, only to return to 0.5 μA at 265 μs. The first maximum is caused by the first minimum of the bubble, after which the bubble rebounds and collapses for the second time as seen from the high-speed images.

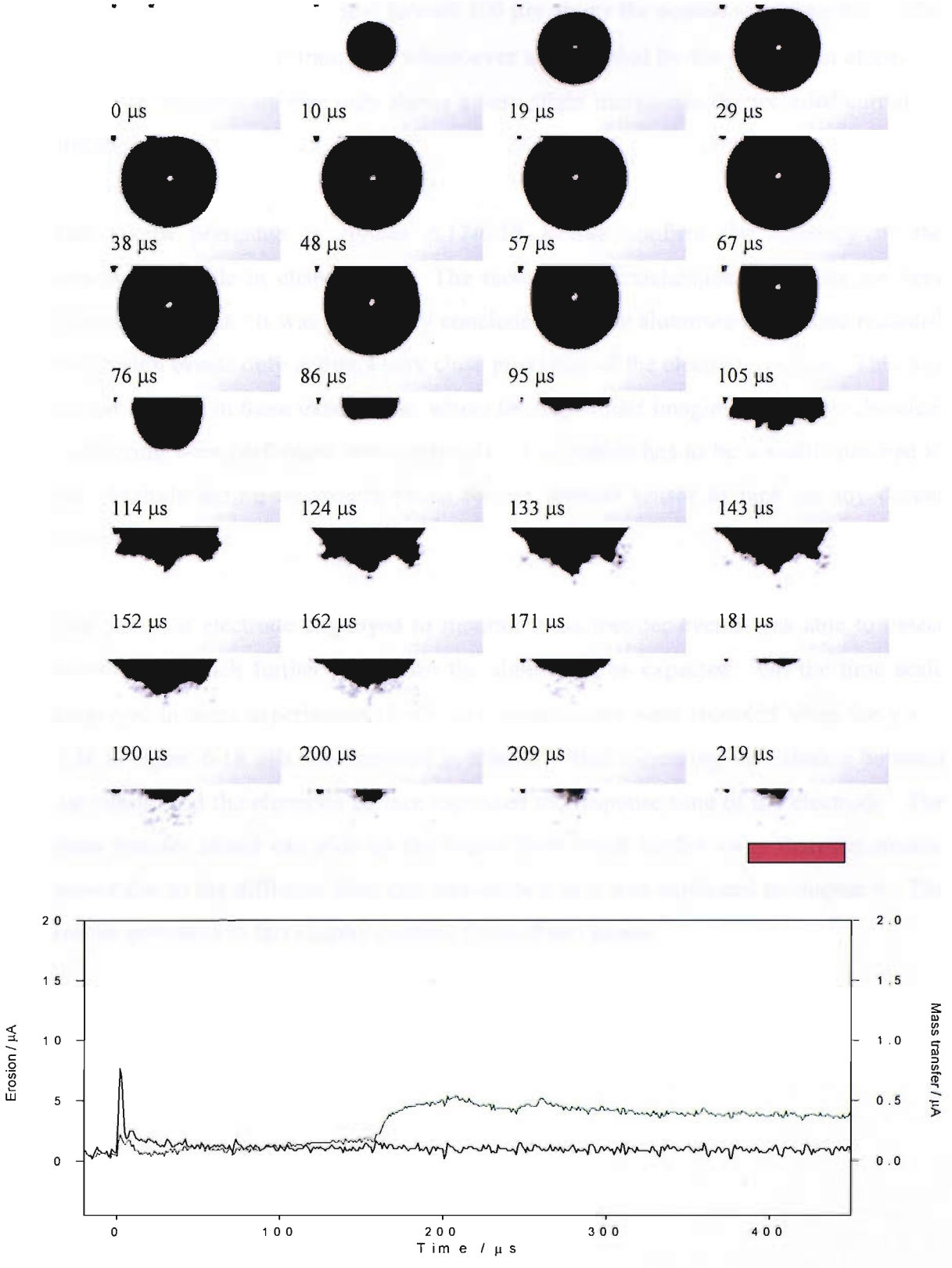

Figure 6.18 Plots showing a) high-speed images when the frame rate was 105 000 fps and b) simultaneously recorded mass transfer on 50 µm Pt and erosion on 250 µm Al electrodes when exposed to laser cavitation events in 0.2 M Na_2SO_4 containing 1 mM KI at room temperature. The position of the electrode was 140 µm above the position in figure 6.17. The laser energy was 11.5 mJ/pulse. Scale bar in the picture is 1 mm.

In figure 6.19 the bubble is now formed 500 μm above the position in figure 6.17. The value for γ is 2.38. No transients whatsoever are recorded by the aluminium electrode, and even the platinum disc only shows a very slight increase in the recorded current at 300 μs.

The results presented in figures 6.17-6.19 further confirm the accuracy of the conclusions made in chapters 3-5. The recorded electrochemical transients are very distant dependant. It was previously concluded that the aluminium electrode recorded the erosion events only within a very close proximity of the electrode surface. This was further verified in these experiments where the high-speed imaging and electrochemical monitoring were performed simultaneously. The bubble has to be actually attached to the electrode during its growth phase for the erosion sensor to pick up any decent erosion transients.

The platinum electrode employed to monitor mass transfer events was able to detect events from much further away than the aluminium as expected. On the time scale employed in these experiments (0-450 μs), some events were recorded when the γ was 2.38 in figure 6.18. It was reported in chapter 4 that increasing the distance between the bubble and the electrode surface increased the response time of the electrode. The mass transfer sensor can pick up the events from much further away than the erosion sensor due to the diffusion field that surrounds it as it was explained in chapter 4. The results presented in this chapter confirm those observations.

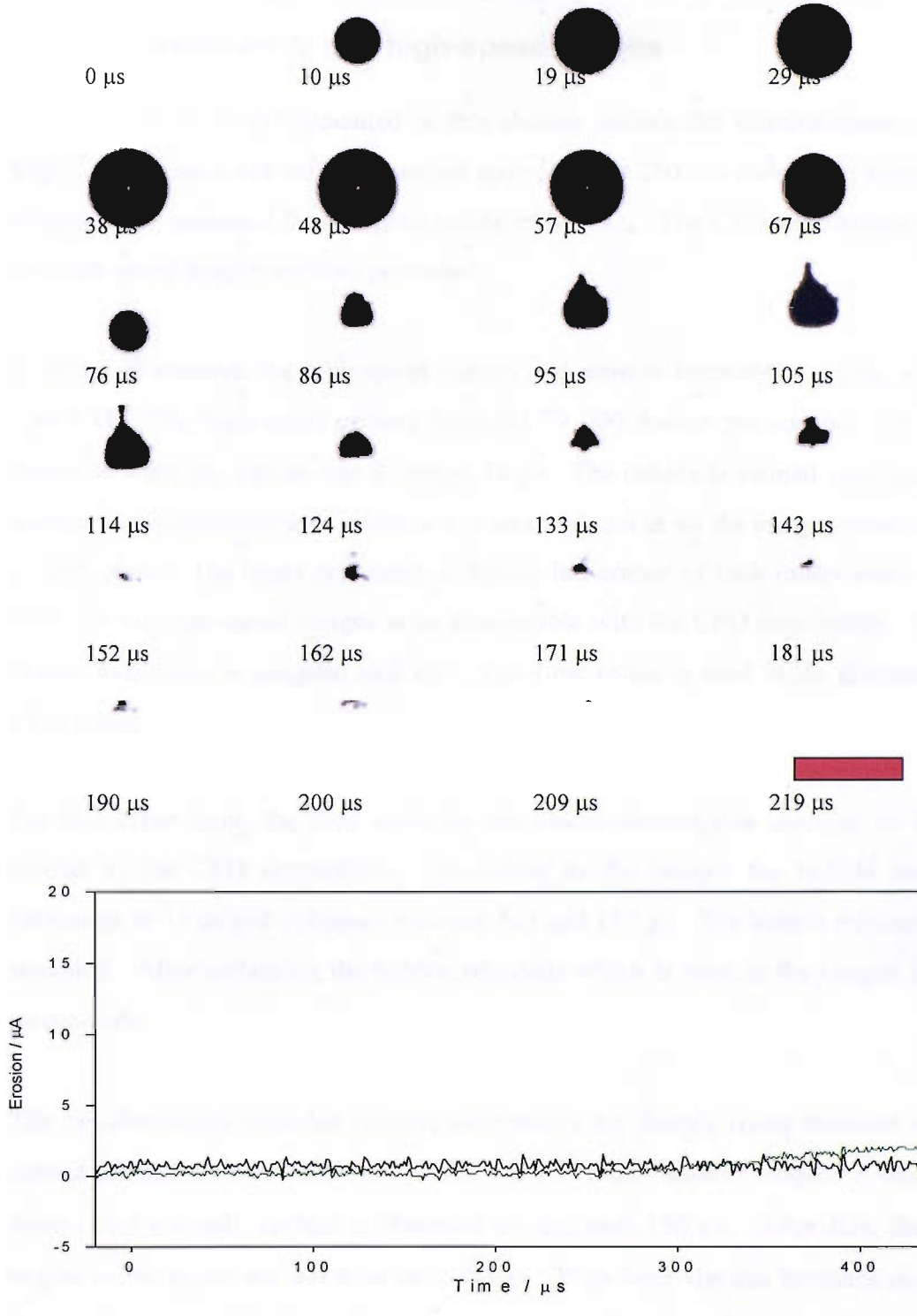

Figure 6.19 Plots showing a) high-speed images when the frame rate was 105 000 fps and b) simultaneously recorded mass transfer on 50 µm Pt and erosion on 250 µm Al electrodes when exposed to laser cavitation events in 0.2 M Na_2SO_4 containing 1 mM KI at room temperature. The position of the electrode was 140 µm above the position in figure 6.17.The laser energy was 11.5 mJ/pulse. Scale bar in the picture is 1 mm.

6.3.3 Erosion, high-speed imaging and CFD simulations

6.3.3.1 Erosion on Al and high-speed images

The final set of results presented in this chapter include the simultaneously recorded high-speed images and erosion transient recorded by a 250 μm aluminium electrode in a solution that contained 5 mM ferrocyanide in Na_2SO_4. The CFD simulations based on the high-speed images are also presented.

Figure 6.20 presents the high-speed images and erosion transient when the value of γ was 0.42. The high-speed camera recorded 70 000 frames per second, and the time frame between the frames was therefore 14 μs. The bubble is formed very close to the surface of the electrode and therefore it is attached to it in all the images taken during its growth phase. The times presented in the top left corner of each image were added in order for the high-speed images to be comparable with the CFD simulations. Note, the bubble maximum is assigned to 0 μs. This time frame is used in the discussion with CFD images.

For this experiment, the time scale for the electrochemistry is changed so that it is similar to the CFD simulations. According to the images the bubble reaches its maximum at 71 μs and collapses between 143 and 157 μs. The bubble minimum is not recorded. After collapsing the bubble rebounds which is seen in the images from 157 μs onwards.

The simultaneously recorded erosion trace shows the sharply rising transient when the optical breakdown takes place at -70 μs. As previously seen in chapter 5, this quickly decays and a steady current is observed for the next 150 μs. After this, the current begins to rise again, but this time very slowly. 20 μs later, the rise becomes steeper and the transient takes the shape familiar from chapter 5. According to these images, the erosion transient reaches its maximum 20 μs after the bubble is at its minimum. However, an error of up to 10 μs could be present in the results. Note that the second image of the series at 0 μs and portrays a picture of a bubble that has already started expanding. However, in previous figures 6.17-6.19 the first image of the series showed no bubble at all at -70 μs. This implies that due to the finite frame speed an error is

apparent in the timing of the frames in figure 6.20. Nevertheless, the shape of the transient that occurs when the bubble collapses is similar to those recorded in chapter 5. In chapter 5 it was concluded that this peculiar shape of the transient was a result of the plastic formation on the surface of the electrode.

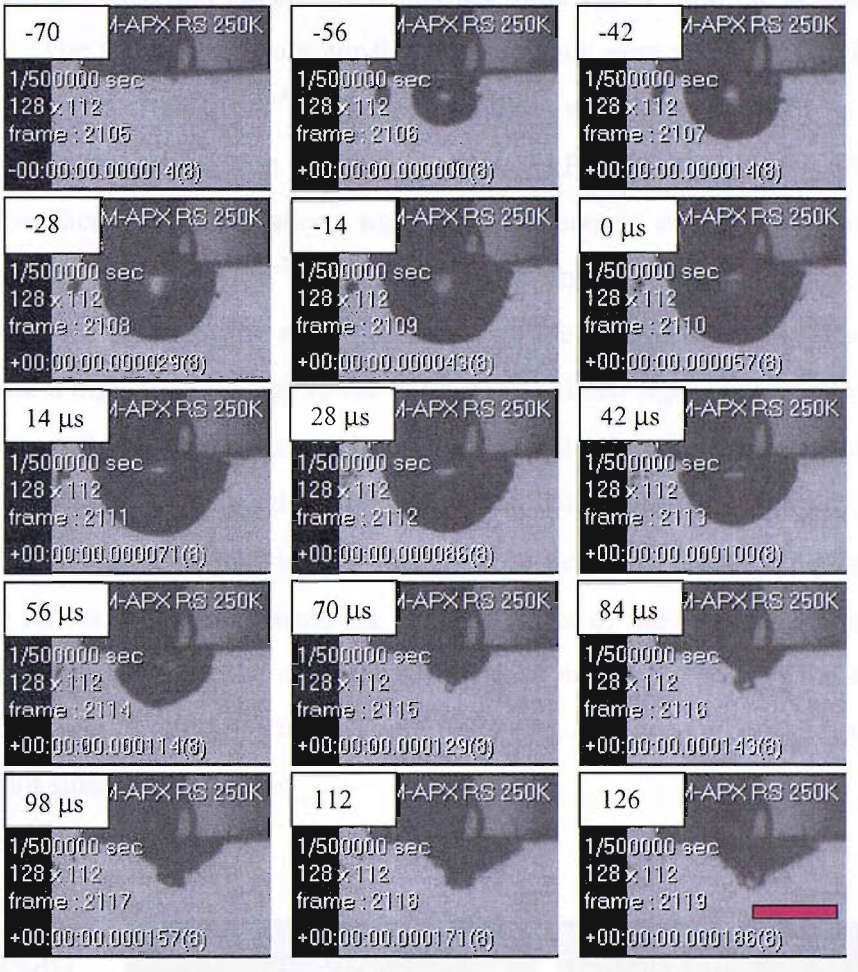

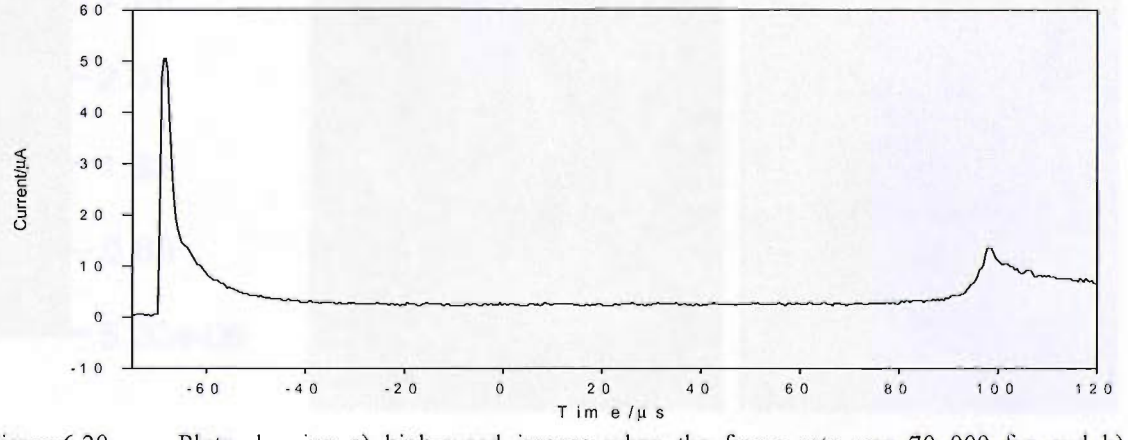

Figure 6.20 Plots showing a) high-speed images when the frame rate was 70 000 fps and b) simultaneously recorded mass transfer on 250 µm Al electrodes when exposed to laser cavitation events in 0.2 M Na_2SO_4 containing 5 mM $K_4Fe(CN)_6$ at room temperature. The laser energy was 11.5 mJ/pulse and the value of $\gamma$was 0.42. Scale bar in the picture is 500 µm.

6.3.3.2 CFD simulations

CFD (computational fluid dynamics) simulations were run based on the bubble presented in figure 6.20. These simulations are presented here. For these CFD simulations, it was assumed that the bubble contained water vapour and the surrounding liquid was water. The initial conditions for the water vapour were pressure, p_v, 23.744 kPa and density $\rho_v = 5\times10^{-6}$ g cm^{-3}. The surrounding water was thought to be at standard atmospheric conditions with pressure $p_w = 101.3$ kPa and density $\rho_w = 0.9854$ g cm^{-3}. The solid surface in the simulations was thought to consist entirely of aluminium which has the density, ρ_{Al}, 2.70 g cm^{-3}. Figure 6.21 presents the simulated bubble when the density was plotted against time at its maximum on the electrode surface, the scale bar for density and a high-speed image of the bubble taken from figure 6.20. The high-speed image presents the bubble at its maximum (taken at 0 μs on the scale presented at the top left corner of each high-speed image in figure 6.20) and for the figure 6.21, the image has been rotated 90°C clockwise in order for it to be easily comparable with the simulations. The letters A and B indicate the different sides of the bubble, A being the side of the bubble furthest from the solid/liquid interface and B the side of the bubble that is closest to the solid/liquid interface. These letters are used throughout this section to refer to different sides of the bubble.

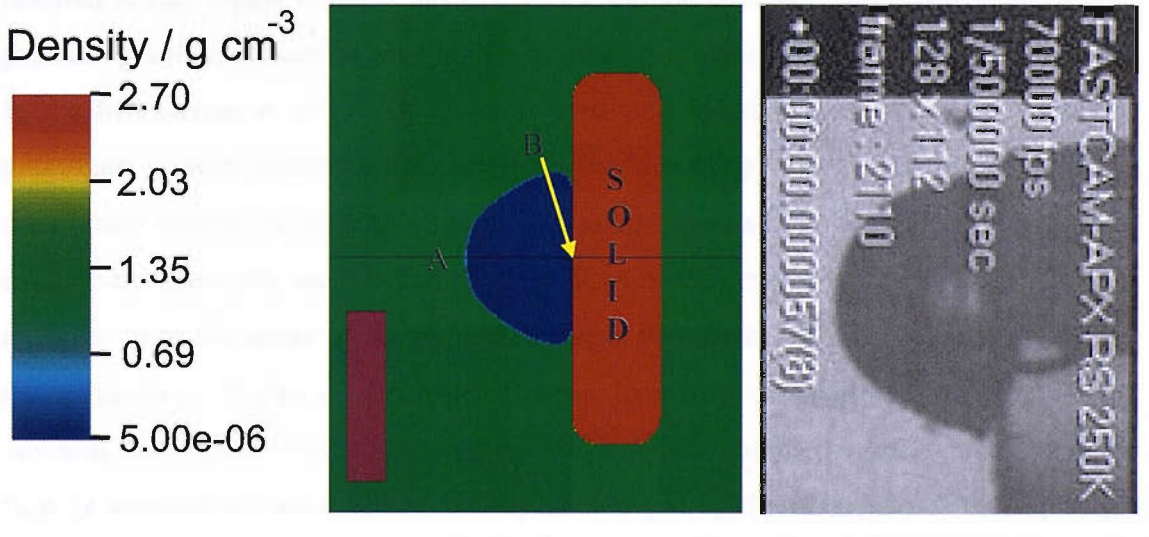

Figure 6.21 Figures showing the scale bar (1 mm) and the computer simulated cavitation at its maximum when its density was plotted against time and the high-speed image of the bubble at its maximum taken from figure 6.20. A and B indicate the different sides of the bubble.

As described previously (see section 6.2), in order to reduce the computing time of the simulations, only half of a bubble is considered due to symmetry of the problem. Figure 6.22 presents the CFD simulations for the bubble in figure 6.20 from its maximum until the first collapse when bubble density and velocity were plotted. The velocity is presented as vectors on top of the bubble density simulations. The scale for the velocity is different for each simulated image and therefore presented individually for each. The scale bar for density for all the simulated images in figures 6.22- 6.24 is the one presented in figure 6.21. Just like earlier on in this chapter in section 6.2, because $\rho_v << \rho_w$, no variation is seen at the density of the bubble. The times given for the simulated images are comparable with the times given in the top left corner for the high-speed images in figure 6.20. For the simulations, the time starts from bubble maximum presented at 0 μs.

In the first set of simulated images in figure 6.21, the images for the first 40 μs after the bubble maximum are presented at every 10 μs. These are followed by simulations for every 1-2 μs until 47 μs where the bubble collapses.

In figure 6.22, just like in the simulations presented in section 6.2, the velocity is higher on the edges of the bubble than in its interior and the direction of the flow is towards the bubble centre. It can also be observed that greater velocities are present on the side labelled A (see figure 6.20). This side of the bubble collapses faster due to the higher pressure gradient present in the liquid surrounding the bubble than on the solid surface. In the first image at 10 μs, the highest predicted speed is 3 m s^{-1}. This simulated maximum velocity increases the during the bubble collapse, and in the image at 40 μs the highest velocity is already 30 m s^{-1}. Due to the small value of γ, the bubble is so close to the electrode surface that the formation of the jet during the collapse is not as apparent from the shape of the bubble as it was in the simulations presented in section 6.2. However, it can be nevertheless seen from the simulations, that from 40 μs onwards the highest velocities are in the middle of the bubble, and the direction of the flow is towards the solid centre, clearly demonstrating the existence of the liquid jet. The velocity further increases in the following simulations at 41-46 μs reaching up to 100 m s^{-1} at 44 μs when the bubble finally collapses and attains its minimum. This is followed by a rapid rebound at 46 μs and 47 μs, where velocities as high as 80 m s^{-1} are

predicted. In these simulations presented in figure 6.22, the bubble reached its minimum in ~44-45 μs. However, in the high-speed images in figure 6.20, the bubble minimum takes place between 70 and 84 μs after its maximum. In section 6,2 the the simulated collapse time matched perfectly with the high-speed images presented in the same chapter. However, such agreement between simulations and high-speed images is not apparent for the simulations in figure 6.22 and high-speed images in figure 6.20.

In figure 6.23 the events surrounding the bubble collapse are studied in more detail with a higher resolution for the images. A close-up of simulated images for every microsecond from 43 μs to 60 μs is shown. A higher resolution makes it easier to observe the simulated velocity vectors. After reaching its minimum at 45 μs, the bubble begins to rebound very fast. Velocities as high as 120 m s^{-1} at 49 μs are simulated. The direction of the flow is now away from the solid/liquid surface. The bubble shape reminds pretty similar throughout its rebound attached to the solid surface. Similarities to the bubble shape on the recorded high-speed images in figure 6.20 can be observed, even if the time scale is different.

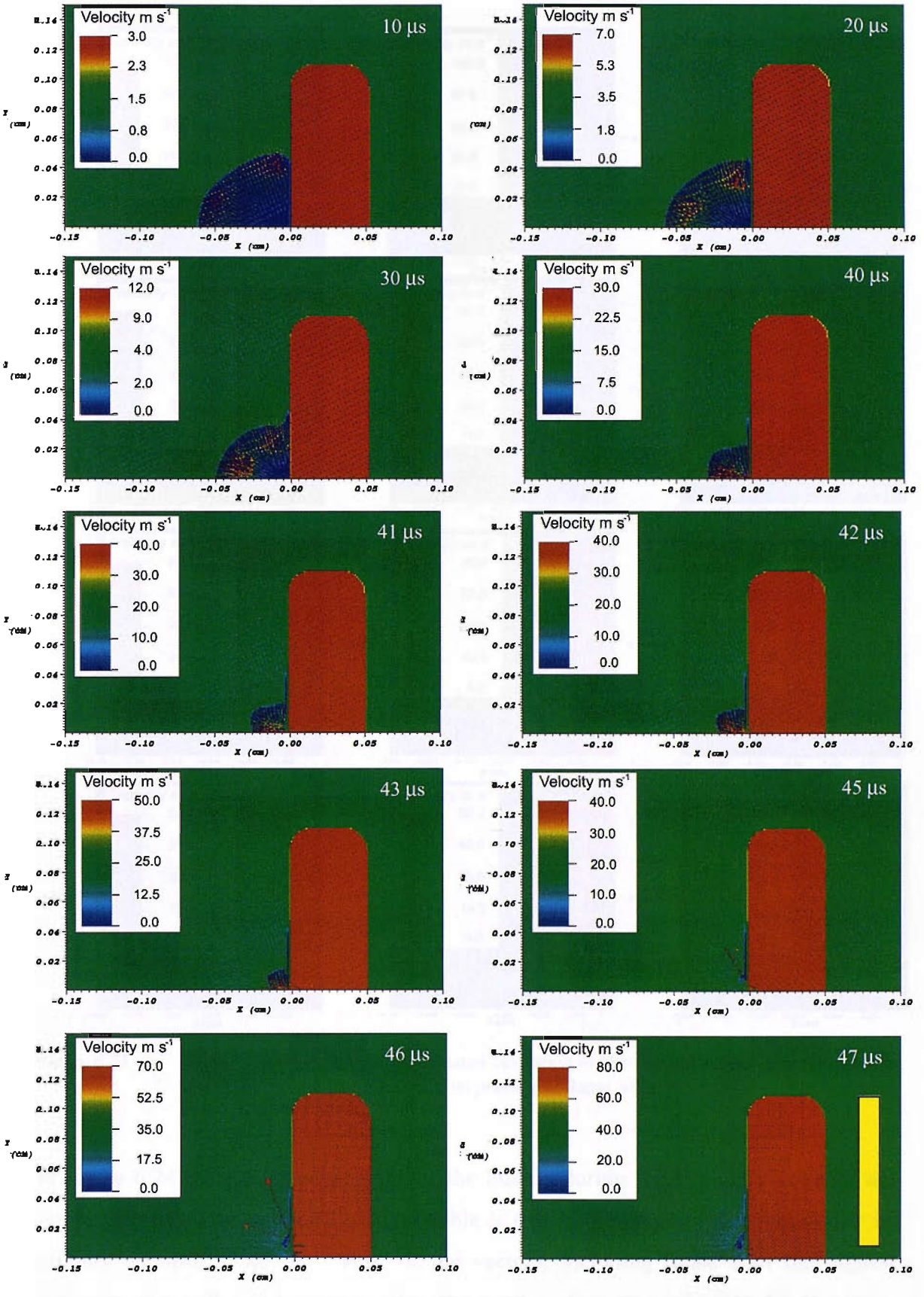

Figure 6.22 Figures showing computer simulated cavitation bubble when its density and velocities were plotted against time from its maximum until the first collapse when the γ is 0.42. The scale bar in the figure is 1 mm.

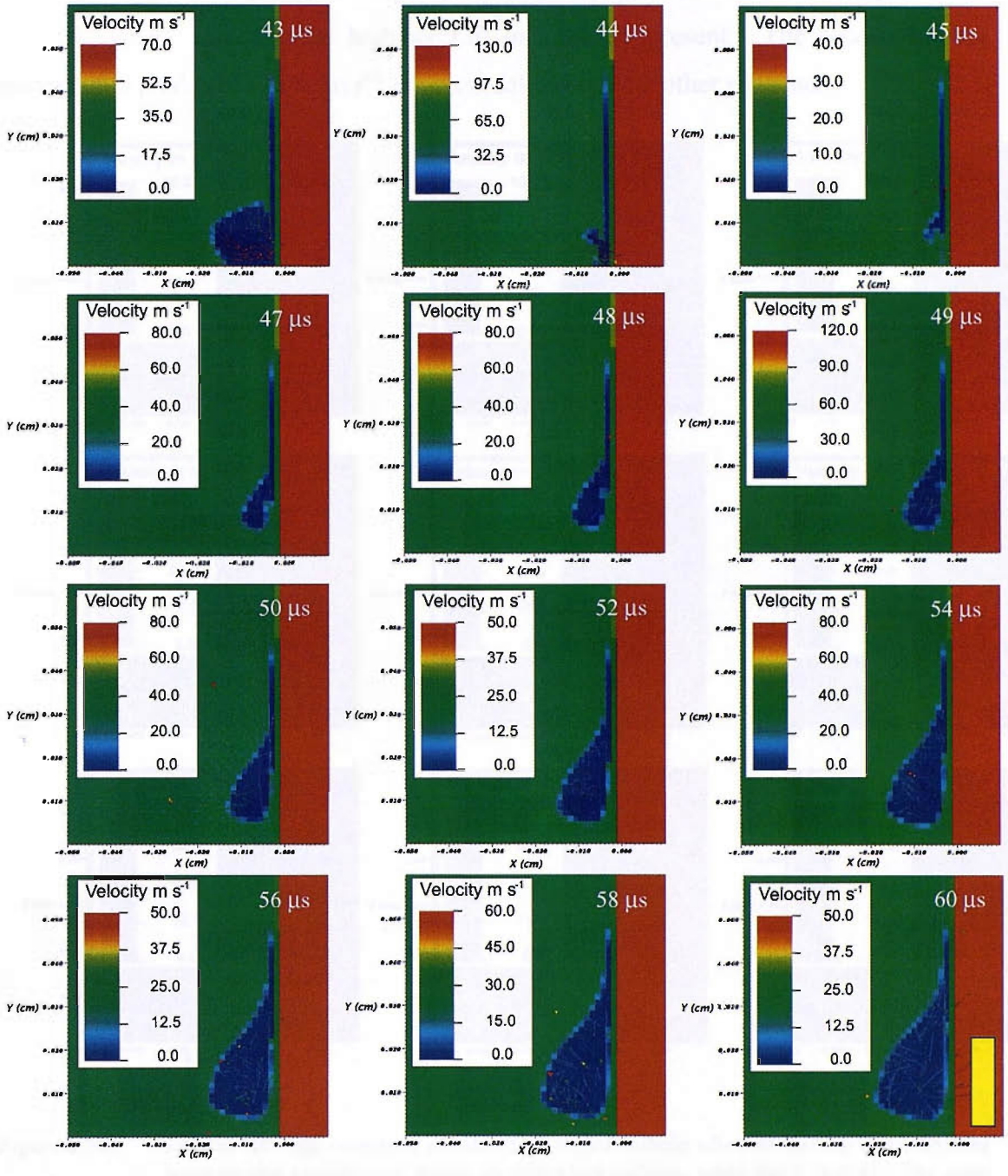

Figure 6.23 Figures showing computer simulated cavitation bubble when its density and velocities were plotted against time during its primary collapse when the γ is 0.42. The scale bar in the figure is 0.2 mm.

In figure 6.24 the simulated images for the bubble during its secondary collapse are presented. In the image at 70 µs the bubble is still in the process of rebound after its primary collapse at 45 µs. Most of the vectors, including those with the highest velocities, are still pointing away from the solid surface (towards side A). However, some of the vectors are now pointing back towards the solid surface. In the next image at 80 µs, the maximum velocity has dropped drastically to only 10 m s^{-1} as the bubble

now begins to collapse. The collapse process is now a lot slower than during the first collapse, where velocities as high as 130 m s^{-1} were present. The second bubble minimum is predicted at 100 m s^{-1}, which is followed by another rebound.

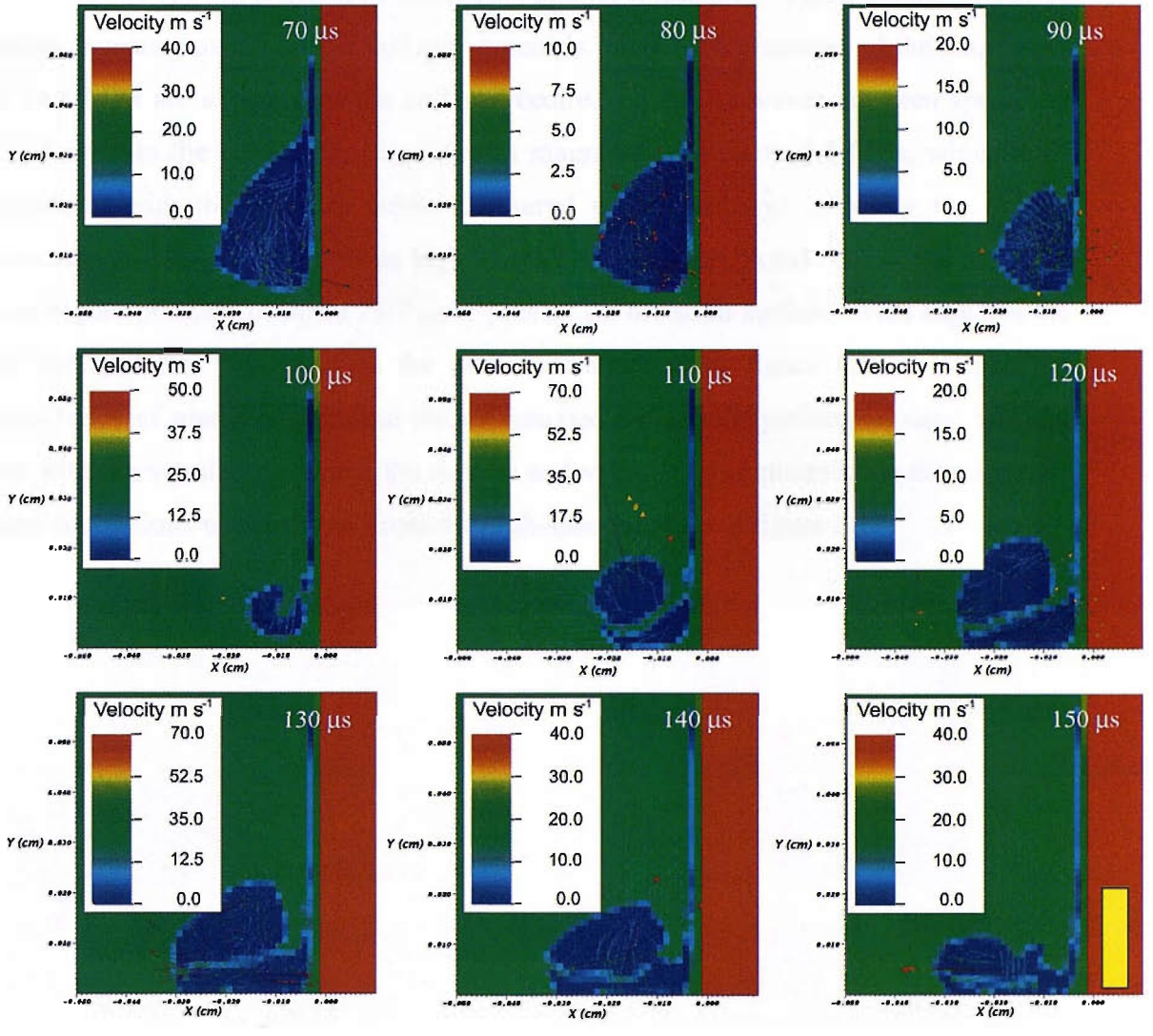

Figure 6.24 Figures showing computer simulated cavitation bubble when its density and velocities were plotted against time during its secondary collapse when the γ is 0.42. The scale bar in the figure is 0.2 mm.

Figures 6.25 presents the CFD simulations of a cavitation bubble from its maximum to its first collapse when the pressure was plotted against time. The scale bar is individual for each simulation and is presented on the right side of each image. The simulated images are presented for every 10 µs until 40 µs and every 1 µs from 40 µs to 47 µs. At 0 µs, the pressure in the liquid surrounding the bubble is uniform and the bubble is attached to the solid surface. As the bubble collapse begins, some changes in the pressure within the liquid close to the bubble are predicted. In the image at 40 µs, a

clear pressure gradient is present on side A (see figure 6.21) of the bubble, where pressures of up to 337 kPa are present. As it was stated earlier in this chapter, the ambient pressure is higher on side A of the bubble. This uneven pressure distribution leads into the uneven collapse of the bubble and jet formation. The pressure on side A further increases as the bubble collapse proceeds. At 44 μs, pressures of the magnitude of 14.8 MPa are expected at the collapse centre. Pressure waves are seen spreading circularly into the surrounding liquid with magnitudes of up to 2.5 MPa, which is in agreement with the pressure pulses measured experimentally. During the bubble minimum at ~45 μs, pressures as high as 63.7 MPa are predicted. After the collapse, even higher pressure of up to 75.7 μs is present on the solid surface. This explains the fast rebound that was seen in the earlier simulations in figure 6.23. Thus, the magnitudes of predicted pressure pulses matched with the experimental data, but just like with the simulations where the density and velocity were plotted, the time scale of these simulations was different from the high-speed images in figure 6.20.

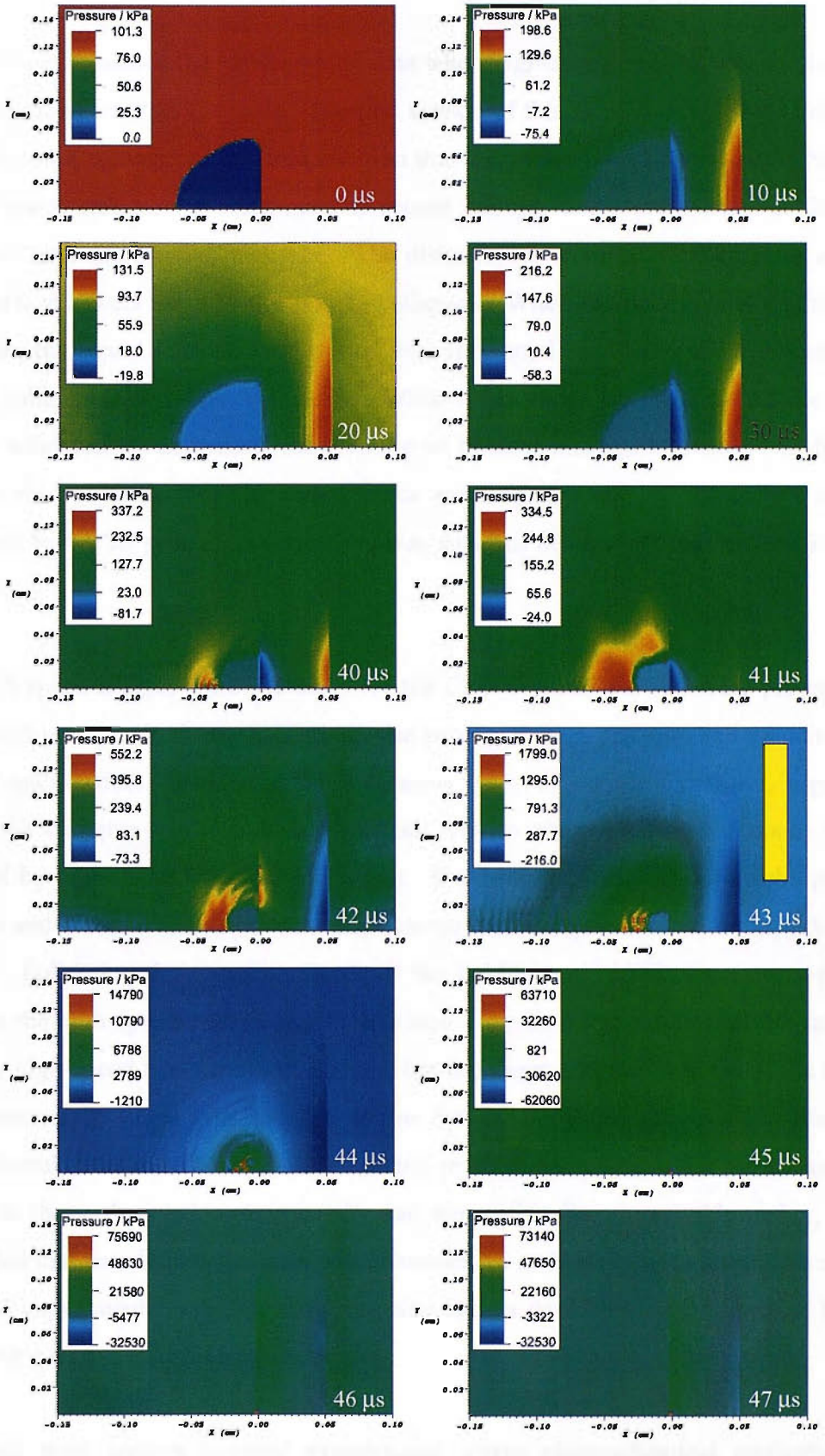

Figure 6.25 Figures showing computer simulated cavitation bubble when the pressure was plotted from its maximum to its first collapse when the γ is 0.42. The scalebar in the figure is 1 mm.

6.4 Conclusions

This chapter presented the experimental data when high-speed camera was employed to record the laser cavitation events. The first section of this chapter covered experiments, where bubbles were generated in a solution that contained 1 mM KI in 0,2 M Na_2SO_4. A high-speed camera was employed to record bubbles that were formed at different distances from the electrode surface. The distance between the bubble centre and the solid surface affects the way the bubble collapses. When the bubble was far from the electrode, the liquid jet that was formed was very small and the bubble rebound and second collapse were rather symmetric. When the distance between the bubble centre and the solid surface decreased, the forming jet became more prominent. The distance between the bubble and the electrode surface was further decreased, the bubble became elongated before its primary collapse and was attached to the electrode surface after the collapse.

The high speed images were the basis for the CFD simulations that were presented in the second section. In these simulations, the bubble density, pressure and velocity were plotted against time. This enabled a detailed study of bubble dynamics, especially during the collapse as the bubble minimum was so short-lived that it could not be captured by high-speed imaging equipment. It was concluded that during the primary collapse and the following events the simulations matched perfectly with the high-speed images. Following the second collapse of the bubble, some differences were present between the high-speed images and simulations. The time frame was still the same for both the high-speed and simulated images, but the shape and the location of the bubble were dissimilar. This was thought to be due to buoyancy forces that affect the experimental bubble. The simulated bubble pressures and predicted velocities were similar to those observed experimentally and reported in literature. Altogether, it was concluded that simulations had been rather successful and matched well with the images recorded experimentally. Therefore, the simulations could be used to predict bubble behaviour near solid surfaces.

The final third section covered experiments where electrochemical methods were combined with high-speed imaging. The electrode systems covered were Au in the

solution containing 5 mM $K_4Fe(CN)_6$ in 0.2 M $Sr(NO_3)_2$ and Pt/Al in solutions containing either KI or $K_4Fe(CN)_6$ in Na_2SO_4.

In the first set of experiments, the Au electrode was employed. The high-speed images were recorded and electrochemistry monitored for two different values of γ. Chapter 4 covered experiments where Au electrode was employed to study mass transfer events. It was then concluded that the size and response time of the electrochemical transients depended strongly on the distance between the bubble and the electrode. The results presented in section 6.3.1 of this chapter further confirmed the accuracy of these results.

Sections 6.3.2 covered the experiments where a Pt/Al electrode was employed in a solution that contained KI in Na_2SO_4. Chapter 5 discusses such experiments in the absence of high-speed imaging systems, and the purpose of section 6.3.2 was to confirm these results. The magnitude of the transients recorded in section 6.3.2 was smaller than those presented in chapter 5 section 5.3, but otherwise similar behaviour was recorded.

In section 6.3.3 Pt/Al electrode was employed on a solution that contained $K_4Fe(CN)_6$ in Na_2SO_4. Chapter 5 reported experiments where this system was studied in detail. Some excellent results were presented in that chapter, and therefore the same system was employed together with a high speed camera. A bubble that collapsed very close to the electrode surface was recorded by both the high-speed camera and electrochemical means. The electrochemical transient recorded was similar to those reported in chapter 5, but there was some disagreement with the time scale between electrochemical and high-speed recordings. A collection of CFD simulations based on the high-speed images reported in section 6.3.3 were also presented. These simulations corresponded well to the shape, location and magnitude of the events observed by high-speed camera, but the time scale was different, predicting a much shorter collapse time. Obviously, more work is needed in this field to ensure that the CFD simulations provide accurate results also when the bubble is formed very close to the solid surface.

Chapter 7

Experimental problems observed with high-speed imaging

Chapters 3, 4 and 5 presented data where laser cavitation events were investigated by electrochemical means. Throughout the experiments a number of problems were encountered when the bubbles were generated by a laser. For example variation in the size of detected currents was present even when the position of the electrode or the laser energy was not changed. It was thought that the size or the position of the generated bubbles varied or multiple bubbles were present at times. It was necessary to employ a high-speed camera to confirm whether such events actually took place. These problems were only observable when high-speed camera was employed and could not be detected accurately by electrochemical means alone.

One of the main problems observed was the formation of multiple bubbles. As explained in chapters 1 and 2, the choice of employed lenses and focussing angles has an important role in the bubble generation. If the focussing angle was too shallow, multiple bubbles are generated as the long beam waist enables the occurring of optical breakdown at multiple locations simultaneously. A focussing angle that is too steep can lead to spherical aberration effects and again multiple bubble formation. Even though a lot of effort was put into optimising the optical arrangement throughout this project, the problem of multiple bubble formation could never be entirely eliminated. Figures 7.1 and 7.2 present examples of high-speed images where multiple bubbles were generated. Figure 7.1 shows a secondary bubble, however it is rather small and does not significantly affect the collapse of the primary bubble. In figure 7.2 the situation is different. The secondary bubble that is formed on the left hand side (opposite to the entry direction of the laser beam) of the primary bubble affects the way the primary bubble collapses. When the bubble is still growing, the side of the bubble that is on the right in the image has a spherical shape, whereas the left side is flattened there where the secondary bubble is formed. When the bubble starts collapsing, the right side is even but a bulge is seen on the left throughout the collapse.

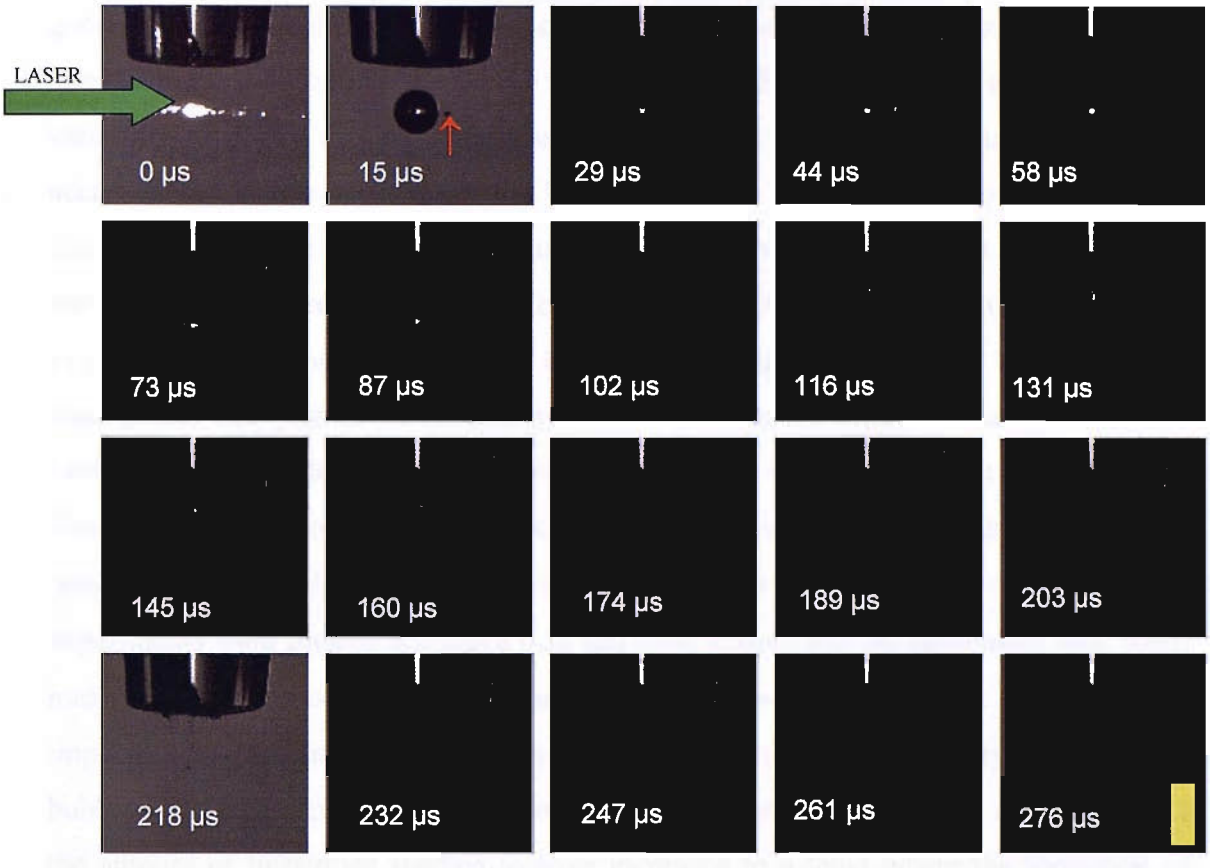

Figure 7.1 Images showing a bubble generated in a solution of KI in Na_2SO_4 at room temperature when the applied laser energy was 9 mJ/pulse. The camera speed was 68 000 fps. The laser beam entered the cell from left (green arrow). The red arrow indicates the forming secondary bubble. The scale bar in the figure is 1mm.

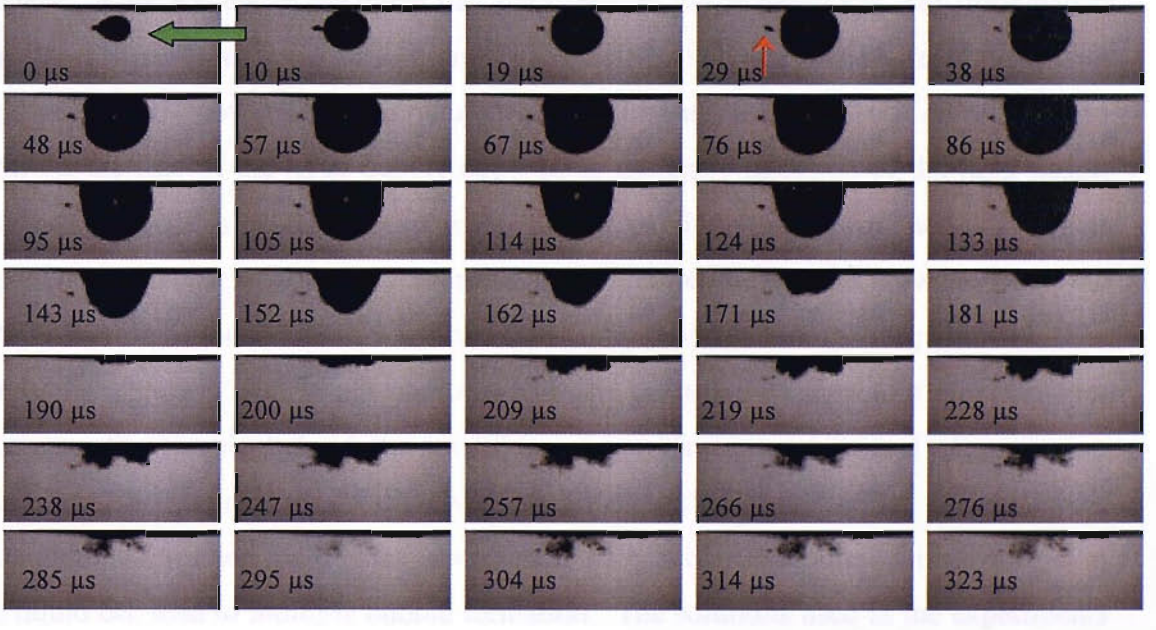

Figure 7.2 Images showing a bubble generated in a solution of KI in Na_2SO_4 at room temperature when the applied laser energy was 11.5 mJ/pulse. The camera speed was 105 000 fps. The laser beam entered the cell from right (green arrow). The red arrow indicates the forming secondary bubble.

However, problems with the focussing optics were not the only reason for the generation of multiple bubbles. In fact, the focussing optics were likely to have only a minor role in the generation of these extra bubbles. Even if the laser energy was not varied, sometimes a single bubble was formed and at other times one large bubble was accompanied by one or more smaller bubbles. As the lenses or their position were not changed during one series of experiments, it could be concluded that these multiple bubbles were not a result of the employed optical arrangement alone. It was explained in chapter 1 that when laser induced breakdown of liquid is generated by nanosecond laser pulses the plasma is formed by a process called cascade ionisation. For the cascade ionisation to occur, some seed electrons need to be present in the liquid. Usually these are provided by dust etc. particles. Therefore it is likely that the multiple bubbles were a result of impurities in the liquid. The employed solutions used in the experiments were filtered through a 0.22 μm filter system and the equipment used when making the solutions was also washed with filtered water to decrease the amount of impurities in the final solution. This seemed to improve the quality of generated bubbles, but only temporarily. Within 30 to 60 minutes after the start of experiments the amount of impurities seemed to have increased to a level where the formation of multiple bubbles became more frequent. It was thought that impurities were introduced in the liquid when the electrode was inserted into it (through, for example, particulate matter). Also, the electrochemical cell employed in the experiments was open which enabled dust particles from air to be imported into the solution. It was also noted that especially on the lower laser energies, the small unwanted bubble was more likely to form on the side of the large bubble opposite to the entry direction of the laser beam. The reason for this could be explained by the moving breakdown model that was described in chapter 1 [45,49]. According to this model the plasma grows towards the entry direction of the laser beam which leads to the formation of one large bubble. The excess laser energy that is not consumed by the plasma may therefore form another much smaller bubble behind the initial larger bubble if suitable seed electrons are present. Also the presence of dissolved gas in the solution can affect the quality of generated bubbles and thereby the electrochemically recorded results. Dissolved gas in the liquid can lead to multiple bubble formation. The solutions used in the experiments were degassed before the start of experiments, but the affect of this was again only temporary.

It was also noticed that after the bubble collapse small bubbles remained in the solution and got trapped onto the electrode surface. Such situation is presented in figure 7.3. The small bubble is barely visible in the first image (pointed by the arrow). But when a large cavitation bubble is generated by the laser, as the cavitation bubble grows in size the small bubble trapped on the electrode surface also grows, eventually becoming part of the cavitation bubble and collapsing with it. There can be several such bubbles trapped on the surface that are also affected by the shock waves generated at optical breakdown and when the cavitation bubble collapses. They also expand and collapse which can affect the recorded electrochemical transients. Such problems could be avoided if the electrode was located below the bubble instead of above it, but this arrangement was not experimentally possible.

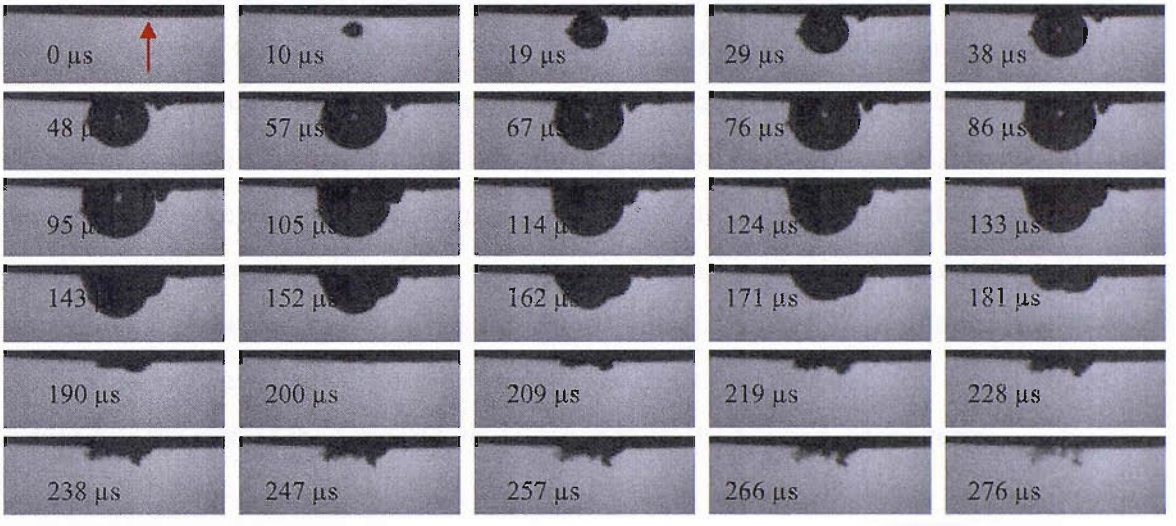

Figure 7.3 Images showing the interaction between a gas bubble trapped on the electrode surface and a laser generated bubble in a solution of KI in Na_2SO_4 at room temperature when the applied laser energy was 11.5 mJ/pulse. The camera speed was 105 000 fps. The red arrow indicates the small bubble trapped on the electrode surface.

Leaking electrodes also posed another problem as can be seen in figure 7.4. The water or other impurities trapped somewhere in the electrode (for example between the wire and epoxy) leaks out during the experiments forming a large bubble on the electrode surface. This obviously affects the quality of recorded electrochemistry significantly. In figure 7.4 a flow of material is seen coming out of the electrode (indicated by an arrow) and creating a large gas bubble on its surface.

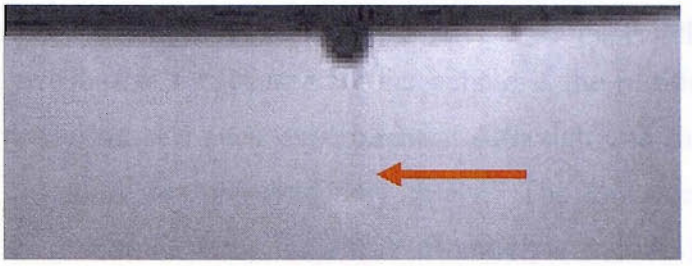

Figure 7.4 Image showing leaking electrode with a gas bubble forming on its surface in a solution of KI in Na_2SO_4 at room temperature. The red arrow indicates the material coming out of the electrode.

Another problem encountered during the experiments was the variation in the size and location of the formed bubble. Figures 7.5 presents three different bubbles at their maximum generated during the same experimental session. All the conditions including the applied laser energy and the position of the camera were exactly the same but yet bubbles of very different size were generated. One reason for this is the aforementioned presence of too many dust particles and dissolved gas in the liquid. If plenty of particles are present on the optical path of the laser beam this can lead to formation of several plasmas that are combined to form one large bubble. On the other hand, some fluctuation of the laser energy is inevitable at the energies employed in the experiments presented in this project (5-50 mJ/pulse). Therefore, a difference of a few millijoules between two different laser pulses can be expected. As it was stated in figure 6.1, the size of the formed bubble depends on the applied laser energy.

Figure 7.5 Images showing three bubbles generated in a solution of KI in Na_2SO_4 at room temperature when the applied laser energy was 11.5 mJ/pulse. The camera speed was 105 000 fps. The scale bar in the figure is 1 mm.

Figure 7.6 presents two bubbles that were captured during one experimental session in exactly similar conditions. As it can be seen from the figures the location where the bubbles are formed is not the same for the two figures. The bubble in figure 7.6 a is located further to left from the bubble in figure 7.6 b. Again, the impurities in the solution can provide an explanation. Ideal particles to provide the seed electrons can be located at different parts of the optical path and result in variations in the location where

the plasma is formed. Obviously this would have a significant impact if the recorded electrochemical events that are caused by the bubble if the position of the electrode remains the same during two such experiments. Although one should also note that such change in location was observed only rarely. The unwanted events described above (difference in bubble size, formation of multiple bubbles) were much more frequent.

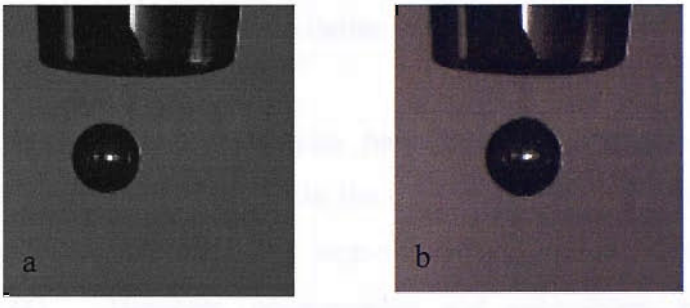

Figure 7.6 Images showing two bubbles generated in a solution of KI in Na_2SO_4 at room temperature when the applied laser energy was 9 mJ/pulse. The camera speed was 68 000 fps.

For all the aforementioned reasons the employment of high-speed camera is highly desirable during laser cavitation experiments. Such changes in the position, size or number of the bubbles could go unnoticed if only electrochemistry was used. Some changes could naturally be observed from the magnitude of the recorded electrochemical transient or from the collapse time that depends on the bubble size. But in order to be certain the employment of high-speed imaging equipment is essential.

Chapter 8

Conclusions and future work

In this thesis, acoustic, electrochemical and high-speed photographic means were employed to study laser generated cavitation events.

In the past electrochemical techniques have been successfully employed to study acoustic cavitation events [93-95]. On the other hand, the cavitation events generated by laser have mostly been studied by high-speed photographic and ex-situ microscopic means [18,20,21]. However, photographic and microscopic means alone do not provide sufficient accuracy required to understand the cavitation damage mechanisms. Microscopic investigation of the surface made after the erosion process alone is also unreliable due to altering of the surface. More accurate spatial and temporal information of the erosion on a solid surface can be gained by using electrodes to record the cavitation events as they occur. Altering the location of the electrode can provide accurate information of the events as similar bubbles can be produced by the laser.

In this project, mass transfer onto the electrode surface and surface erosion were investigated by employing several different electrode materials and solutions. Initially, a Pb/Pt dual microelectrode was used to study erosion and mass transfer simultaneously. These results were presented in chapter 3. Even though some good results were gained, it was obvious that as a material lead was not the best choice to study optical cavitation. Some heating effects were present and therefore lead was not an ideal material for erosion studies. The response time of lead was too long. Events that were detected at the optical breakdown took too long to return to the 0 A -level and the effects of bubble collapse could not be detected properly. Later on, the lead electrode was replaced by aluminium and some excellent results were achieved (see chapter 5). A large current transient was observed at 0 s when the optical breakdown occurred, but more interestingly, another event was observed at 140-250 μs (depending on the bubble size that is proportional to the collapse time) when the bubble collapsed. These results indicated that a significant part of the erosion was caused by the laser and the collapse

of the bubble was not the only cause of surface erosion. This would not be observed if microscopic methods alone were employed.

Mass transfer was studied simultaneously with erosion employing a 50 μm Pt disc (chapters 3, 5 and 6) and alone by employing a 25 μm gold disc (chapter 4). The affect of different laser energies and the position of the electrode on the detected current were investigated. It was noted, that the size of the observed current was dependant on both applied laser energy and the distance between the electrode surface and the bubble. This indicated that the electrochemical methods were well-suited to study laser generated cavitation. Diffusion coefficients of the magnitude up to 5.0×10^{-6} cm^2 s^{-1} were observed when the mass transfer on gold disc was studied in the absence of erosion sensor.

When the mass transfer and erosion sensors were employed simultaneously, it was noted that erosion was only detected when the bubble was formed very close to the electrode surface. Moving the electrode upwards (z-direction) from the bubble just by 100 μm resulted in significant decrease in the magnitude of the observed transients. The recorded transients were also very sensitive to movement in horizontal (x,y) directions. On the other hand, mass transfer sensors were able to observe movement in liquid (caused by bubble formation and collapse) from much greater distances as can be expected.

High-speed cameras were employed to record the cavitation events. The camera enabled the accurate determination of the bubble size and the distance between the bubble and the solid surface. Bubble collapse dynamics could also be studied more accurately by high-speed photographic means. CFD (computational fluid dynamics) simulations were run based on the high-speed images taken during this project. In these simulations, the bubble density, pressure and velocity were plotted. These simulations enabled more precise investigation of the bubble dynamics at its minimum which is too short-lived to be captured by high-speed imaging in detail. For the value γ = 1.8, the simulation matched very well with the recorded high-speed images until the second collapse of the bubble. When γ = 0.42, the shape of the simulated bubble was similar to the one high-speed images, but the time scale was slightly different.

Significant amount of time during this project was spent for designing the experimental set-up. The experiment was much more difficult than predicted and constructing and improving the performance of the experimental rig was found very time-consuming.

The simultaneous employment of laser, electrochemical, acoustic and high-speed imaging techniques was already a challenge in itself and therefore the experimental set-up required constant improvement and adjustments. In addition, several experimental and technical problems were encountered throughout the project. These included multiple bubble formation, differences in bubble size and location, leaking electrodes, noise, slow response times and breaking equipment (laser, high-speed cameras).

By the end of this project, the experimental set-up was sufficient to produce good quality results. However, there are still several things one could do to improve the experiment. Suggested improvements to the experimental set-up include:

- focussing
    - attaching the lens directly to the cell wall enables shorter focus
- employing a cubic cell or cuvette
    - reduce acoustic noise
    - easier to construct
    - shorter focus easier to employ and better access for the electrode to the cell could be provided
- improving the electrode holder
    - fixed positioning for electrode: enabling the position of the electrode to be constant. By the aid of camera it was possible to make sure the electrode was at the same position in z direction between different experiments. However differences were always present on x,y plane between different experiments.
    - firmer hold: electrode held uniformly from each side (it was noted that the electrode was often not direct as it was pushed towards one direction by the tightened screws)
- electrode (problems encountered that need fixing)
    - coupling
    - leaking

    - damaged quickly
    - brought impurities into the liquid
- power attenuation: the laser fluctuation is decreased at higher powers (could be done for example by polariser and half wave plate, was attempted once unsuccessfully. However, the results achieved at this point were satisfactory and no further attempts were done).
- Impurities: dust and other particles were present in the liquid. Filtering and degassing only provided temporary solution
    - clean lab
    - covering the bench
    - filtering in regular intervals to remove dirt brought into the cell by the electrode
    - covered cell
    - constant air blow over the bench to remove dust [67]

In the future, it would be beneficial to employ 1064 nm (IR) wavelength instead of 532 nm. The breakdown threshold is lower for 532 nm than for 1064 nm. The employment of 1064 nm might enable the elimination of some of the problems discussed in chapter 7 such as formation of multiple bubbles. This wavelength has different absorption properties to 532 nm which could improve the reproducibility of the experiments.

Good understanding and new knowledge of the laser cavitation process were obtained during this project. However, it would be useful to complete further studies about the mechanisms responsible for surface erosion, possibly by employing different materials. Combination of electrochemistry and laser cavitation would also be a good experimental system to study the erosion resistance of different coating once the erosion mechanism is fully understood. Such studies would also be industrially relevant.

Publications

1. H.M. Hirsimäki, P. R. Birkin, J. G. Frey and T. G. Leighton, The laser-Induced formation of plasma bubbles in water-electrochemical measurements, *IOA Spring Conference,* Southampton, IOA, 876-884 (2006)

2. P. R. Birkin, H.M. Hirsimäki, J. G. Frey and T. G. Leighton , Mass transfer enhancement produced by laser induced cavitation, *Electrochemistry Communications*, **8**(10), 1603 (2006)

3. P. R. Birkin, H.M. Hirsimäki, J. G. Frey and T. G. Leighton, Time resolved erosion from single laser induced cavitation events, *In Preparation*, 2007

4. P. R. Birkin, H.M. Hirsimäki, C. Vian, J. G. Frey and T. G. Leighton, A comparison of cavitation events generated from power ultrasound and a laser., *In Preparation*, 2007

Appendix A

Visual Basic Codes

1. Stepper motor

```
Dim Distance

Private Sub Command1_Click()
'Execute a move

MSComm1.CommPort = 4            ' Set the port number
MSComm1.Settings = "9600,N,8,1"   ' Set UART parameters
MSComm1.PortOpen = True         ' Required, might lock port
MSComm1.Output = "1ON" & Chr$(13)
MSComm1.Output = "1LIMITS(3,0,0)" & Chr$(13)    ' Send data
Distance = NumEditDistance.Value
If ButtonUpDown.Value = True Then Distance = Distance * -1   'Decides whether to go up or down
step$ = (Distance / 0.0025) * 10 ' calculates the number of steps
MSComm1.Output = "1D" + step$ & Chr$(13)  ' Send data
MSComm1.Output = "1G" & Chr$(13)    ' Send data
MSComm1.PortOpen = False          ' Required, might lock port

End Sub

Private Sub Command2_Click()

MSComm1.CommPort = 4            ' Set the port number
MSComm1.Settings = "9600,N,8,1"   ' Set UART parameters
MSComm1.PortOpen = True         ' Required, might lock port
MSComm1.Output = "1S" & Chr$(13)    ' Send data
MSComm1.PortOpen = False          ' Required, might lock port

End Sub

Private Sub Command3_Click()
MSComm1.CommPort = 4            ' Set the port number
MSComm1.Settings = "9600,N,8,1"   ' Set UART parameters
MSComm1.PortOpen = True         ' Required, might lock port
MSComm1.Output = "1OFF" & Chr$(13)    ' Send data
MSComm1.PortOpen = False          ' Required, might lock port


End Sub

Private Sub CWButton1_ValueChanged(ByVal Value As Boolean)
End Sub
```

2. Acquisition software

```
Const BoardNum% = 1            ' Board number
Const NumPoints& = 2000        ' Number of data points to collect
Const FirstPoint& = 0          ' set first element in buffer to transfer to array
                    ' dimension an array to hold the input values
Dim MemHandle&                 ' define a variable to contain the handle for
Dim ADData%(NumPoints&)        ' memory allocated by Windows through cbWinBufAlloc%()
Dim HighChan%
Dim EngUnits(NumPoints)
Dim Data(1000, NumPoints)
Dim counter As Integer
Dim timeframe
Dim time(NumPoints)
Dim datatoview As Integer
Dim Datax(20000)
Dim DataY(20000)
Dim StopAq
Dim plotcounter
Dim Mark(1000)
Dim s As Integer


Private Sub cmdBacktoYt_Click()

   Form5.Visible = False
   Form2.Visible = True

End Sub

Private Sub cmdStart_Click()


   Form5.Caption = "Trigger Program"
   StopAq = 0

   timeframe = InputBox("Enter event timeframe in microseconds (>50)", "Event Timeframe", 100)

   If timeframe >= 50 Then
      If IsNumeric(timeframe) Then
         cmdView.Enabled = False
         cmdBacktoYt.Enabled = False
         File.Enabled = False

         cmdStart.Visible = False
         cmdStop.Visible = True
      Else
      MsgBox "Invalid Timeframe. Please Try Again", vbCritical, "Error"
      Exit Sub
      End If
   Else
   MsgBox "Invalid Timeframe. Please Try Again", vbCritical, "Error"
   Exit Sub
   End If

   Do

   dummy% = DoEvents()
```

```
If StopAq = 1 Then
Exit Sub
End If

' Collect the values with cbAInScan%()
' Parameters:
'  BoardNum%   :the number used by CB.CFG to describe this board
'  LowChan%    :the first channel of the scan
'  HighChan%   :the last channel of the scan
'  CBCount&    :the total number of A/D samples to collect
'  CBRate&     :sample rate
'  Gain        :the gain for the board
'  ADData%     :the array for the collected data values
'  Options     :data collection options

If Option1.Value = True Then
   HighChan% = 0
   LowChan% = 0
End If

If Option2.Value = True Then
   HighChan% = 1
   LowChan% = 1
End If

If Option3.Value = True Then
   HighChan% = 2
   LowChan% = 2
End If

If Option4.Value = True Then
   HighChan% = 3
   LowChan% = 3
End If

CBCount& = NumPoints&              ' total number of data points to collect
CBRate& = 1000000 * (NumPoints& / timeframe)   ' sampling rate (samples per second)
Options = CONVERTDATA + EXTTRIGGER  ' return data as 12-bit values
Gain = BIP5VOLTS                   ' set the gain

If MemHandle& = 0 Then Stop    ' check that a handle to a memory buffer exists

If CWButton1.Value = False Then TrigType% = 0
If CWButton1.Value = True Then TrigType% = 1

gai = 10 ^ Slider1.Value
TrigCurrent! = CWNumEdit1.Value * 10 ^ CWNumEdit2.Value
TrigVoltage! = TrigCurrent! * gai

Ulstat% = cbFromEngUnits(BoardNum%, Range%, TrigVoltage!, TrigValue%)

Ulstat% = cbSetTrigger(BoardNum%, TrigType%, TrigValue%, TrigValue%)

Ulstat% = cbAInScan(BoardNum%, LowChan%, HighChan%, CBCount&, CBRate&, Gain,
MemHandle&, Options)

If Ulstat% = 30 Then MsgBox "Change the Gain argument to one supported by this board.", 0,
"Unsupported Gain"
If Ulstat% <> 0 And Ulstat% <> 91 Then Stop
```

```
    ' Transfer the data from the memory buffer set up by Windows to an array for use by Visual Basic

    Ulstat% = cbWinBufToArray(MemHandle&, ADData%(0), FirstPoint&, CBCount&)
    If Ulstat% <> 0 Then Stop

    counter = counter + 1
    datatoview = counter
    lblNoEvents.Caption = counter
    CWNumEdit3.Maximum = counter
    For N = 0 To NumPoints - 1
       Ulstat% = cbToEngUnits(BoardNum%, Gain, ADData(N), EngUnits(N))
       If Ulstat% <> 0 Then Stop
       Data(counter, N) = EngUnits(N) / gai
    Next N


    'If counter = 1 Or counter = 10 Then

       'CWGraph1.ClearData
       'For np = 0 To NumPoints - 1
       '   If np = 0 Then time(np) = 0
       '   If np > 0 Then time(np) = time(np - 1) + (timeframe / NumPoints)
       '   CWGraph1.ChartXvsY time(np), Data(counter, np)
       'Next np
    'End If

    Loop Until counter = 1000
End Sub

Private Sub cmdStop_Click()

    'ULStat% = cbWinBufFree(MemHandle&)      ' Free up memory for use by
                                    ' other programs
    'If ULStat% <> 0 Then Stop
    StopAq = 1
    'tmrTrigger.Enabled = False
    cmdStop.Visible = False
    cmdStart.Visible = True
    cmdView.Enabled = True
    cmdBacktoYt.Enabled = True
    File.Enabled = True

End Sub

Private Sub cmdQuit_Click()
Dim yesno

yesno = MsgBox("Are you sure you want to quit?", vbQuestion + vbYesNo, "Quit")

If yesno = 6 Then End

End Sub

Private Sub cmdView_Click()
Dim N
    datatoview = CWNumEdit3.Value
    If datatoview > 0 Then
    If datatoview <= counter Then
     If IsNumeric(datatoview) Then
    CWGraph1.ClearData
```

```
   For N = 0 To NumPoints - 1
      If N = 0 Then time(N) = 0
      If N > 0 Then time(N) = time(N - 1) + (timeframe / NumPoints)
     CWGraph1.ChartXvsY time(N), Data(datatoview, N)
   Next
  Else
  MsgBox "Invalid Dataset. Please try again", vbCritical, "Error"
  End If
  Else
  MsgBox "Invalid Dataset. Please try again", vbCritical, "Error"
  End If
  Else
  MsgBox "Invalid Dataset. Please try again", vbCritical, "Error"
  End If

End Sub

Private Sub cmdReset_Click()
List1.Clear
counter = 0
CWNumEdit3.Maximum = 0
lblNoEvents.Caption = "0"
   s = -1

End Sub

Private Sub Command1_Click()


s = s + 1
Mark(s) = counter - 1
List1.AddItem Mark(s)
End Sub



Private Sub Command2_Click()
Dim N

CWGraph1.ClearData
datatoview = Mark(List1.ListIndex)

   For N = 0 To NumPoints - 1
      If N = 0 Then time(N) = 0
      If N > 0 Then time(N) = time(N - 1) + (timeframe / NumPoints)
     CWGraph1.ChartXvsY time(N), Data(datatoview, N)
   Next
End Sub

Private Sub CWNumEdit3_ValueChanged(Value As Variant, PreviousValue As Variant, ByVal
OUTOFRANGE As Boolean)
cmdView.TabIndex = 0
End Sub

Private Sub Form_Load()
Dim Ulstat%


   s = -1
```

```
    ' declare revision level of Universal Library

    Ulstat% = cbDeclareRevision(CURRENTREVNUM)

    ' Initiate error handling
    '  activating error handling will trap errors like
    '  bad channel numbers and non-configured conditions.

    '  Parameters:
    '    PRINTALL    :all warnings and errors encountered will be printed
    '    DONTSTOP    :if an error is encountered, the program will not stop,
    '                 errors must be handled locally

    Ulstat% = cbErrHandling(PRINTALL, DONTSTOP)
    If Ulstat% <> 0 Then Stop

    ' If cbErrHandling% is set for STOPALL or STOPFATAL during the program
    ' design stage, Visual Basic will be unloaded when an error is encountered.
    ' We suggest trapping errors locally until the program is ready for compiling
    ' to avoid losing unsaved data during program design.  This can be done by
    ' setting cbErrHandling options as above and checking the value of ULStat%
    ' after a call to the library. If it is not equal to 0, an error has occurred.

    MemHandle& = cbWinBufAlloc(NumPoints&)      ' set aside memory to hold data
    If MemHandle& = 0 Then Stop

End Sub



Private Sub List1_Click()
CWNumEdit3.Value = Mark(List1.ListIndex)
End Sub

Private Sub Open_Click()

Dim nop
Dim No
Dim E$
Dim i$

    Form5.filebox.CancelError = True
    On Error GoTo ErrHandle
    Form5.filebox.FileName = "*.dat"
    Form5.filebox.InitDir = "C:\doug\data"
    Form5.filebox.Action = 1
    Form5.Caption = Form5.filebox.FileName
    Open Form5.filebox.FileName For Input As #5

    No = -1

    Do
       No = No + 1
       Input #5, E$
       Datax(No) = Val(E$)
       Input #5, i$
       DataY(No) = Val(i$)
    Loop Until EOF(5)
    Close #5
 CWGraph1.ClearData
```

```
    For nop = 0 To No
      CWGraph1.ChartXvsY Datax(nop), DataY(nop)
    Next

ErrHandle:    Exit Sub

End Sub

Private Sub Option1_Click()

    MsgBox "Remember to Set Trigger Channel in InstaCal", vbExclamation, "Reminder"

End Sub

Private Sub Option2_Click()

    MsgBox "Remember to Set Trigger Channel in InstaCal", vbExclamation, "Reminder"

End Sub

Private Sub Option3_Click()

    MsgBox "Remember to Set Trigger Channel in InstaCal", vbExclamation, "Reminder"

End Sub

Private Sub Option4_Click()

    MsgBox "Remember to Set Trigger Channel in InstaCal", vbExclamation, "Reminder"

End Sub

Private Sub Save_Click()

 Dim ns

 Form5.filebox.CancelError = True

    On Error GoTo ErrHandle
    Form5.filebox.Flags = &H2&
    Form5.filebox.FileName = "*.dat"
    Form5.filebox.InitDir = "C:\doug\data"
    Form5.filebox.Action = 2
    Form5.Caption = Form5.filebox.FileName
    Open Form5.filebox.FileName For Output As #2

    ns = -1

    Do
      ns = ns + 1
      Print #2, time(ns); ","; Data(datatoview, ns)
    Loop Until ns = NumPoints - 1

    Close #2
ErrHandle:    Exit Sub
End Sub
Private Sub SaveAll_Click()
 Dim ns

 Form5.filebox.CancelError = True
```

```
    On Error GoTo ErrHandle
    Form5.filebox.Flags = &H2&
    Form5.filebox.FileName = "*.dat"
    Form5.filebox.InitDir = "C:\doug\data"
    Form5.filebox.Action = 2
    Form5.Caption = Form5.filebox.FileName
    Open Form5.filebox.FileName For Output As #7

    For N = 0 To NumPoints - 1
       If N = 0 Then time(N) = 0
       If N > 0 Then time(N) = time(N - 1) + (timeframe / NumPoints)
    Next N
For p = 0 To NumPoints - 1
fileline$ = time(p)
  For q = 1 To counter
       fileline$ = fileline$ & "," & Data(q, p)
Next q
Print #7, fileline$
Next p

    Close #7
ErrHandle:    Exit Sub
End Sub
```

3. Solenoid trigger for single pulses

```
' File:                    ULDO01.MAK

' Library Call Demonstrated:    cbDOut%()

' Purpose:                  Writes a byte to digital output ports.

' Demonstration:            Configures FIRSTPORTA for output and writes
'                       a value to the port.

' Other Library Calls:      cbDConfigPort%()
'                       cbErrHandling%()

' Special Requirements:     Board 0 must have a digital output port.
'                       Board 0 must have programmable digital ports.

' (c) Copyright 1995-2002, Measurement Computing Corp.
' All rights reserved.
'==========================================================================

Const BoardNum = 1          ' Board number

'Const PortNum% = FIRSTPORTA    ' use first digital port
Const PortNum% = 1

Const Direction% = DIGITALOUT    ' program digital port A for output
```

```
Private Sub cmdEndProgram_Click()

  DataValue% = 0

  ULStat% = cbDOut(BoardNum, PortNum%, DataValue%)
  If ULStat% <> 0 Then Stop

  End

End Sub



Private Sub CWButton1_ValueChanged(ByVal Value As Boolean)

Select Case CWButton1.Value
Case True
DataValue% = 255
Case False
DataValue% = 0
End Select

ULStat% = cbDOut(BoardNum, PortNum%, DataValue%)

  If ULStat% <> 0 Then Stop
End Sub

Private Sub Form_Load()

  ' declare revision level of Universal Library

  ULStat% = cbDeclareRevision(CURRENTREVNUM)

  ' Initiate error handling
  '  activating error handling will trap errors like
  '  bad channel numbers and non-configured conditions.
  '  Parameters:
  '    PRINTALL    :all warnings and errors encountered will be printed
  '    DONTSTOP    :if an error is encountered, the program will not stop,
  '                 errors must be handled locally


  ULStat% = cbErrHandling(PRINTALL, DONTSTOP)
  If ULStat% <> 0 Then Stop

  ' If cbErrHandling% is set for STOPALL or STOPFATAL during the program
  ' design stage, Visual Basic will be unloaded when an error is encountered.
  ' We suggest trapping errors locally until the program is ready for compiling
  ' to avoid losing unsaved data during program design.  This can be done by
  ' setting cbErrHandling options as above and checking the value of ULStat%
  ' after a call to the library. If it is not equal to 0, an error has occurred.


  ' configure FIRSTPORTA for digital output
  '  Parameters:
  '    BoardNum    :the number used by CB.CFG to describe this board
  '    PortNum%    :the output port
  '    Direction%  :sets the port for input or output

  ULStat% = cbDConfigPort(BoardNum, PortNum%, Direction%)
```

```
  If ULStat% <> 0 Then Stop

End Sub
```

4. Camera Trigger

```
' File:                    ULAI01.MAK

' Library Call Demonstrated:   cbAIn%()

' Purpose:                 Reads an A/D Input Channel.

' Demonstration:           Displays the analog input on a user-specified
'                          channel.

' Other Library Calls:     cbErrHandling%()

' Special Requirements:    Board 0 must have an A/D converter.
'                          Analog signal on an input channel.

' (c) Copyright 1995-2002, Measurement Computing Corp.
' All rights reserved.
'==========================================================================
Const PortNum% = 1
Const Direction% = DIGITALOUT    ' program digital port A for output
Const BoardNum% = 1              ' Board number


Private Sub cmdStartConvert_Click()

  cmdStartConvert.Visible = False
  cmdStopConvert.Visible = True
  cmdStopConvert.Default = True
  tmrConvert.Enabled = True

End Sub

Private Sub cmdStopConvert_Click()

  tmrConvert.Enabled = False
  End

End Sub

Private Sub Form_Load()

  ' declare revision level of Universal Library

  ULStat% = cbDeclareRevision(CURRENTREVNUM)

  ' Initiate error handling
  '  activating error handling will trap errors like
  '  bad channel numbers and non-configured conditions.
  '  Parameters:
  '    PRINTALL    :all warnings and errors encountered will be printed
  '    DONTSTOP    :if an error is encountered, the program will not stop,
  '                 errors must be handled locally
```

```
  ULStat% = cbErrHandling(PRINTALL, DONTSTOP)
  If ULStat% <> 0 Then Stop

  ' If cbErrHandling% is set for STOPALL or STOPFATAL during the program
  ' design stage, Visual Basic will be unloaded when an error is encountered.
  ' We suggest trapping errors locally until the program is ready for compiling
  ' to avoid losing unsaved data during program design.  This can be done by
  ' setting cbErrHandling options as above and checking the value of ULStat%
  ' after a call to the library. If it is not equal to 0, an error has occurred.

End Sub

Private Sub tmrConvert_Timer()

  ' Collect the data with cbAIn%()

  '  Parameters:
  '    BoardNum%    :the number used by CB.CFG to describe this board
  '    Chan%        :the input channel number
  '    Gain         :the gain for the board.
  '    DataValue%   :the name for the value collected

  Gain = BIP5VOLTS            ' set the gain
  Chan% = Val(txtNumChan.Text)  ' set input channel

  Do
  DoEvents
  ULStat% = cbAIn(BoardNum%, Chan%, Gain, DataValue%)
  If ULStat% = 30 Then MsgBox "Change the Gain argument to one supported by this board.", 0,
"Unsupported Gain"
  'If ULStat% <> 0 Then Stop

  ULStat% = cbToEngUnits(BoardNum%, Gain, DataValue%, EngUnits!)
  'If ULStat% <> 0 Then Stop

  'lblShowData.Caption = Format$(DataValue%, "0")   ' print the counts
  'lblShowVolts.Caption = Format$(EngUnits!, "0.000") + " Volts"   ' print the voltage
   volt = Format$(EngUnits!, "0.000")


   Loop Until volt > 0.4 ' trigger from the photodiode the flash and camera.

   DataValue% = 255 ' pulse
   ULStat% = cbDOut(BoardNum, PortNum%, DataValue%)
   DataValue% = 0
   ULStat% = cbDOut(BoardNum, PortNum%, DataValue%)

  If ULStat% <> 0 Then Stop
End Sub
```

References

1. W. Lauterborn Ed, *Cavitation and Inhomogenities in Underwater Acoustics*, Springer, Berlin, Germany (1980).

2. C. E. Brennen, *Cavitation and bubble dynamics*, Oxford University Press, UK, (1995).

3. F. Ronald Young, *Cavitation*, McGraw-Hill Book Company, Maidenhead, England, 1989

4. L. Rayleigh, Phil. Mag., **34**, 94 (1917).

5. T.J. Mason, *Prog. Biophys. Mol. Bio.*, **83**(103), 166 (2007)

6. F. Lugli, F. Zerbetto, *Phys. Chem. Chem. Phys.* **9**, 2447 (2007)

7. P. Cintas, J.L. Luche, *Green Chemistry*, **1**, 115 (1999)

8. J.P. Franc, J.M. Micel, *Fundamentals of cavitation (Fluid Mechanics and Its Applications)*, Springer (2004)

9. W. Tillner, H. Fritsch, R. Kruft, W. Lehmann, H. Louis, G. Masendorf, *Avoidance of Cavitation Damage: Principles, Methods of Test, Applications, Experience,* Wiley, 2005

10. S.J. Shaw, W.P. Schiffers, T.P. Gentry, D.C. Emmony, *J. Phys. D: Appl. Phys.*, **32**, 1612 (1999).

11. S.C. Li (Ed.), *Cavitation of Hydraulic Machinery*, World Scientific Publishing, (2000)

12. K.S. Suslick, Y. Didenko, M.M. Fang, T. Hyeon, K. Kolbeck, W.B. McNamara III, M.M. Mdleleni, M. Wong, *Phil. Trans. Roy. Soc. A.*, **357**(1751), 335 (1999)

13. K. Suslick, *IEEE Ultrasonics Symposium Proceedings*, **1-2**, 523 (1997)

14. K.S. Suslick, D.A. Hammerton, R.E. Cline, *J. Am. Chem. Soc.*, **108**(18), 5641 (1986)

15. S.J. Shaw, W.P. Schiffers, D.C. Emmony, *J. Acoust. Soc. Am.*, **110**, 1822, (2001).

16. T. G. Leighton, *The Acoustic Bubble*, Academic Press Limited, London, (1994).

17. Y.T. Didenko, K.S. Suslick, *Nature*, **418**, 394 (2002).

18. W. Lauterborn, *Acustica*, **31**, 51 (1974).

19. K.J. Ebeling, *Acustica*, **40**, 229 (1978).

20. Y. Tomita, A. Shima, *Acustica*, **71**, 161 (1990).

21. A. Philipp, W. Lauterborn, *J. Fluid. Mech.*, , **361**, 75 (1998).

22. J.C. Isselin, A.P. Alloncle, M. Autric, *J. Appl. Phys.*, **84**, 5766 (1998)

23. W. Lauterborn, H. Bolle, *J. Fluid. Mech.*, **72**, 391 (1975).

24. A. Vogel, W. Lauterborn, R. Timm, *J. Fluid. Mech.*, **206**, 299 (1989).

25. J. Hecht, *Understanding lasers*, 2nd edition, IEEE Press, John Wiley & Sons, New Jersey, USA (2001).

26. E. Hecht, *Optics*, Addison Wesley, 4th Edition (2001)

27. Max Born, *Principles of Optics: Electromagnetic Theory of Propagation, Interference and Diffraction of Light*, 7th edition, Cambridge Univeristy Press, (1999)

28. D.L. Andrews, *Laser in Chemistry*, 3rd edition, Springer, Berlin, Germany, (1997)

29. O. Svelto, *Principles of Lasers,* Plenum Press, New York (1998)

30. A. Philipp, *Kavitationerosion durch lasererzeugte Einzelblasen*, PhD Thesis, die Technische Hochschule Darmstadt, Darmstadt, Germany (1995).

31. A. Brodeaur, F.A. Ilkov, S.L. Chin, *Optics Communications*, **129**, 193 (1996)

32. M.M.T. Loy, Y.R. Shen, *IEEE J. Quant. Electronics*, **QE-9**(3), 409 (1973)

33. M.J. Soileau, W.F. Williams, N. Mansour, E.W. Van Stryland, *Opt. Eng.*, **4**, 1133 (1989)

34. S.J. Gitomer, R. D. Jones, *IEEE Trans. Plasma. Sci.*, **19**(6), 1209 (1991).

35. A.Vogel, K. Nahen, D. Theisen, J. Noack, *IEEE Journal of Selected Topics in Quantum Electronics*, **2**(4), 847 (1996).

36. P.K. Kennedy, D.X. Hammer, B.A. Rockwell, *Prog. Quant. Electr.*, **21**(3), 155 (1997).

37. C. H. Fan, J.P. Longtin, *ASME International Mechanical Engineering Congress and Exposition*, HTD Vol 3, November 5-10, Orlando, Florida (2000).

38. A. Vogel, *Phys. Med. Biol.*, **42**(5), 895-912 (1997)

39. J.P. Sylvestre, A.V. Kabashin, E. Sacher, M. Meunier, *Appl. Phys. A.*, **80**, 753 (2005)

40. C. DeMichelis, *IEEE J. Quant. Electronics*, **QE-5**(4), 188 (1964)

41. N. Bloembergen, *IEEE J. Quant. Electronics*, **QE-10**(3), 375 (1974)

42. G. Bekefi (Ed.), *Principles of Laser Plasmas*, John Wiley & Sons, New York (1976)

43. F. Ready, *Effects of High-Power laser radiation*, Academic Press, London (1971)

44. A. Vogel, P. Schweiger, A. Frieser, M.N. Asiyo, R. Birngruber, *IEEE J. Quant. Electronics*, **26**(12), 2240 (1990)

45. J. Noack, D.X. Hammer, G.D. Noojin, B.A.Rockwell, A. Vogel, *J. Appl. Phys.* **83**(12), 7488 (1998)

46. M.P. Felix, A.T. Ellis, *Appl. Phys. Lett.*, **19**(11), 484 (1971)

47. A. Vogel, S. Busch, U. Parlitz, *J. Acoust. Soc. Am.*, **100**(1), 148 (1996)

48. P. K. Kennedy, *IEEE J. Quant. Electronics*, **31**(12), 2241 (1995)

49. F. Docchio, P. Regondi, M.R.C. Capon, J. Mellerio, *Appl. Opt.*, **27**(17), 3661 (1988)

50. F. Docchio, P. Regondi, M.R.C. Capon, J. Mellerio, *Appl. Opt.*, **27**(17), 3669 (1988)

51. F. Docchio, C.A. Sacchi, J. Marshall, *Laser Ophthalmol.*, **1**, 83, 1986

52. C.A. Sacchi, *J. Opt. Soc. Am. B.*, **8**(2), 337 (1991)

53. Y.R. Shen, *Principles of Non-Linear Optics*, Wiley, New York 1984)

54. M.Bass, H.H. Barrett, *IEEE J. Quant. Electronics*, **QE-8**(3), 338 (1972)

55. A Vogel, W. Lauterborn, *J. Acoust. Soc. Am.*, **84**, 719 (1988)

56. J.B. Daiber, H.M. Thompson, *Phys. Fluids*, **10**(6), 1162 (1967)

57. A. Vogel, S. Busch, *J. Acoust. Soc. Am.*, **100**(1), 148 (1996)

58. P.A. Barnes, K.E. Rieckhoff, *Appl. Phys. Lett.*, **13**(8), 282 (1968)

59. Yu. P. Raizer, *Sov. Phys. Usp.*, **8**, 650 (1966)

60. M. Harrison, *J. Acoust. Soc. Am.*, **24**(4), 776 (1952)

61. T.B. Benjamin, A.T. Ellis, *Phil. Trans. R. Soc. Lond. A*, **260**, 221 (1966)

62. I. Akhatov, O. Lindau, A. Topolnikov, R. Mettin, N. Vakhitova, W. Lauterborn, *Phys. Fluids*, **13**(10), 2805 (2001)

63. W. Lauterborn, C.D. Ohl, *Ultrasonics Sonochemistry*, **4**, 65 (1997)

64. A. Philipp, W. Lauterborn, *Acustica*, **83**, 223 (1997)

65. S.J. Shaw, W.P. Schiffers, T.P. Gentry, D.C. Emmony, *J. Acoust. Soc. Am.*, **107**(6), 3065 (2000)

66. Y. Tomita, A. Shima, *J. Fluid Mech.*, **169**, 535 (1986)

67. O. Lindau, *Untersuchungen zur Lasererzeugte Kavitation*, PhD Thesis, Georg-August-Universität-Göttingen, Der Andere Verlag, Osnabrück, Germany (2001)

68. X. Chen, R.Q. Xu, Z.H. Shen, J. Lu, X.W. Ni, *Optics & Laser Technology*, **36**, 197 (2003)

69. P.B. Robinson, J.R. Blake, T. Kodama, A. Shima, Y. Tomita, *J. Appl. Phys.*, **89**(12), 8225 (2001)

70. A. Prosperetti, *Ultrasonics*, **22**, 115 (1984).

71. J.P. Chen, X.W. Ni, J. Lu, B.M. Bian, Y.W. Wang, *Microwave and Optical Technology Letters*, **25**, 307 (2000).

72. S.J. Shaw, Y.H. Jin, W.P. Schiffers, D.C. Emmony, *J. Acoust. Soc. Am.*, **99**, 2811 (1996).

73. M.S. Plesset, R.B. Chapman, *J. Fluid. Mech.*, **47**, 283 (1971).

74. O. Lindau, W. Lauterborn, *J. Fluid. Mech.*, **479**, 327, (2003).

75. *Characterisation and Determination of Erosion Resistance*, ASTM, 1969, Philadelphia

75. J. Klima, C. Bernard, C. Degrand, *J. Electroanal. Chem.*, **399**, 147 (1995)

76. K. S. Suslick, *Science*, **247**, 1439 (1990)

77. E. B. Flint, K. S. Suslick, *J. Am. Chem. Soc.*, **111**, 6987 (1989)

78. T. J. Mason, *Sonochemistry, The Uses of Ultrasound in Chemistry*, Royal Society of Chemistry, Cambridge (1989)

79. J. P. Lorimer, T. J. Mason, *Chem. Soc. Rev.*, 1987, **16**, 239-274

80. A.J Bard, *Anal. Chem.*, **35**, 1125 (1963)

81. P. R. Birkin, S. Silva-Martinez, J. Chem. Soc. Chem. Comm., 1807 (1995

82. J. Klima, C. Bernard, C. Degrand, *J. Electroanal. Chem.*, **367**, 297 (1994)

83. C.R.S. Hagan, L. A. Coury. *Anal. Chem.,* Vol. **66**, 399 (1994)

84. H. D. Dewald, B. A. Peterson., *Anal. Chem.*, 1990, **62**, 779 - 782

85. C. M. Preece, I. H. Hansson, *Adv. Mech. Phys. Surf.*, **1**, 199 (1981)

86. S. A. Perusich and R. C. Alkire. *J. Electrochem. Soc.,* **138,** part I , 700 (1991)

87. S. A. Perusich and R. C. Alkire. *J. Electrochem. Soc.,* **138,** part II, 708 (1991)

88. H. Zhang, L. A. Coury. *Anal. Chem.,* **65**, 1552 (1993)

88. N. A. Madigan, C. R. S. Hagan, L. A Coury, *J. Electrochem. Soc.*, **141**, L23 (1994)

89. R.G. Compton, J.C. Eklund, S.D. Page, G.H.W. Sanders, J. Booth, *J. Phys. Chem.*, **98**, 12410 (1994)

90. R.G. Compton, J.C. Eklund, S.D. Page, T.O. Rebbitt, *J. Chem. Soc., Dalton Trans.*, (3), 389 (1995)

91. R.G. Compton, J.C. Eklund, F. Marken, T.O. Rebbitt, R.P. Akkermans, D.N. Weller, *Electrochimica Acta*, **42**, 2919 (1997)

92. R. M. Wightman, D. O. Wipf, *J. Electroanal. Chem.*, **15**, 267 (1989)

93. P.R. Birkin, R. O'Connor, C, Rapple, S. Silva-Martinez, *J. Chem. Soc., Faraday Trans.*, **94**, 3365 (1998).

94. P. R. Birkin, D. G. Offin and T. G. Leighton, *Electrochemistry Communications*, **6**, 1174 (2004)

95. D.G. Offin, *Acoustoelectrochemical Characterisation of Cavitation and Its Use in the Study of Surface Processes*, PhD Thesis, University of Southampton (2005)

96. http://www.mellesgriot.com/products/optics/oc_4_1.htm

97. S. Silva-Martinez, *Application of Ultrasound in Electrochemistry*, PhD thesis, University of Southampton (1997)

98. J.F. Smalley, L. Geng, A. Chen, S.W. Feldberg, N.S. Lewis, G. Cali, *J. Electroanal. Chem.*, **549**, 13 (2003)

99. L.B. Lowe, S.H. Brewer, S. Krämer, R.R. Fuierer, G. Qian, C.O. Agbasi-Porter, S. Moses, S. Franzen, D.L. Feldheim, *J. Am. Chem. Soc.*, **125**(47), 14258 (2003)

100. C. Phipps, *Laser Ablation and Its Applications*, Springer, USA (2006)

101. H.W. Kang, A.J. Welch, *J. Appl. Phys.*, **101**(8), 083101 (2007)

101. R.C. Anderson, P.E. Fasm, *Inspection of Metals, Volume II, Destructive Testing*, ASM, USA (1988)

102. G.V. Samsonov, *Handbook of the Physicochemical Properties of Elements*, IFI Pleneum, New York, USA (1968)

103. M. Pourbaix, *Atlas of Electrochemical Equilibria in Aqueous Solutions*, Pergamon, New York (1966)

104. G.S. Frankel, C.V. Jahnes, V. Brusic, A.J. Davenport, *J. Electrochem. Soc.*, **142**(7), 2290 (1995)

105. R.P. Tong, W.P. Schiffers, S.J. Shaw, J.R. Blake, D.C. Emmony, *J. Fluid. Mech.*, **380**, 339 (1999)

106. K.S. Tan, A.W. Hassel, M. Stratman, *Mat.-wiss. U. Werkstofftech.*, **36**(1), 13 (2005)

107. Shaw *et al.*, *J. Acoust. Soc. Am.*, **110** (4), 1822 (2001)